INTERACTION OF ELECTROMAGNETIC WAVES WITH DIELECTRIC DISKS AND RODS

By

HASSAN ULLAH

QUAID-I-AZAM UNIVERSITY
Department of Electronics

Author's Declaration

I, **Hassan Ullah** hereby state that my PhD thesis titled **"Interaction of Electromagnetic Waves with Dielectric Disks and Rods"** is my own work and has not been submitted previously by me for taking degree from **Department of Electronics, Quaid-i-Azam University** Or anywhere else in the country/world.

At any time if my statement is found to be incorrect even after my graduation, the university has the right to withdraw my PhD degree.

Hassan Ullah

Date: 04 NOV, 2021

QUAID-I-AZAM UNIVERSITY
Department of Electronics

Plagiarism Undertaking

I solemnly declare that research work presented in the thesis titled

"Interaction of Electromagnetic Waves with Dielectric Disks and Rods"

is solely my research work with no significant contribution from any other person. Small contribution/help wherever taken has been duly acknowledged and that complete thesis has been written by me.

I understand the zero tolerance policy of the HEC and Quaid-i-Azam University towards plagiarism. Therefore, I as an Author of the above titled thesis, declare that no portion of my thesis has been plagiarized and any material used as reference is properly referred/cited.
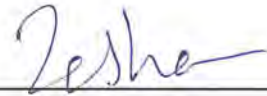
I undertake that if I am found guilty of any formal plagiarism in the above titled thesis even after award of PhD degree, the University reserves the rights to withdraw/revoke my PhD degree and that HEC and the University has the right to publish my name on the HEC/University Website on which names of students are placed who submitted plagiarized thesis.

Student/Author Signature: _____

Name: **Hassan Ullah**

CERTIFICATE

It is certified that **Mr. Hassan Ullah** has carried out the work contained in this dissertation under my supervision

(Prof. Dr. Zeeshan Akbar Awan)

Department of Electronics,

Quaid-i-Azam University,

Islamabad, Pakistan.

Submitted Through

Chairman

(Prof. Dr. Syed Aqeel Abbas)

Department of Electronics,

Quaid-i-Azam University,
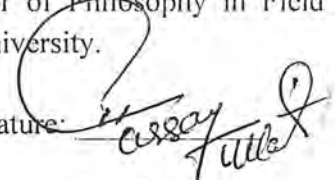
Islamabad, Pakistan.

QUAID-I-AZAM UNIVERSITY

Department of Electronics

Certificate of Approval

This is to certify that the research work presented in this thesis, entitled "**Interaction of Electromagnetic Waves with Dielectric Disks and Rods**" was conducted by **Mr. Hassan Ullah** under the supervision of **Dr. Muhammad Zeeshan Akbar.** No part of this thesis has been submitted anywhere else for any other degree. This thesis is submitted to the **Department of Electronics, Quaid-i-Azam University** in partial fulfilment of the requirements for the degree of Doctor of Philosophy in Field of **Electronics,** Department of Electronics, Quaid-i-Azam University.

Student Name: **Mr. Hassan Ullah**   Signature:
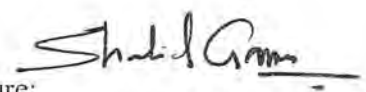
Examination Committee:

A. Prof, Dr. Sajid Qamar   Signature:
   Chairman, Department of Physics,
   COMSATS University, Park Road, Chak Shahzad,
   Islamabad.

B. Dr. Shahid Qamar   Signature:
   Department of Physics and Applied Mathematics,
   Pakistan Institute of Engineering and Applied Sciences (PIEAS),
   Nilore, Islamabad.

C. Dr. Muhammad Zeeshan Akbar   Signature:
   Assistant Professor & Supervisor
   Department of Electronics
   Quaid-i-Azam University, Islamabad.

Supervisor Name: **Dr. Muhammad Zeeshan Akbar**   Signature:

Name of Chairman: **Prof, Dr. Syed Aqeel A. Bukhari**   Signature:

To My Parents and Family.

Table of Contents

Acknowledgements

In the name of Allah, the most gracious, the most merciful. All thanks to Allah, the lord of both worlds, and my prayers and peace be upon our Holy Prophet Muhammad (S.A.W.A).

I would like to express my sincere gratitude towards my Supervisor, Prof. Dr. Zeeshan Akbar Awan, whose talent and enthusiasm has inspired me to devote myself into the path of seeking truth and knowledge. I learned from him how to analyze a problem from the first physical principle, and to move upon a solution based on careful logical deduction, experienced mathematical derivation, and genuine physical insights. It has been a pleasant journey learning from and working with him.

My profound thanks and incalculable depth of gratitude are also due to all the faculty members and staff members for being so considerate and caring whose guidance and hardwork made me capable of doing work, especially, Prof. Dr. Aqeel Abbas (Chairman), Dr. Qaisar Abbas Naqvi, Dr. M. Farhan Saif, Dr. Hasan Mahmood, Dr. Muhammad Zia, Dr. Muhammad Aqeel Ashraf, Dr. Musarat Abbas, Dr. Arshad Hussain, Dr. Qurrat-ul-Ain Minhas, Dr. Muhammad Arshad Fiaz, Dr.Naeem Ali Bhatti and Dr. Azhar Abbas Rizvi.

I would like to thank all my colleagues and friends at the Department of Electronics, Quaid-i-Azam University for their friendship and encourgement. Special thanks to

List of publications

1. Hassan Ullah, Arshed Hussain, and Z. A. Awan, "Back-scattering cross section from a tilted thin circular dielectric disk," *Optik - International Journal for Light and Electron Optics*, vol. 203, (2020), 163862.

2. Hassan Ullah, and Z. A. Awan, "Scattering of electromagnetic waves from a thin triangular dielectric disk," *Optik - International Journal for Light and Electron Optics*, vol. 227, (2021), 165224.

3. Z. A. Awan, Hassan Ullah, Ahsan ullah, Afshan Ashraf "Effective parameters of a metamaterial composed of dielectric coated conducting cylindrical rods" *IJMWT - International Journal of Microwave and Wireless Technologies*, Volume 12, Special Issue 8 (Special Issue EuMW 2019. Part II) October 2020 , pp. 797-808

4. Hassan Ullah, Arshed Hussain, and Z. A. Awan, "Back-scattered cross section from a sparse distribution of tilted thin dielectric disks," *Optik - International Journal for Light and Electron Optics*, vol. 234, (2021), 166551.

5. Hassan Ullah, and Z. A. Awan, "Back-scattering cross section from a Sparse distribution of tilted thin Triangular Dielectric Disks," *(Submitted)*.

6. Hassan Ullah, and Z. A. Awan, "Scattering of electromagnetic waves from a Pentagonal Dielectric Disk," *(To be submitted very soon)*.

7. Hassan Ullah, and Z. A. Awan, "Back-scattering from a hexagonal dielectric disk," *To be submitted very soon*.

Abstract

In this dissertation, the interaction of electromagnetic waves with dielectric disks and rods are investigated. The challenging objective of this study is to investigate the enhancements and reductions of the scattered electric field from these targets using the well known existing models. The reduction in the radar cross section (RCS) from these targets is extremely important in designing of the modern remote sensing systems i.e., radar and stealth technologies. This dissertation is divided into two parts. In the first part of the dissertation, an analytical solution is provided to investigate the effects of tilt angles upon the back-scattering cross section of a thin dielectric circular disk. This analytical solution is based upon three different scattering approximations such as Rayleigh-Gans, Volume Integral Physical Optics and Koh-Sarabandi by considering both types of incident polarization i.e., horizontal and vertical. It is investigated that by varying the orientation of the disk, the back-scattering cross section can be enhanced or diminished as compared to the disk having no tilt. It is further studied that for the specific tilt and size parameter of a low loss Gallium Arsenide (GaAs) disk, the back-scattering cross sections can be made almost equal to zero for both types of incident polarizations. Later on, the disk-shape effects of a thin dielectric disk upon the back-scattering cross sections for both types of incident polarizations have been studied. For the solution of this problem, an analytic theory for the scattering of electromagnetic waves from various shapes of thin dielectric disks is developed. This proposed theory is based on the Koh-Sarabandi (KS) approximation for the electromagnetic wave scattering from a thin dielectric disk along with the spectral representation of the dyadic Green's function. The considered disk shapes

are triangular, elliptical, circular, semi-circular and square disks having same elec-tromagnetic and geometrical parameters. It is studied that the back scattering cross sections for a low loss Gallium Arsenide (GaAs) triangular disk at a specific incidence angle can be made almost zero for both types of incident polarizations is the lowest for both types of incident polarizations. Attention is then focused upon the computation of the coherent electromagnetic wave scattering from a sparsely distributed N-tilted thin circular disks. The influences of the various parameters including incident angle, size parameter of the disk, relative permittivity of the disk and spacing among disks upon the back-scattered cross sections have been studied for incident horizontal and vertical polarizations. Some conditions are discussed where a pair of sparsely located tilted low loss Gallium Arsenide disks significantly reduced the back-scattered cross section as a compared to a single tilted Gallium Arsenide disk.

In the second major part of this dissertation, I primarily focused on the scattering characteristics of the electromagnetic Metamaterials. Firstly, an analytical theory is developed and studied for the scattering characteristics of an isolated dielectric and dielectric coated conducting rods. The types of dielectric materials considered are Barium Strontium Titanate (BST) $Ba_{0.5}Sr_{0.5}TiO_3$, Magnetodielectric, Gallium Arsenide (GaAs) and Silicon Carbide (SiC). It is found that the gallium arsenide coating can be used to significantly reduce the scattering width from a thin perfectly electric conducting cylindrical rod at specific observation angles. Later on, the ef-fective permittivity and permeability of metamaterials composed of two dimensional periodic arrangements of these dielectric coated cylindrical rods have been studied. An increase in the double negative bandwidth of a metamaterial composed of barium

strontium titanate coated conducting rods has been observed in contrast to the corresponding bandwidth of a metamaterial composed of only barium strontium titanate $Ba_{0.5}Sr_{0.5}TiO_3$ (BST) material rods. Also an additional plasmonic epsilon negative bandwidth has been found in case of a metamaterial composed of barium strontium titanate coated conducting rods. It is further observed that the widest epsilon negative, mu negative and double negative bandwidths exist for a metamaterial composed of gallium arsenide rods.

Chapter 1

Introduction

1.1 Overview

The amazing beauty of the electromagnetic wave lies in the fact that it carries information and propagates anywhere in the free space. Modern remote sensing systems are being used to monitor the surfaces and atmosphere of the earth. In real life environments such as ice-covered land, vegetation and forested covered canopies (such as trees, crops and bushes) involve objects (such as leaves, branches, trunk, and stem with different physical sizes and geometrical properties) that may appear in the wireless communication channels. These objects can be approximated as canonical dielectric structures such as cylinders, spheres, wedges and disks of various sizes and dielectric properties [1-17]. Various scattering models for the electromagnetic wave interaction with these canonical dielectric structures can be found in many classical electromagnetics textbooks and research papers [18-39]. An accurate understanding of the electromagnetic wave interaction with these scatterers is extremely important in the designing of remote sensing systems, radar engineering problems and meta-materials. More recently there has been a growing interest in the computation of

scattering cross sections from these scatterers or targets. Many techniques and enhancements are being rapidly developed and improved in this active area of research [40-45].

The electromagnetic wave scattering from a dielectric disk is an important and fundamental research topic with application to remote sensing, metamaterials and wireless communication. A disk is basically made by taking a slice with small thickness from a cylinder of arbitrary cross section. It is widely known in the radar remote sensing community that the broad leaves of a deciduous tree are modeled as a thin dielectric disk with arbitrary cross-section such as circular, elliptical, square, or other cross-sectional shape boundaries. In recent years, many numerical and analytical approximate solutions have been proposed in the literature for the electromagnetic wave scattering from a dielectric disk [46-57]. A numerical approximation for the scattering from a dielectric disk whose diameter is almost equal to an operating wavelength has been developed by Weil and Chu [46]. Schiffer and Thielheim developed an analytical solution for the electromagnetic scattering from a small dielectric disk based on the Rayleigh scattering theory [47]. A high frequency disk scattering solution based on the volumetric integral physical optics (VIPO) approach has been studied by Levine et al. [48-50]. Karam and co-workers [51-53] have developed an analytical solution for the electromagnetic scattering from a dielectric disk whose cross sectional area is comparable with an operating wavelength which is known as the Generalized Rayleigh-Gans (GRG) approximation [51-54]. Oh and Hong have studied the radar cross section of a thin lossy dielectric disk based upon the Generalized Rayleigh-Gans (GRG) and the physical optics (PO) approximations [55]. Koh and sarabandi proposed an intermediate frequency solution for electromagnetic wave scattering from

thin dielectric disk and is known as Koh-Sarabandi (KS) approximation [56-57]. In the radar remote sensing community, it is well known that an exact scattering formulation for the thin dielectric disk with acceptable performance over the wide range of frequencies has not yet been provided. However, some scattering approximations such as: Rayleigh-Gans (low-frequency solution), Volumetric Integral Physical Optics (VIPO) (high frequency solution), and Koh-Sarabandi (intermediate frequency solution), have been widely used for the calculation of the scattering from a thin dielectric circular disk.

This dissertation is divided into two major parts. In the first major part of this dissertation, three problems are investigated. In these problems, the dielectric disk is assumed to be made of a realistic material, i.e, low loss Gallium Arsenide (GaAs). The effects of various real and imaginary parts of the relative permittivity of the disk have also been investigated. In the first problem, the effects of tilt angles upon the back-scattering cross section of a thin dielectric circular disk based upon three different scattering approximations such as RG, VIPO and KS approximations have been investigated. It is investigated that for the specific tilt angle and size parameter of a low loss Gallium Arsenide (GaAs) disk, the back-scattering cross sections for both types of considered incident polarizations are almost equal to zero. In this way, we can hide a GaAs disk in the back-scattered direction to the incoming horizontally and vertically polarized waves. This interesting result finds applications in the field of stealth technology and can not be obtained for a GaAs disk having no tilt. In the second problem, the shape effects upon the back-scattering cross section of a thin dielectric disk are investigated. For the solution of this problem, an analytic solution for the scattering of electromagnetic waves from a thin dielectric

triangular disk is developed. The proposed theory is based on the Koh-Sarabandi approximation for the electromagnetic wave scattering from a thin dielectric disk along with the spectral representation of the dyadic Green's function. The validity of the proposed formulation is justified by comparing it with the numerical method such as method of moments. For completeness, the scattering cross sections of a triangular disk for horizontal and vertical incident polarizations are compared with their respective scattering cross sections of elliptical, circular, semi-circular and square disks having same electromagnetic and geometrical parameters. It is studied that the back scattering cross sections for a low loss Gallium Arsenide triangular disk at a specific incidence angle can be made almost zero for both types of incident polarizations. This type of almost zero back scattering has applications in the stealth technology and remote sensing. In the third problem, an analytic formulation for the back scattering from a sparse distribution of N tilted thin dielectric circular disks has been developed based upon the Rayleigh-Gans (RG), Volumetric Integral Physical Optics (VIPO) and Koh-Sarabandi (KS) methods. The effects of incident angle, size parameter of the disk, relative permittivity of the disk and spacing among disks of sparsely distributed dielectric disks upon the back-scattered cross sections have been investigated for both types of incident polarizations, i.e., horizontal and vertical. During the study, it is found that a pair of tilted Gallium Arsenide (GaAs) disks significantly reduced the back-scattered cross sections for horizontal and vertical polarizations at a specific incident polar angle as compared to a single GaAs tilted disk having same orientation as that of a pair of tilted disks. Likewise, it is also concluded that two specific sparsely located tilted GaAs disks reduce the back-scattered cross sections significantly as compared to a single tilted GaAs disk having same geometrical

and electrical parameters. Such types of reduced back scattering are desirable in many radar engineering problems like stealth technology.

In the second major part of this dissertation, I primarily focused on the electromagnetic wave interaction with the electromagnetic Metamaterials. Metamaterials are broadly defined as the artificially designed electromagnetic structures with unusual electromagnetic properties which are not readily found in nature (i.e., materials with the electric permittivity and the magnetic permeability (constitutive parameters), single or both negative). These metamaterials can be classified as a single negative (SNG) and double negative (DNG) metamaterials. The single negative (SNG) metamaterial can be epsilon negative (ENG) metamaterial or mu negative (MNG) metamaterial. The ENG metamaterial has real part of its effective permittivity as negative whereas MNG metamaterial has real part of its effective permeability as negative. Likewise, the DNG metamaterial has real parts of its effective permittivity and effective permeability as negative simultaneously. The range of frequencies where the real part of the effective permittivity is negative can be defined as an epsilon negative bandwidth. Similarly, the range of frequencies where the real part of the effective permeability is negative defines as mu negative bandwidth. The range of frequencies for which ENG and MNG bandwidths overlap gives rise to a double negative bandwidth. Recently, there has been a great deal of interest in the physics and engineering of metamaterials due to their important technical applications, see for example [58-80]. The concept of metamaterial has been introduced by Veselago in 1967 [58]. He suggested a new type of material which has simultaneously negative permittivity and permeability. He also presented general properties of electromagnetic wave propagation in such a material. He theoretically created a lossless metamaterial and showed

the extraordinary properties of this material which is not found in nature. Following the work of Veselago, Pendry et al. theoretically studied the negative permittivity [59] material. They studied that an array of metallic wires with suitably chosen spacing and radius can be constructed to form a negative permittivity material. Pendry and his co-workers also proposed a negative permeability material based on the metallic split ring resonators [60]. Later on, Smith et al. proposed a metamaterial which shows simultaneously negative permittivity and permeability. They also carried out microwave experiments to test unusual properties of metamaterial [61]. Shelby et al. performed first experiment to show negative refraction of metamaterial which consists of two-dimensional array of repeated unit cells of copper strips and split ring resonators [62].

Alu et al. [63-64] have studied that pairing of ENG and MNG slabs under certain conditions give some interesting features like resonance, tunneling, zero reflection and transparency. Some other interesting potential applications of SNG and DNG metamaterials have been studied and discussed by Alu and Engheta [65], Engheta et al. [66] and Kshetrimayum [67]. Recently, Awan has studied the effects of ENG or MNG background metamaterials upon the reflection and transmission characteristics of a lossy wire grid [68] and the realization of a DNG metamaterial based upon the realistic material coated spherical particles [69]. It is known that a wire medium or metamaterial has spectrum of its effective permittivity as plasmonic [70-71], i.e., it has negative permittivity from zero frequency to the plasma cutoff frequency. Based upon this, we have defined a plasmonic ENG negative bandwidth as the range of frequencies from zero to the plasma frequency. Contrary to this, there also exists another type of epsilon negative metamaterial whose effective permittivity spectrum

is resonant, see for example, [72-74]. This is because of the finite size of the inclusions forming an ENG metamaterial. In this case, it is found that the effective permittivity of such metamaterial is negative from resonance frequency to plasma frequency. We take this range of frequencies as a resonant ENG bandwidth. The disadvantage of the resonant ENG metamaterials is that they have narrow ENG bandwidth.

A metamaterial composed of dielectric rods has been studied by many authors [75-80]. Silveirinha has proposed the nonlocal homogenization theory for a periodic lattice composed of long thin ϵ-negative rods [75]. He argued that spatial dispersion effects can not be ignored in case of an electromagnetic crystal. Peng and co-workers [76] have analyzed the left-handed properties of a metamaterial composed of BST dielectric rods theoretically and experimentally. Later on, the effective permittivity and permeability of a metamaterial composed of BST rods have been studied theoretically by Vynck et al. [77]. They also derived mathematical expressions for the electric and magnetic dipole moments of a cylindrical rod based on Mie scattering coefficients. Anisotropic effects in a metamaterial composed of dielectric cylindrical rods have been investigated by Peng and co-workers [78] theoretically and they also verified their results numerically. According to them, anisotropic effects are introduced by turning the square lattice symmetry to the rectangular lattice. Li and Ling [79] have derived the expressions for effective permittivity and permeability of a rod array composed of water filled cylindrical rods. They also studied the transmission loss incurred by random heights and random positioning of rods forming a rod array. According to them, the randomizations have little effects on the behavior of rod array at low frequencies. Valero and Vesperinas [80] have investigated the behavior of a metamaterial composed of ordered and disordered dielectric rods. They concluded

that strong scattering by disordered rods extinguishes most of the incident energy and hence no negatively refracted forward beam is observed. Some of the authors have studied the electromagnetic characteristics of a metamaterial composed of dielectric coated conducting rods, e.g., [81-82]. Valagiannopoulos and Tretyakov have proposed a symmetric absorbers based upon a single infinite grating of perfectly conducting rods covered by ordinary dielectrics [81]. They also provided a realistic absorber design which have an absorption of 97%. A concept of digital metamaterial has been introduced by Giovampaola and Engheta based upon analytical and numerical study [82]. They have used cylindrical or spherical core-shell inclusions for their design. They also applied their proposed methodology to the design of various digital lenses. From all the references cited above, no one has studied the scattering characteristics along with the effective parameters of a metamaterial composed of dielectric coated conducting rods with realistic dielectric materials such as $Ba_{0.5}Sr_{0.5}TiO_3$ (BST) dielectric, magnetodielectric, low loss Gallium Arsenide (GaAs) and Silicon Carbide (SiC). Likewise, comparative analysis of scattering characteristics and effective parameters of metamaterials composed of perfectly electric conducting (PEC), dielectric and dielectric coated PEC rods based upon these realistic materials have not been reported previously. They are studied in this dissertation. Here, cylindrical rods are of infinite extent so tilted rods can cause to touch or cross each other. Therefore, these tilted effects can not be modelled properly and have not been considered for dielectric disks previously.

An analytically theory has been developed for the scattering characteristics of an isolated dielectric coated conducting rod. The various types of realistic dielectric materials as mentioned above have been considered as coating materials for a dielectric

coated PEC rod and rod materials for an uncoated rod. The scattering characteristics of a dielectric coated PEC rod is also compared with the PEC and realistic material rods having the same radii. During this study, it is found that the GaAs coating significantly reduced the scattering width of a small radius PEC cylindrical rod at specific observation angles. In this way, we can hide a thin cylindrical PEC rod from the incoming wave at these specific observation angles which find applications in the stealth technology. It is also studied that by increasing the inner core radius of PEC rod inside the magnetodielectric coated conducting rod, the forward scattering width can be reduced whereas its backward scattering width can be enhanced. Such type of enhanced backscattering is of an interest for radar engineering problems. In this second major part, the effective parameters of a metamaterial composed of dielectric coated conducting rods have also been studied. It is found that the widest plasmonic ENG bandwidth is observed for a metamaterial composed of PEC rods and the narrowest plasmonic ENG bandwidth exists for a metamaterial composed of magnetodielectric coated conducting rods. A % increase of 0.6135 % in a DNG bandwidth for a metamaterial composed of BST coated conducting rods has been observed as compared to a metamaterial composed of only BST rods which were reported by Vynck et al. [77]. There also exists an additional plasmonic ENG bandwidth for a metamaterial composed of BST coated conducting rods. For a metamaterial composed of magnetodielectric rods there exists non-overlapping ENG and MNG bandwidths which implies that there is no DNG bandwidth. Contrary to this, it is analyzed that a metamaterial composed of magnetodielectric coated conducting rods has overlapping ENG and MNG bandwidths which gives rise to a relatively wider DNG bandwidth as compared to a DNG bandwidth of a metamaterial composed of

BST coated PEC rods. Likewise, it is studied that the widest ENG, MNG and DNG bandwidths are observed in case of a metamaterial composed of GaAs rods whereas there exists no DNG bandwidth for a metamaterial composed of GaAs coated conducting rods. In case of a metamaterial composed of SiC rods, we have only resonant ENG bandwidth whereas for a metamaterial composed of SiC coated conducting rods, we have resonant as well as plasmonic ENG bandwidths. For both of these metamaterials, there exists no MNG and DNG bandwidths. These above mentioned findings based upon the proposed theory signify the novelty of the current work and have not been studied previously. This proposed theoretical study is also helpful in designing of ENG, MNG and DNG metamaterials based on coated or uncoated cylindrical rods.

1.2 Fundamental Concepts and Theorems

When an incident radar beam illuminates the target scatterer with an electric field $\boldsymbol{E}_i$, it intercepts the incident plane wave and absorbs some part of the incident energy while scatters the remaining part along many directions as shown in Fig.1.1

1.3 Scattering calculation conventions

The scattering behaviour of the target is described in two main types of coordinate system conventions such as the Forward Scattering Alignment (FSA) and the Backward Scattering Alignment (BSA) Conventions. Both conventions give exclusive information about the interaction of the electromagnetic waves with the given target. Forward scattering alignment convention is preferred for the calculation of the bistatic radar scattering from the target. However, backward scattering alignment convention provides the useful information and insight for the monostatic radar
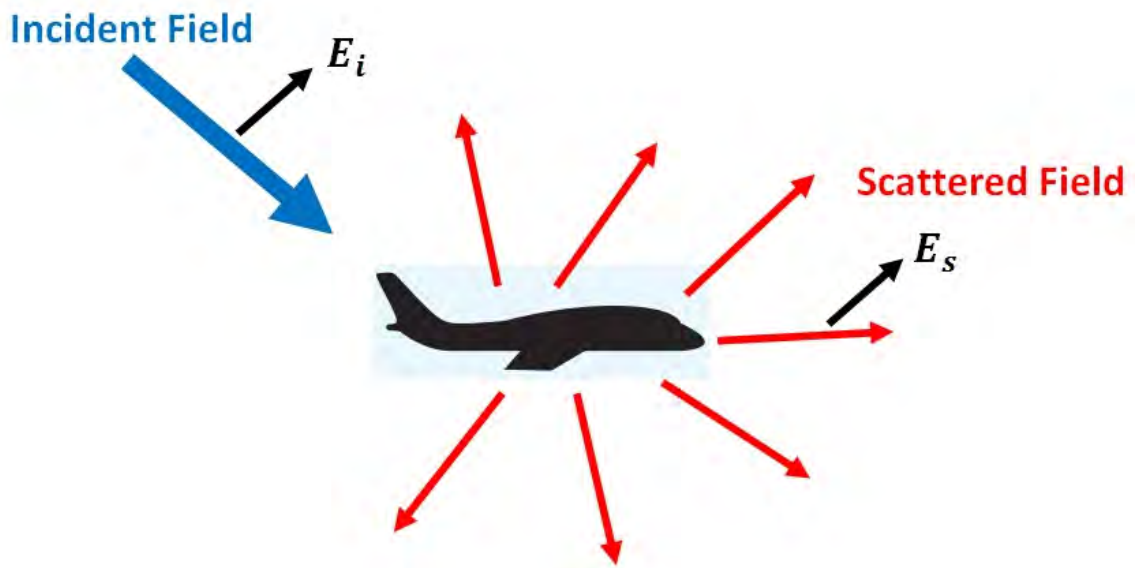
Figure 1.1: Radar incident beam illuminates an object is scattered along many directions.

scattering from the given target. In bistatic radar scattering systems, the transmitting and the receiving antennas are situated at different locations whereas in the monostatic or backscattering radar systems both the transmiting and the receiving antennas are placed at the same location. Since both conventions are used in this dissertation. Brief description of the scattering geometry and the coordinate system for each convention will be given in the following subsections.

1.3.1 Forward Scattering Alignment (FSA) Convention

The forward scattering alignment (FSA) convention is a wave-oriented convention that the polarization directions of the incident and the scattered fields along the vertical unit vector ($\hat{\mathbf{v}}$) and the horizontal unit vector ($\hat{\mathbf{h}}$) are always characterized with respect to direction of propagation of the wave ($\hat{\mathbf{k}}$). Furthermore, this set of unit vectors ($\hat{\mathbf{k}}, \hat{\mathbf{v}}, \hat{\mathbf{h}}$) can be expressed in usual spherical coordinate system ($\hat{\mathbf{r}}, \hat{\theta}, \hat{\phi}$)
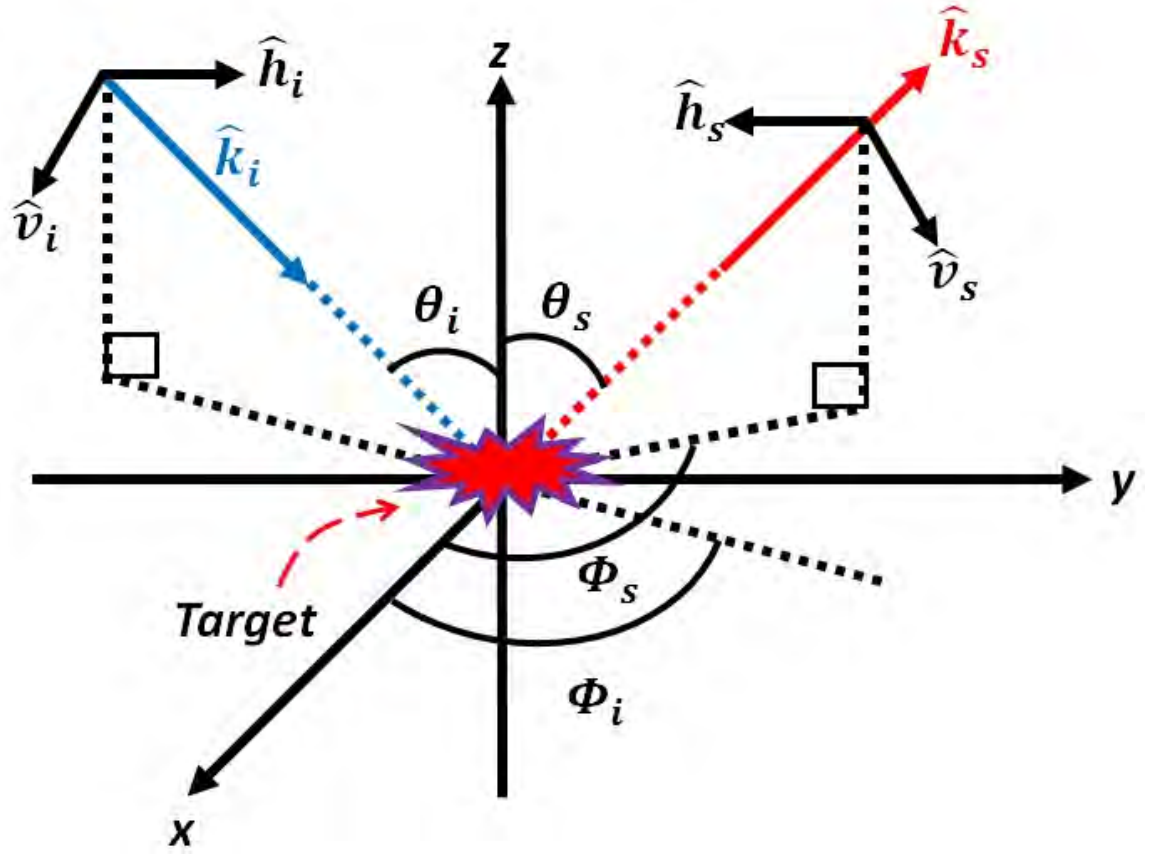
Figure 1.2: Scattering geometry and the coordinate system for the forward scattering alignment (FSA) convention.

for both the incident and the scattered waves. The incident electromagnetic wave along the direction $\hat{\mathbf{k}}_i$ moving towards the target and the scattered wave moving along the direction $\hat{\mathbf{k}}_s$ can be specified by the two sets of spherical angles (θ_i, ϕ_i) and (θ_s, ϕ_s), respectively as shown in figure 2. The vector set $(\hat{\mathbf{k}}_i, \hat{\mathbf{v}}_i, \hat{\mathbf{h}}_i)$ represents the incident wave and the vector set $(\hat{\mathbf{k}}_s, \hat{\mathbf{v}}_s, \hat{\mathbf{h}}_s)$ represents the scattered wave are given by the following expressions,

$$\hat{\mathbf{k}}_i = \hat{\mathbf{x}}\cos\phi_i\sin\theta_i + \hat{\mathbf{y}}\sin\phi_i\sin\theta_i - \hat{\mathbf{z}}\cos\theta_i \tag{1.a}$$

$$\hat{\mathbf{h}}_i = \frac{\hat{\mathbf{z}}\times\hat{\mathbf{k}}_i}{|\hat{\mathbf{z}}\times\hat{\mathbf{k}}_i|} = -\hat{\mathbf{x}}\sin\phi_i + \hat{\mathbf{y}}\cos\phi_i \tag{1.b}$$

$$\hat{\mathbf{v}}_i = \hat{\mathbf{h}}_i\times\hat{\mathbf{k}}_i$$

$$= -\hat{\mathbf{x}}\cos\phi_i\cos\theta_i - \hat{\mathbf{y}}\sin\phi_i\cos\theta_i - \hat{\mathbf{z}}\sin\theta_i \tag{1.c}$$

$$\hat{\mathbf{k}}_s = \hat{\mathbf{x}}\cos\phi_s\sin\theta_s + \hat{\mathbf{y}}\sin\phi_s\sin\theta_s + \hat{\mathbf{z}}\cos\theta_s \tag{1.d}$$

$$\hat{\mathbf{h}}_s = \frac{\hat{\mathbf{z}}\times\hat{\mathbf{k}}_s}{|\hat{\mathbf{z}}\times\hat{\mathbf{k}}_s|} = -\hat{\mathbf{x}}\sin\phi_s + \hat{\mathbf{y}}\cos\phi_s \tag{1.e}$$

$$\hat{\mathbf{v}}_s = \hat{\mathbf{h}}_s\times\hat{\mathbf{k}}_s$$

$$= \hat{\mathbf{x}}\cos\phi_s\cos\theta_s + \hat{\mathbf{y}}\sin\phi_s\cos\theta_s - \hat{\mathbf{z}}\sin\theta_s \tag{1.f}$$

The explicit expressions for the forward scattering alignment (FSA) convention with reference to scattering geometry shown in Fig.1.2, it is required that $\theta_s = \pi - \theta_i$ and $\phi_s = \phi_i$, and are given by

$$\hat{\mathbf{k}}_s = \hat{\mathbf{k}}_i \tag{2.a}$$

$$\hat{\mathbf{v}}_s = \hat{\mathbf{v}}_i \tag{2.b}$$

$$\hat{\mathbf{h}}_s = \hat{\mathbf{h}}_i \tag{2.c}$$

1.3.2   Backward Scattering Alignment (BSA) Convention

For the backward scattering alignment (BSA) convention , the scattering geometry is shown in Fig.1.3. In this case, the vector set $(\hat{\mathbf{k}}_i, \hat{\mathbf{v}}_i, \hat{\mathbf{h}}_i)$ represents the incident wave whereas the vector set $(\hat{\mathbf{k}}_s, \hat{\mathbf{v}}_s, \hat{\mathbf{h}}_s)$ represents the scattered wave and are given by the following expressions,
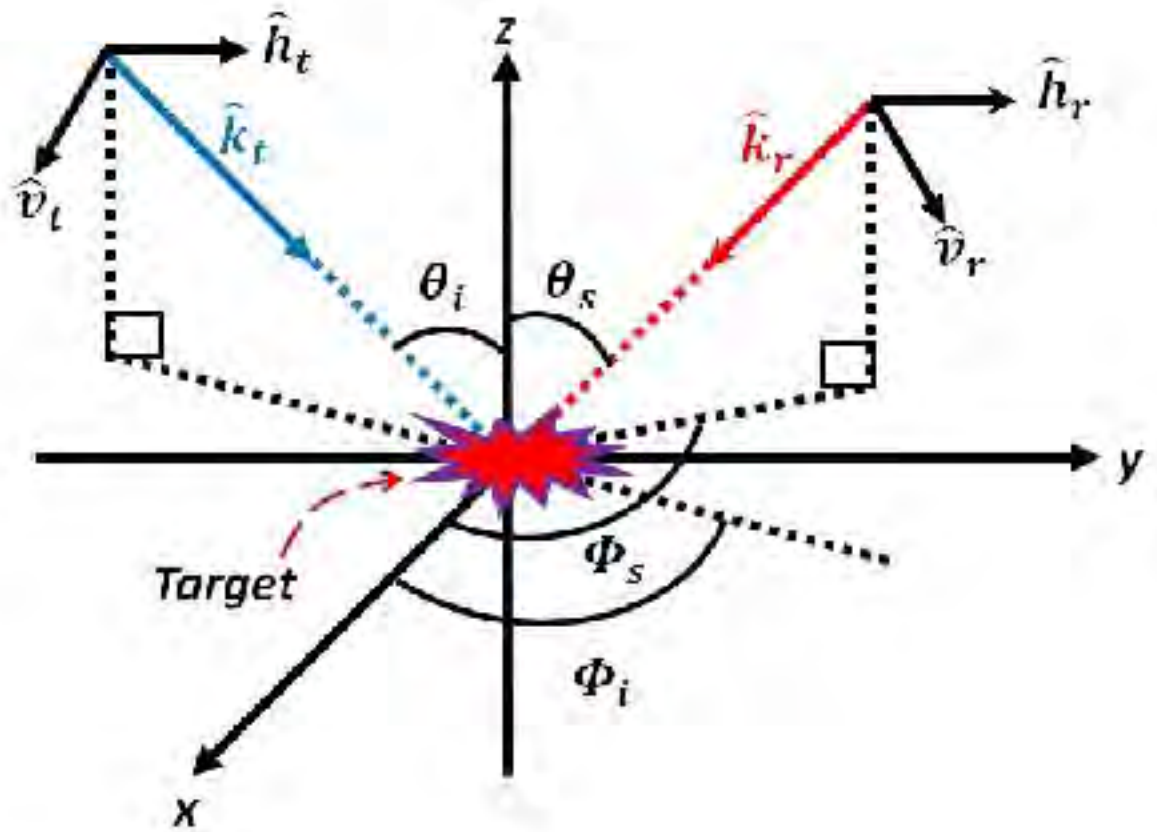
Figure 1.3: Scattering geometry and the coordinate system for the backward scattering alignment (BSA) convention.

$$\hat{\mathbf{k}}_t = \hat{\mathbf{k}}_i = \hat{\mathbf{x}}\cos\phi_i\sin\theta_i + \hat{\mathbf{y}}\sin\phi_i\sin\theta_i - \hat{\mathbf{z}}\cos\theta_i \tag{3.a}$$

$$\hat{\mathbf{h}}_t = \hat{\mathbf{h}}_i = \frac{\hat{\mathbf{z}}\times\hat{\mathbf{k}}_i}{|\hat{\mathbf{z}}\times\hat{\mathbf{k}}_i|} = -\hat{\mathbf{x}}\sin\phi_i + \hat{\mathbf{y}}\cos\phi_i \tag{3.b}$$

$$\hat{\mathbf{v}}_t = \hat{\mathbf{v}}_i = \hat{\mathbf{h}}_i\times\hat{\mathbf{k}}_i$$

$$= -\hat{\mathbf{x}}\cos\phi_i\cos\theta_i - \hat{\mathbf{y}}\sin\phi_i\cos\theta_i - \hat{\mathbf{z}}\sin\theta_i \tag{3.c}$$

$$\hat{\mathbf{k}}_r = -\hat{\mathbf{k}}_s = -\hat{\mathbf{x}}\cos\phi_s\sin\theta_s - \hat{\mathbf{y}}\sin\phi_s\sin\theta_s - \hat{\mathbf{z}}\cos\theta_s \tag{3.d}$$

$$\hat{\mathbf{h}}_r = -\hat{\mathbf{h}}_s = \frac{\hat{\mathbf{z}}\times\hat{\mathbf{k}}_s}{|\hat{\mathbf{z}}\times\hat{\mathbf{k}}_s|} = \hat{\mathbf{x}}\sin\phi_s - \hat{\mathbf{y}}\cos\phi_s \tag{3.e}$$

$$\hat{\mathbf{v}}_r = \hat{\mathbf{v}}_s = \hat{\mathbf{h}}_s\times\hat{\mathbf{k}}_s$$

$$= \hat{\mathbf{x}}\cos\phi_s\cos\theta_s + \hat{\mathbf{y}}\sin\phi_s\cos\theta_s - \hat{\mathbf{z}}\sin\theta_s \tag{3.f}$$

The explicit expressions for the backward scattering alignment (BSA) convention with reference to scattering geometry shown in Fig.1.3, it is required that $\theta_s = \theta_i$, and $\phi_s = \phi_i + \pi$, and are given by

$$\hat{\mathbf{k}}_s = -\hat{\mathbf{k}}_i \tag{4.a}$$

$$\hat{\mathbf{v}}_s = \hat{\mathbf{v}}_i \tag{4.b}$$

$$\hat{\mathbf{h}}_s = -\hat{\mathbf{h}}_i \tag{4.c}$$

1.3.3 Scattering Matrix of the Target

The electric field vector of the incident wave in terms of a horizontally polarized component $\mathbf{E}_h^i(\theta_i, \phi_i)\hat{\mathbf{h}}_i$, and a vertically polarized component $\mathbf{E}_v^i(\theta_i, \phi_i)\hat{\mathbf{v}}_i$, is given by

$$\mathbf{E}_i = \mathbf{E}_h^i(\theta_i, \phi_i)\hat{\mathbf{h}}_i + \mathbf{E}_v^i(\theta_i, \phi_i)\hat{\mathbf{v}}_i \tag{1.3.1}$$

where $\hat{\mathbf{h}}_\mathbf{i} = \dfrac{\hat{\mathbf{k}}_i \times \hat{\mathbf{z}}}{|\hat{\mathbf{k}}_\mathbf{i} \times \hat{\mathbf{z}}|}$, and $\hat{\mathbf{v}}_\mathbf{i} = \hat{\mathbf{h}}_\mathbf{i} \times \hat{\mathbf{k}}_\mathbf{i}$ are the unit vectors along the horizontal and the vertical directions, respectively and are characterized with respect to the propagation direction of the incident wave $\hat{\mathbf{k}}_\mathbf{i}$.

Similarly, the electric field vector $\mathbf{E}_s$ of the scattered wave in terms of a horizontally polarized component $\mathbf{E}_h^s(\theta_s, \phi_s)\hat{\mathbf{h}}_s$, and a vertically polarized component $\mathbf{E}_v^s(\theta_s, \phi_s)\hat{\mathbf{v}}_s$ can be written as,

$$\mathbf{E}^s = \mathbf{E}_h^s(\theta_s, \phi_s)\hat{\mathbf{h}}_s + \mathbf{E}_v^s(\theta_s, \phi_s)\hat{\mathbf{v}}_s \tag{1.3.2}$$

where $\hat{\mathbf{h}}_s = \dfrac{\hat{\mathbf{k}}_s \times \hat{\mathbf{z}}}{|\hat{\mathbf{k}}_s \times \hat{\mathbf{z}}|}$, and $\hat{\mathbf{v}}_s = \hat{\mathbf{h}}_s \times \hat{\mathbf{k}}_s$ are the unit vectors along the horizontal and the vertical directions, respectively and are characterized with respect to direction of propagation of the scattered wave $\hat{\mathbf{k}}_\mathbf{s}$. The incidence electric field vector $(\mathbf{E}^i)$, and the scattered electric field vector $(\mathbf{E}^s$ from the target are related to one another by the complex scattering matrix $\overline{\overline{\mathbf{S}}})$ of the target as

$$\mathbf{E}^\mathbf{s} = \frac{e^{ik_o r}}{\mathbf{r}} \ \overline{\overline{\mathbf{S}}} \cdot \mathbf{E}^i$$

$$\begin{pmatrix} \mathbf{E}_v^s \\ \mathbf{E}_h^s \end{pmatrix} = \frac{\mathbf{e^{ik_o r}}}{\mathbf{r}} \begin{pmatrix} S_{vv} & S_{vh} \\ S_{hv} & S_{hh} \end{pmatrix} \begin{pmatrix} \mathbf{E}_v^i \\ \mathbf{E}_h^i \end{pmatrix} \tag{1.3.3}$$

The scattering matrix elements $(S_{vv}, S_{hh}, S_{vh}, S_{hv})$, are the complex quantities and can be expressed as:

$$\begin{aligned} S_{vv} &= \hat{\mathbf{v}}_s \cdot \overline{\overline{\mathbf{S}}} \cdot \hat{\mathbf{v}}_i \\ S_{vh} &= \hat{\mathbf{v}}_s \cdot \overline{\overline{\mathbf{S}}} \cdot \hat{\mathbf{h}}_i \\ S_{hv} &= \hat{\mathbf{h}}_s \cdot \overline{\overline{\mathbf{S}}} \cdot \hat{\mathbf{v}}_i \\ S_{hh} &= \hat{\mathbf{h}}_s \cdot \overline{\overline{\mathbf{S}}} \cdot \hat{\mathbf{h}}_i \end{aligned} \tag{1.3.4}$$

It should be noted that the radar polarimetric response of the target can be computed from the scattering matrix elements $(S_{vv}, S_{hh}, S_{vh}, S_{hv})$ of the target.

1.3.4 Radar Cross Section (RCS)

The radar cross section (RCS) or scattering echo area is a measure of the scattered power in a specified direction when an object is illuminated by the radar incident beam. The qualitative analysis of the scattering characteristics of the target is measured through the radar cross section. The radar cross-section for horizontally (σ_{hh}) and vertically polarized (σ_{vv}) scattering from an object can be calculated as

$$\sigma_{hh} = 4\pi|\mathbf{S}_{hh}|^2$$
$$\sigma_{vv} = 4\pi|\mathbf{S}_{vv}|^2$$

(1.3.5)

or, the Radar Cross Section (RCS) in terms of the incident electric field ($\mathbf{E^i}$) and the scattered electric field ($\mathbf{E^s}$) can be expressed as,

$$\sigma = \lim_{r\to\infty} 4\pi r^2 \frac{|\mathbf{E}^s|^2}{|\mathbf{E}^i|^2}$$

(1.3.6)

where $\mathbf{r}$ is the distance between the target and the receiver. The radar cross-section (RCS) strongly depends on the following parameters.

- the size of the target (i.e., geometrical parameters of the target)

- the shape of the target (i.e., circular, square, triangular)

- the material composition of the target (i.e., lossless/lossy dielectric composition)

- target's aspect angle (i.e., orientation of the target relative to the radar)

- the angle of the incident wave

- the frequency of the incident wave

- the polarization of the incident wave (i.e., horizantally or vertically polarized wave)

For a two dimensional target, the scattering cross section is referred to as the scattering width of the target or alternatively the radar cross-section (RCS) per unit length. In radar remote sensing community, the radar cross section reduction is the most active research area because of its application in the radar and modern stealthy systems. The first paramount objective of this thesis is to achieve the specific reduction in the radar cross section of the target.

1.3.5 Dissertation Overview

The Chapter 2 introduces the various approximate scattering solutions (such as Rayleigh-Gans (low-frequency solution), Volumetric Integral Physical Optics (VIPO) (high frequency solution), and Koh-Sarabandi (intermediate frequency solution) for an electromagnetic scattering from a thin dielectric disk, along with the spectral representation of the Dyadic Green's function. The Chapter 3 describes an analysis about the back-scattering cross section from an arbitrary oriented thin circular dielectric disk (tilted disk). In Chapter 4, the effects of various disk-shapes upon backscattering cross sections have been studied. In Chapter 5, an analytic method is provided to compute the electromagnetic coherent scattering from a sparse distribution of N-dielectric tilted thin circular disks. In Chapter 6, the scattering characteristics of isolated or dielectric and dielectric coated conducting rod and the effective parameters of a metamaterial composed of these cylindrical rods are analytically developed and studied. In chapter 7, a summary of the work performed in this dissertation is presented. It should be noted that time convention e^{iwt} has been studied and suppered

throughout.

Chapter 2

Electromagnetic scattering from a thin circular dielectric disk

It is widely known in the radar remote sensing community that the broad leaves of a deciduous tree are modeled as thin dielectric disks with arbitrary cross-section such as circular, elliptical, square, or other cross-sectional shape boundaries. The literature contains many approximate scattering formulations that have focused on the computation of the scattering from the thin circular dielectric disks. In this chapter, three most widely used scattering approximations such as Rayleigh-Gans (low frequency approximation), Volume integral physical optics (high frequency approximation) and Koh-Sarabandi (intermediate frequency approximation) are briefly reviewed for their applications and limitations based on the simulation results for the vertical and the horizontal polarization. The effects of incident angle, size parameter of disk and its relative permittivity upon the magnitudes of scattering elements have been studied.

Some techniques have also been developed to formulate the electromagnetic scattering from dielectric structures using the Partial Differential Equations (PDE) derived from the well-known Maxwell's eqauations. These PDE's are solved either by discretizing the simulation domain into small elements and the field quantities upon

these small elements results into a set of linear equations with sparse matrix (e.g. FEM, FDTD). In the literature, Some authors [21-22,30,38] computed the electromagnetic scattering from dielectric structures with arbitrary shape and size based on the partial differential equations. However, these techniques are very cumbersome. In this dissertation, we focused on the volume integral equation methods for the computation of the electromagnetic fields from the dielectric objects.

2.1 Approximate solutions for scattering from a circular dielectric disk

Consider a thin dielectric circular disk illuminated by the incident plane wave $\mathbf{E}^i = \mathbf{E}_o\, e^{ik_o\hat{\mathbf{k}}_i\cdot\mathbf{r}}$ in free space. Figure 2.1 shows the wave scattering configuration for the dielectric circular disk. The incident electric field induces a polarization current $\mathbf{J}(x, y, z)$ inside the disk, which satisfy the following Fredholm volume integral equation.

$$\mathbf{J}(\mathbf{r}) - k_o^2(\epsilon_r - 1)\mathbf{E}^i = -ik_oY_o(\epsilon_r - 1)\mathbf{E}^i \int_v \overline{\overline{\mathbf{G}}}(\mid \mathbf{r} - \mathbf{r}' \mid).\mathbf{J}(\mathbf{r}')dv \qquad (2.1.1)$$

where $Y_o = \frac{1}{Z_o}$, Z_o is the free-space wave impedance and k_o is the free-space wave number. $\mathbf{E}^i$ is the incident wave on the dielectric circular disk, and $\overline{\overline{\mathbf{G}}}(.)$ is the free-space dyadic Green's function [4]. The thickness of the disk, relative permittivity and radius are taken to be t, ϵ_r, and a, respectively. It is assumed that the thickness is very small, i.e.,$k_ot << 1$ which represents a thin disk, $t \ll \lambda$. The polarization current induced inside the thin dielectric circular disk can be expressed in terms of the polarizability tensor ($\overline{\overline{\boldsymbol{P}}}$) of the thin dielectric circular disk, and is given as

$$\mathbf{J} = -ik_o Y_o(\epsilon_r - 1)\overline{\overline{\boldsymbol{P}}}.\mathbf{E}^i = -ik_o Y_o(\epsilon_r - 1)\begin{pmatrix} P_{xx} & P_{xy} & P_{xz} \\ P_{yx} & P_{yy} & P_{yz} \\ P_{zx} & P_{zy} & P_{zz} \end{pmatrix} \cdot \mathbf{E}^i \qquad (2.1.2)$$
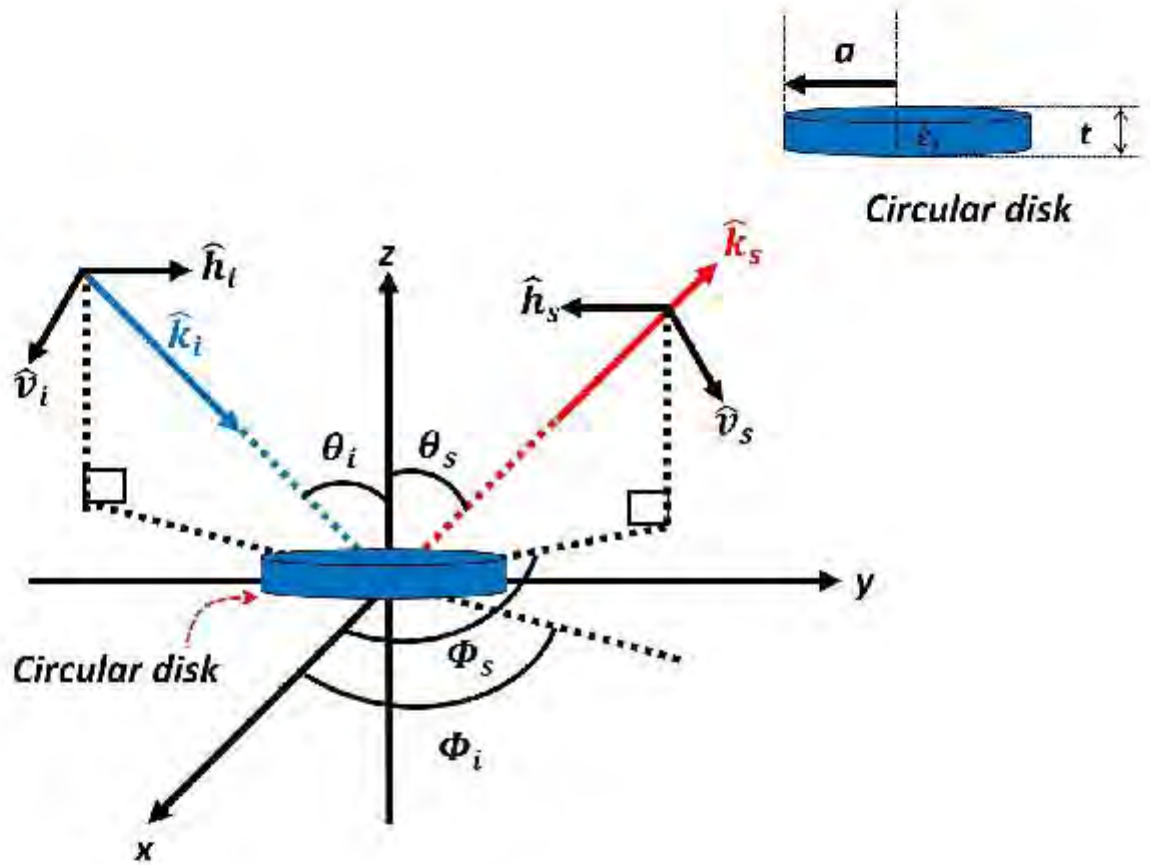
Figure 2.1: Standard wave scattering coordinate system for a thin dielectric circular dielectric disk.

Here, the polarizability tensor $\overline{\overline{P}}$ of the thin dielectric circular disk can be obtained analytically by using an approximate solution such as; Rayleigh-Gans (RG) (low-frequency solution), Volumetric Integral Physical Optics (VIPO) (high-frequency solution), Koh-Sarabandi (KS) (between low and high-frequency solution)). For these techniques, $\overline{\overline{P}}$ reduced to a diagonal matrix, which can be written as,

$$\overline{\overline{\mathbf{P}}} = \begin{pmatrix} P_{xx} & 0 & 0 \\ 0 & P_{yy} & 0 \\ 0 & 0 & P_{zz} \end{pmatrix} \tag{2.1.3}$$

The off-diagonal elements of the polarizability tensor $\overline{\overline{\mathbf{P}}}$, are zero (i.e. $P_{xy} = P_{xz} = P_{yx} = P_{yz} = P_{zx} = P_{zy} = 0$). Finally, the scattered field in the far-field region from a thin dielectric circular disk based on the resulting polarizability tensor can be formulated as

$$\mathbf{E}_{disk}^s = \frac{-k_o^2}{4\pi} \frac{e^{ik_o r}}{r} \left[\hat{\mathbf{k}}_s \times \hat{\mathbf{k}}_s \times \left(\overline{\overline{\mathbf{P}}}.\mathbf{E_o} \right) \right] \frac{2A_{(disk)} J_1(\sqrt{a^2(A^2 + B^2)})}{\sqrt{a^2(A^2 + B^2)}} \tag{2.1.4}$$

where $A_{(disk)} = \pi a^2$ is the physical area of the thin dielectric circular disk. $A = k_o(\hat{\mathbf{k}}_i - \hat{\mathbf{k}}_s).\hat{\mathbf{x}}$, $B = k_o(\hat{\mathbf{k}}_i - \hat{\mathbf{k}}_s).\hat{\mathbf{y}}$, and $\mathbf{J}_1(\cdot)$ is the bessel function of first order. $\hat{\mathbf{k}}_i$ is the propagation vector along the incident direction and $\hat{\mathbf{k}}_s$ denotes the scattering direction. For a particular incident and scattered polarization configuration, the scattering matrix elements $(S_{vv}, S_{vh}, S_{hv}, S_{hh})$ of the thin dielectric circular disk are

the complex quantities, and can be easily calculated as:

$$S_{vv} = \frac{k_o^2}{4\pi}[\hat{\boldsymbol{v}}_s \cdot \overline{\overline{\mathbf{P}}} \cdot \hat{\boldsymbol{v}}_i] \frac{2A_{(disk)}J_1(k_o a\sqrt{(k_x^i - k_x^s)^2 + (k_y^i - k_y^s)^2})}{(k_o a\sqrt{(k_x^i - k_x^s)^2 + (k_y^i - k_y^s)^2})}$$

$$S_{hh} = \frac{k_o^2}{4\pi}[\hat{\boldsymbol{h}}_s \cdot \overline{\overline{\mathbf{P}}} \cdot \hat{\boldsymbol{h}}_i] \frac{2A_{(disk)}J_1(k_o a\sqrt{(k_x^i - k_x^s)^2 + (k_y^i - k_y^s)^2})}{(k_o a\sqrt{(k_x^i - k_x^s)^2 + (k_y^i - k_y^s)^2})}$$

$$S_{hv} = \frac{k_o^2}{4\pi}[\hat{\boldsymbol{h}}_s \cdot \overline{\overline{\mathbf{P}}} \cdot \hat{\boldsymbol{v}}_i] \frac{2A_{(disk)}J_1(k_o a\sqrt{(k_x^i - k_x^s)^2 + (k_y^i - k_y^s)^2})}{(k_o a\sqrt{(k_x^i - k_x^s)^2 + (k_y^i - k_y^s)^2})}$$

$$S_{vh} = \frac{k_o^2}{4\pi}[\hat{\boldsymbol{v}}_s \cdot \overline{\overline{\mathbf{P}}} \cdot \hat{\boldsymbol{h}}_i] \frac{2A_{(disk)}J_1(k_o a\sqrt{(k_x^i - k_x^s)^2 + (k_y^i - k_y^s)^2})}{(k_o a\sqrt{(k_x^i - k_x^s)^2 + (k_y^i - k_y^s)^2})}$$

(2.1.5)

2.1.1 Rayleigh-Gans formulation for scattering from a thin dielectric circular disk

The Rayleigh-Gans formulation is valid only for very thin ($k_o t << 1$) or very small ($k_o a << 1$) disk. It is assumed that one dimension of the thin dielectric circular disk (the z-dimension) is much smaller than the operating wavelength, as shown in Fig. (2.1). For Rayleigh-Gans approximation, the elements of the polarizability tensor ($\overline{\overline{\mathbf{P}}}$) of the thin dielectric circular disk, with the relative permittivity space ϵ_r can be easily obtained as [47, 57],

$$P_{xx} = 1$$
$$P_{yy} = 1 \qquad\qquad (2.1.6)$$
$$P_{zz} = \frac{1}{\epsilon_r}$$

The off-diagonal elements of the polarizability tensor ($\overline{\overline{\mathbf{P}}}$) are zero (i.e. $P_{xy} = P_{xz} = P_{yx} = P_{yz} = P_{zx} = P_{zy} = 0$).

2.1.2 Volumetric Integral Physical Optics (VIPO) formulation for scattering from a thin dielectric circular disk

The Volumetric Integral Physical Optics (VIPO) formulation for scattering from a thin dielectric circular disk can generate the results to an accuracy that is sufficient for most practical purposes, independent of the thickness. This formulation also predicts the same scattering formula as given by Eq. (2.1.4), however the elements of the polarizability tensor $(\overline{\overline{\mathbf{P}}})$ of the thin dielectric circular disk with the relative permittivity ϵ_r must be modified as

$$
\begin{aligned}
P_{xx} &= \frac{(1+R_h)e^{i\left(k_z'-k_z\right)\frac{t}{2}}}{1+R_h e^{ik_z't}} \\
P_{yy} &= \frac{(1+R_h)e^{i\left(k_z'-k_z\right)\frac{t}{2}}}{1+R_h e^{ik_z't}} \\
P_{zz} &= \frac{1}{\epsilon_r},
\end{aligned}
\tag{2.1.7}
$$

for horizontal polarization, and

$$
\begin{aligned}
P_{xx} &= \frac{(1-R_v)e^{i\left(k_z'-k_z\right)\frac{t}{2}}}{1-R_v e^{ik_z't}} \\
P_{yy} &= \frac{(1-R_v)e^{i\left(k_z'-k_z\right)\frac{t}{2}}}{1-R_v e^{ik_z't}} \\
P_{zz} &= \frac{1}{\epsilon_r}\frac{(1+R_v)e^{i\left(k_z'-k_z\right)\frac{t}{2}}}{1+R_v e^{ik_z't}},
\end{aligned}
\tag{2.1.8}
$$

for vertical polarization. where $k_z'^2 = k_o^2(\epsilon_r - 1) + k_z^2$, $k_z = \hat{\mathbf{k}}_i.\hat{\mathbf{z}}$ and R_h ,R_v are the Fresnal Reflection Coefficients for the h-polarization and v-polarization respectively.

2.1.3 Koh-Sarabandi (KS) formulation for scattering from a thin dielectric circular disk

The Rayleigh-Gans approximation provides accurate results only for a very small/thin disk. VIPO can produce accurate results independent of the thickness, but completely

fails at near-grazing incidence. Volumetric equivalent theorem states that the scatterer embedded in the host medium with permittivity ϵ_o can be replaced with a volumetric current distribution of $\mathbf{J}$, which satisfy the following Fredholm integral equation as given by Eq. (2.1.1). In this case, the elements of the polarizability tensor of the thin dielectric circular disk can be expressed as

$$
\begin{aligned}
P_{xx} &= \frac{k_z^i}{k_z^i - \alpha k_o^2} \\
P_{yy} &= \frac{k_z^i}{k_z^i - \alpha k_o^2} \\
P_{zz} &= 0,
\end{aligned}
\tag{2.1.9}
$$

for horizontal polarization, and

$$
\begin{aligned}
P_{xx} &= \frac{1}{1 - \alpha k_z^i} \\
P_{yy} &= \frac{1}{1 - \alpha k_z^i} \\
P_{zz} &= \frac{k_z^i}{\epsilon_r k_z^i - \alpha k_z^{i2}},
\end{aligned}
\tag{2.1.10}
$$

for vertical polarization.

The comparison of all these above three techniques for the magnitudes of forward scattering elements (S_{hh}, S_{vv}) has been shown in Fig. 2.2. In this figure, (S_{hh}, S_{vv}) as a function of incident angle θ_i, size parameter $k_o a$, and the relative permittivity ϵ_r have been considered. It is evident from the Fig. (2.2) that Rayleigh-Gans overestimates the forward scattering elements (S_{hh}, S_{vv}) over the entire comparison region. However, the Rayleigh-Gans (low frequency) approximation becomes inaccurate while VIPO and KS give good results as the $k_o a$ increases. It should be mentioned that the simulation results presented in the Figures. (2.2) and (2.3) are all based on the free space environment, and a time convention e^{-iwt} is assumed and suppressed.

2.2   Summary and Conclusions

An analysis for the three most widely used scattering approximations such as Rayleigh-Gans (low frequency approximation), Volume integral physical optics (high frequency approximation) and Koh-Sarabandi (intermediate frequency approximation) are briefly reviewed for their applications and limitations. They are studied based on the simulation results as shown in Fig. 2.(a-f) Where the results are in good agreement with the previously published work [56, 57]. In Fig. 2.3 (a-d), it is seen that forward scattering coefficients (S_{hh} and S_{vv}) are in smaller in magnitudes for increasing value of $\left(\frac{t}{\lambda}\right)$ as compared to increasing value of $\left(\frac{t}{a}\right)$ for all the three considered techniques. For completeness, the effects of $k_o a$ upon S_{vv} and the influences of ϵ_r upon the S_{hh} and S_{vv} have also been studied which are not reported previously in the literature.
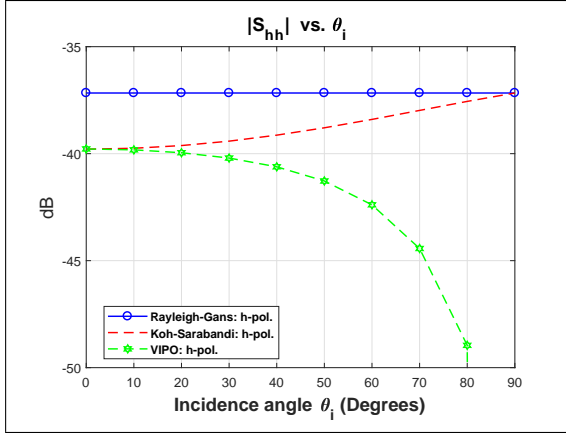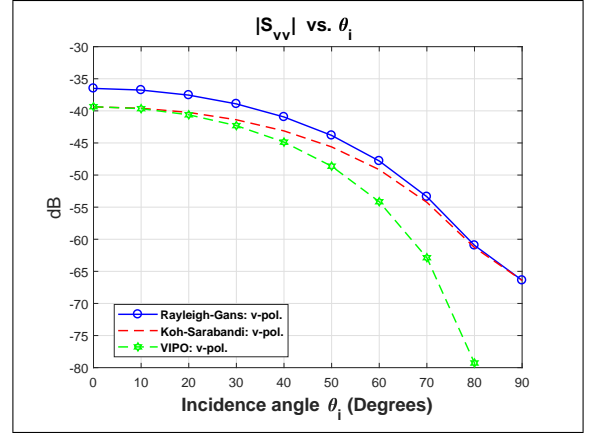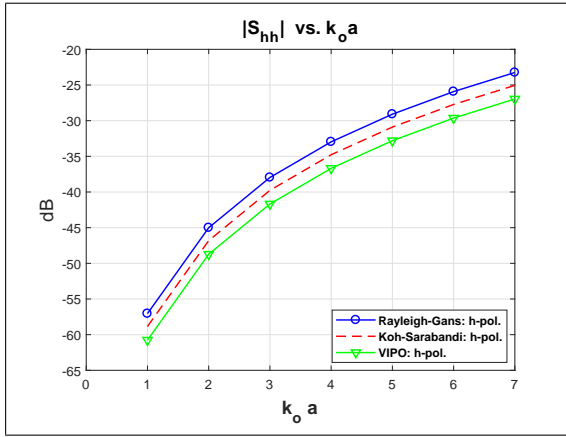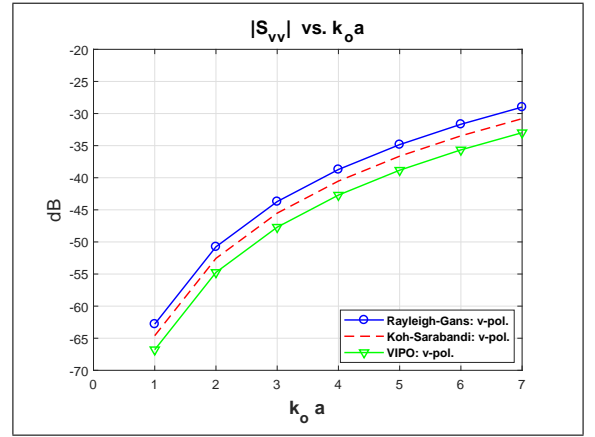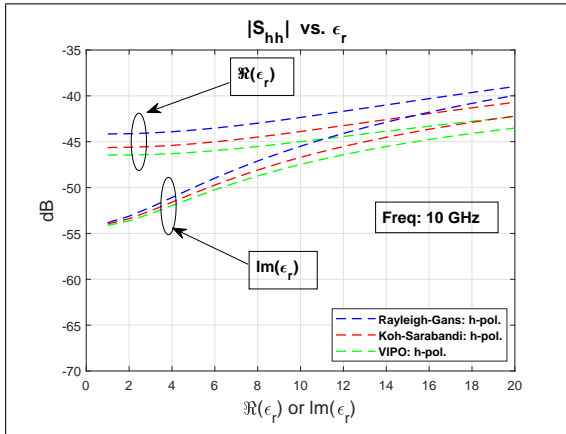
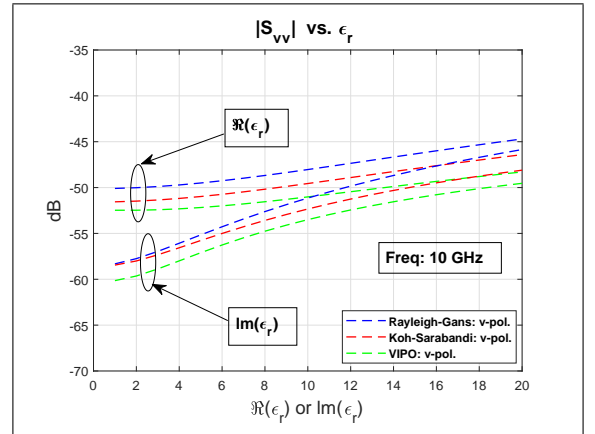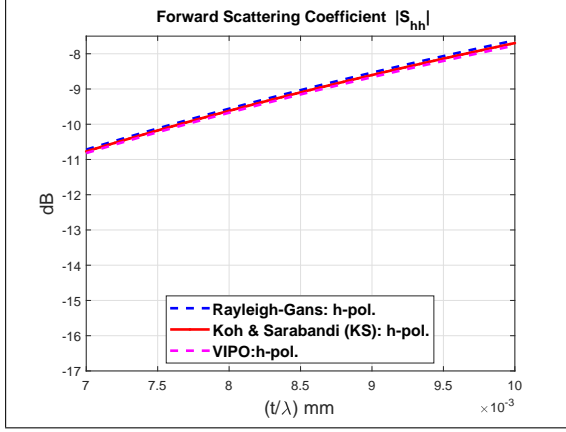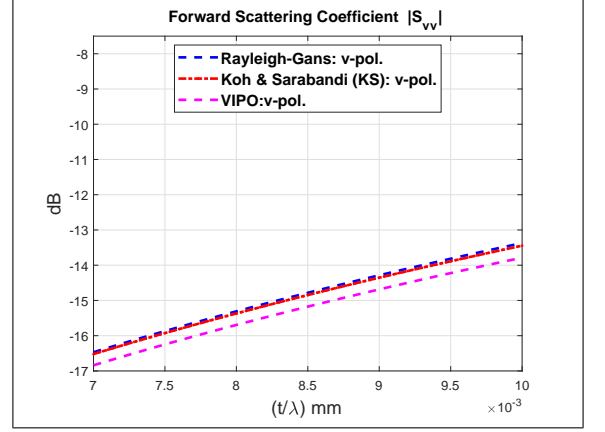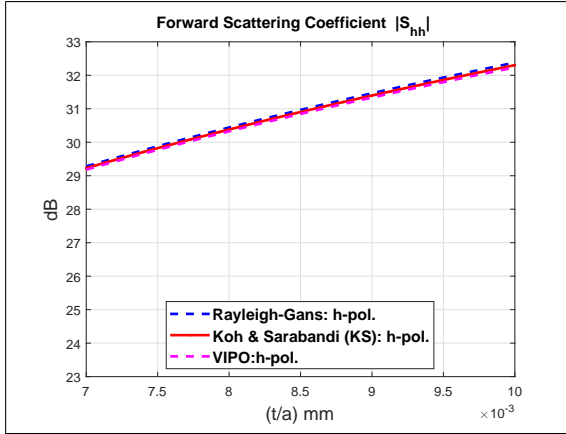Figure 2.2: Magnitude of forward scattering elements (S_{hh}, S_{vv}) from a thin dielectric circular disk as a function of incidence angles θ_i (Figs. (2.a-2.b), k_oa (2.c-2.d), and ϵ_r of the disk (Figs. (2.e-2.f). Frequency is set at 10 GHz and the relative permittivity, thickness, and radius of the disk are $\epsilon_r = 28.6 + i * 12.56$, 0.02 cm and 1.5 cm, respectively. These results are based on RG, VIPO, and KS approaches.
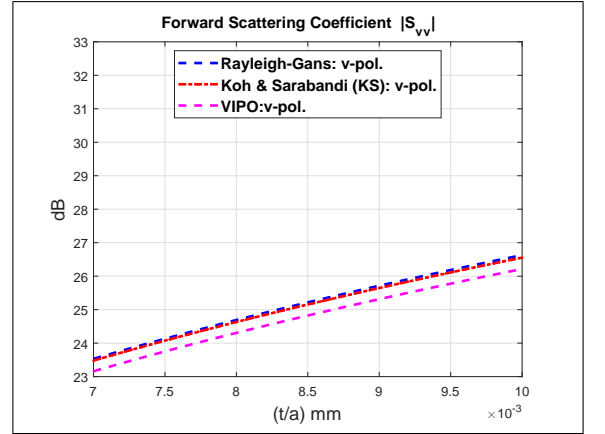
Figure 2.3: Magnitude of forward scattering elements (S_{hh}, S_{vv}) from a dielectric circular disk as a function of ratio of thickness to wavelength (t/λ) (Figs. 2.3a-2.3b), and as a function of ratio of thickness to radius of the disk ($Figs.2.3c - 2.3d$), Frequency is set at 10 GHz and the relative permittivity are $\epsilon_r = 26.6 + i * 11.56$ respectively. These results are based on the Rayleigh-Gains (RG) (low frequency approximation), Koh-Sarabandi (KS) (intermediate frequency approximation) and Volume Integral Physical Optics $VIPO$ (high frequency approximation) scattering approaches.

Chapter 3

Back-scattering cross section from a tilted thin circular dielectric disk

In this chapter, back-scattering cross section from a tilted thin circular dielectric disk based upon the three different approximations, i.e., Rayleigh Gans, Koh-Sarabandi and Volumetric Integral Physical Optics is presented. It is investigated that by varying the orientation of the disk, the back-scattering cross section can be enhanced or diminished as compared to the disk having no tilt. It is further studied that for the specific tilt and size parameter of a low loss Gallium Arsenide disk, the back-scattering cross sections can be made almost equal to zero for both types of incident polarizations, i.e., horizontal and vertical. Such type of almost zero back-scattering cross section find applications in the stealth technology. The effects of the various geometrical and dielectric parameters on the tilted thin dielectric disk for both the horizontal and the vertical incident polarization are also presented.

In section (3.1) , mathematical formulation for the numerical calculation of the Back-scattering cross section from a tilted thin circular dielectric disk numerical results is described. In section (3.2), simulation results for the backscattering cross

sections are presented to illustrate the effects of various physical and geometrical parameters of the dielectric disk. A brief summary of the research work performed in this study followed by the important conclusions is presented in section (3.3) .

3.1 Formulation of the problem

Consider a tilted thin dielectric circular disk as shown in Fig. 3.1. The disk is assumed to non-magnetic with the relative permittivity of ϵ_r. The radius of disk is a and its thickness is t with $k_0 t <<1$. Here k_0 is the free space wave number. In global coordinates, the orientation of the disk is described by a unit vector $\hat{\mathbf{n}}$ which is given as,

$$\hat{\mathbf{n}} = \sin\theta_t \cos\phi_t \hat{\mathbf{x}} + \sin\theta_t \sin\phi_t \hat{\mathbf{y}} + \cos\theta_t \hat{\mathbf{z}} \qquad (3.1.1)$$

where magenta tilt angles θ_t and ϕ_t represent the elevation and azimuth angles of the disk. In case if the disk has orientation angles of $\theta_t = \phi_t = 0^o$ then the disk lies in the xy–plane. An incident plane wave which is propagating in the direction $\hat{\mathbf{k}}_i$ and polarized along the unit vector $\hat{\mathbf{q}}_i$ can be written as,

$$\mathbf{E}_i = \hat{\mathbf{q}}_i E_o e^{ik_0 \hat{\mathbf{k}}_i \cdot \mathbf{r}} \qquad (3.1.2)$$

where E_o is the magnitude. Here, $\hat{\mathbf{q}}_i = \hat{\mathbf{v}}_i$ or $\hat{\mathbf{h}}_i$. Also $\hat{\mathbf{h}}_i = (\hat{\mathbf{k}}_i \times \hat{\mathbf{z}})/(|\hat{\mathbf{k}}_i \times \hat{\mathbf{z}}|)$ and $\hat{\mathbf{v}}_i = \hat{\mathbf{h}}_i \times \hat{\mathbf{k}}_i$ represent the horizontal and vertical unit vectors respectively. Here $|\cdot|$ represents the magnitude of a vector. The vector $\hat{\mathbf{k}}_i$ is the unit vector along the propagation direction of an incident wave and can be represented in terms of the usual spherical coordinates as $\hat{\mathbf{k}}_i = \cos\phi_i \sin\theta_i \hat{\mathbf{x}} + \sin\phi_i \sin\theta_i \hat{\mathbf{y}} + \cos\theta_i \hat{\mathbf{z}}$. This incident wave impinges upon a dielectric disk and induces current inside it. Once the induced current density inside a thin dielectric circular disk is known then the far
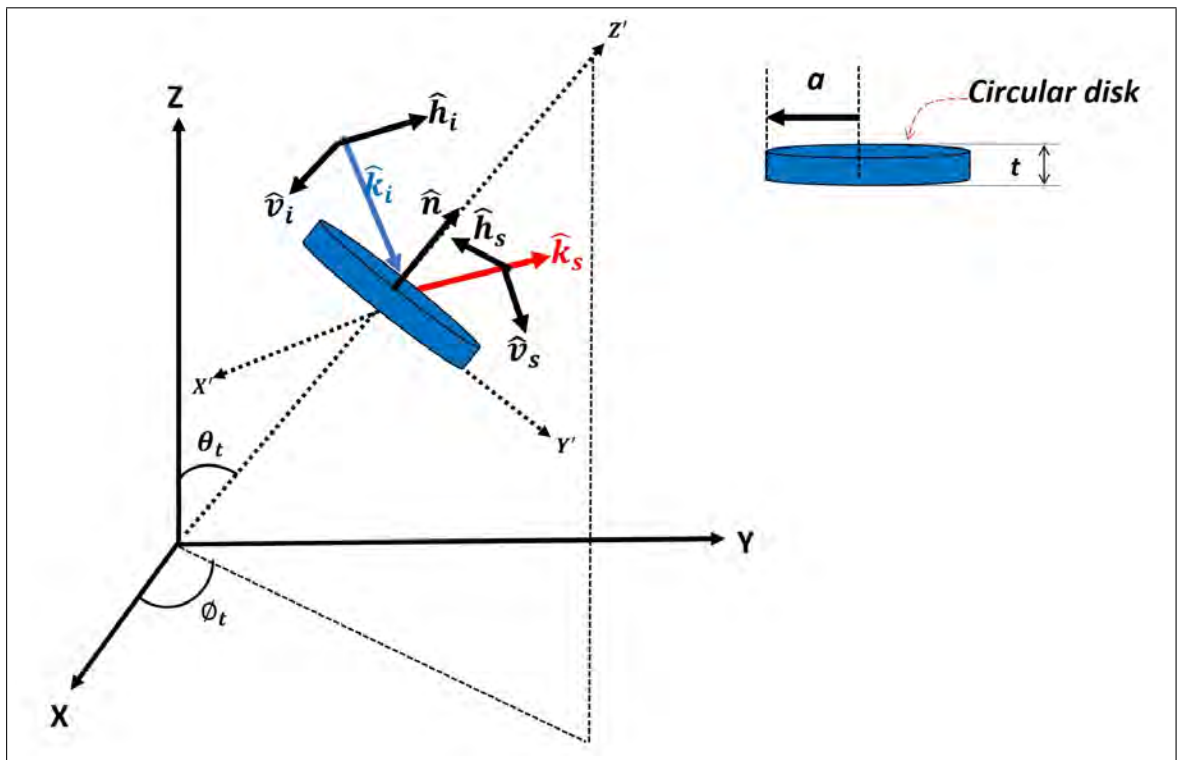
Figure 3.1: Scattering geometry of a tilted thin dielectric circular disk in global coordinate system. In fact disk is located at the origin of coordinate system (X,Y,Z), but for clarity of local coordinate system (X', Y', Z') it is shown displaced in figure.

zone scattered electric field from a tilted disk using KS approach [56] can be written as,

$$\begin{aligned}
\mathbf{E}_s^g &= \frac{-k_0^2}{4\pi} \frac{e^{ik_0 r}}{r} \hat{\mathbf{k}}_s^g \times \hat{\mathbf{k}}_s^g \times [\overline{\overline{\mathbf{P}}}^g \cdot \mathbf{E}_i^g] \frac{2t A_{(disk)} J_1(\sqrt{a^2(C^2 + D^2)})}{\sqrt{a^2(C^2 + D^2)}} \\
&= \frac{e^{ik_0 r}}{r} \overline{\overline{\mathbf{S}}}^g \cdot \mathbf{E}_i^g = \frac{e^{ik_0 r}}{r} \begin{pmatrix} S_{vv}^g & 0 \\ 0 & S_{hh}^g \end{pmatrix} \cdot \mathbf{E}_i^g
\end{aligned} \qquad (3.1.3)$$

The elements of scattering matrix $\overline{\overline{\mathbf{S}}}^g$ can be computed using $S_{vv}^g = \hat{\mathbf{v}}_s \cdot \overline{\overline{\mathbf{S}}}^g \cdot \hat{\mathbf{v}}_i$ and $S_{hh}^g = \hat{\mathbf{h}}_s \cdot \overline{\overline{\mathbf{S}}}^g \cdot \hat{\mathbf{h}}_i$ with $\hat{\mathbf{h}}_s = (\hat{\mathbf{k}}_s \times \hat{\mathbf{z}})/(|\hat{\mathbf{k}}_s \times \hat{\mathbf{z}}|)$ and $\hat{\mathbf{v}}_s = \hat{\mathbf{h}}_s \times \hat{\mathbf{k}}_s$. In this case, $\hat{\mathbf{k}}_s$ is the unit vector along the direction of scattering or observation point and can be expressed mathematically as, $\hat{\mathbf{k}}_s = \cos\phi_s \sin\theta_s \hat{\mathbf{x}} + \sin\phi_s \sin\theta_s \hat{\mathbf{y}} - \cos\theta_s \hat{\mathbf{z}}$. The superscript "g" indicates the global coordinates and $A_{(disk)} = \pi a^2$ is the physical area of a thin dielectric circular disk. The factor $J_1(.)$ is the first kind Bessel function of order unity. The tensor $\overline{\overline{\mathbf{P}}}^g$ is the new polarizability tensor associated with the tilted thin dielectric circular disk which is oriented at angles (θ_t, ϕ_t) and can be written as,

$$\overline{\overline{\mathbf{P}}}^g = \overline{\overline{T}}^{-1} \cdot \overline{\overline{\mathbf{P}}} \cdot \overline{\overline{T}} \qquad (3.1.4)$$

where $\overline{\overline{\mathbf{P}}}$ is the polarizability tensor when the disk is oriented at $(\theta_t, \phi_t) = (0^o, 0^o)$ and given in [56]. Here $\overline{\overline{T}}$ is the coordinate transformation matrix that transforms the global coordinate system to the local coordinate system and given by [92],

$$\overline{\overline{\mathbf{T}}} = \begin{pmatrix} \cos\theta_t \cos\phi_t & \cos\theta_t \sin\phi_t & -\sin\theta_t \\ -\sin\phi_t & \cos\phi_t & 0 \\ \sin\theta_t \cos\phi_t & \sin\theta_t \sin\phi_t & \cos\theta_t \end{pmatrix} \qquad (3.1.5)$$

Also $C = k_0(\hat{\mathbf{k}}_i^g - \hat{\mathbf{k}}_s^g) \cdot \hat{\mathbf{x}}$ and $D = k_0(\hat{\mathbf{k}}_i^g - \hat{\mathbf{k}}_s^g) \cdot \hat{\mathbf{y}}$. The expressions for the transformed vectors $\hat{\mathbf{k}}_i^g$, $\hat{\mathbf{k}}_s^g$ and $\mathbf{E}_i^g$ appearing in Eq.(3) can be written in terms of $\hat{\mathbf{k}}_i$, $\hat{\mathbf{k}}_s$ and $\mathbf{E}_i$ as $\hat{\mathbf{k}}_i^g = \overline{\overline{\mathbf{T}}}^{-1} \cdot \hat{\mathbf{k}}_i$, $\hat{\mathbf{k}}_s^g = \overline{\overline{\mathbf{T}}}^{-1} \cdot \hat{\mathbf{k}}_s$ and $\mathbf{E}_i^g = \overline{\overline{\mathbf{T}}}^{-1} \cdot \mathbf{E}_i$. Using values of $\overline{\overline{\mathbf{T}}}$ and $\overline{\overline{\mathbf{P}}}$ in

Eq.(4), the new polarizability tensor $\overline{\overline{\mathbf{P}}}^g$ for a tilted thin dielectric circular disk can be found. Once the scattering amplitudes S_{hh}^g and S_{vv}^g of a thin dielectric circular disk are known then the back-scattering cross section for horizontally polarized σ_{hh} and vertically polarized σ_{vv} scattering can be written as,

$$\sigma_{hh} = 4\pi \mid S_{hh}^g(\hat{\mathbf{k}}_i, \hat{\mathbf{k}}_s = -\hat{\mathbf{k}}_i) \mid^2$$
$$\sigma_{vv} = 4\pi \mid S_{vv}^g(\hat{\mathbf{k}}_i, \hat{\mathbf{k}}_s = -\hat{\mathbf{k}}_i) \mid^2$$

(3.1.6)

The elements of the polarizability tensor $\overline{\overline{\mathbf{P}}}$ for both types of incident polarizations using RG, KS and VIPO techniques are given in [56, 57], [57] and [48, 50] respectively.

3.2   Numerical Results

In this section, the effects of various parameters including incident angle, size parameter and the permittivity of the disk upon the back-scattering cross sections, i.e., σ_{hh} and σ_{vv} of a tilted thin circular dielectric disk have been shown and discussed. For this, the back-scattering cross sections have been computed using three different approaches, i.e., the Rayleigh-Gans (RG), the Koh-Sarabandi (KS) and the volumetric integral physical optics (VIPO). It should be noted that for all the figures, three different sets of tilt angles have been considered and these results are also compared with the disk having no tilt. The three different sets of tilt angles considered here are $(\theta_t, \phi_t) = (30^o, 30^o)$, $(45^o, 45^o)$ and $(90^o, 90^o)$. One of the incident angle ϕ_i is assumed to be fixed, i.e., $\phi_i = 10°$ and the thickness of a disk is taken to be $t = 0.01\lambda_0$ for all the figures. In order to validate the proposed formulation of a tilted thin circular dielectric disk with previous works [56, 57] of a horizontal disk, it is desired to take $(\theta_t, \phi_t) = (0^o, 0^o)$. In this case, we take the relative permittivity ϵ_r of a disk as $2 + i10$
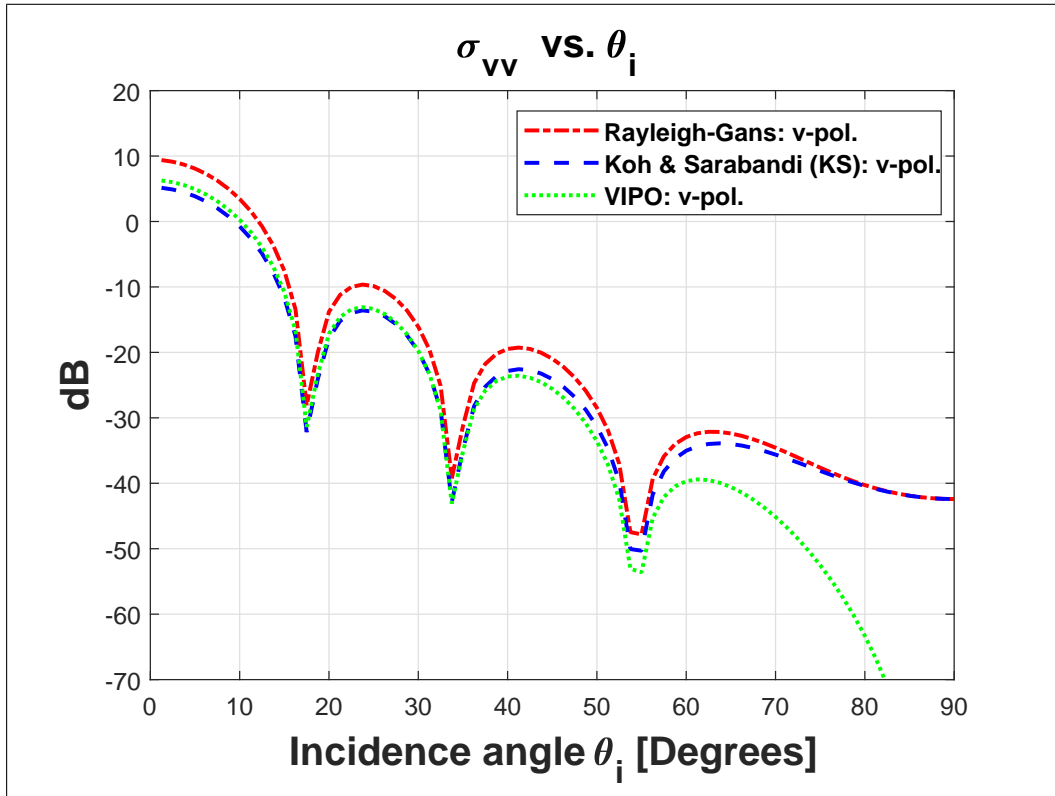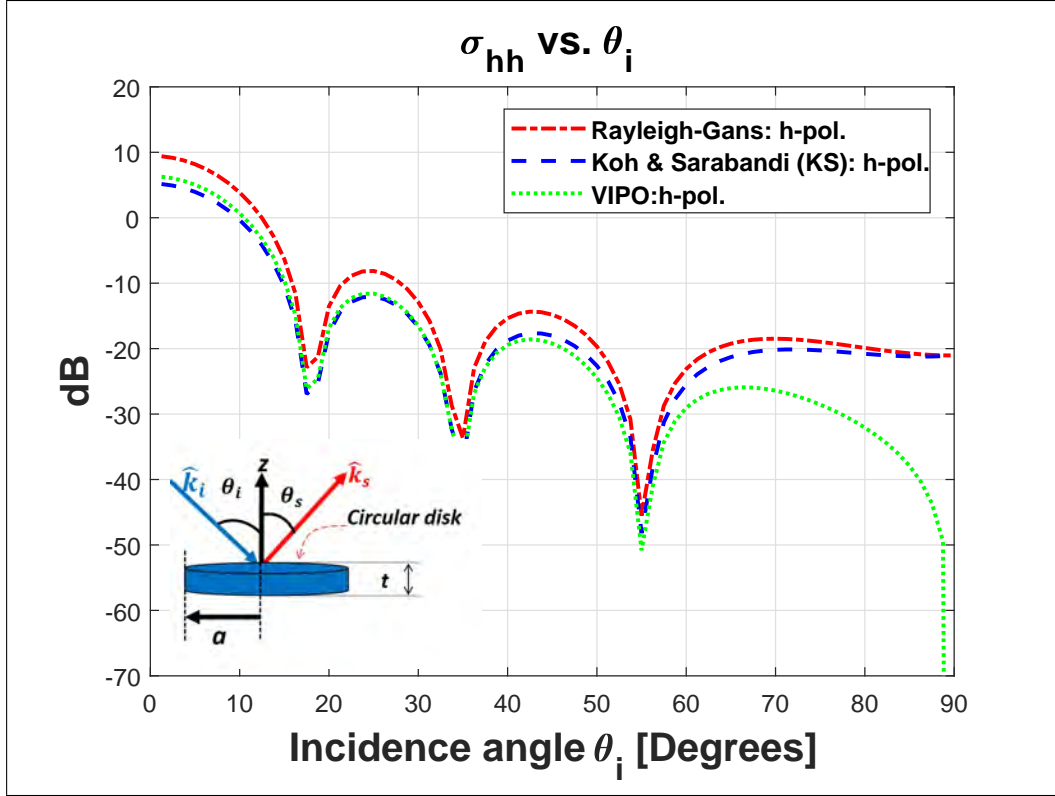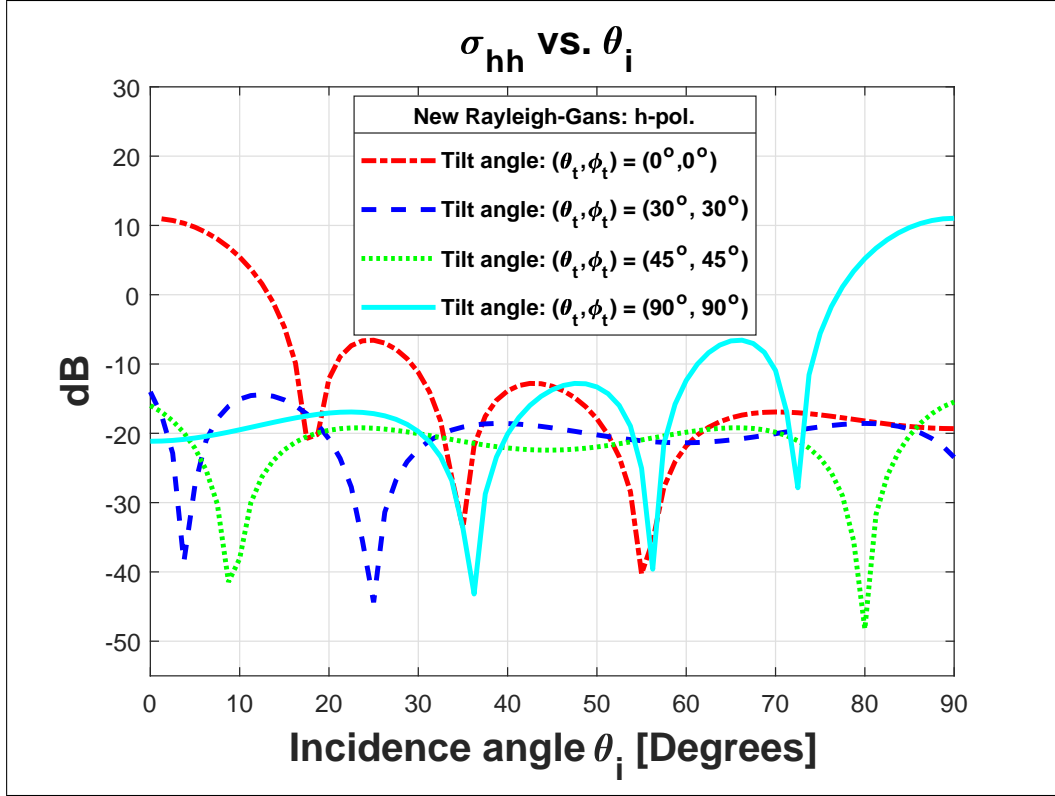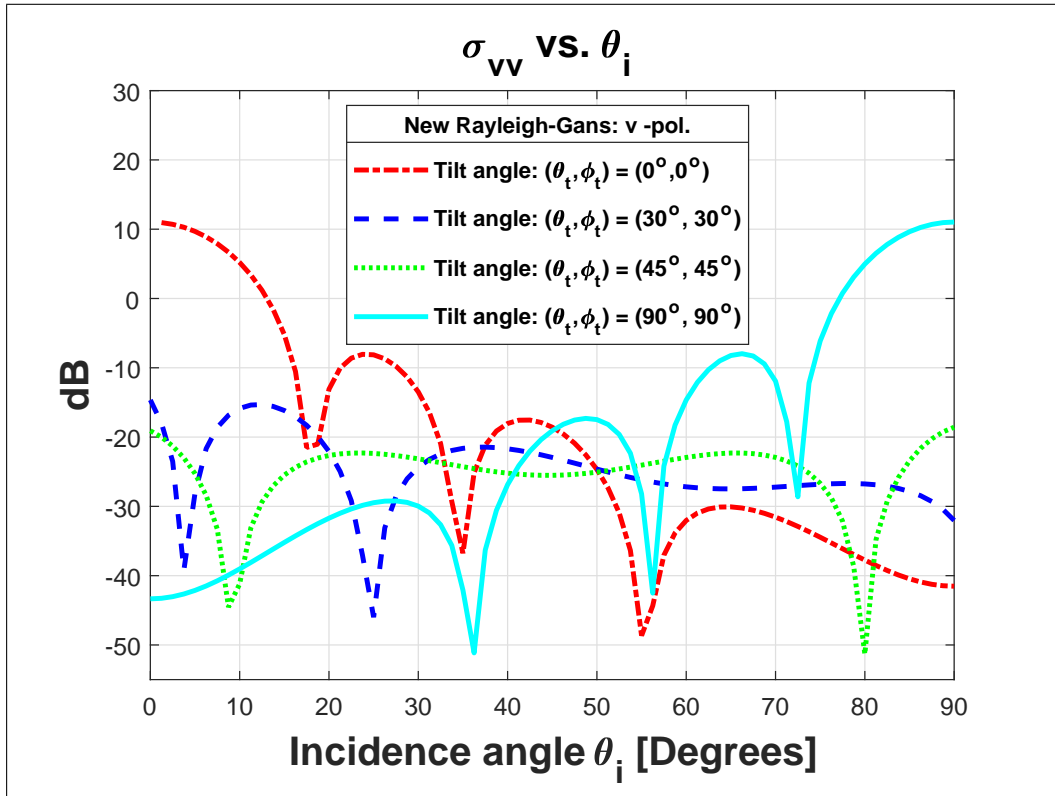
(a)

(b)

Figure 3.2: The back-scattering cross sections (a) σ_{hh} and (b) σ_{vv} from a thin dielectric circular disk with $\theta_t = \phi_t = 0^o$ as a function of incident angle θ_i. Using the same geometrical and electrical parameters as given in [37], it is found that σ_{hh} is in good agreement with Chapter 6 (Fig. 9) of Ref. [56].
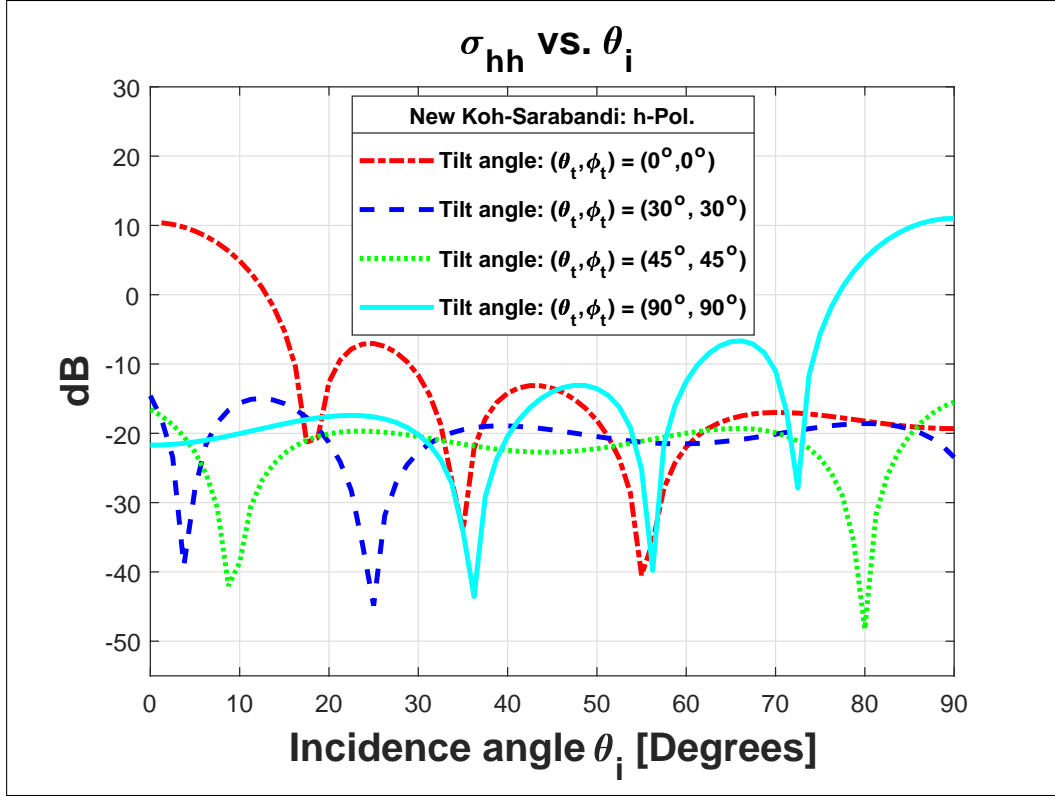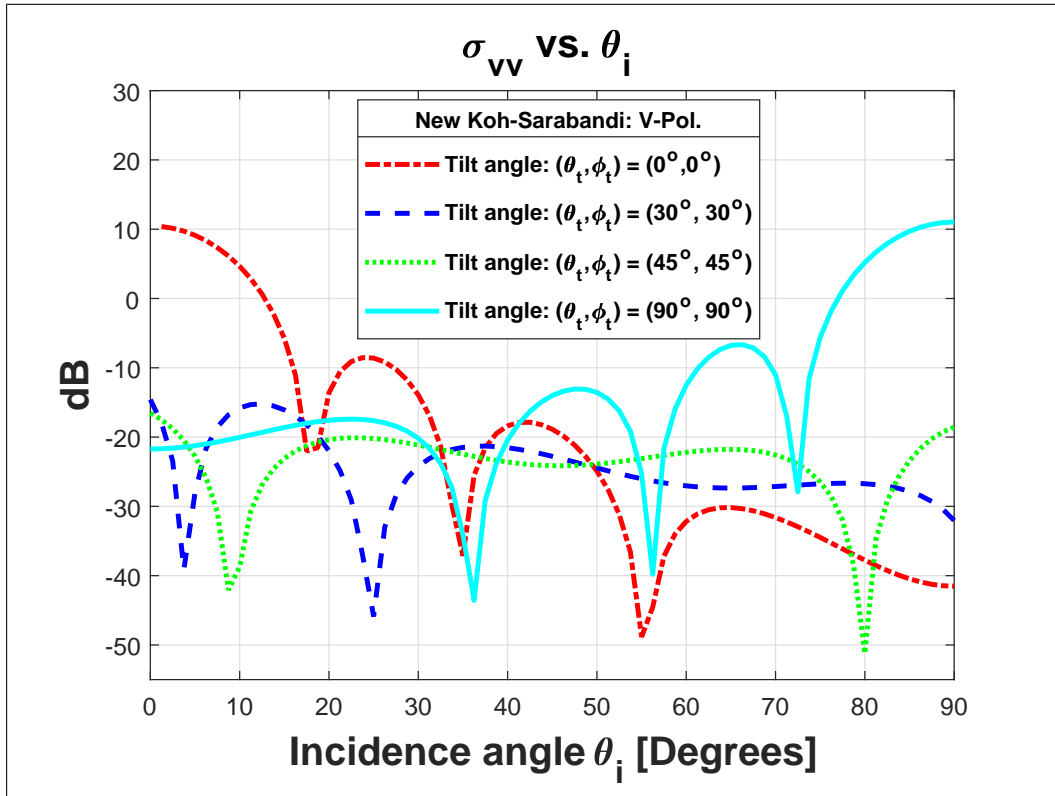
(a)

(b)

Figure 3.3: The back-scattering cross sections (a) σ_{hh} and (b) σ_{vv} from a tilted thin dielectric circular disk with the orientations (θ_t, ϕ_t) of $(30^o, 30^o)$, $(45^o, 45^o)$ and $(90^o, 90^o)$ as a function of incident angle θ_i. The results presented here are based on the newly proposed formulation of a tilted disk using Rayleigh-Gans approximation which is a low frequency approximation.
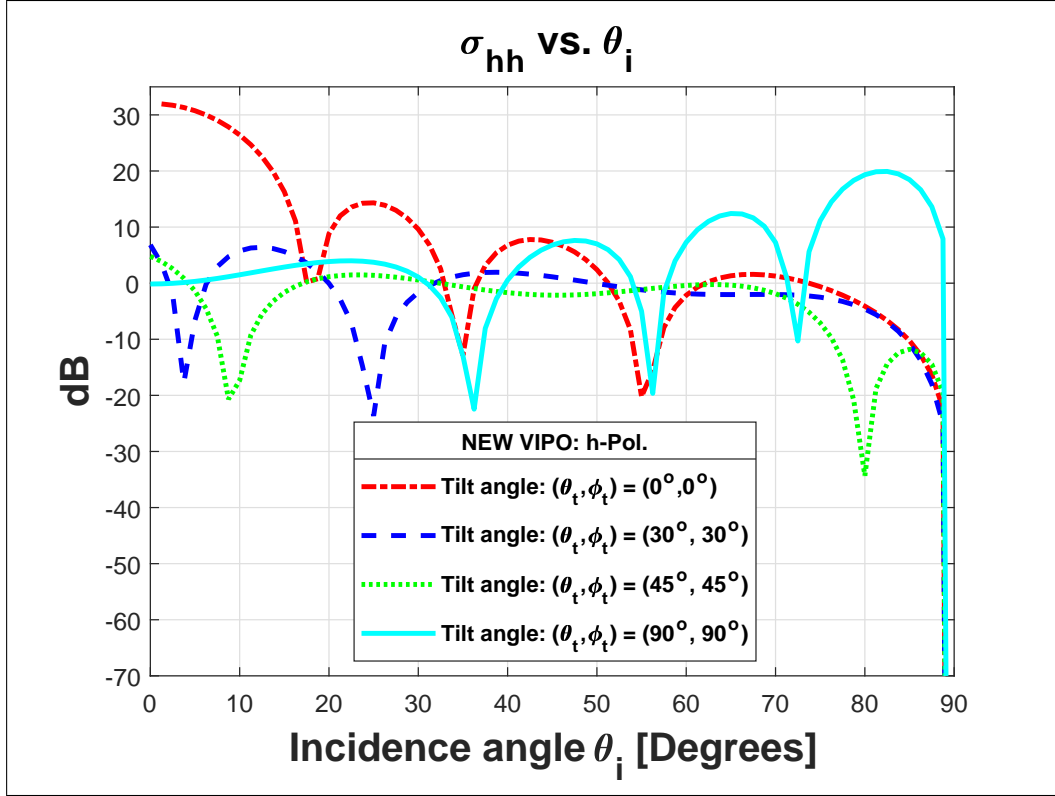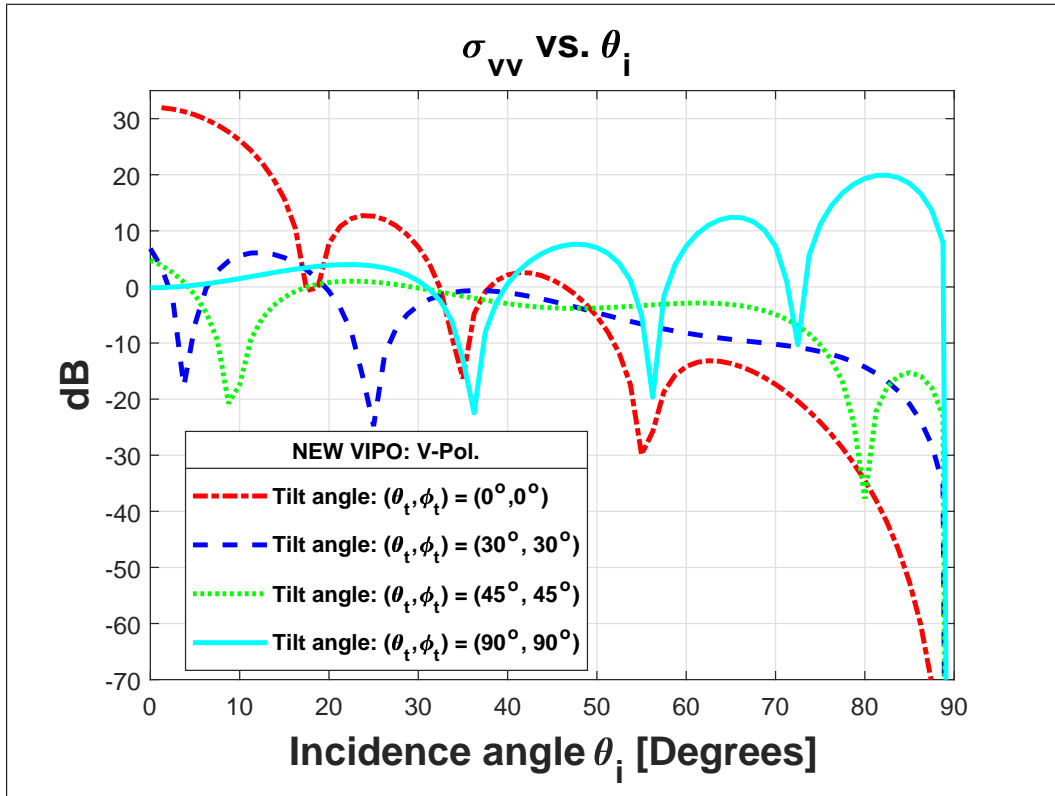
Figure 3.4: The back-scattering cross sections (a) σ_{hh} and (b) σ_{vv} from a tilted thin dielectric circular disk as a function of incident angle θ_i with the same set of orientations as considered in Fig. (3.3). The presented results are based on the newly proposed formulation of Koh-Sarabandi (KS) approach. This approach is valid for the intermediate range of frequencies.
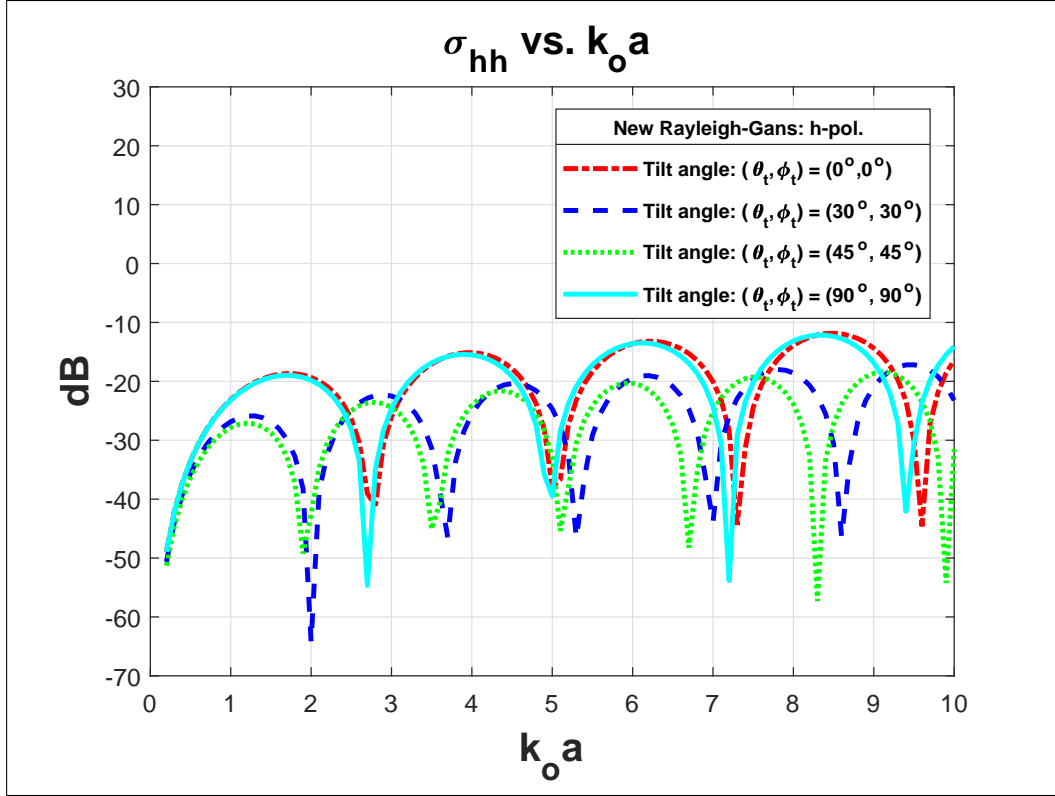
(a)

(b)

Figure 3.5: The effects of tilt angles upon the back-scattering cross sections (a) σ_{hh} and (b) σ_{vv} from a tilted thin dielectric circular disk as a function of incident angle θ_i with the same set of tilt angles as considered in Fig. (3.3) The presented results are based on the newly proposed formulation of the tilted disk using VIPO method which is valid at higher frequencies.
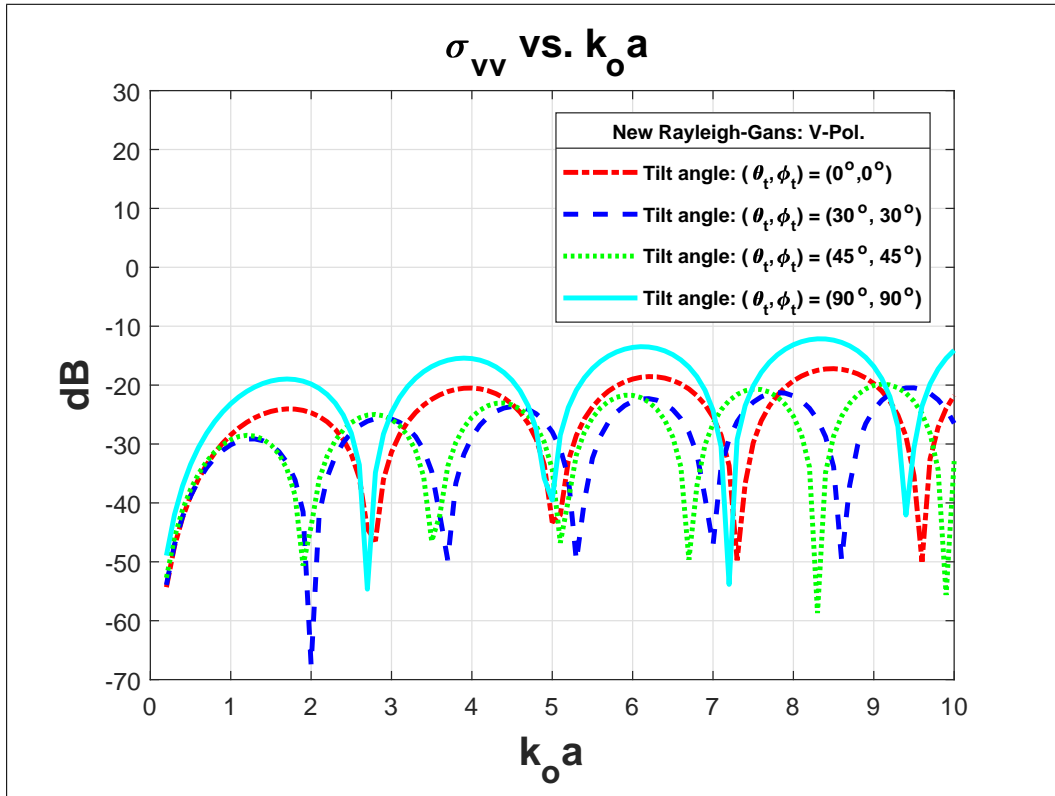
Figure 3.6: The effects of tilt angles upon the back-scattering cross sections (a) σ_{hh} and (b) σ_{vv} from a tilted thin dielectric circular disk as a function of disk size parameter $k_0 a$. The presented results are based on the low frequency Rayleigh-Gans approach.

Figure 3.7: The influences of tilt angles upon the back-scattering cross sections (a) σ_{hh} and (b) σ_{vv} from a tilted thin dielectric circular disk as a function of disk size parameter k_0a. The presented results are based on the intermediate frequency solution of Koh-Sarabandi (KS) approach.
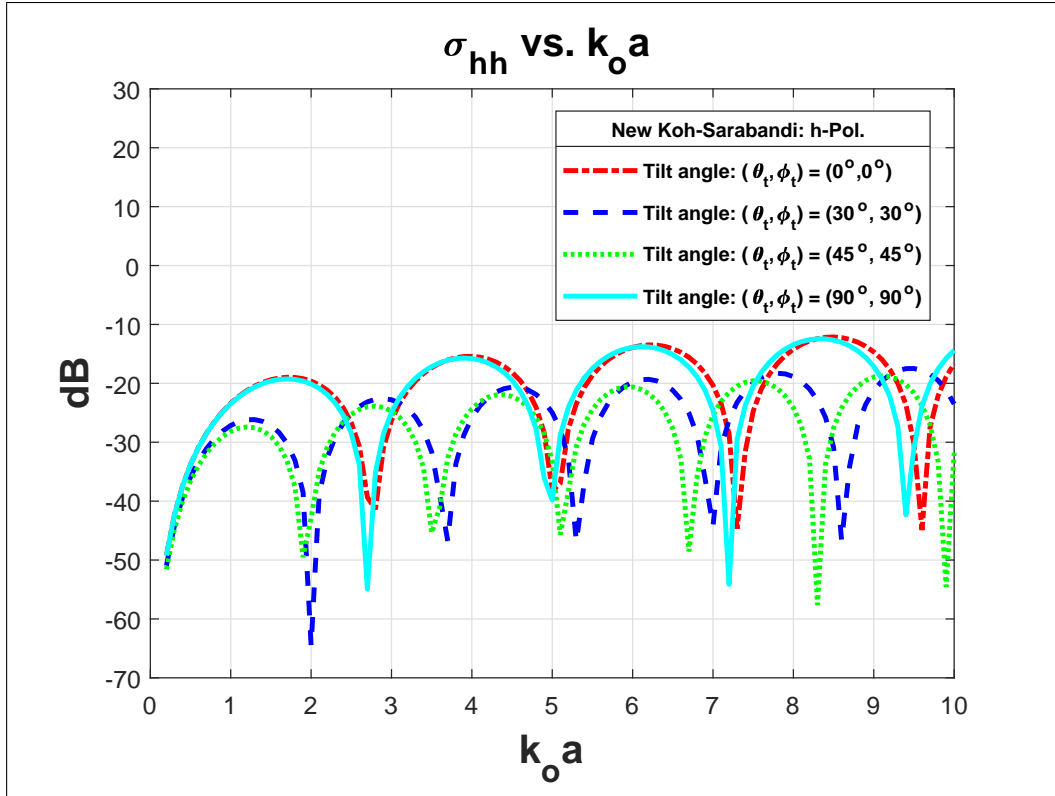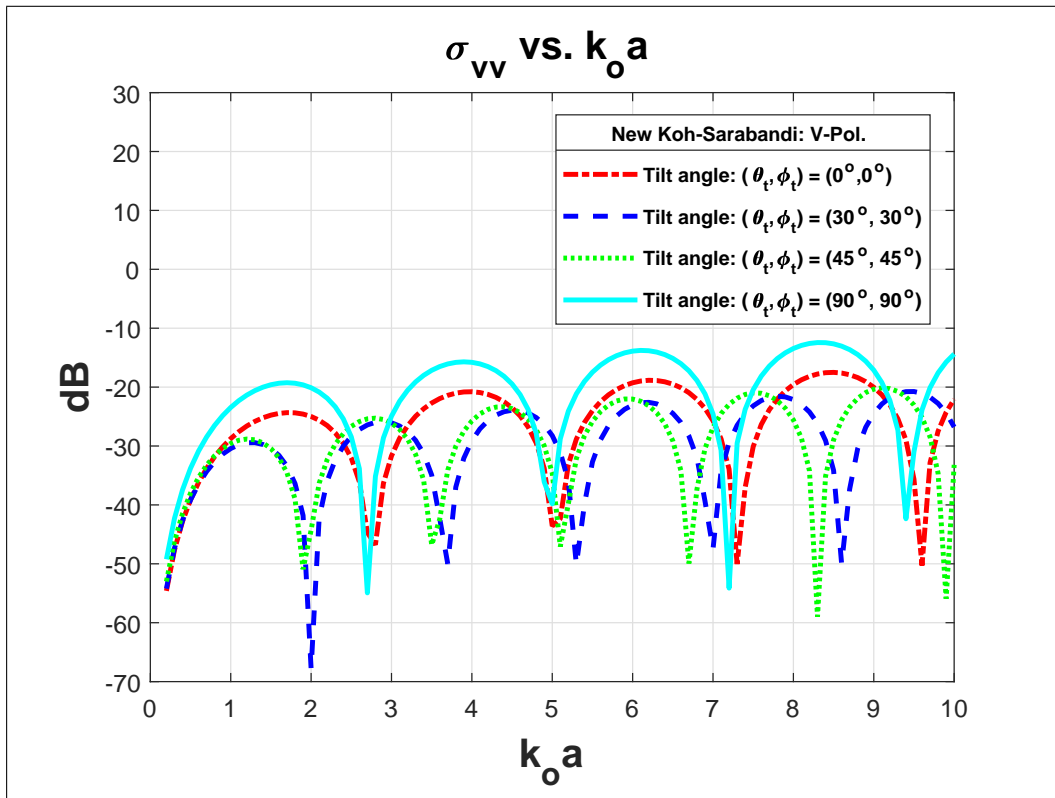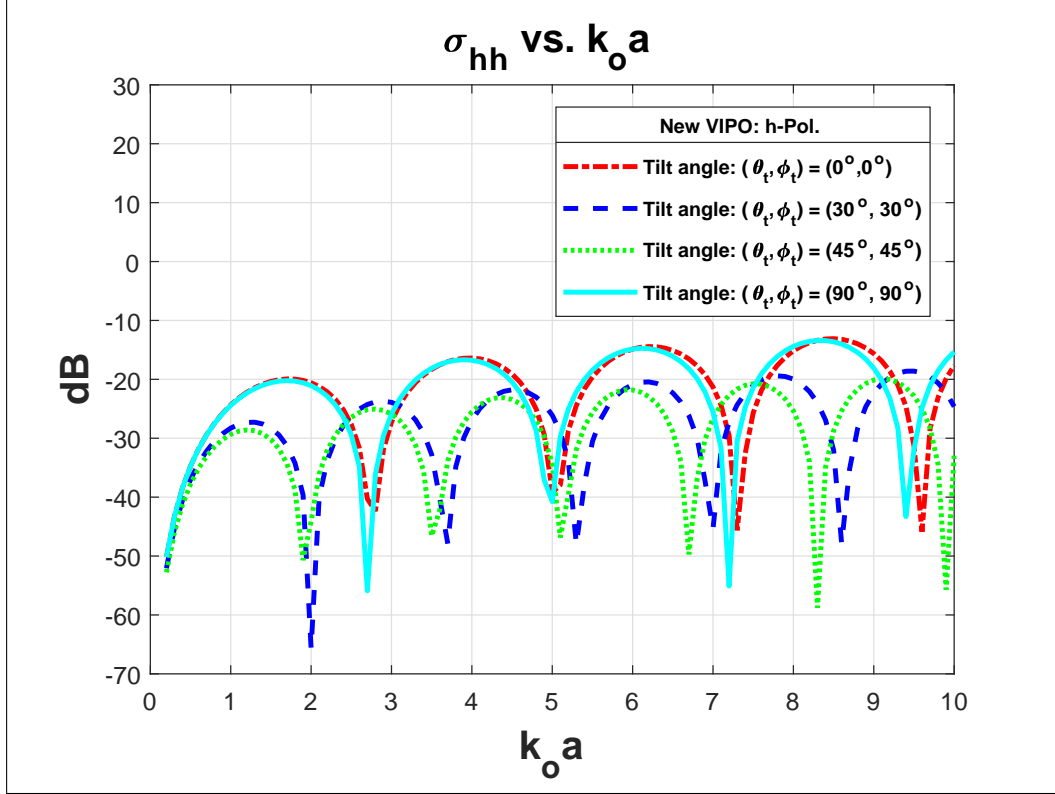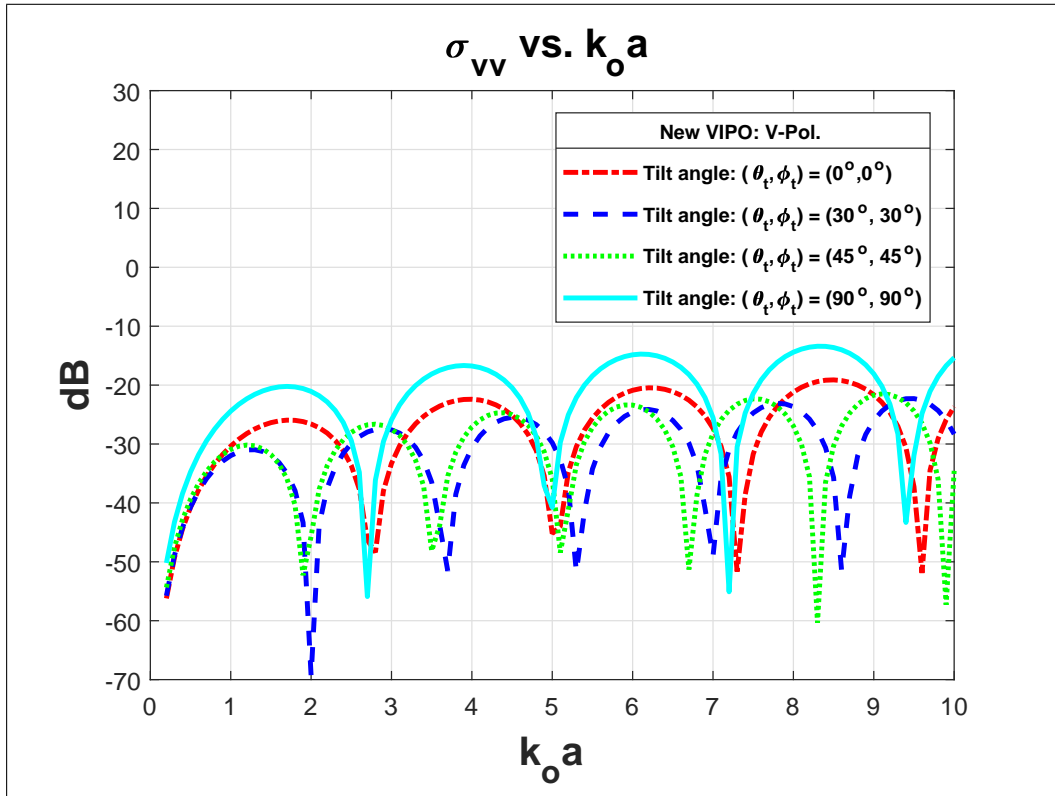
Figure 3.8: The effects of tilt angles upon the back-scattering cross sections (a) σ_{hh} and (b) σ_{vv} from a tilted thin dielectric circular disk as a function of disk size parameter $k_0 a$. Here the presented results are based on the high frequency solution of VIPO method.
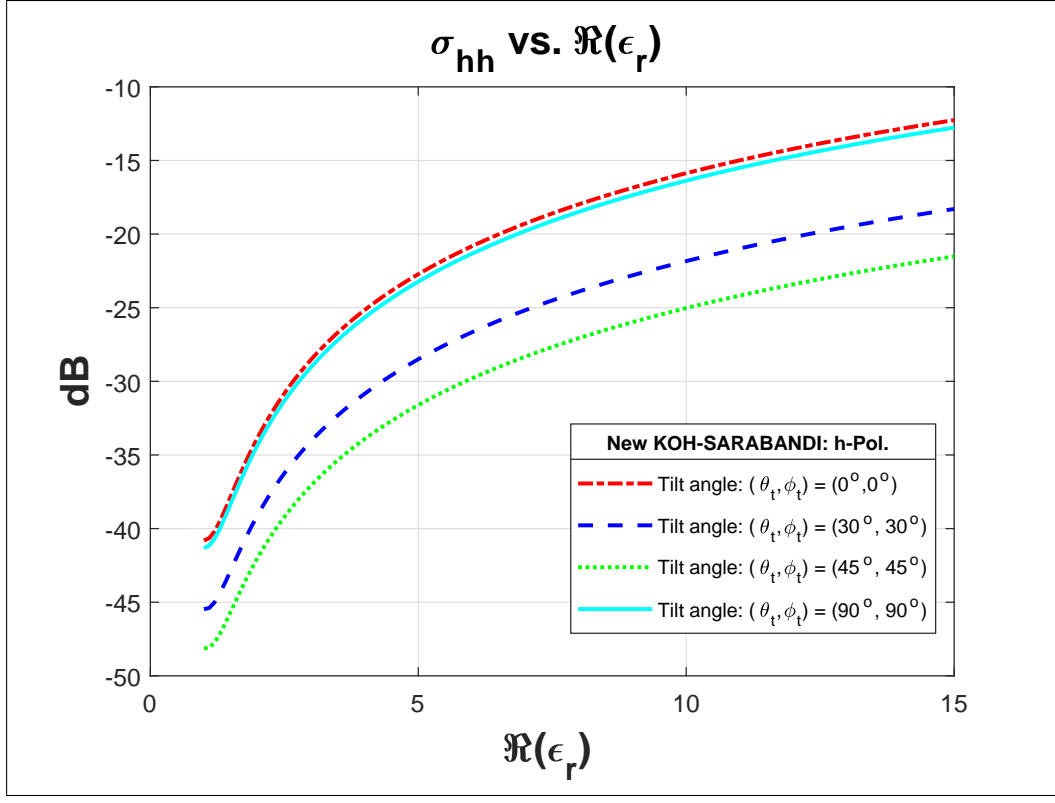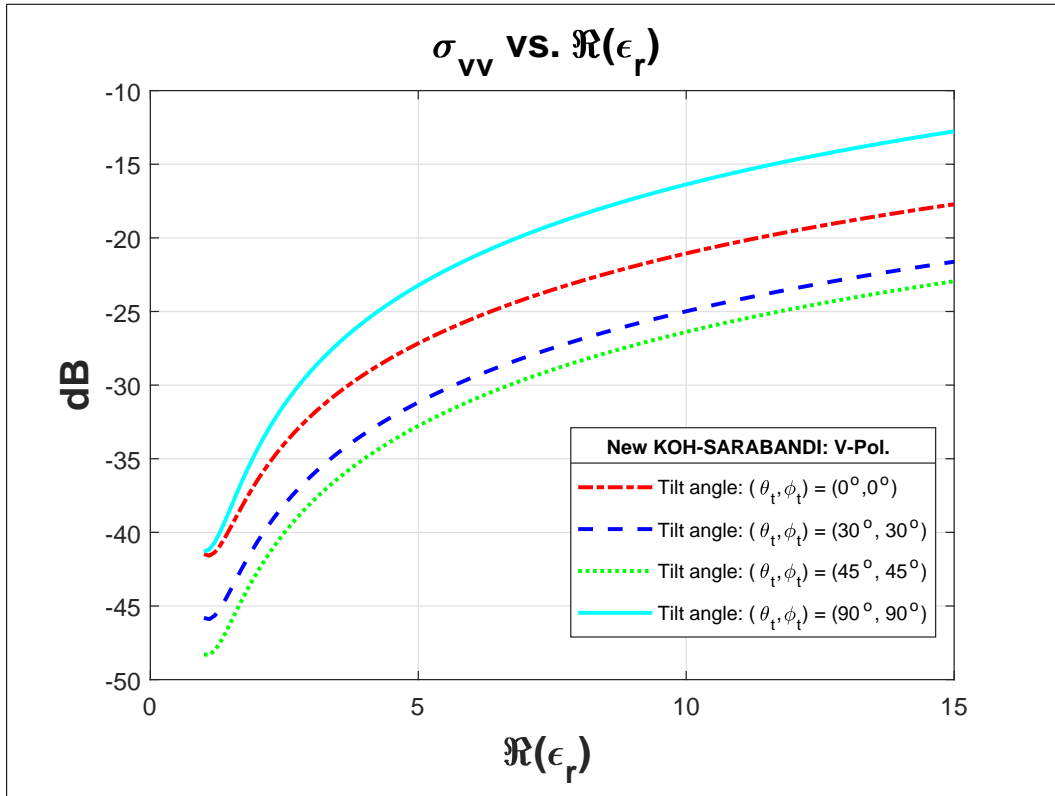
Figure 3.9: The back-scattering cross sections (a) σ_{hh} and (b) σ_{vv} from a tilted dielectric disk as a function of the real part of the relative permittivity $\Re(\epsilon_r)$ of a disk. Here, incident angle θ_i is assumed to be 45° and the presented results are based on the Koh-Sarabandi (KS) approach.

(a)
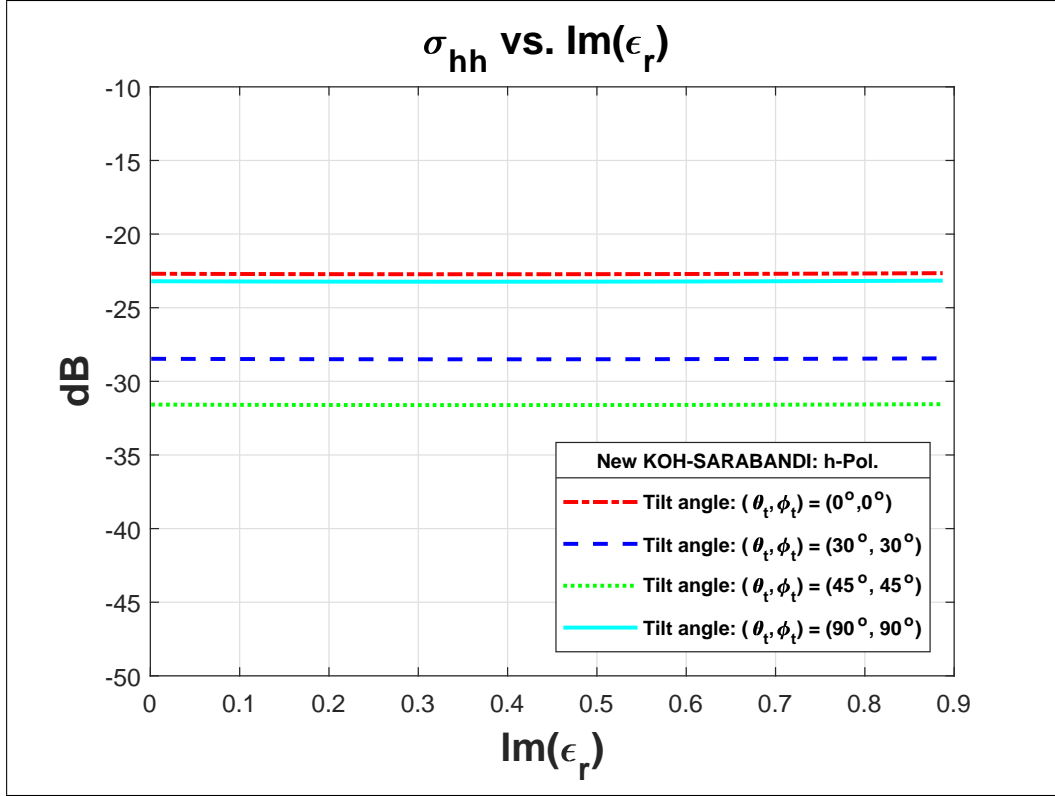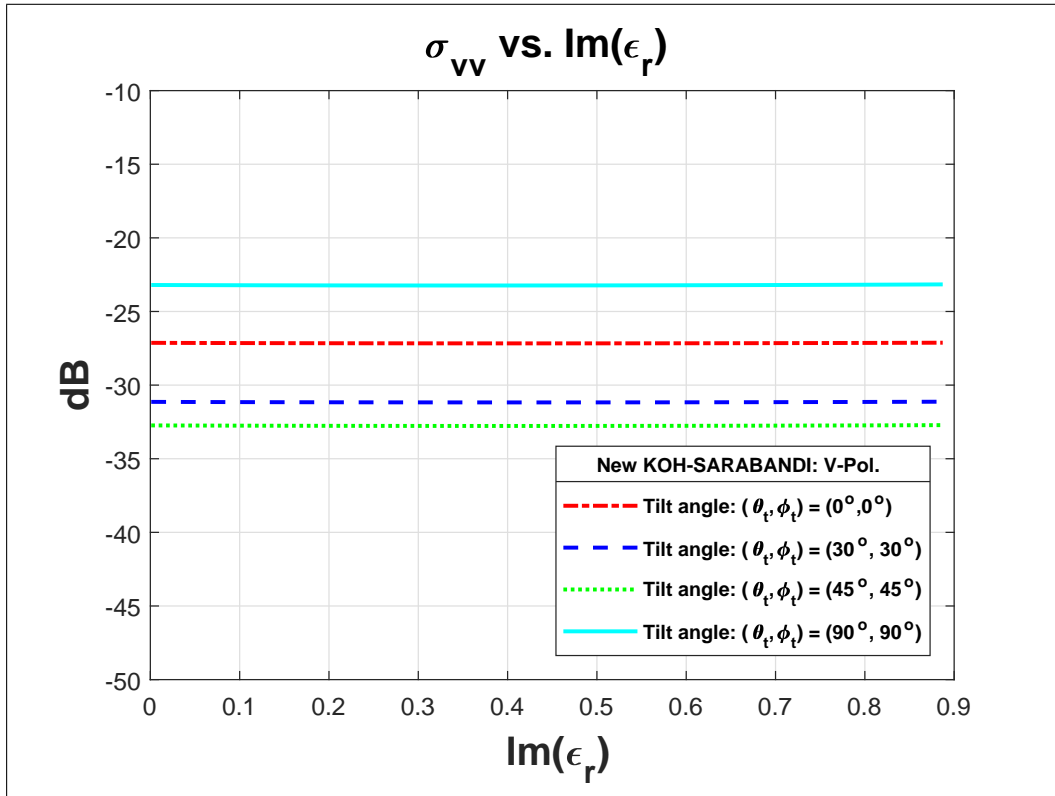

(b)

Figure 3.10: The back-scattering cross sections (a) σ_{hh} and (b) σ_{vv} from a tilted dielectric disk as a function of the imaginary part of the relative permittivity $\Im(\epsilon_r)$ of a disk. Here, incident angle θ_i is assumed to be $45°$ and the presented results are based on the Koh-Sarabandi (KS) approach.

whereas the radius of a disk is taken to be equal to one free space wavelength λ_0 at an operating frequency of 10 GHz. Using these information, it is seen that the simulation results are in excellent agreement with the previously results published over the entire comparison region [57] provided that if the disk has no tilt, i.e., $(\theta_t, \phi_t) = (0^o, 0^o)$. It is also studied that VIPO method fails at the grazing incidence, i.e., incident angle θ_i close to 90° which is expected [56] whereas the KS approach does not fail for these angles (Fig.2).

Figs. (3.3-3.5) deal with the effects of incident angle θ_i upon σ_{hh}, σ_{vv} for a tilted thin circular disk using the new Rayleigh-Gans, Koh-Sarabandi and VIPO techniques. An operating frequency of 35 GHz with radius equal to λ_0 have been assumed. In this case, the dielectric disk is assumed to be made of low loss Gallium Arsenide (GaAs) whose relative permittivity is $\epsilon_r = 12.88 + i0.0004$ [93] in the GHz frequency range. From Figs. (3.3-3.5), it is observed that for $(\theta_t, \phi_t) = (0^o, 0^o)$, $(30^o, 30^o)$ and $(45^o, 45^o)$ cases, the overall patterns of σ_{vv} are nearly same as that of σ_{hh} patterns for incident angles lying in the range $0^o \leq \theta_i \leq 60^o$ for all the considered three approaches. For these cases, there exist significant changes in σ_{vv} patterns for angles $60^o \leq \theta_i \leq 90^o$ as compared to σ_{hh} patterns. In case of $(\theta_t, \phi_t) = (90^o, 90^o)$, the overall patterns of σ_{hh} and σ_{vv} are same for KS and VIPO approaches whereas σ_{hh} and σ_{vv} patterns are different in case of RG approach. It is important to mention that the VIPO approach deteriorates rapidly at near-grazing incidence, i.e., edge-on effect has not been addressed by this approach.

In Figs. (3.6-3.8), the effects of various tilt angles upon the back-scattering cross sections $(\sigma_{hh}, \sigma_{vv})$ as a function of size parameter $k_o a$ of the disk using the Rayleigh-Gans, Koh-Sarabandi and VIPO approaches have been shown. For these figures, we

assume GaAs disk and $\theta_i = 45^o$. It is observed that the σ_{vv} curves are apparently different from the σ_{hh} curves in case of $(\theta_t, \phi_t) = (0^o, 0^o)$ for Rayleigh-Gans, Koh-Sarabandi and VIPO approaches. However, this difference in the σ_{hh} and σ_{vv} curves decreases for the disk orientation of $(\theta_t, \phi_t) = (30^o, 30^o)$ and $(\theta_t, \phi_t) = (45^o, 45^o)$ respectively for all the considered three approaches. Finally, for $(\theta_t, \phi_t) = (90^o, 90^o)$ case, the σ_{hh} and σ_{vv} patterns become same which are obvious from Figs. (3.6-3.8). From the comparative study of Figs. (3.6-3.8) for the disk orientation of $\theta_t = \phi_t = 30^o$ having size parameter of $k_0 a = 2$, it is found that the back-scattering cross sections for both types of considered incident polarizations are less than -60 dB which can be treated as zero. This is an interesting result and significantly used to hide a disk from the incoming horizontally and vertically polarized waves which may find applications in the stealth technology.

In Figs. 9 and 10, we illustrate the effects of various tilt angles upon the back-scattering cross sections σ_{hh} and σ_{vv} as a function of the real and imaginary parts of the relative permittivity of the disk using Koh-Sarabandi approach. In these cases, the operating frequency is fixed at 35 GHz with radius of a disk is taken to be one wavelength. In order to highlight the effects of the real part of the relative permittivity for different tilt angles, it is assumed that $\Im(\epsilon_r)$ is fixed at relatively smaller value of 0.5 for Figs. 9(a)-9(b). It is observed from Fig. 9(a) that the back scattering cross sections σ_{hh} for considered tilted disks are smaller than the back scattering cross section σ_{hh} of a disk having no tilt for the considered range of $\Re(\epsilon_r)$. In Fig. 9(b), it is found that the σ_{vv} curve is different from σ_{hh} curve for $(\theta_t, \phi_t) = (0^o, 0^o)$ case, i.e., $\sigma_{hh} > \sigma_{vv}$ over the entire considered range of $\Re(\epsilon_r)$. However, this difference gradually decreases for the disk orientation of $(\theta_t, \phi_t) = (30^o, 30^o)$ and $(\theta_t, \phi_t) = (45^o, 45^o)$

respectively. But for the $(\theta_t, \phi_t) = (90^o, 90^o)$ case, it is studied that the difference in σ_{hh} and σ_{vv} curves reduced to zero for the considered range of $\Re(\epsilon_r)$. In Figs. (3.18-3.19), the real part of the relative permittivity $\Re(\epsilon_r)$ of the disk is assumed to be fixed, i.e., $\Re(\epsilon_r) = 5$. It is clear from these figures that for the assumed tilt angles, the overall curves for σ_{hh} and σ_{vv} are horizontal straight lines and are independent of the considered range of $\Im(\epsilon_r)$. It is further studied from Figs. 10(a) and 10(b) that the curves for σ_{hh} and σ_{vv} are same only for tilt angles $(\theta_t, \phi_t) = (90^o, 90^o)$ whereas these curves are different for the other considered tilt angles.

3.3   Closing Remarks

The influences of various tilt angles upon the back-scattering cross section of a thin dielectric circular disk have been investigated numerically. For this, both types of incident polarizations have been considered, i.e., horizontal and vertical. The proposed formulation for the calculation of the back-scattering cross section from a tilted disk is based upon three different approaches, i.e., Rayleigh Gans, Koh-Sarabandi and Volumetric Integral Physical Optics. It is found that by varying the tilt angles of a tilted dielectric disk, one can enhance and diminish the back-scattering cross section as compared to the back-scattering cross section of the dielectric disk having no tilt for both types of considered incident polarizations. It is also investigated that for a low loss GaAs dielectric disk having tilt angles of $30°$ with the size parameter of 2, the back-scattering cross sections for both types of incident polarizations are almost equal to zero. In this way, we can hide a GaAs disk in the back-scattered direction to the incoming horizontally and vertically polarized waves. This result is interesting which finds applications in the stealth technology and can not be obtained for the

GaAs disk having no tilt.

Chapter 4

Scattering of electromagnetic waves from a thin triangular dielectric disk

In Chapter 4, an analytic theory is described to illustrate the disk-shape effects on the scattering characteristics from a thin dielectric disk with the main emphasis on the backscattering cross section from a thin triangular dielectric disk. The proposed theory is based on the Koh-Sarabandi (KS) approximation for the electromagnetic wave scattering from a thin dielectric disk along with the spectral representation of the dyadic Green's function. The validity of the proposed formulation is justified by comparing it with the numerical method such as method of moments. For completeness, the scattering cross sections of a triangular disk for horizontal and vertical incident polarizations are compared with their respective scattering cross sections of elliptical, circular, semi-circular and square disks having same electromagnetic and geometrical parameters. It is studied that the back scattering cross sections for a low loss Gallium Arsenide (GaAs) triangular disk at a specific incidence angle can be made almost zero for both types of incident polarizations. This type of almost zero back scattering has applications in the stealth technology and remote sensing.

In section (4.1) , mathematical formulation for the scattering of electromagnetic waves from a thin dielectric triangular disk is presented. In section (4.2), simulation results are presented and discussed for the backscattering cross section from a thin triangular dielectric disk (i.e., both for horizontal and vertical incident polarizations). These results are compared with their respective backscattering cross sections of elliptical, circular, semi-circular and square disks having the identical electromagnetic and geometrical parameters. In the simulation results, the validity of the proposed formulation is also justified by comparing it with the numerical method such as method of moments. In section (4.3) a brief summary of the research work performed in this study followed by the important conclusions is described.

4.1 Electromagnetic scattering from a thin triangular dielectric disk

Consider a non-magnetic triangular disk having the relative permittivity ϵ_r in the xy-plane is considered. The thickness of the disk is assumed to be t and L is taken to be the length of each side of an equilateral triangle. It is assumed that $k_o t << 1$ which ensures that the disk is thin and k_o is the free space propagation constant. This thin dielectric disk is illuminated by an incident plane wave in the free space background and given as,

$$\mathbf{E}^i = \hat{\mathbf{u}}_i E_o e^{ik_o \hat{\mathbf{k}}_i \cdot \mathbf{r}} \tag{4.1.1}$$

where E_o is the magnitude of incident electric field. The unit vector $\hat{\mathbf{k}}_i$ is a vector along the propagation direction of an incident wave which can be expressed in usual spherical coordinates as $\hat{\mathbf{k}}_i = \cos\phi_i \sin\theta_i \hat{\mathbf{x}} + \sin\phi_i \sin\theta_i \hat{\mathbf{y}} + \cos\theta_i \hat{\mathbf{z}}$. The electric field
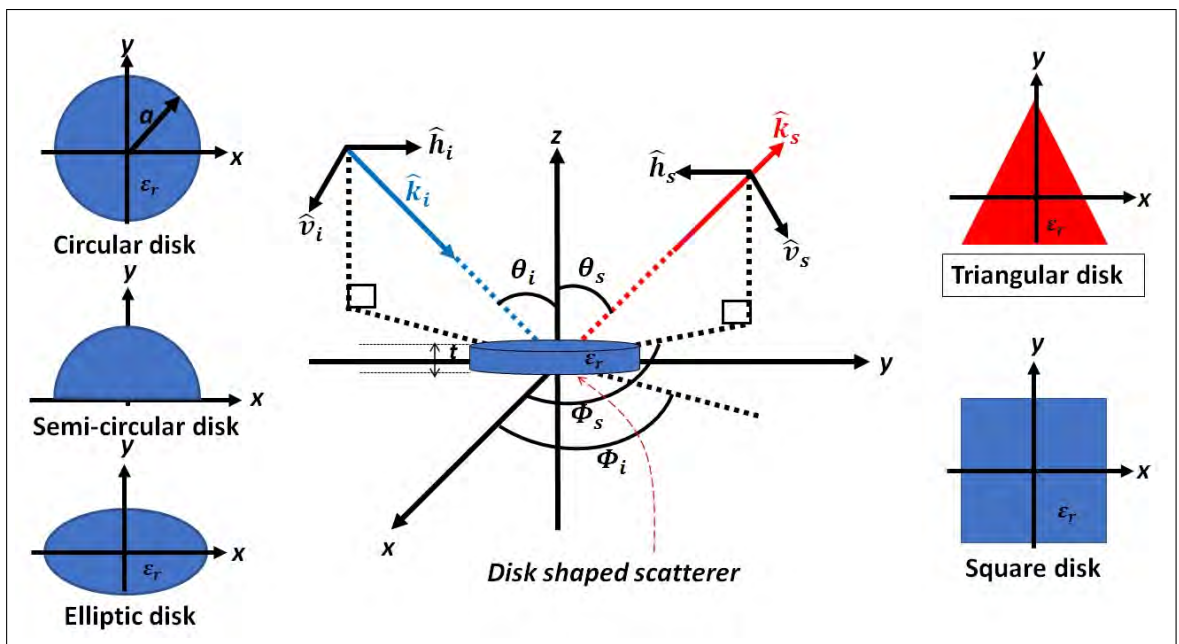
Figure 4.1: Scattering geometry of the thin triangular dielectric disk and their comparisons with various types of dielectric disks including square, elliptic, circular and semi-circular. They are shown in the standard coordinate system.

polarization unit vector is $\hat{\mathbf{u}}_i = \hat{\mathbf{v}}_i$ or $\hat{\mathbf{h}}_i$ with $\hat{\mathbf{h}}_i = (\hat{\mathbf{k}}_i \times \hat{\mathbf{z}})/(|\hat{\mathbf{k}}_i \times \hat{\mathbf{z}}|)$ and $\hat{\mathbf{v}}_i = \hat{\mathbf{h}}_i \times \hat{\mathbf{k}}_i$ where $|\mathbf{A}|$ is the magnitude of a vector $\mathbf{A}$. Interaction of this incident wave with a triangular disk induces volumetric equivalent current $\mathbf{J}$ inside it and is given by,

$$
\begin{aligned}
\mathbf{J} &= -i(k_o/\eta_o)(\epsilon_r - 1)\overline{\overline{\mathbf{P}}} \cdot \mathbf{E}^t \\
&= -i(k_o/\eta_o)(\epsilon_r - 1) \begin{pmatrix} P_{xx} & P_{xy} & P_{xz} \\ P_{yx} & P_{yy} & P_{yz} \\ P_{zx} & P_{zy} & P_{zz} \end{pmatrix} \cdot \mathbf{E}^t
\end{aligned}
\tag{4.1.2}
$$

where η_o is the intrinsic impedance of free space. Here $\overline{\overline{\mathbf{P}}}$ is the polarizability tensor of the disk and $\mathbf{E}^t$ is the total electric field vector inside the disk which is sum of the incident electric field vector $\mathbf{E}^i$ and the scattered electric field vector $\mathbf{E}^s$. Using Fredholm integration equation of second form and spectral representation of dyadic Green's function, we can find volumetric equivalent current $\mathbf{J}$ as given in [56]. Once volumetric current $\mathbf{J}$ is known then the scattered electric field from a triangular thin disk in the far zone can be written as,

$$
\begin{aligned}
\mathbf{E}_s &= \frac{-k_o^2}{4\pi} \frac{e^{ik_o r}}{r} t\left(\hat{\mathbf{k}}_s \times \hat{\mathbf{k}}_s \times (\overline{\overline{\mathbf{P}}}_m \cdot \mathbf{E}_i) \right) \\
&= \frac{e^{ik_o r}}{r} \overline{\overline{\mathbf{S}}}^m \cdot \mathbf{E}_i = \frac{e^{ik_o r}}{r} \begin{pmatrix} S_{vv}^m & 0 \\ 0 & S_{hh}^m \end{pmatrix} \cdot \mathbf{E}_i
\end{aligned}
\tag{4.1.3}
$$

where $\overline{\overline{\mathbf{P}}}_m$ is the modified polarizability tensor and can be written as,

$$
\overline{\overline{\mathbf{P}}}_m = \overline{\overline{\mathbf{P}}} I(\hat{\mathbf{k}}_i, \hat{\mathbf{k}}_s)
\tag{4.1.4}
$$

$$
I(\hat{\mathbf{k}}_i, \hat{\mathbf{k}}_s) = \int\int_{S'} e^{i[(k_s^x - k_i^x) + (k_s^y - k_i^y)]} \, ds'
\tag{4.1.5}
$$

Here $S_{vv}^m = \hat{\mathbf{v}}_s \cdot \overline{\overline{\mathbf{S}}}^m \cdot \hat{\mathbf{v}}_i$ and $S_{hh}^m = \hat{\mathbf{h}}_s \cdot \overline{\overline{\mathbf{S}}}^m \cdot \hat{\mathbf{h}}_i$. In this case, $\hat{\mathbf{h}}_s = (\hat{\mathbf{k}}_s \times \hat{\mathbf{z}})/(|\hat{\mathbf{k}}_s \times \hat{\mathbf{z}}|)$ and $\hat{\mathbf{v}}_s = \hat{\mathbf{h}}_s \times \hat{\mathbf{k}}_s$. The vector $\hat{\mathbf{k}}_s$ is the unit vector along the direction of scattering and can be written as, $\hat{\mathbf{k}}_s = \cos\phi_s \sin\theta_s \hat{\mathbf{x}} + \sin\phi_s \sin\theta_s \hat{\mathbf{y}} - \cos\theta_s \hat{\mathbf{z}}$. The integral $I(\hat{\mathbf{k}}_i, \hat{\mathbf{k}}_s)$

appearing in Eq. (4.5) can be taken as a shape integral where the integration is performed over the surface area S' of the dielectric disk. The polarizability tensor $\overline{\overline{\mathbf{P}}}$ as given in Eqs. (4.1.2), (4.1.4) can be computed using the KS approach [56, 57]. After some manipulations, the shape integral I in case of a thin triangular disk can be written as,

$$I(\hat{\mathbf{k}}_i, \hat{\mathbf{k}}_s) = \left[\frac{0.5e^{-i0.57LC}\left[1 - e^{i(1.15L)C} - 2.7e^{i\alpha} + e^{i\beta}\right]}{C^2 + 0.5CD} + \frac{e^{(0.5L)[0.5C+D]}(e^{-i[0.5L(D)]} - 1)}{CD} \right] \tag{4.1.6}$$

where $C = k_o(\hat{\mathbf{k}}_s - \hat{\mathbf{k}}_i) \cdot \hat{\mathbf{x}}$, $D = k_o(\hat{\mathbf{k}}_s - \hat{\mathbf{k}}_i) \cdot \hat{\mathbf{y}}$, $\alpha = (0.5L)[1.732C + D]$ and $\beta = (0.5L)[0.5C - D]$. In case of an elliptic thin dielectric disk having major and minor axes of a and b respectively, this shape integral is given by [56],

$$I(\hat{\mathbf{k}}_i, \hat{\mathbf{k}}_s) = \frac{2A_e J_1\left(\sqrt{(aC)^2 + (bD)^2}\right)}{\sqrt{(aC)^2 + (bD)^2}} \tag{4.1.7}$$

where $J_1(\cdot)$ is the first order Bessel function and A_e is the physical area of an elliptical disk, i.e., $A_e = \pi ab$. For a circular disk having radius a, the shape integral I can be computed from Eq. (4.1.7) by taking $a = b$. For semicircular dielectric disk, the shape integral I becomes half of the shape integral of a circular disk. Likewise, in case of a square disk having length L_1 of each side, the shape integral I becomes as,

$$I(\hat{\mathbf{k}}_i, \hat{\mathbf{k}}_s) = L_1^2 \operatorname{sinc}\left[\frac{CL_1}{2}\right] \operatorname{sinc}\left[\frac{DL_1}{2}\right] \tag{4.1.8}$$

The scattering geometry of a thin triangular disk and all considered disks have been shown in Fig. 4.1. It is known that the radar cross section (RCS) for the horizontal and the vertical incident polarizations can be expressed in terms of the scattering elements S_{hh}^m, S_{vv}^m which are given below,

$$\sigma_{hh}(\hat{\mathbf{k}}_i, \hat{\mathbf{k}}_\mathbf{s}) = 4\pi \mid S_{hh}^m(\hat{\mathbf{k}}_i, \hat{\mathbf{k}}_\mathbf{s}) \mid^2$$

$$\sigma_{vv}(\hat{\mathbf{k}}_i, \hat{\mathbf{k}}_\mathbf{s}) = 4\pi \mid S_{vv}^m(\hat{\mathbf{k}}_i, \hat{\mathbf{k}}_\mathbf{s}) \mid^2 \tag{4.1.9}$$

It should be noted that the forward scattering cross sections can be computed using $\hat{\mathbf{k}}_i = \hat{\mathbf{k}}_s$ and the backward scattering cross sections using $\hat{\mathbf{k}}_i = -\hat{\mathbf{k}}_s$ in Eq. (4.1.9) for both types of incident polarizations. For the present study, we are interested in the back scattering cross sections for both types of incident polarizations.

4.2 Numerical Results

In this section, the numerical results are presented which illustrate the effects of various parameters including incidence angle, frequency and the dielectric constant of the disk upon back scattering cross sections of thin triangular disk except Figs. 2, where forward scattering cross section is discussed. The back scattering cross sections σ_{hh}, σ_{vv} of triangular disk are also compared with other various types of dielectric disks, i.e., square, elliptic, circular and semi-circular. The thickness of all the disks are taken to be thin which has a fixed value of $t = 0.01\lambda_o$ at an operating wavelength of λ_o. In order to highlight the comparative study of the influences of various parameters upon the back scattering cross sections, the physical areas of all the disks are taken to be same and equal to $\pi\lambda_o^2$. The operating wavelength for all figures have been assumed to be 0.03 except for Fig. 4 where it is variable.

In Figs. 2, the forward scattering coefficients, i.e., S_{hh}^m, S_{vv}^m for thin dielectric triangular disk based upon the proposed formulation and their comparisons with numerical technique such as method of moments [37] have been shown. It is found that the scattering coefficients are in good agreement with the MOM for the incidence angles lying in the range of $0 \leq \theta_i \leq 45°$. However, this agreement slightly begins to deteriorate for angles lying in the range of $45 \leq \theta_i \leq 90°$. It is studied that at near-grazing incidence angles, the disagreement for S_{hh}^m is up to 1 dB and for S_{vv}^m it
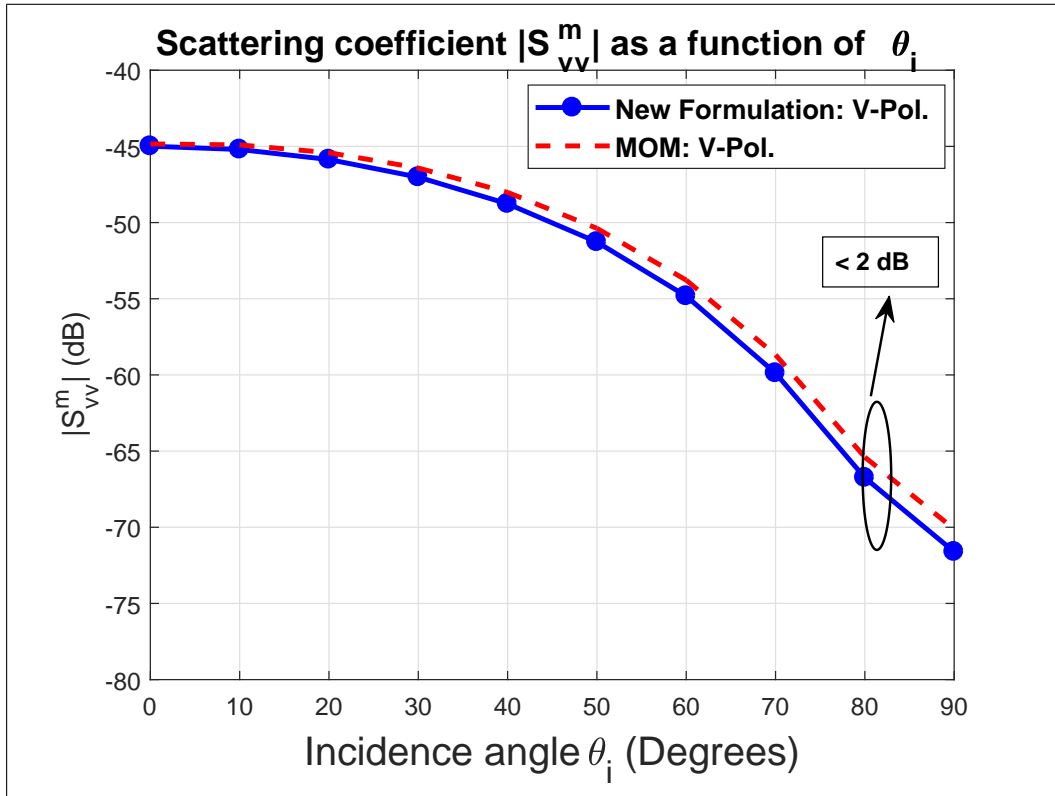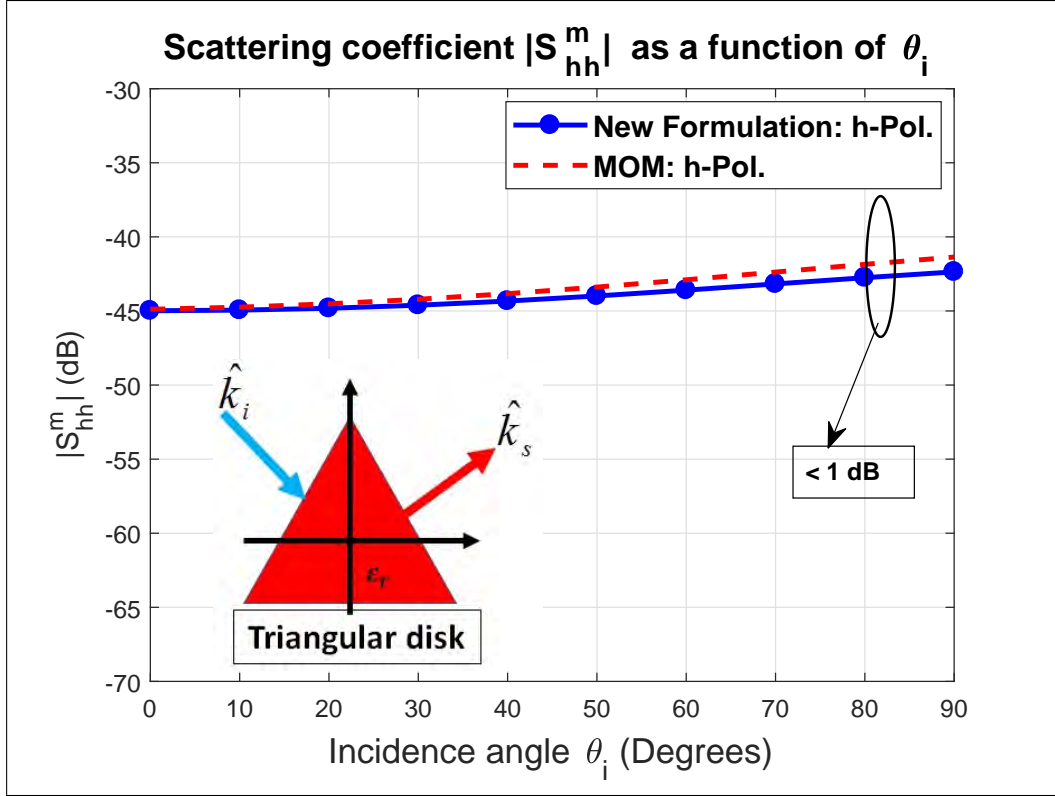
(a)

(b)

Figure 4.2: The magnitudes of the forward scattering coefficients (a) S_{hh}^m (b)S_{vv}^m as a function of incidence angle θ_i for the thin dielectric triangular disk and their comparisons with the Method of Moments (MOM) technique [37]. The proposed formulation is found to be in good agreement with the MOM. The relative permittivity of the triangular disk is taken from [56] which is $\epsilon_r = 26.6 + i11.56$.
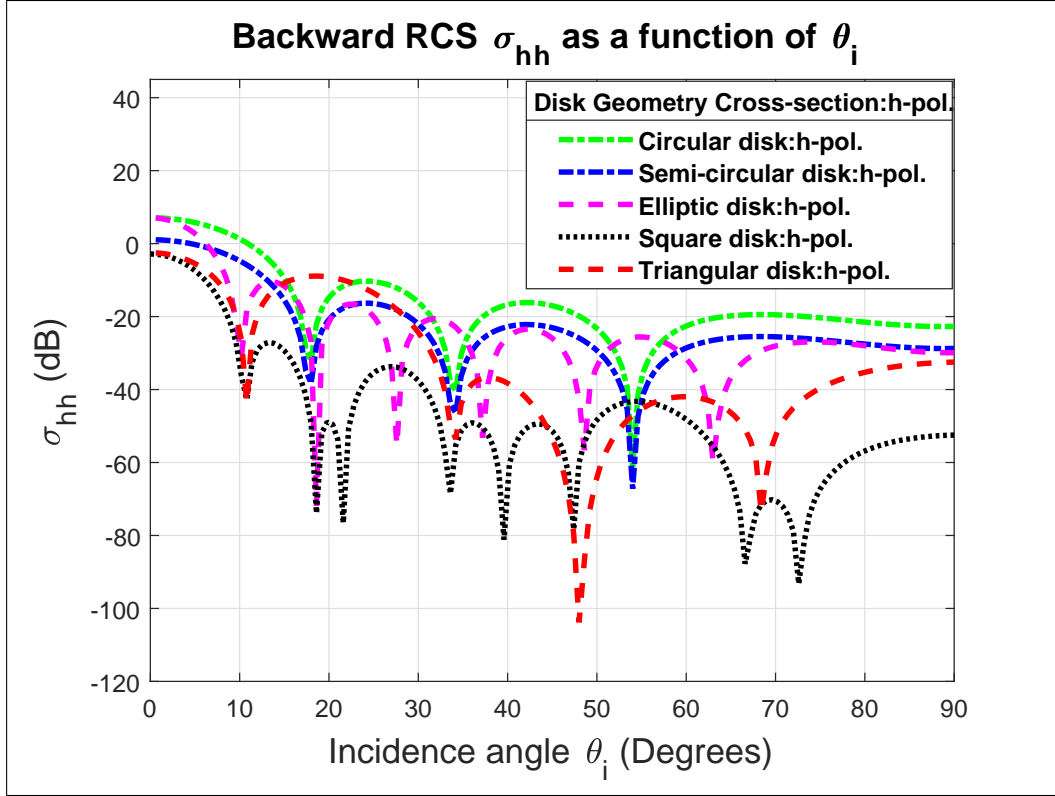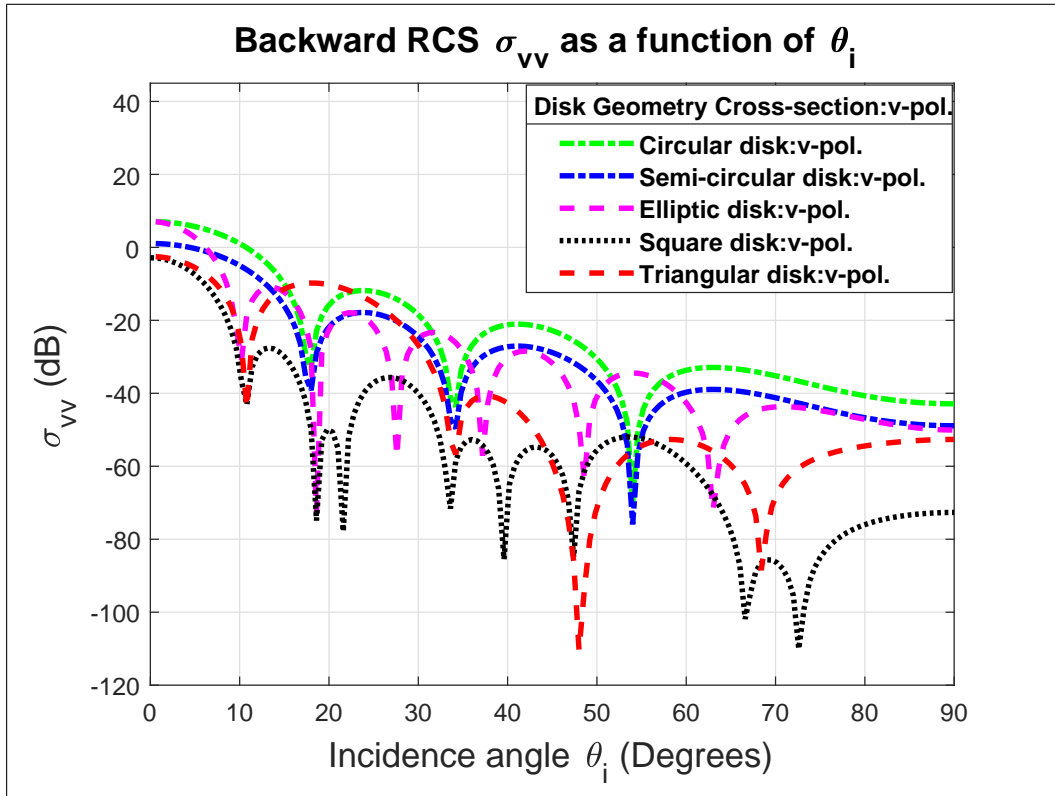
Figure 4.3: The back-scattering cross sections (a)σ_{hh} and (b)σ_{vv} from a thin triangular dielectric disk and their comparisons with different shapes of the disks including elliptic, circular, semi-circular and square as a function of incident angle θ_i. Here, we have $\phi_i = 60°$. The relative permittivity of all the disks are taken to be $\epsilon_r = 2 + i10$ and this value has been taken from Chapter 6 of [57].
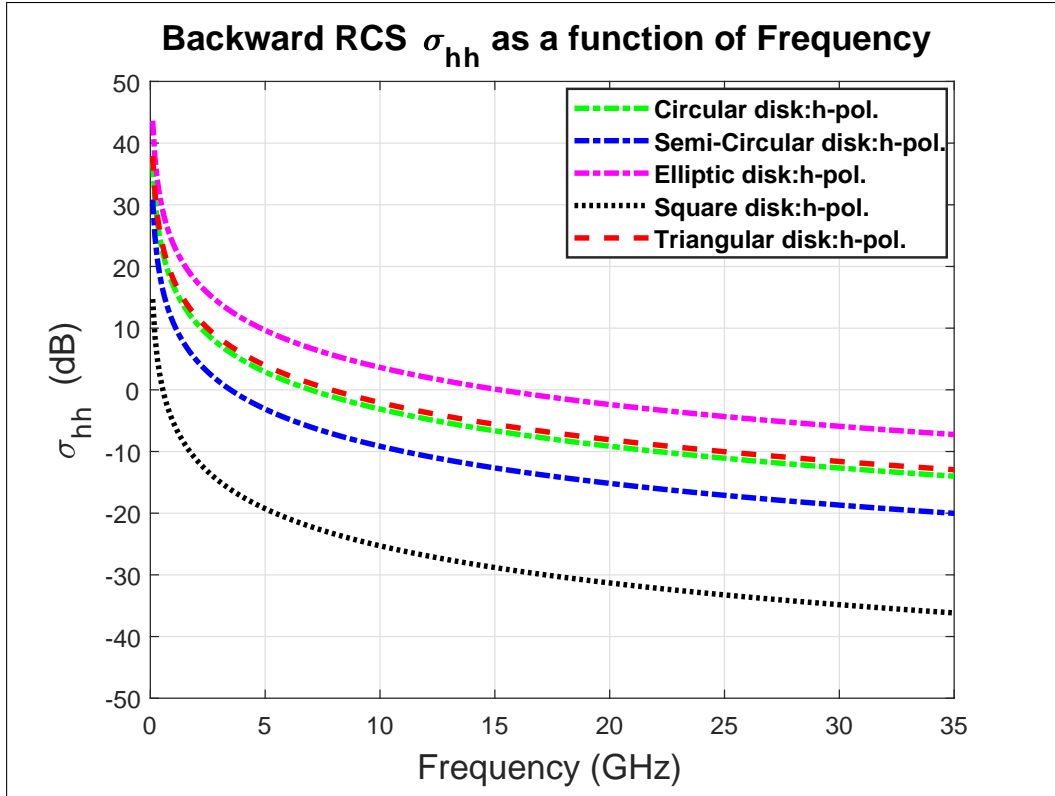
(a)
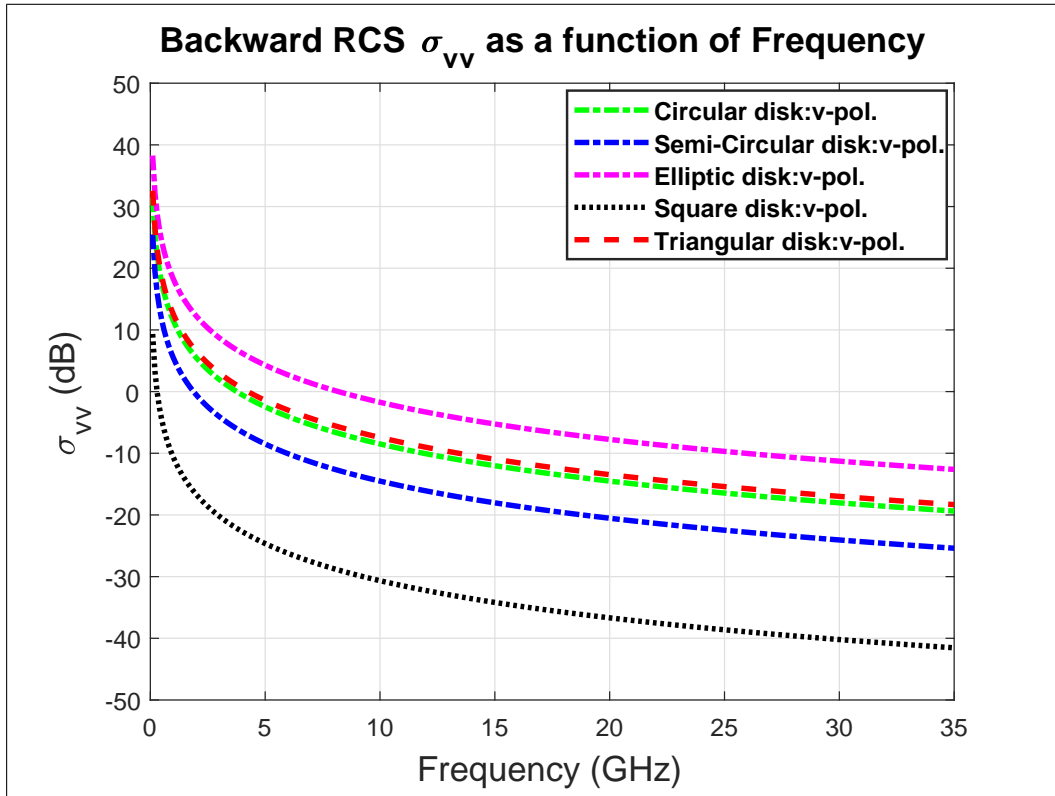
(b)

Figure 4.4: The comparative analysis of the back-scattering cross sections (a)σ_{hh} and (b)σ_{vv} of various types of considered dielectric disks as a function of frequency. In this case, it is assumed that all the disks are made of low loss Gallium Arsenide (GaAs) whose relative permittivity is taken to be $\epsilon_r = 12.88 + i0.0004$ [87].
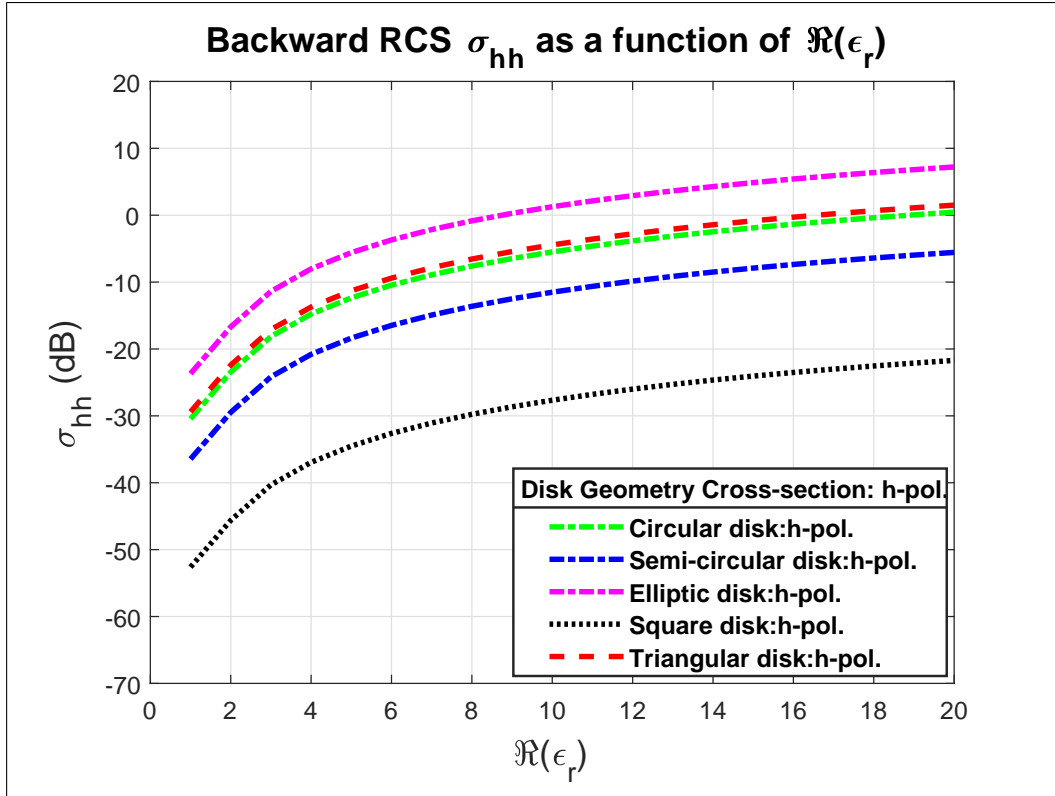
Figure 4.5: The effects of the real part of the relative permittivity of the disk upon the back-scattering cross sections (a)σ_{hh} and (b)σ_{vv} of various types of considered dielectric disks. Here the imaginary part of the relative permittivity is taken to be relatively small, i.e., 0.0004 for all the disks.

(a)

(b)

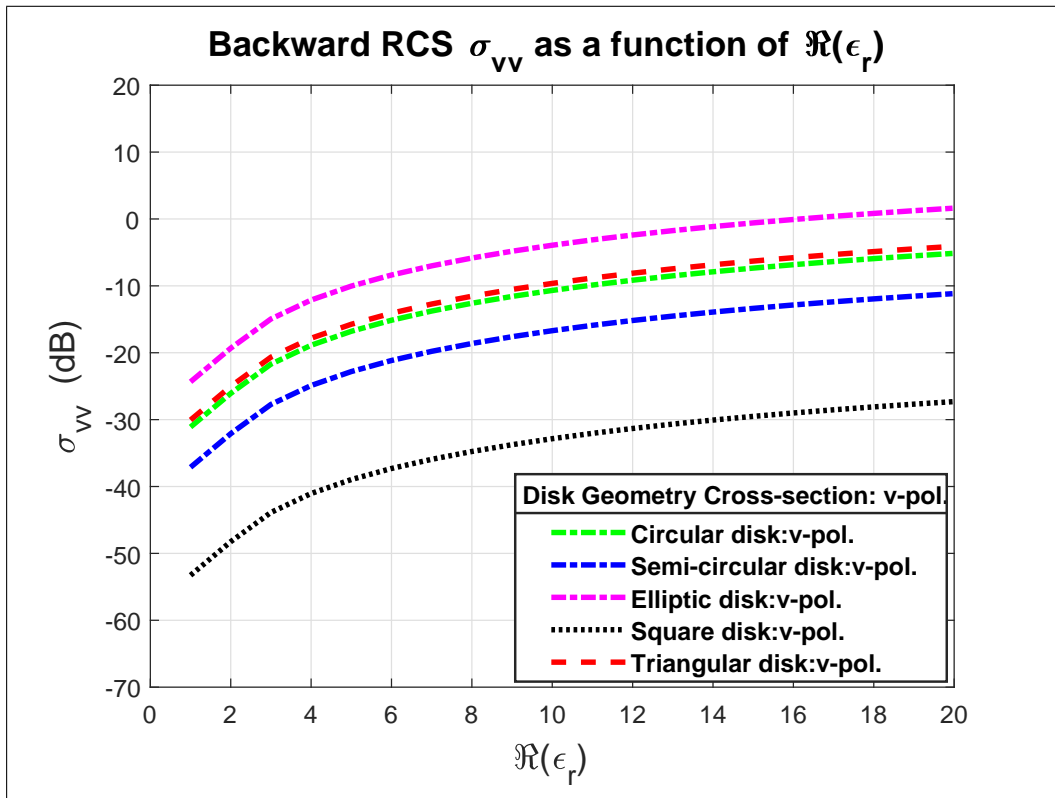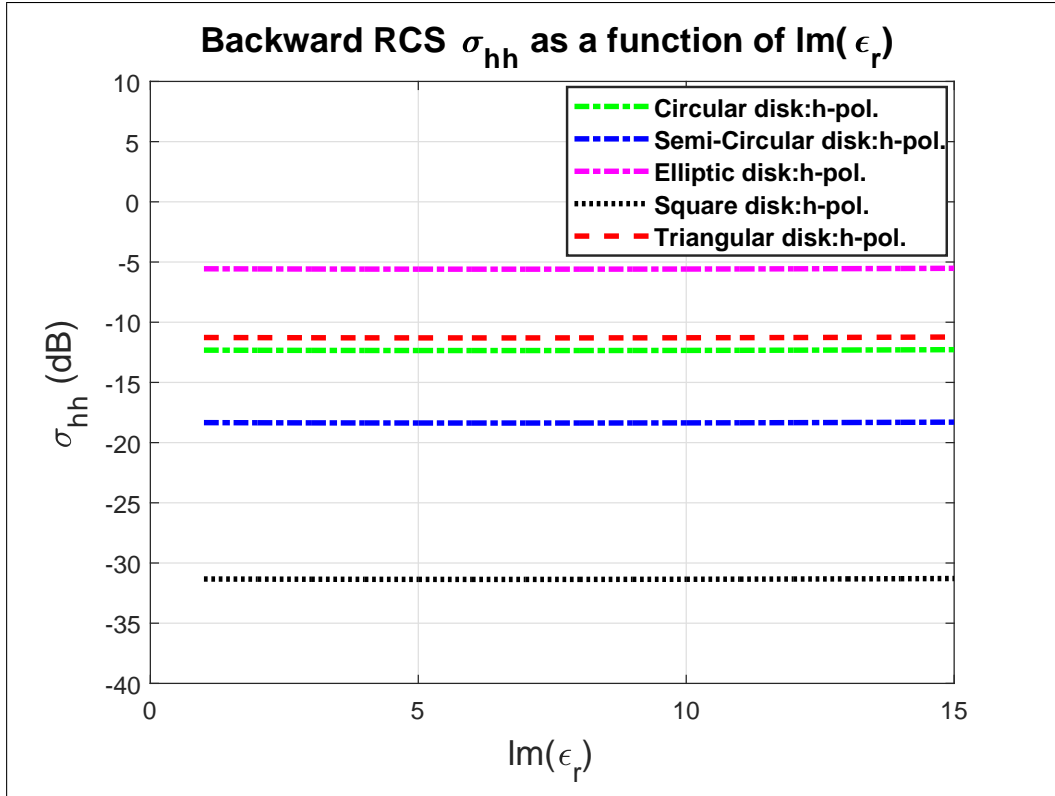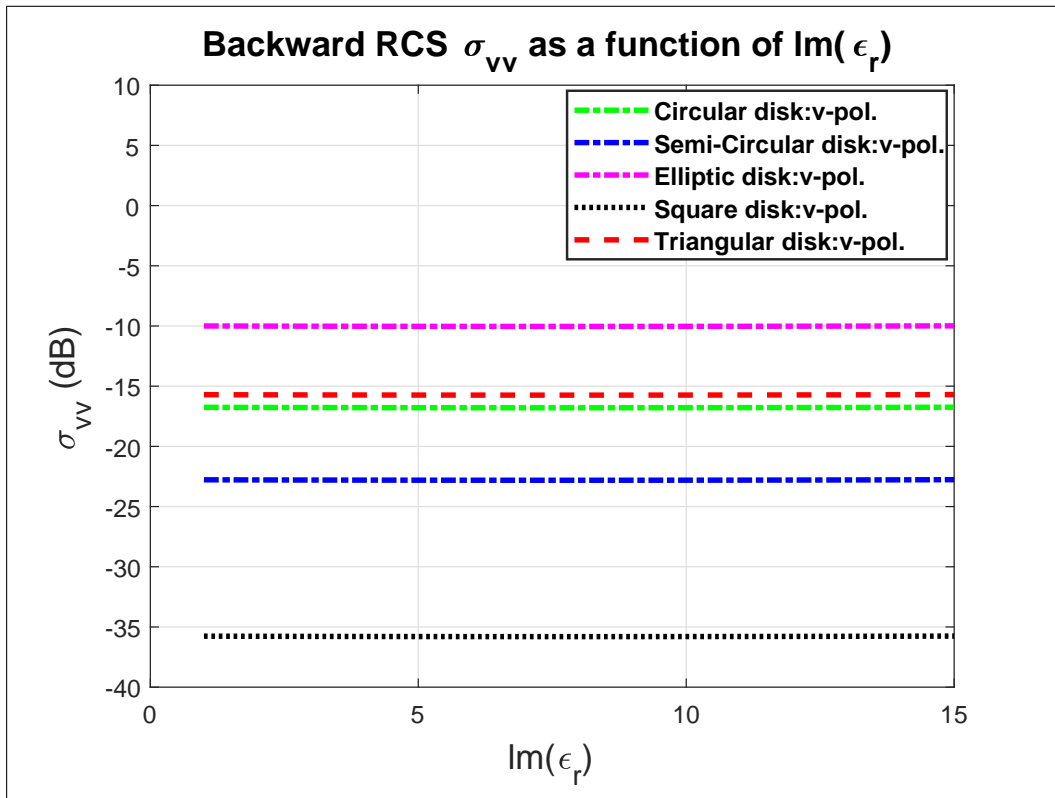Figure 4.6: The influences of the imaginary part of the relative permittivity of the disk upon the back-scattering cross sections (a)σ_{hh} and (b)σ_{vv} of various types of considered dielectric disks. In this case, the real part of the relative permittivity is taken to be relatively large, i.e., 12.88 for all the disks.

is up to 2 dB. The Fig. 3 deals with the back scattering cross sections of various types of considered disks as a function of incidence angle θ_i. It is clear from Fig. 3 that the fluctuating pattern of σ_{hh} of a thin dielectric circular disk is in excellent agreement with that reported by Koh [57] in Fig. 9 of Chapter 6. It is seen that $\sigma_{hh} = \sigma_{vv}$ for all types of the considered disks provided that if the angle θ_i lies in the range of $0° \leq \theta_i \leq 35°$. However σ_{vv} decreases as compared to σ_{hh} for all types of considered disks for relatively larger values of incidence angle θ_i, i.e., $35^o \leq \theta_i \leq 90^o$. The significant decrease in σ_{vv} as compared to σ_{hh} for all disks occurs at the grazing incidence angle, i.e., $\theta_i = 90°$. For a square disk, the back scattering cross sections for both types of incident polarizations are small as compared to their respective back scattering cross sections of circular disk. In this case, the minimum value of σ_{hh} is -93.23 dB and the minimum value of σ_{vv} is -108.5 dB where both values occur at $\theta_i = 72°$. Likewise, for a triangular disk, the minimum values of σ_{hh}, σ_{vv} are -103.1 dB and -110.1 dB respectively at $\theta_i = 48°$. Thus, it is concluded that back scattering cross sections for a triangular disk can be significantly reduced, i.e., below -100 dB using both types of horizontal and vertical incident polarizations at a specific incidence angle. This type of almost zero back scattering is an interesting result and has applications in the stealth technology and remote sensing.

In Figs. 4-6, the incidence angles are assumed to fixed, i.e., $\phi_i = 10.6°$ and $\theta_i = 45°$. The back scattering cross sections σ_{hh}, σ_{vv} as a function of frequency for various types of considered disks have been shown in Fig. 4. All the disks are assumed to be made up of the low loss GaAs material whose relative permittivity in the microwave regime is given by $\epsilon_r = 12.88 + 0.0004i$ [87]. It is observed that the overall back scattering cross sections σ_{hh}, σ_{vv} decreases with the increase in the frequency for all

the disks. It is also found that $\sigma_{hh} > \sigma_{vv}$ for all the considered disk geometries over the entire comparison frequency region. It is further argued that the back scattering cross sections of the circular and triangular GaAs disks are almost same for both types of incident polarizations over the considered range of frequencies. In Fig. 5, the influences of the real part of the relative permittivity of all types of considered disks upon the back scattering sections σ_{hh}, σ_{vv} have been shown. It is found that the back scattering cross sections for both types of polarizations increases with the increase in the real part of the relative permittivity. Likewise, it is seen that $\sigma_{hh} > \sigma_{vv}$ for all the considered disk geometries over the entire comparison region of the $Im(\epsilon_r)$. The highest values of σ_{hh}, σ_{vv} are observed for an elliptic disk whereas the lowest values of σ_{hh}, σ_{vv} are found for a square disk. The overall values of σ_{hh} and σ_{vv} for a triangular disk are slightly different from that of a circular disk. The Fig. 6 deals with the the effects of the imaginary part of the relative permittivity of all the considered disks upon the back scattering cross sections, i.e., σ_{hh} and σ_{vv}. It is studied that the back scattering cross sections are constant straight lines for all the considered disk geometries. It is also found that σ_{hh} and σ_{vv} are independent of the considered range of the imaginary part of the relative permittivity of all the disks. Once again it is observed that $\sigma_{hh} > \sigma_{vv}$ for all the considered disks over the entire comparison region of $Re(\epsilon_r)$. The values of σ_{hh} and σ_{vv} for a triangular disk are slightly higher than the corresponding back scattering cross sections of a circular disk.

4.3   Conclusions

The scattering of electromagnetic waves from a thin dielectric triangular disk is presented based on Koh-Sarabandi approach along with the spectral representation of

the dyadic Green's function. The proposed formulation is validated by comparing it with the method of moments. An excellent agreement between the proposed theory and MOM is found for all incident polar angles. In order to highlight the scattering properties of a triangular disk, the back scattering cross sections of a triangular disk have been compared with other various shapes of the disks including elliptical, circular, semi-circular and square under horizontal and vertical incident polarizations. In this case, the electromagnetic and geometrical areas of all the disks are taken to be the same. The influences of incident angles, operating frequency and the relative permittivity of the disk upon the back scattering cross section of all the considered disks have also been discussed. It is found that the back scattering cross sections of all the considered disks decrease with the increase in the frequency for both types of incident polarizations. During the study, it is found that the back scattering cross sections for a low loss GaAs triangular disk at a specific incidence angle can be made less than -102 dB for both types of incident polarizations, i.e., horizontal and vertical. This type of almost zero back scattering find applications in the field of stealth technology and remote sensing.

Chapter 5

Scattering of electromagnetic waves from a sparse distribution of N-tilted thin circular dielectric disks

In Chapter 5, the back-scattered cross section from a sparse distribution of N-tilted thin circular dielectric disks have been investigated using numerical simulations. Three widely known scattering approximations from a dielectric disk such as Rayleigh-Gans (RG), Koh-Sarabandi (KS) and volumetric integral physical optics (VIPO) have been used for the proposed theory. The influences of the various parameters including incident angle, size parameter of the disk, relative permittivity of the disk and spacing among disks upon the back-scattered cross sections have been studied for incident horizontal and vertical polarizations. Some conditions are discussed where a pair of sparsely located tilted low loss Gallium Arsenide disks significantly reduced the back-scattered cross section as a compared to a single tilted Gallium Arsenide disk. This type of reduced back scattering for both types of incoming horizontally and vertically polarized waves is desired in the stealth technology.

In section (5.1), the mathematical formulation for the back-scattered radar cross section from a sparse distribution of tilted thin circular dielectric disks is described. In section (5.2), numerical results are presented and discussed in detail. In section (5.3) a brief summary of the important research elements performed in this work followed by the important conclusions is described.

5.1 Back-scattered radar cross section from N-tilted thin circular dielectric disks

It is assumed that there are N-dielectric circular disks placed periodically in the free space background medium. The center to center spacing among two consecutive disks are taken to be d and all dielectric disks lie in the xy-plane. Each of the disk is taken to be non-magnetic with relative permittivity of ϵ_r. It is assumed that radius of each disk is a and t is the thickness of the disk. Each disk is assumed to thin, i.e., $k_o t \ll 1$ where k_o is the free space wave number. In this case, the separation among disks are taken to be sparse which shows that d is of the order of one wavelength or greater than one wavelength, i.e., $d \geq \lambda_o$. Here the parameter λ_o is the free space wavelength. For sparse distribution of disks, the multiple scattering effects are negligible and the total scattered field is simply the sum of the individual scattered field from each disk in isolation. On the other hand, if these thin disks are closely placed and we have either $d < \frac{\lambda_o}{2}$ for an oblique incidence and $d < \lambda_o$ for normal incidence then multiple scattering effects can not be ignored. In this case, the disk medium becomes dense rather than sparse. For this type of dense medium, we can use the homegenization theory and assign effective permittivity and effective permeability to a such medium. This is further discussed in detail in the coming

Chapter 6. At relatively higher frequencies, the adapted homogenization technique become non-local. The word non-local is used because its effective parameters re function of incident wave vector. An important theory about nonlocal homogenization of microstructured artificial materials (metamaterials) has been established in the seminal work of Silveirinha [89]. He reviews the Lorentz 's pioneers work in the field of macroscopic electromagnetism and proposed the Generalized Lorentz-Lorentz model to describe the electrodynamic properties of the microstructured artificial materials. He analyzed the spatial dispersion effect to negative-index composites at relatively higher frequencies where effective medium is characterized as nonlocal. The nonlocal effective parameters are mainly focused and calculated by Simovski [90-92]. Recently, Awan [69] has studied the conducting cylindrical wires of finite length based on the nonlocal epsilon negative medium.

A plane wave which propagates along $\hat{\mathbf{k}}_i$ is assumed to be incident upon these N-dielectric disks which can be mathematically expressed as below,

$$\boldsymbol{E}^i = \hat{\mathbf{q}}_i E_o e^{ik_o\hat{\mathbf{k}}_i\cdot\mathbf{r}} = \mathbf{E}_i e^{ik_o\hat{\mathbf{k}}_i\cdot\mathbf{r}} \tag{5.1.1}$$

where E_o is the magnitude and $\hat{\mathbf{q}}_i = \hat{\mathbf{v}}_i$ or $\hat{\mathbf{h}}_i$. Here $(\hat{\mathbf{k}}_i, \hat{\mathbf{v}}_i, \hat{\mathbf{h}}_i)$ and $(\hat{\mathbf{k}}_s, \hat{\mathbf{v}}_s, \hat{\mathbf{h}}_s)$ can be expressed in terms of usual spherical angles (θ_i, ϕ_i) for incident wave and (θ_s, ϕ_s) for scattered wave as given below,

$$
\begin{aligned}
\hat{\mathbf{k}}_i &= \sin\theta_i\cos\phi_i\hat{\mathbf{x}} + \sin\theta_i\sin\phi_i\hat{\mathbf{y}} + \cos\theta_i\hat{\mathbf{z}} \\
\hat{\mathbf{h}}_i &= \frac{\hat{\mathbf{k}}_i\times\hat{\mathbf{z}}}{|\hat{\mathbf{k}}_i\times\hat{\mathbf{z}}|}, \quad \hat{\mathbf{v}}_i = \hat{\mathbf{h}}_i\times\hat{\mathbf{k}}_i \\
\hat{\mathbf{k}}_s &= \sin\theta_s\cos\phi_s\hat{\mathbf{x}} + \sin\theta_s\sin\phi_s\hat{\mathbf{y}} - \cos\theta_s\hat{\mathbf{z}} \\
\hat{\mathbf{h}}_s &= \frac{\hat{\mathbf{k}}_s\times\hat{\mathbf{z}}}{|\hat{\mathbf{k}}_s\times\hat{\mathbf{z}}|}, \quad \hat{\mathbf{v}}_s = \hat{\mathbf{h}}_s\times\hat{\mathbf{k}}_s
\end{aligned}
\tag{5.1.2}
$$

This incident electric field given by Eq. (5.1.1) when interacts with these dielectric

disks, it induces current inside each of the disk. This induced current in each disk produces the scattered electric fields from these disks.

It is important to note that the strength of the induced current inside the disk is dependent upon many parameters, e.g., polarization of the incident electric field, geometrical and electrical parameters of the disk. By varying these parameters, one can control the induced current inside the disk and hence the scattered electric field. One of the important geometrical parameter of a thin circular dielectric disk is the orientation of the disk. Keeping this in view, it is assumed that each disk is tilted and the orientation of each disk is defined by a unit vector $\hat{\mathbf{s}}$ which is given as,

$$\hat{\mathbf{s}} = \sin\theta_t \cos\phi_t \hat{\mathbf{x}} + \sin\theta_t \sin\phi_t \hat{\mathbf{y}} + \cos\theta_t \hat{\mathbf{z}} \tag{5.1.3}$$

where the tilt angles θ_t and ϕ_t represent the elevation and azimuthal angles of the disk and are shown in Fig. 5. 1(a). The total far zone scattered electric field $\mathbf{E}^s$ from these sparsely distributed thin circular dielectric disks can be taken as the coherent addition of the scattered electric fields from these dielectric disks. Based upon this information, it is found that the total scattered electric field from the N-titled thin circular dielectric disks which are oriented at angle (θ_t, ϕ_t) can be written as [56-57 and Chapter 3],

$$\begin{aligned}
\mathbf{E}^s &= \frac{-k_o^2}{4\pi} \frac{e^{ik_o r}}{r} t \left(\hat{\mathbf{k}}_s^g \times \hat{\mathbf{k}}_s^g \times \left(\sum_{n=1}^{N} \overline{\overline{\mathbf{P}}}_n^g \cdot \mathbf{E}_i^g \right) \right) \\
&= \frac{e^{ik_o r}}{r} \overline{\overline{\mathbf{S}}} \cdot \mathbf{E}_i^g = \frac{e^{ik_o r}}{r} \begin{pmatrix} S_{hh} & 0 \\ 0 & S_{vv} \end{pmatrix} \cdot \mathbf{E}_i^g
\end{aligned} \tag{5.1.4}$$

$$\overline{\overline{\mathbf{P}}}_n^g = e^{i\Phi_n^g} \frac{2A_{(disk)} J_1(\sqrt{a^2(C^2 + D^2)})}{\sqrt{a^2(C^2 + D^2)}} \overline{\overline{\mathbf{P}}}^g \tag{5.1.5}$$

where the factor $\Phi_n^g = [(\hat{\mathbf{k}}_i^g - \hat{\mathbf{k}}_s^g) \cdot \mathbf{r}_n^g]$ is the phase compensation term associated with an nth tilted dielectric disk which is located at the position vector of $\mathbf{r}_n^g$. Likewise,

$\overline{\overline{\mathbf{P}}}_n^g$ represents the polarizability tensor of an nth tilted dielectric circular disk. Here $J_1(.)$ is the first order Bessel function of first kind and $A_{(disk)} = \pi a^2$ is cross sectional area of the circular disk. All the transformed quantities defined in Eqs. (5.1.4) and (5.1.5), and the elements of the polarizability tensor $\overline{\overline{\mathbf{P}}}^g$ for both types of incident polarizations using RG, KS and VIPO techniques can be found from Eqs. (3.1.4) and (3.1.5) of Chapter 3. Based upon the information given above, the radar cross section (RCS) or scattering cross section for horizontally polarized wave σ_{hh} and for vertically polarized wave σ_{vv} from a sparse distribution of N tilted thin dielectric circular disks can be written in terms of the scattering matrix elements S_{hh}, S_{vv} as below,

$$
\begin{aligned}
\sigma_{hh} &= 4\pi \left| S_{hh}(\hat{\mathbf{k}}_i^g, \hat{\mathbf{k}}_s^g) \right|^2 \\
\sigma_{vv} &= 4\pi \left| S_{vv}(\hat{\mathbf{k}}_i^g, \hat{\mathbf{k}}_s^g) \right|^2
\end{aligned}
\tag{5.1.6}
$$

In the design of modern remote sensing systems, one of the important quantity is the backward radar cross section (RCS) or back-scattered cross section. That is why, we are interested in the back-scattered cross sections for both types of incident polarizations. The back-scattered cross sections can be found from Eq. (5.6) by taking $\hat{\mathbf{k}}_s^g = -\hat{\mathbf{k}}_i^g$. On the other hand, the forward scattering cross sections can be computed by taking $\hat{\mathbf{k}}_s^g = \hat{\mathbf{k}}_i^g$ in Eq. (5.6). In order to simplify the analysis for the numerical results, it is assumed that $N = 2$ and tilted thin circular dielectric disks are sparsely placed at $(x_1, 0, 0)$ and $(-x_1, 0, 0)$ which are shown in Fig. 5.1(b).

5.2 Summary and Numerical Results

In this section, the influences of various parameters including incident angle, size parameter, the permittivity of the disk and spacing among disks upon the backward radar cross section (RCS) or back-scattering cross sections, i.e., σ_{hh} and σ_{vv} of sparse
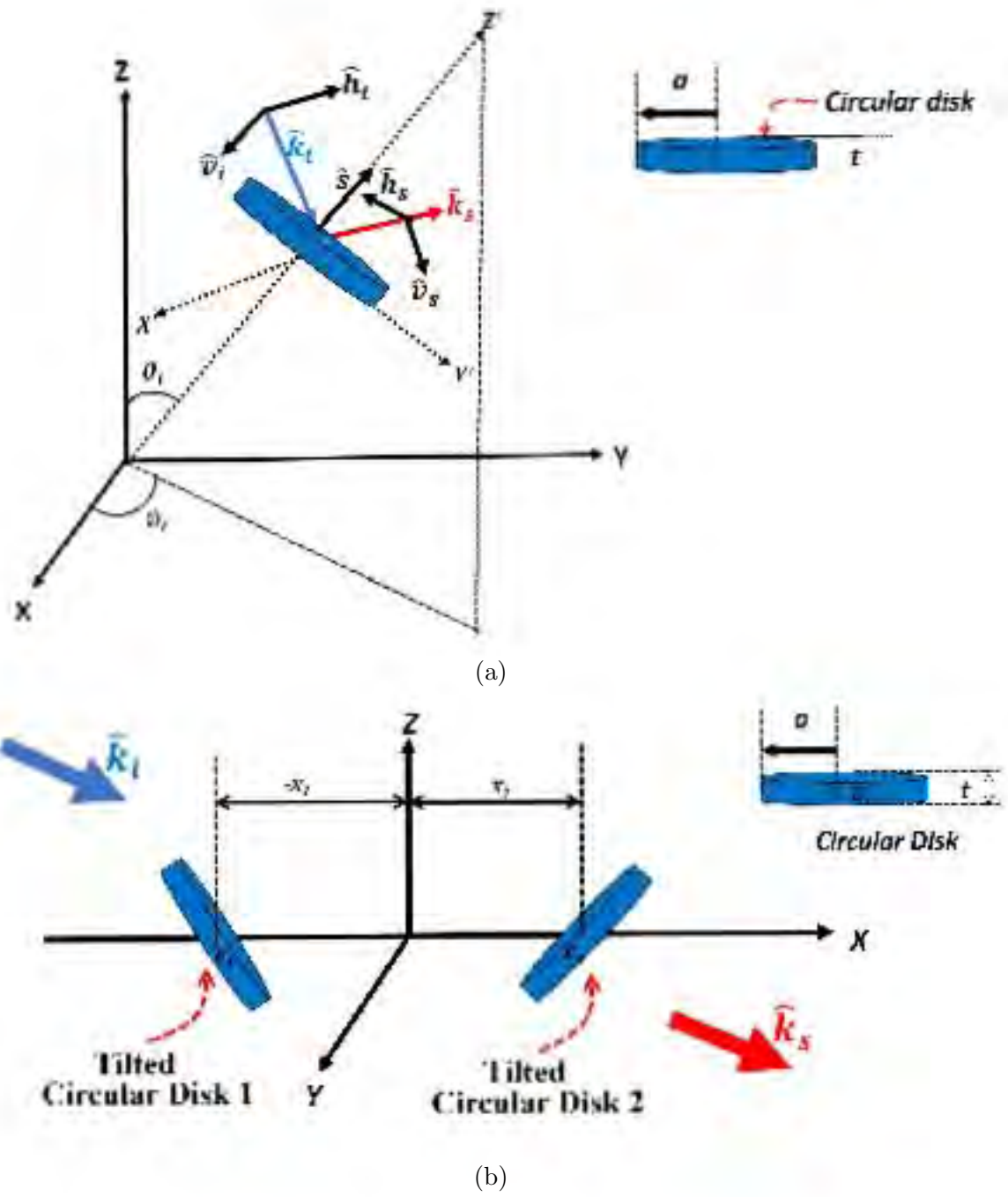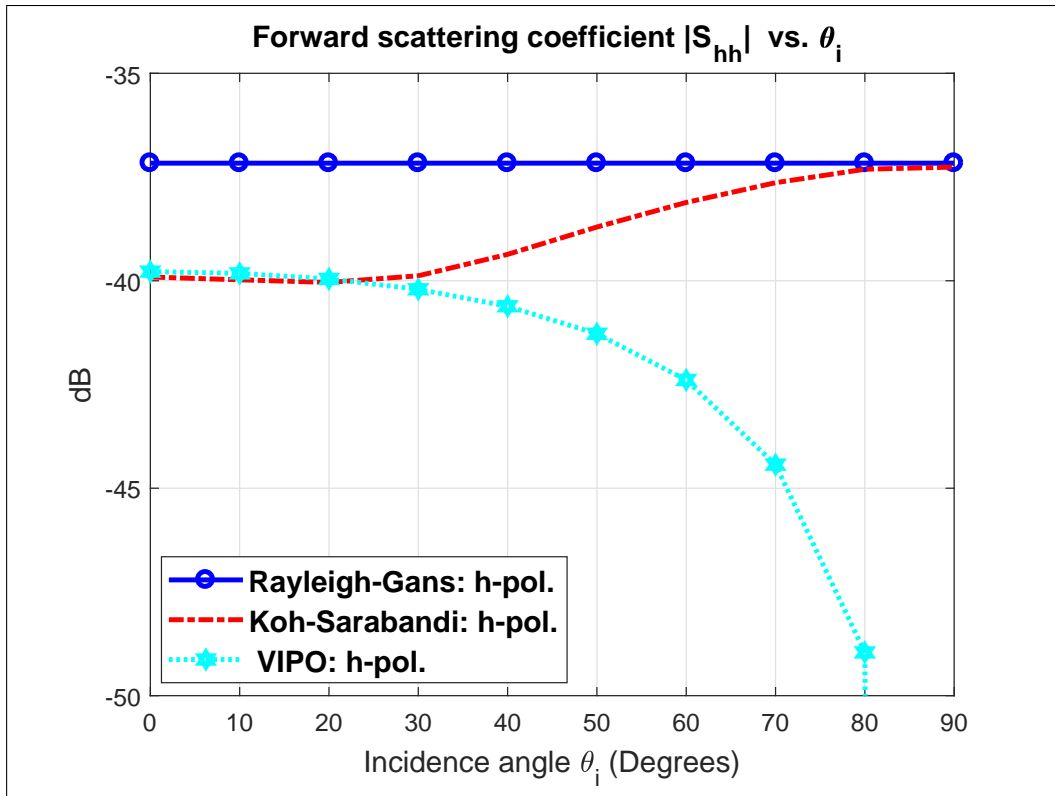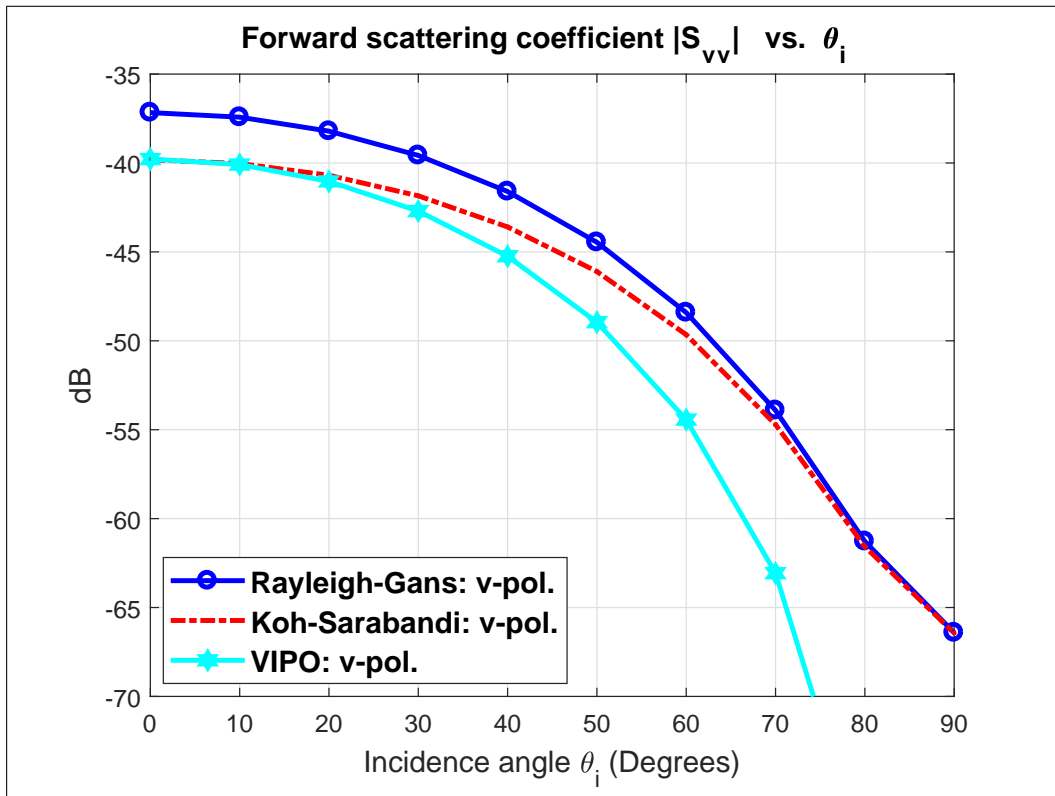
(a)

(b)

Figure 5.1: (a) The scattering geometry of a tilted thin dielectric circular disk is shown in the global coordinate system (X, Y, Z) and local coordinate system (X', Y', Z'). (b) The geometrical configuration of two tilted thin circular dielectric disks which are sparsely placed at $(x_1, 0, 0)$ and $(-x_1, 0, 0)$.

Figure 5.2: Magnitudes of the forward scattering coefficients (a) $|S_{hh}|$ and (b) $|S_{vv}|$ for the three dielectric thin circular disks as a function of the incidence angle θ_i. The reproduced results for $|S_{hh}|$ agree quite well with the Fig. 7a of Chapter 6 and the results for $|S_{vv}|$ are in good agreement with Fig. 8a of Chapter 6 [57].
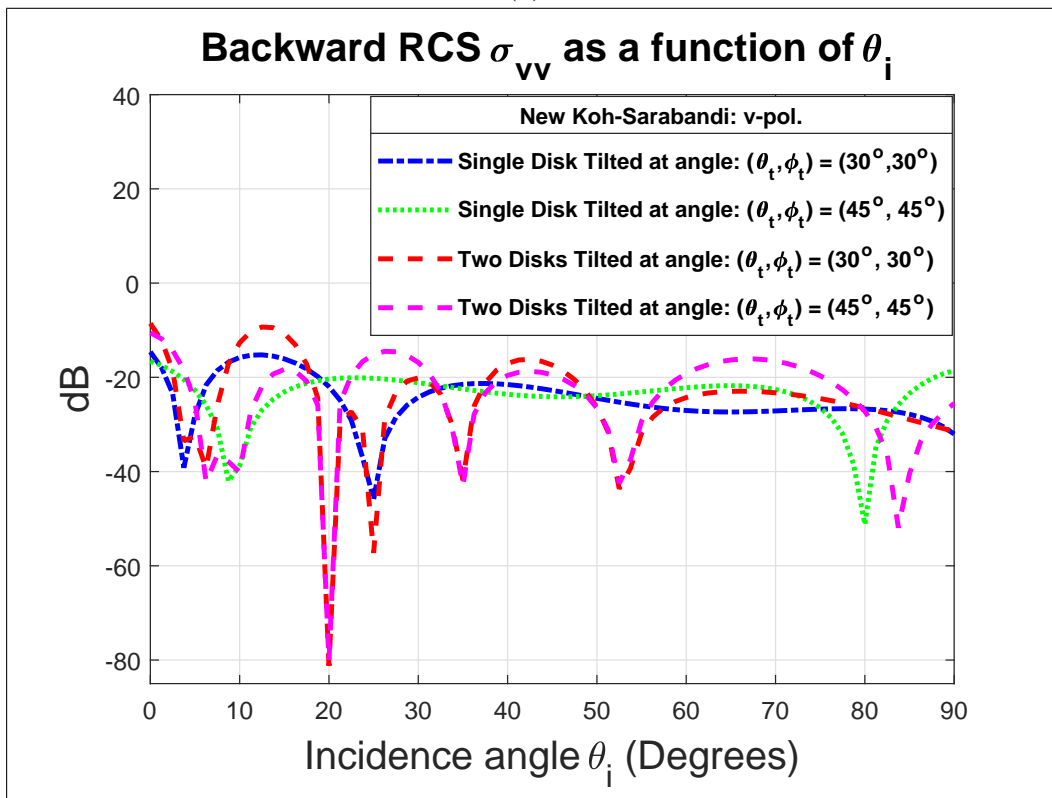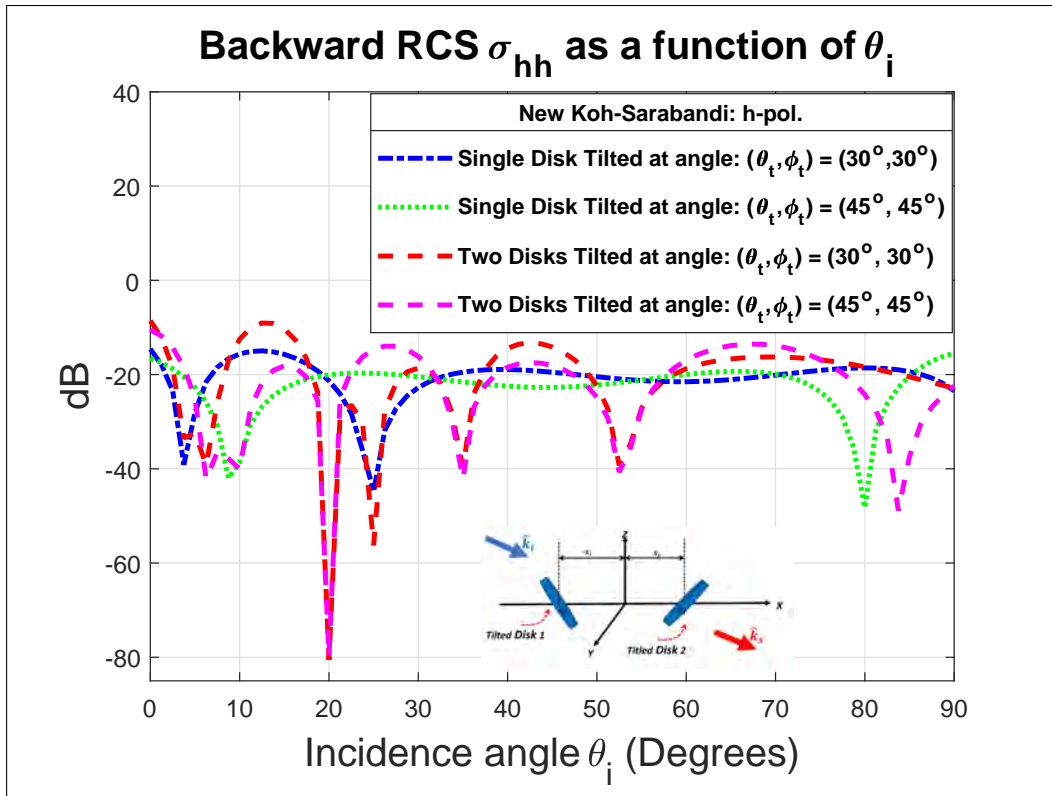
(a)

(b)

Figure 5.3: The back-scattered cross sections (a) σ_{hh} (b) σ_{vv} for a pair of tilted thin dielectric circular disks placed at (1,0,0)cm and (-1,0,0)cm and its comparison with a single tilted disk as a function of incident angle θ_i. All the other electrical and geometrical parameters are considered same as given in Fig.7 of Chapter3. The results presented here are based on the New Koh-Sarabandi method.
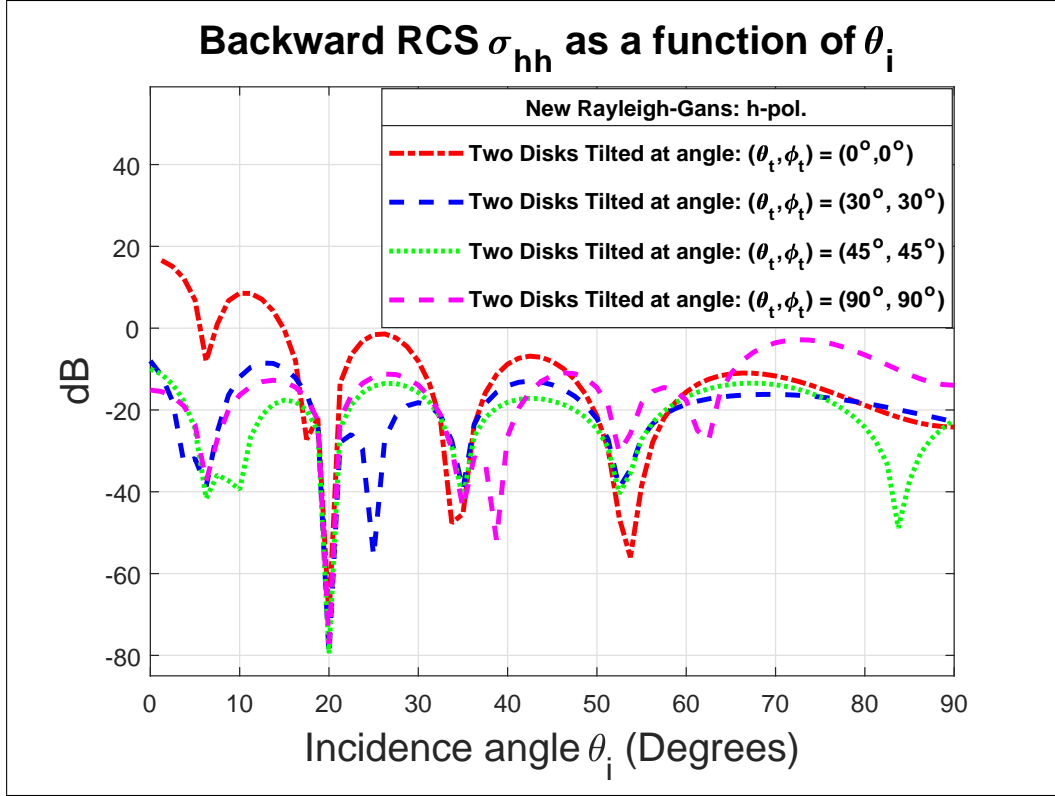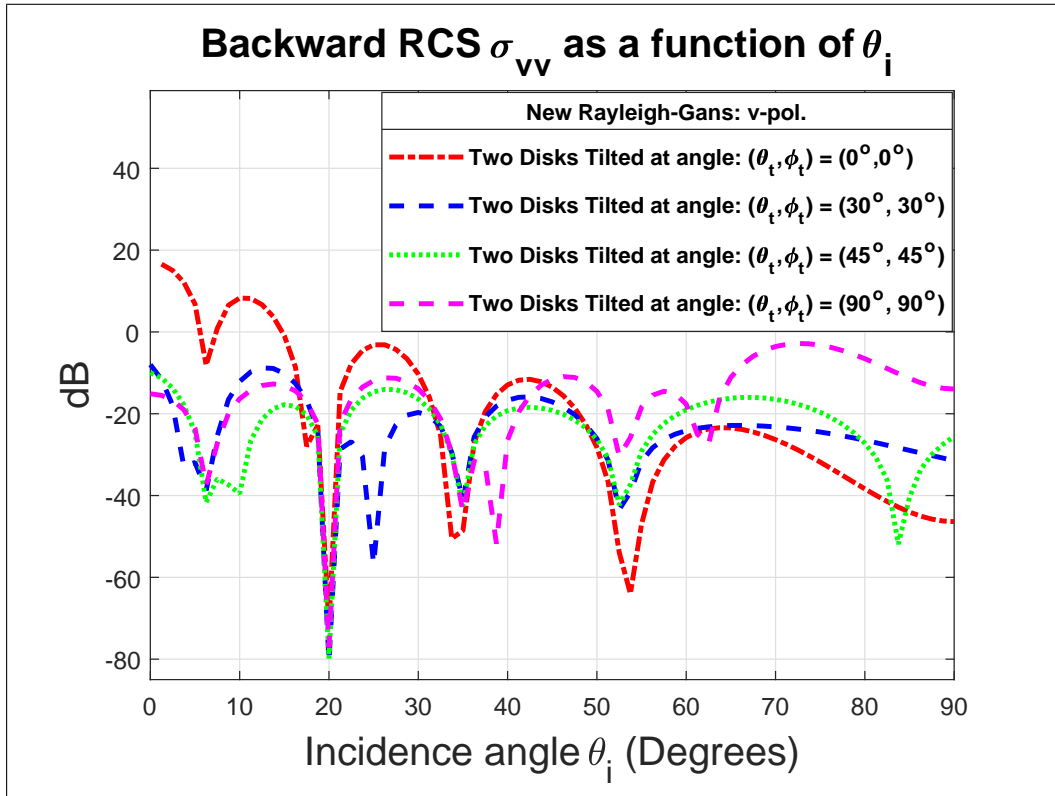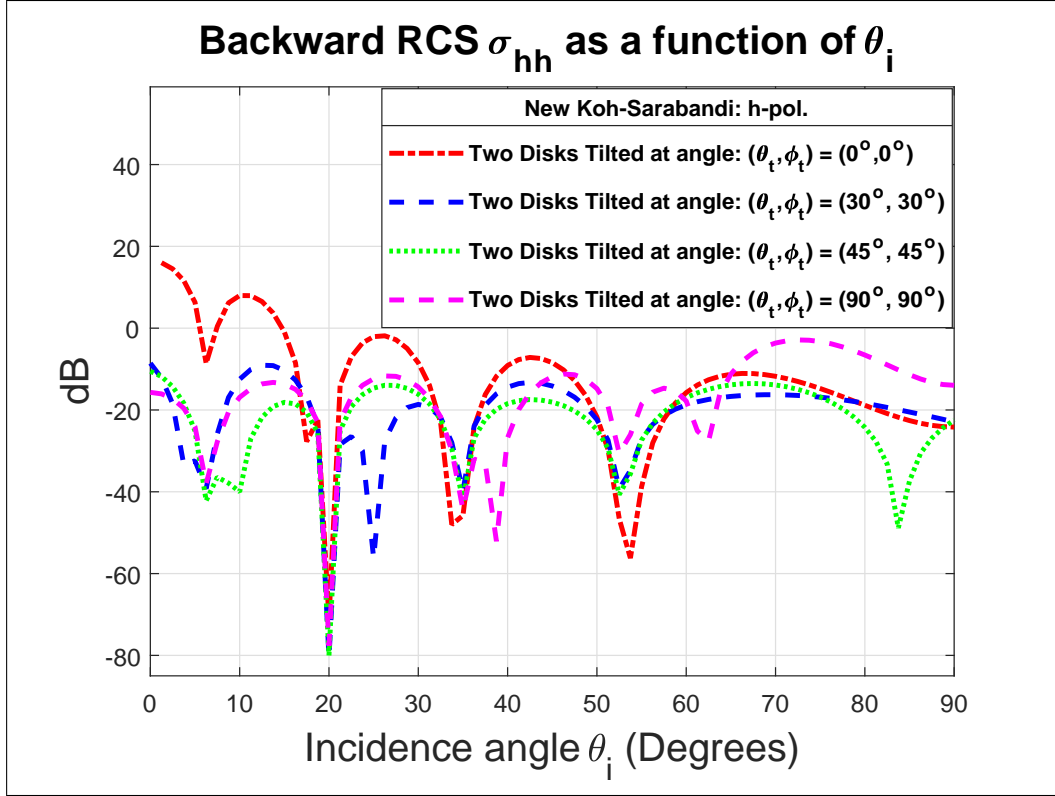
Figure 5.4: The back-scattering cross sections (a) σ_{hh} and (b) σ_{vv} for a pair of tilted thin GaAs circular disks placed at $(1,0,0)$cm and $(-1,0,0)$cm with the orientations (θ_t, ϕ_t) of $(30^o, 30^o)$, $(45^o, 45^o)$ and $(90^o, 90^o)$ as a function of incident angle θ_i. The results presented here are based on the newly proposed formulation of a tilted disk using Rayleigh-Gans approximation which is a low frequency approximation.
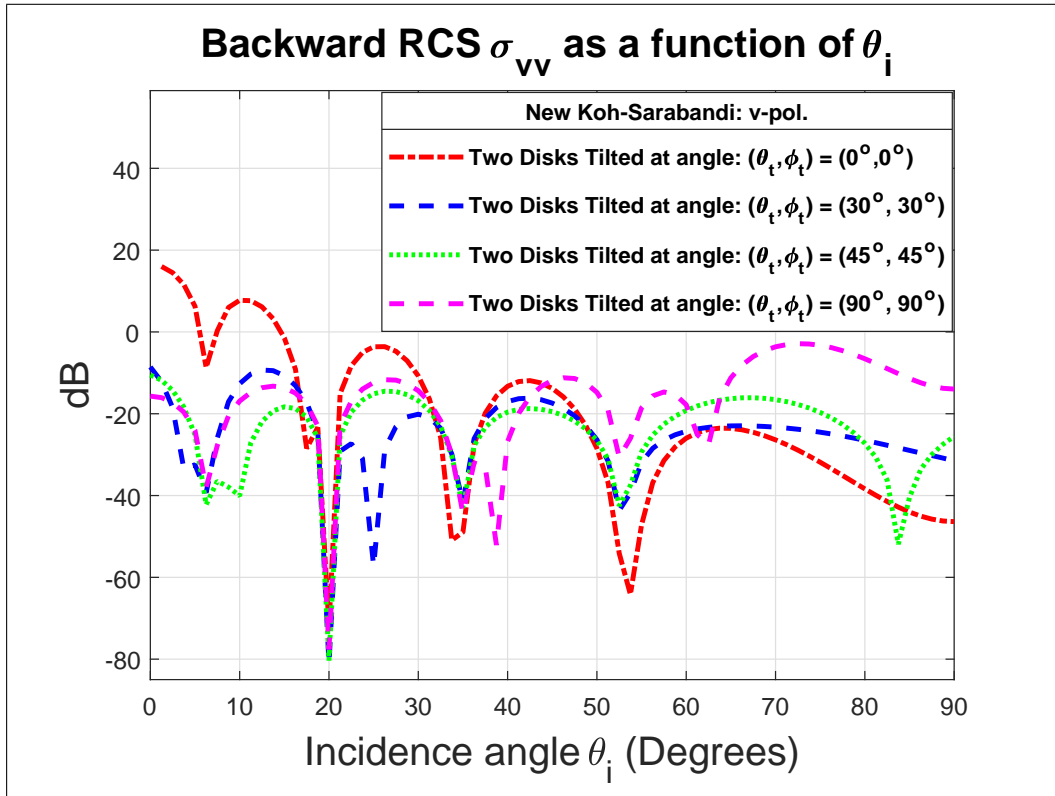
(a)

(b)

Figure 5.5: The back-scattering cross sections (a) σ_{hh} and (b) σ_{vv} for a pair of tilted thin GaAs circular disks placed at $(1,0,0)$cm and $(-1,0,0)$cm with the orientations (θ_t, ϕ_t) of $(30^o, 30^o)$, $(45^o, 45^o)$ and $(90^o, 90^o)$ as a function of incident angle θ_i. The results presented here are based on the newly proposed formulation of a tilted disk using Koh-Sarabandi approximation which is a intermediate frequency approxima-
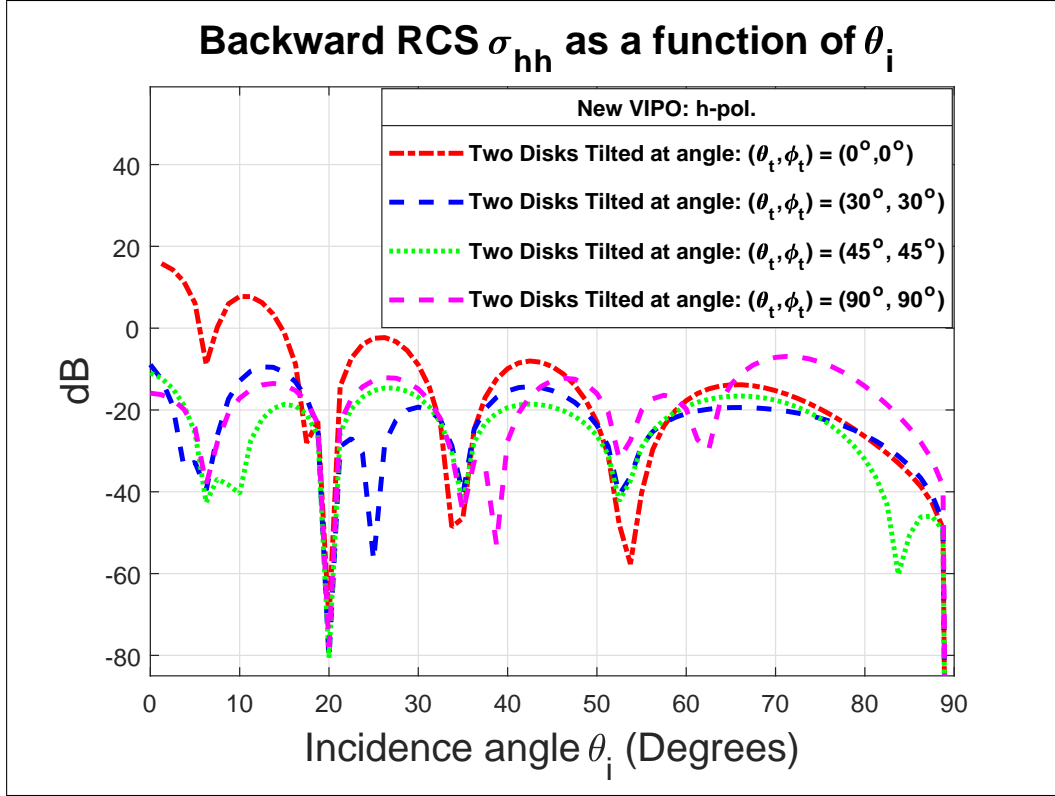
Figure 5.6: The back-scattering cross sections (a) σ_{hh} and (b) σ_{vv} for a pair of tilted thin GaAs circular disks placed at $(1,0,0)$cm and $(-1,0,0)$cm with the orientations (θ_t, ϕ_t) of $(30^o, 30^o)$, $(45^o, 45^o)$ and $(90^o, 90^o)$ as a function of incident angle θ_i. The results presented here are based on the newly proposed formulation of a tilted disk using VIPO approximation which is a high frequency approximation.
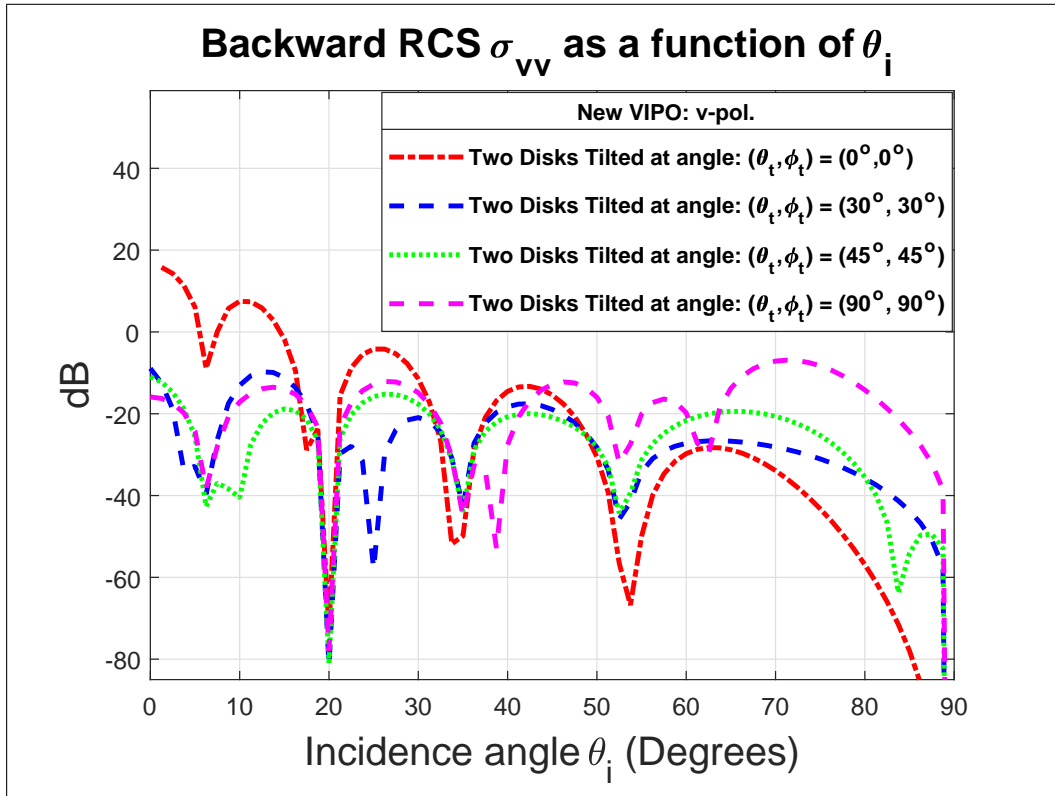
Figure 5.7: The back-scattering cross sections (a) σ_{hh} and (b) σ_{vv} for a pair of tilted thin GaAs circular disks placed at $(1.5,0,0)$cm and $(-1.5,0,0)$cm with the orientations (θ_t, ϕ_t) of $(30^o, 30^o)$, $(45^o, 45^o)$ and $(90^o, 90^o)$ as a function of disk size parameter $k_o a$. The results presented here are based on the New Rayleigh-Gans method.

Figure 5.8: The back-scattering cross sections (a) σ_{hh} and (b) σ_{vv} for a pair of tilted thin GaAs circular disks placed at (1.5,0,0)cm and (-1.5,0,0)cm with the orientations (θ_t, ϕ_t) of $(30^o, 30^o)$, $(45^o, 45^o)$ and $(90^o, 90^o)$ as a function of disk size parameter $k_o a$. The results presented here are based on the New Koh-Sarabandi method.
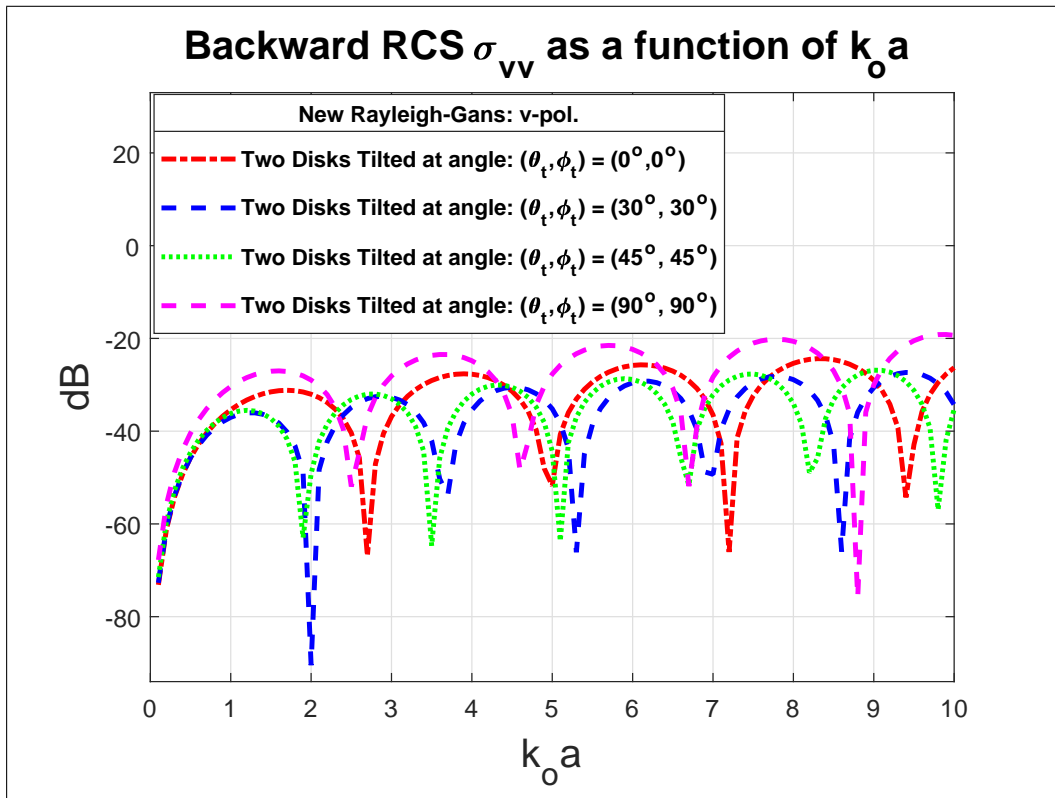
Figure 5.9: The back-scattering cross sections (a) σ_{hh} and (b) σ_{vv} for a pair of tilted thin GaAs circular disks placed at (1.5,0,0)cm and (-1.5,0,0)cm with the orientations (θ_t, ϕ_t) of $(30^o, 30^o)$, $(45^o, 45^o)$ and $(90^o, 90^o)$ as a function of disk size parameter $k_o a$. The results presented here are based on the New VIPO method.
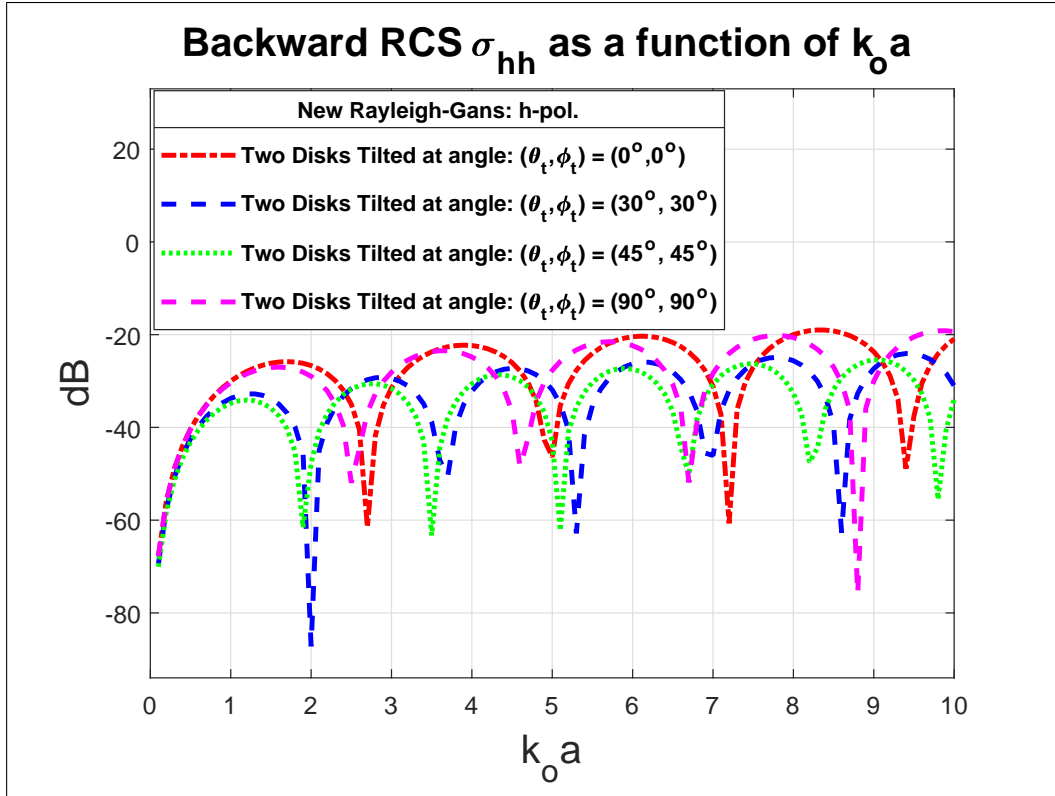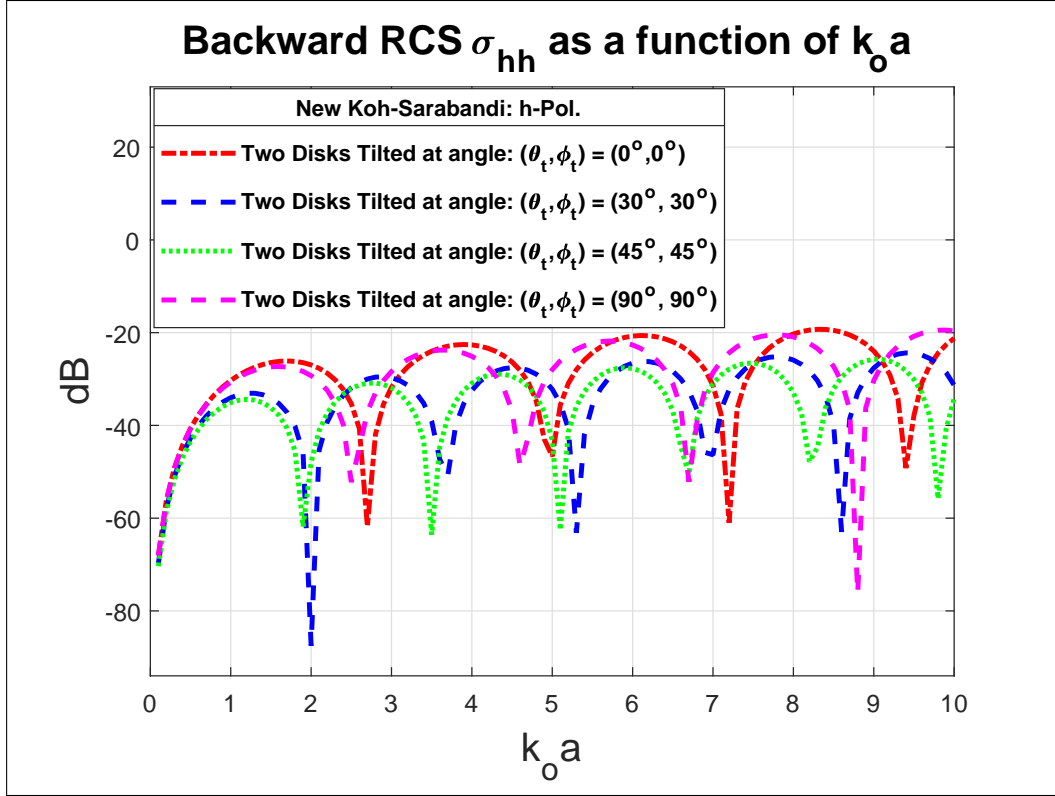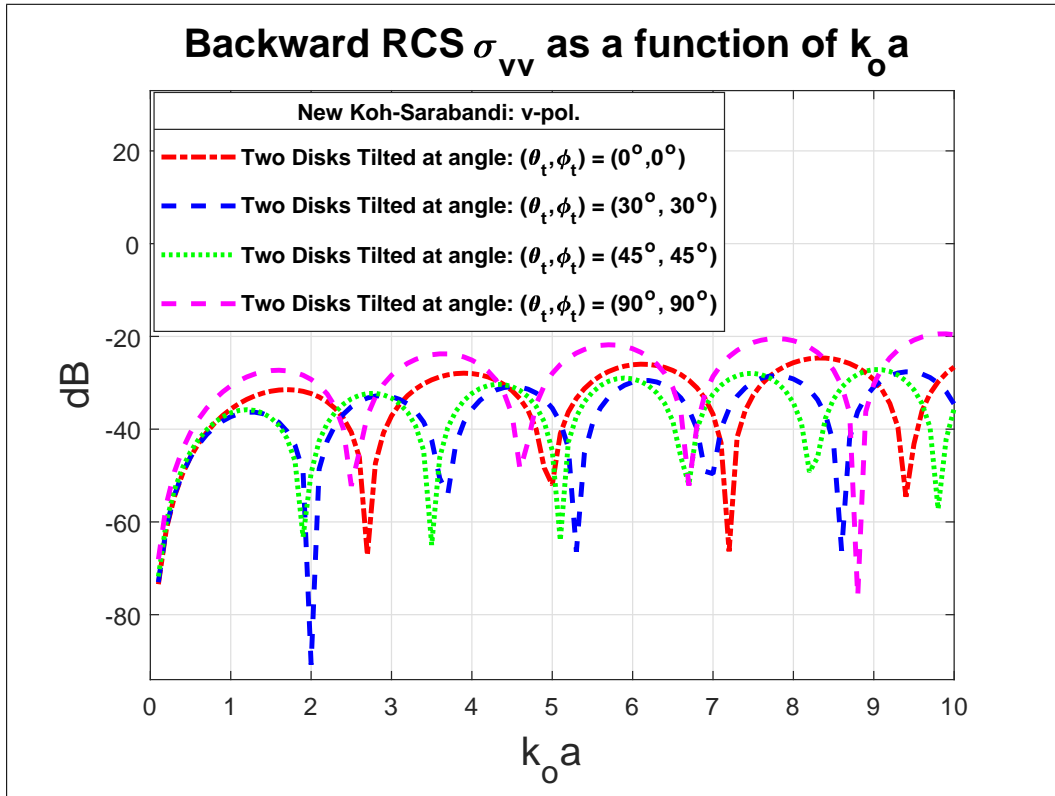
Figure 5.10: The back-scattering cross sections (a) σ_{hh} and (b) σ_{vv} for a pair of tilted thin GaAs circular disks placed at (1.5,0,0)cm and (-1.5,0,0)cm with the orientations (θ_t, ϕ_t) of $(30^o, 30^o)$, $(45^o, 45^o)$ and $(90^o, 90^o)$ upon the real part of relative permittivity. The results presented here are based on the New RG method. Here the $\text{Im}(\epsilon_r)$ is fixed at 0.5

Figure 5.11: The back-scattering cross sections (a) σ_{hh} and (b) σ_{vv} for a pair of tilted thin GaAs circular disks placed at (1.5,0,0)cm and (-1.5,0,0)cm with the orientations (θ_t, ϕ_t) of $(30^o, 30^o)$, $(45^o, 45^o)$ and $(90^o, 90^o)$ upon the real part of relative permittivity. The results presented here are based on the New Koh -Sarabandi method. Here the $\text{Im}(\epsilon_r)$ is fixed at 0.5
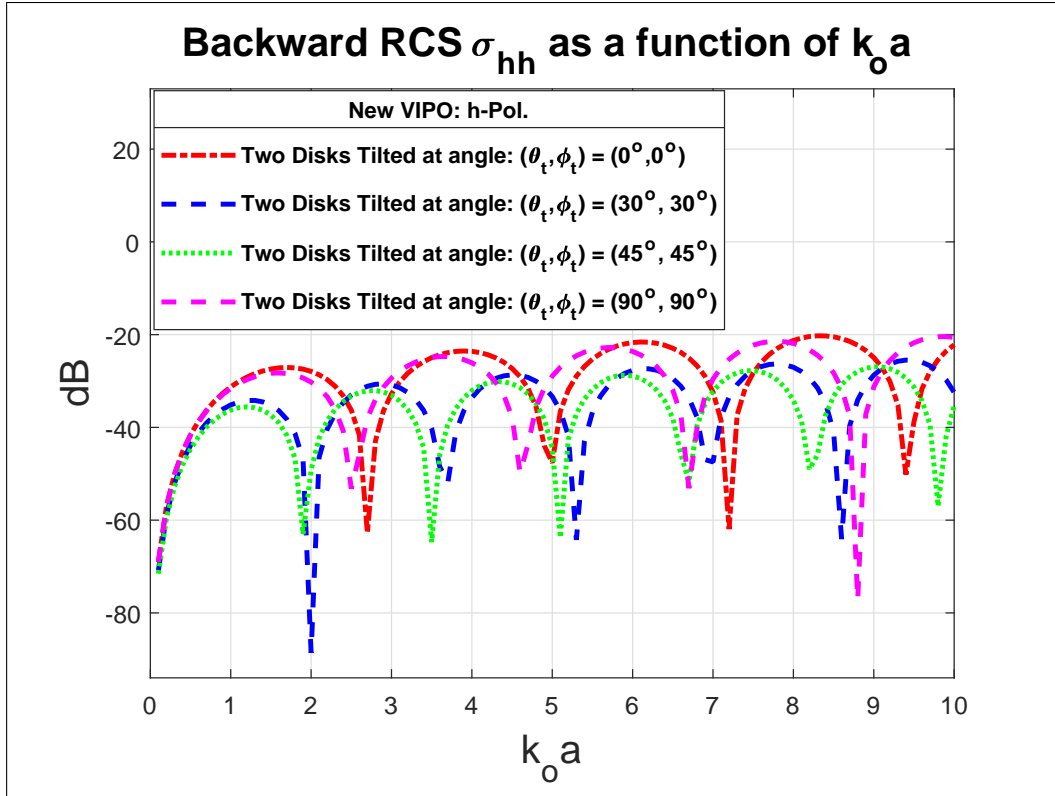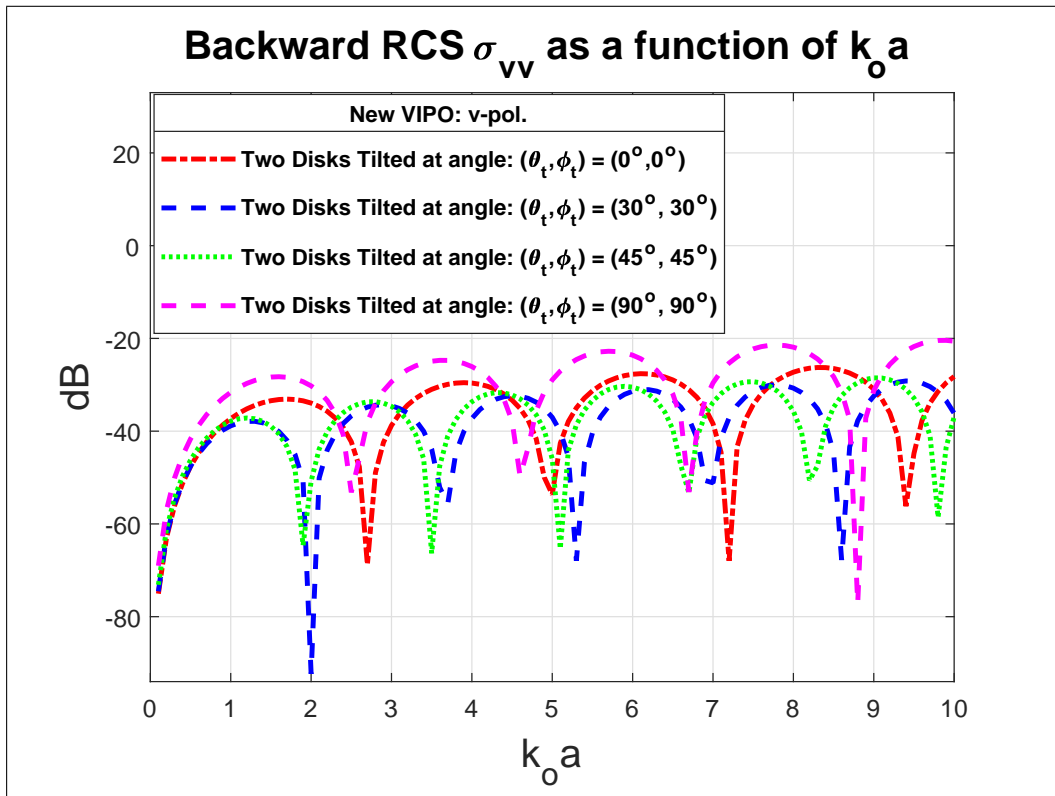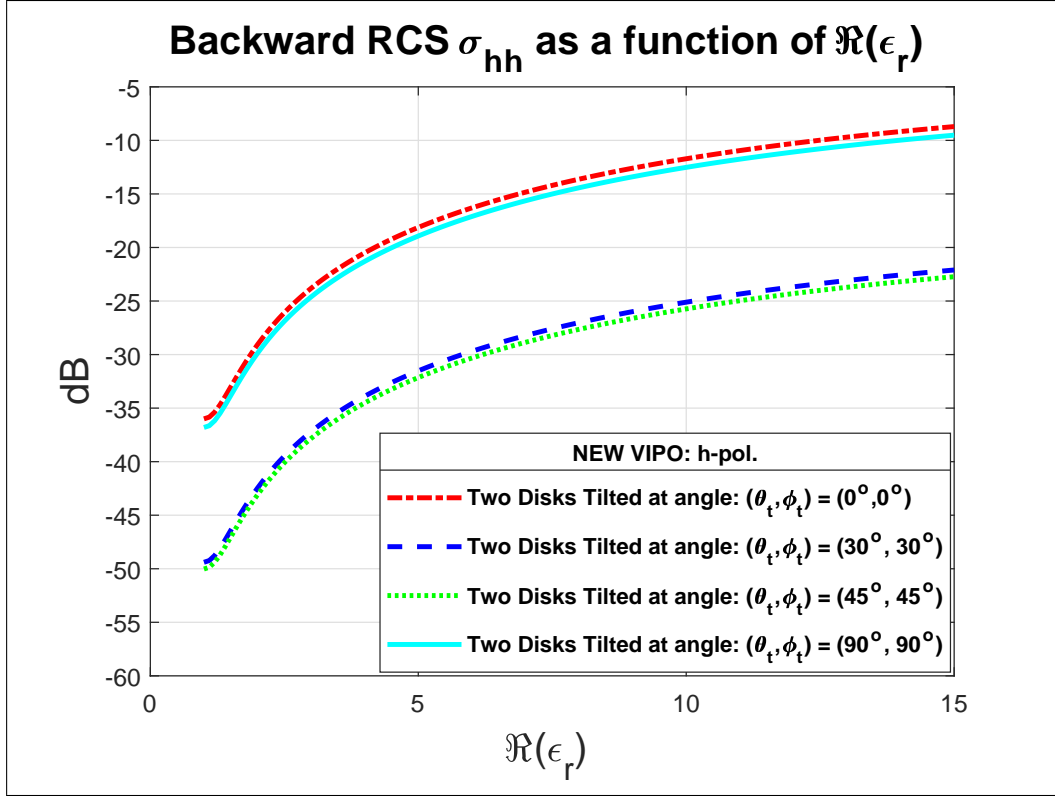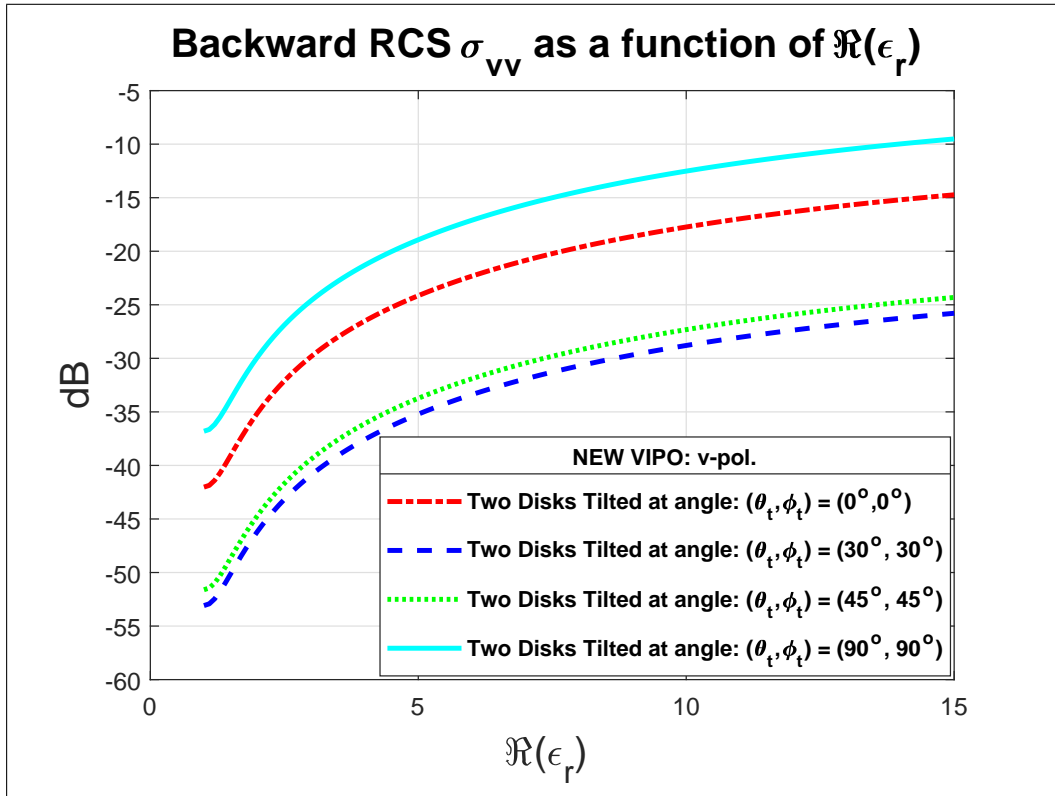
Figure 5.12: The back-scattering cross sections (a) σ_{hh} and (b) σ_{vv} for a pair of tilted thin GaAs circular disks placed at $(1.5,0,0)$cm and $(-1.5,0,0)$cm with the orientations (θ_t, ϕ_t) of $(30^o, 30^o)$, $(45^o, 45^o)$ and $(90^o, 90^o)$ upon the real part of relative permittivity. The results presented here are based on the New VIPO method. Here the $\text{Im}(\epsilon_r)$ is fixed at 0.5
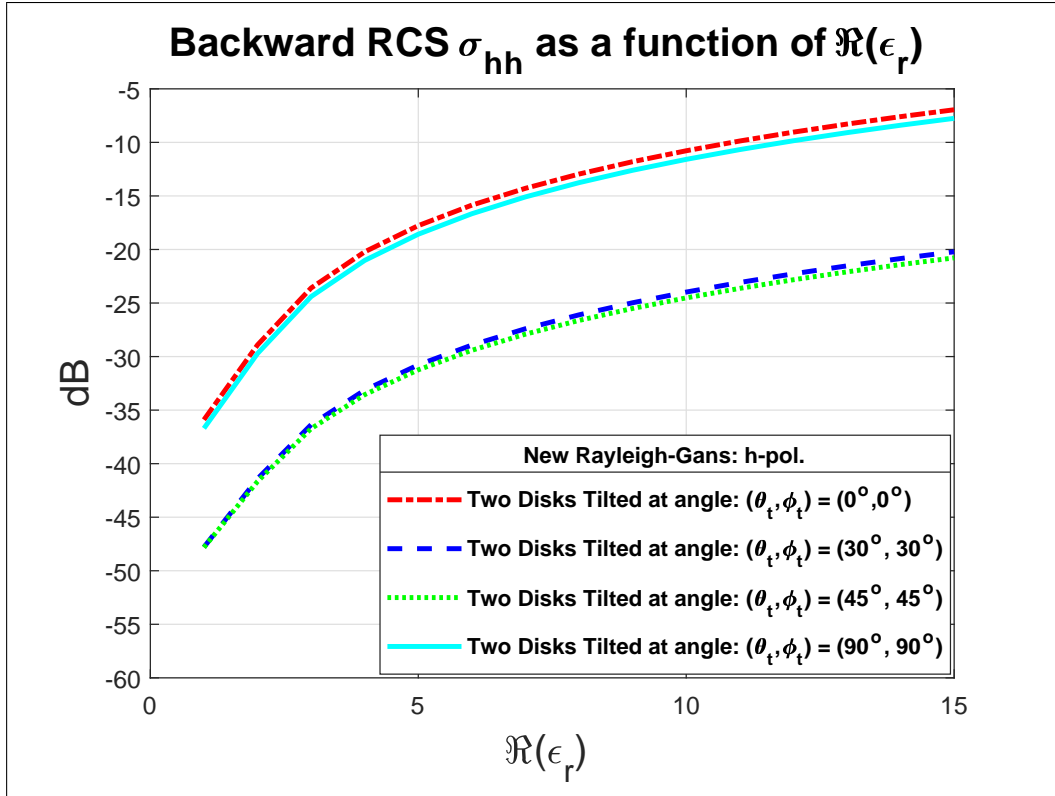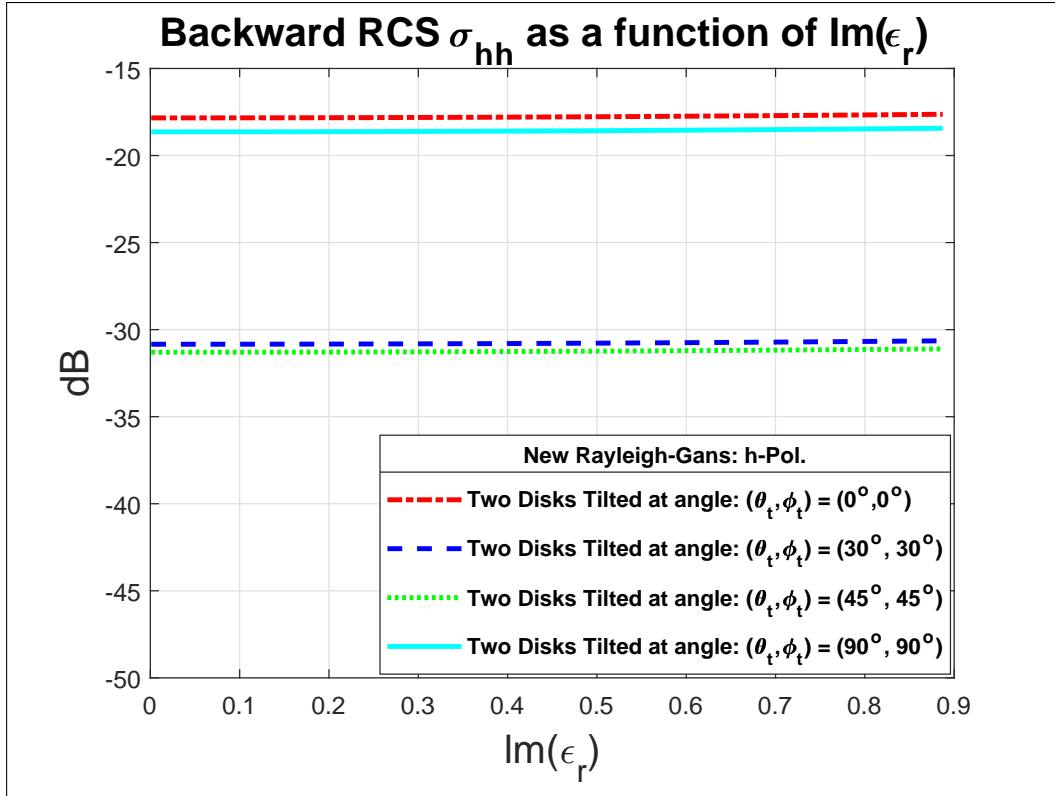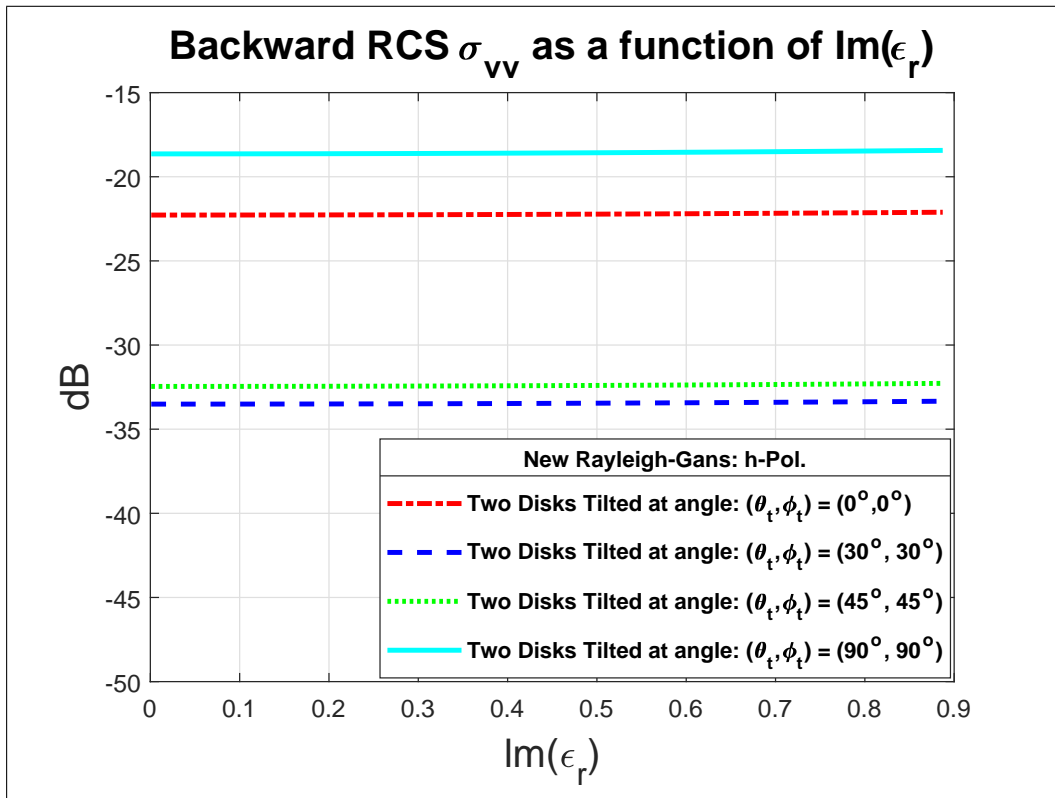
Figure 5.13: The back-scattering cross sections (a) σ_{hh} and (b) σ_{vv} for a pair of tilted thin GaAs circular disks placed at (1.5,0,0)cm and (-1.5,0,0)cm with the orientations (θ_t, ϕ_t) of $(30^o, 30^o)$, $(45^o, 45^o)$ and $(90^o, 90^o)$ upon the imaginary part of relative permittivity. The results presented here are based on the New RG method. Here the $\text{Re}(\epsilon_r)$ is fixed at 5
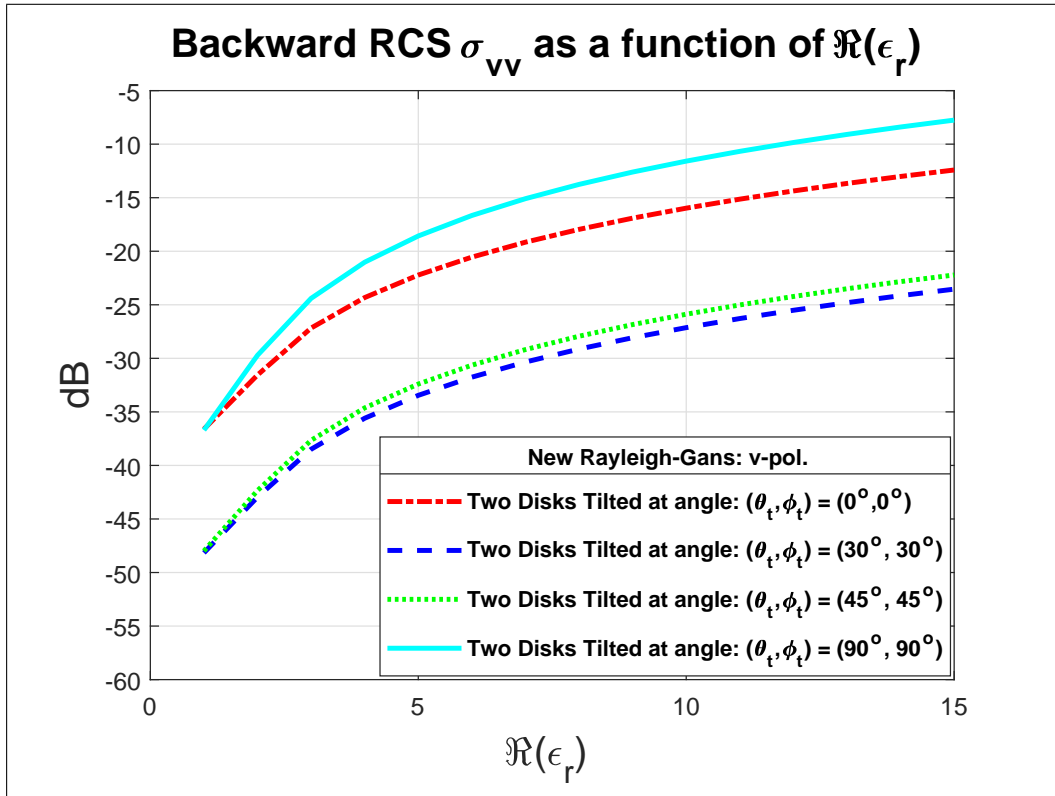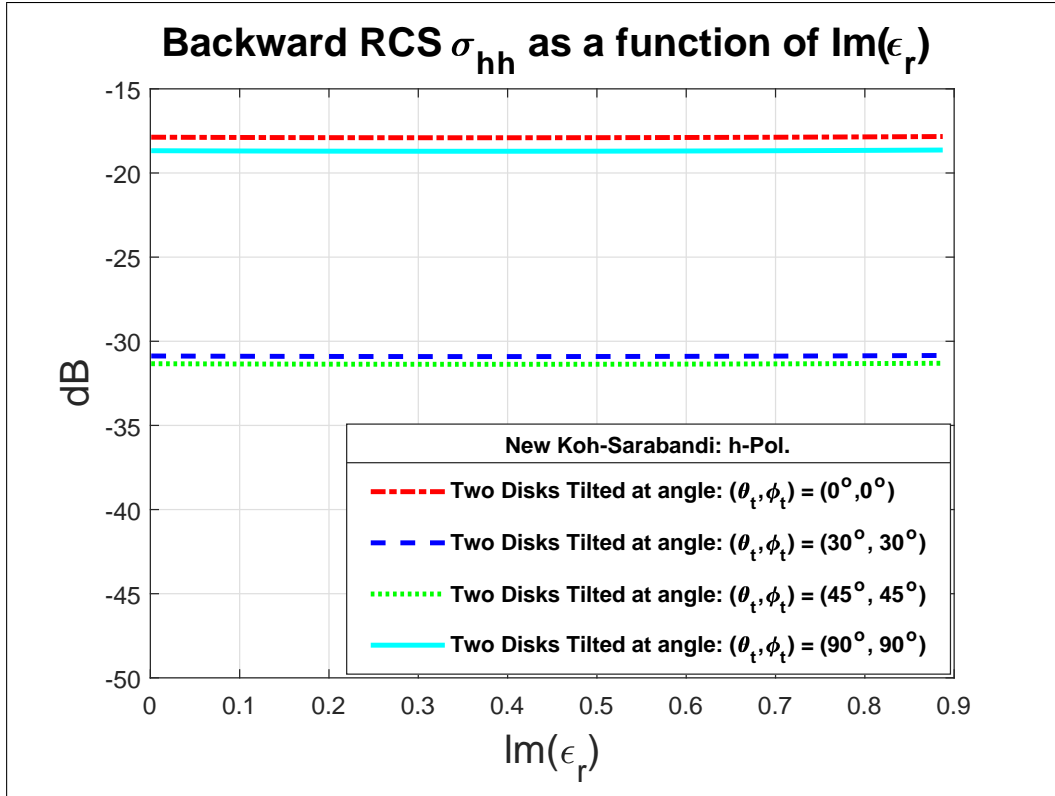
(a)
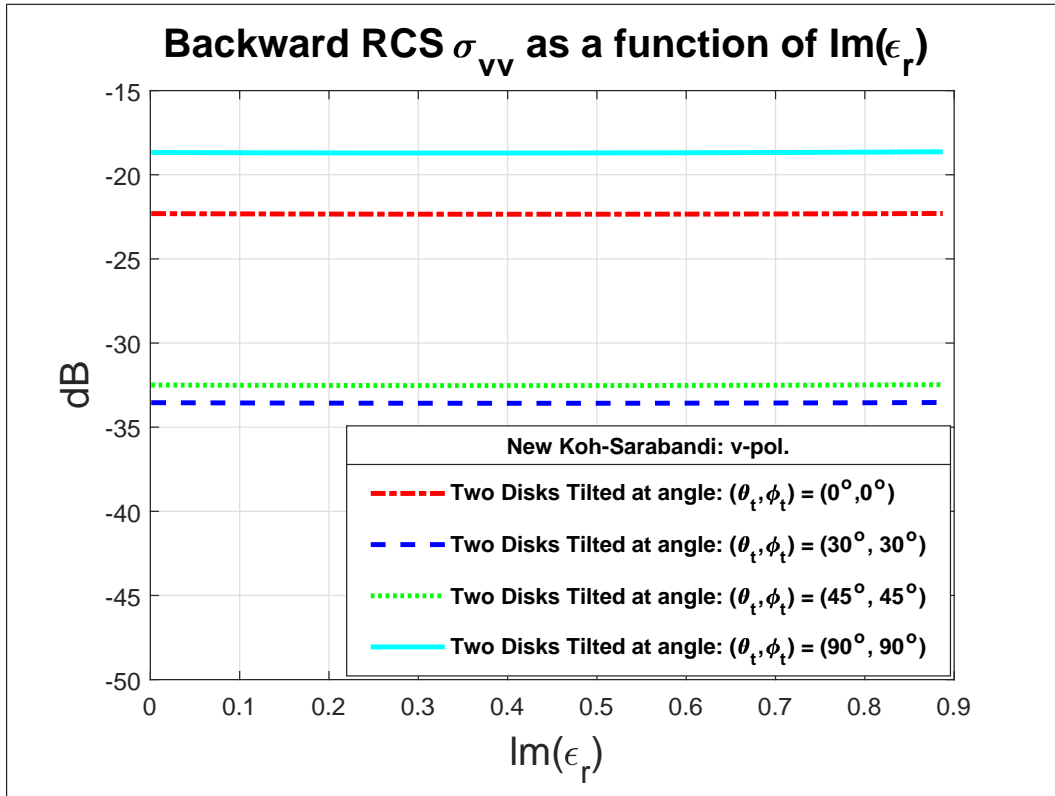
(b)

Figure 5.14: The back-scattering cross sections (a) σ_{hh} and (b) σ_{vv} for a pair of tilted thin GaAs circular disks placed at (1.5,0,0)cm and (-1.5,0,0)cm with the orientations (θ_t, ϕ_t) of $(30^o, 30^o)$, $(45^o, 45^o)$ and $(90^o, 90^o)$ upon the imaginary part of relative permittivity. The results presented here are based on the New KOH-Sarabandi method. Here the $Re(\epsilon_r)$ is fixed at 5
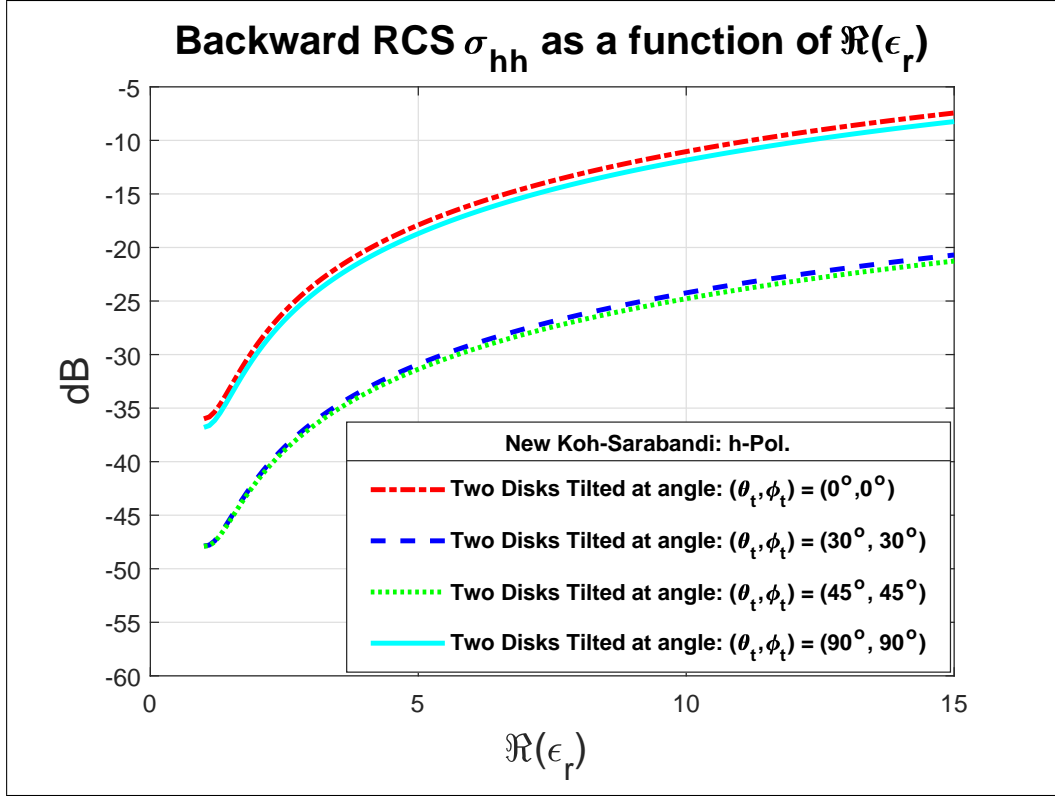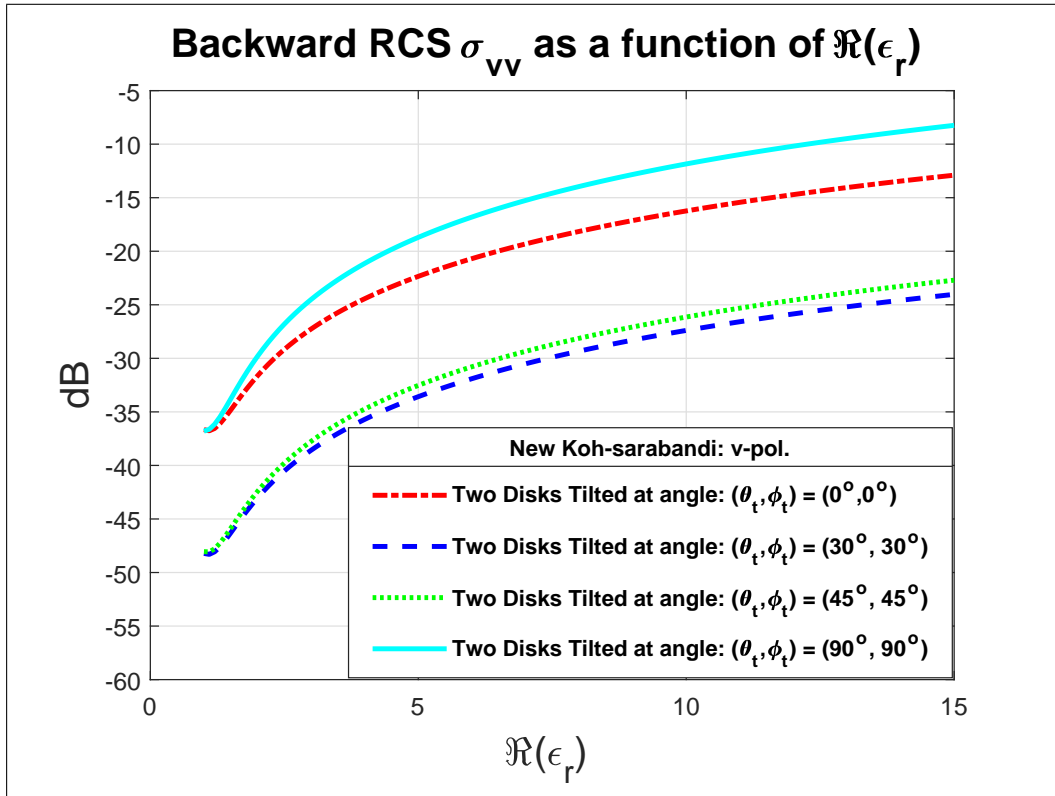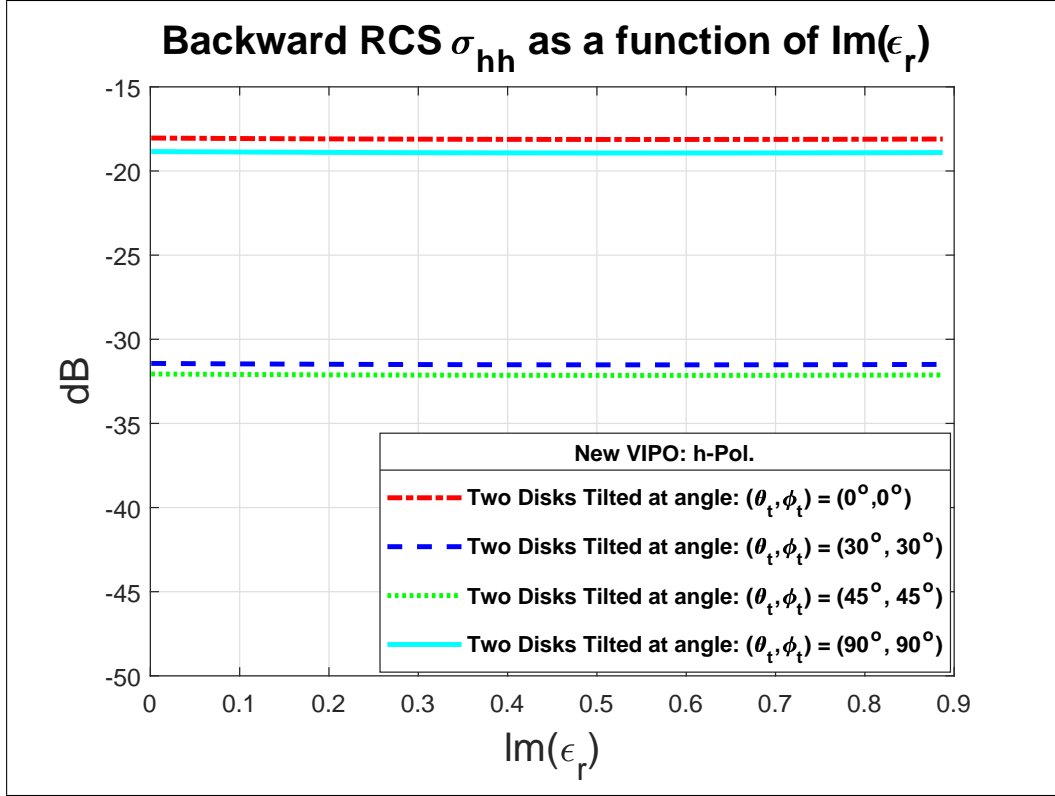
(a)
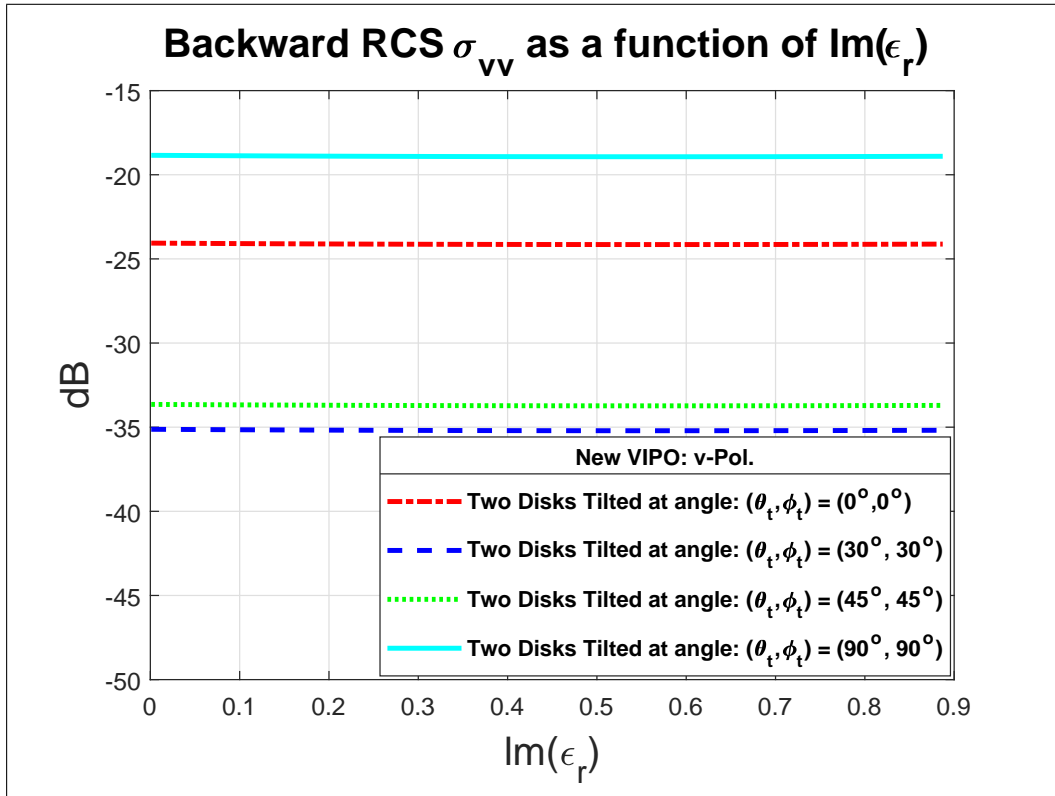
(b)

Figure 5.15: The back-scattering cross sections (a) σ_{hh} and (b) σ_{vv} for a pair of tilted thin GaAs circular disks placed at (1.5,0,0)cm and (-1.5,0,0)cm with the orientations (θ_t, ϕ_t) of $(30^o, 30^o)$, $(45^o, 45^o)$ and $(90^o, 90^o)$ upon the imaginary part of relative permittivity. The results presented here are based on the New VIPO method. Here the $\text{Re}(\epsilon_r)$ is fixed at 5

(a)

(b)
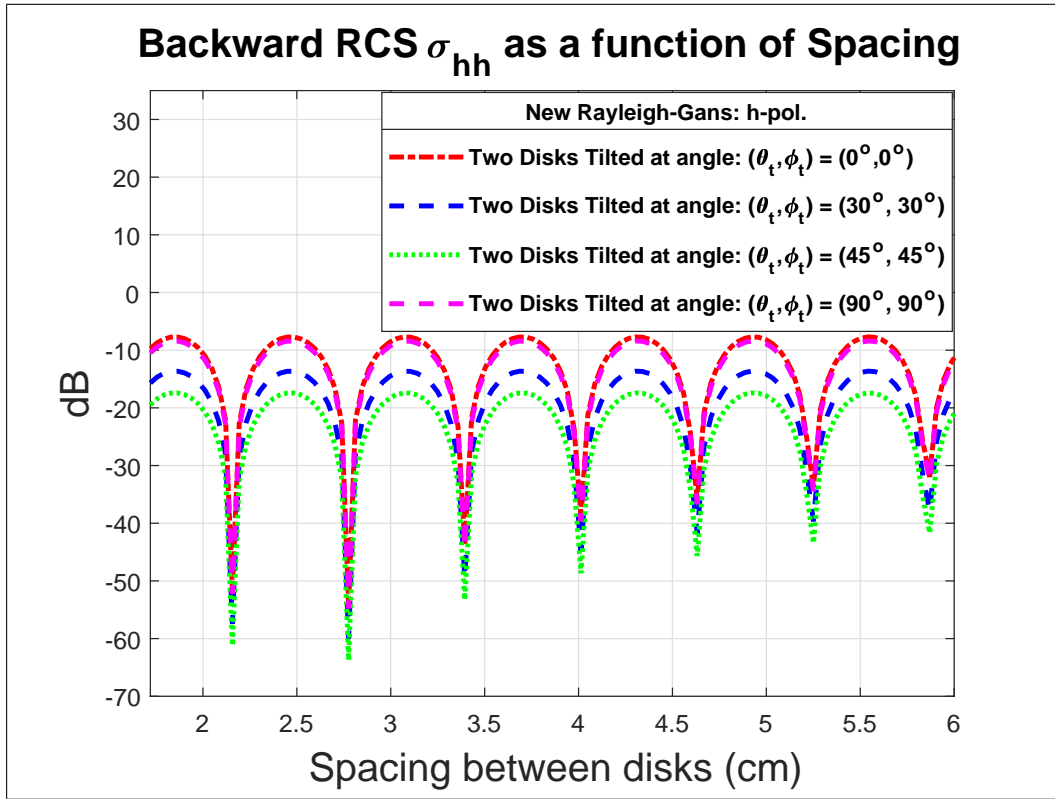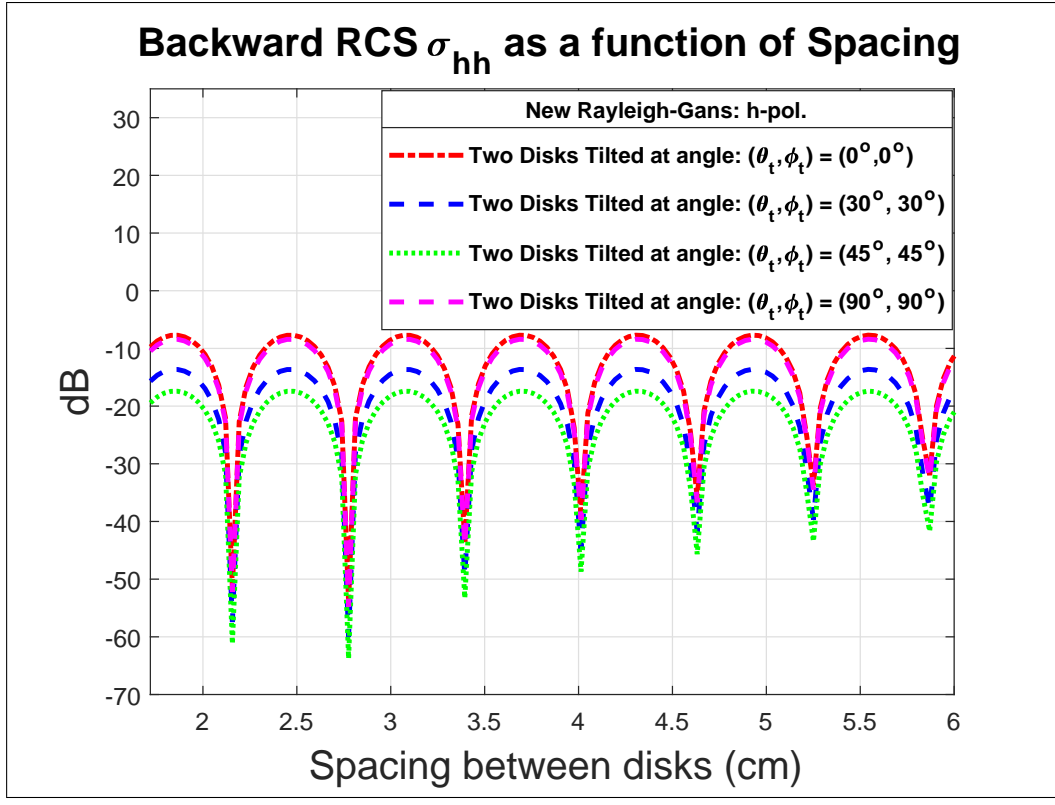
Figure 5.16: The back-scattering cross sections (a) σ_{hh} and (b) σ_{vv} as a function of the spacing between the pair of tilted thin GaAs circular disks with the orientations (θ_t, ϕ_t) of $(30^o, 30^o)$, $(45^o, 45^o)$ and $(90^o, 90^o)$. The results presented here are based on the New RG method.

(a)

(b)
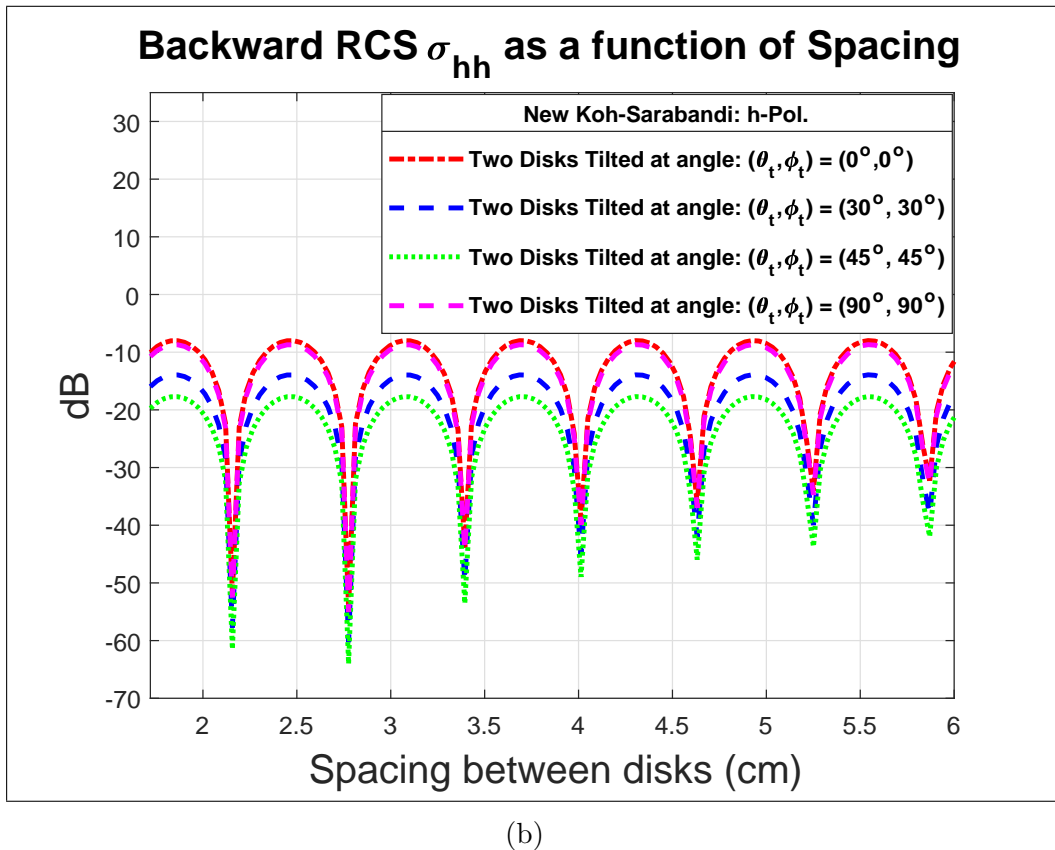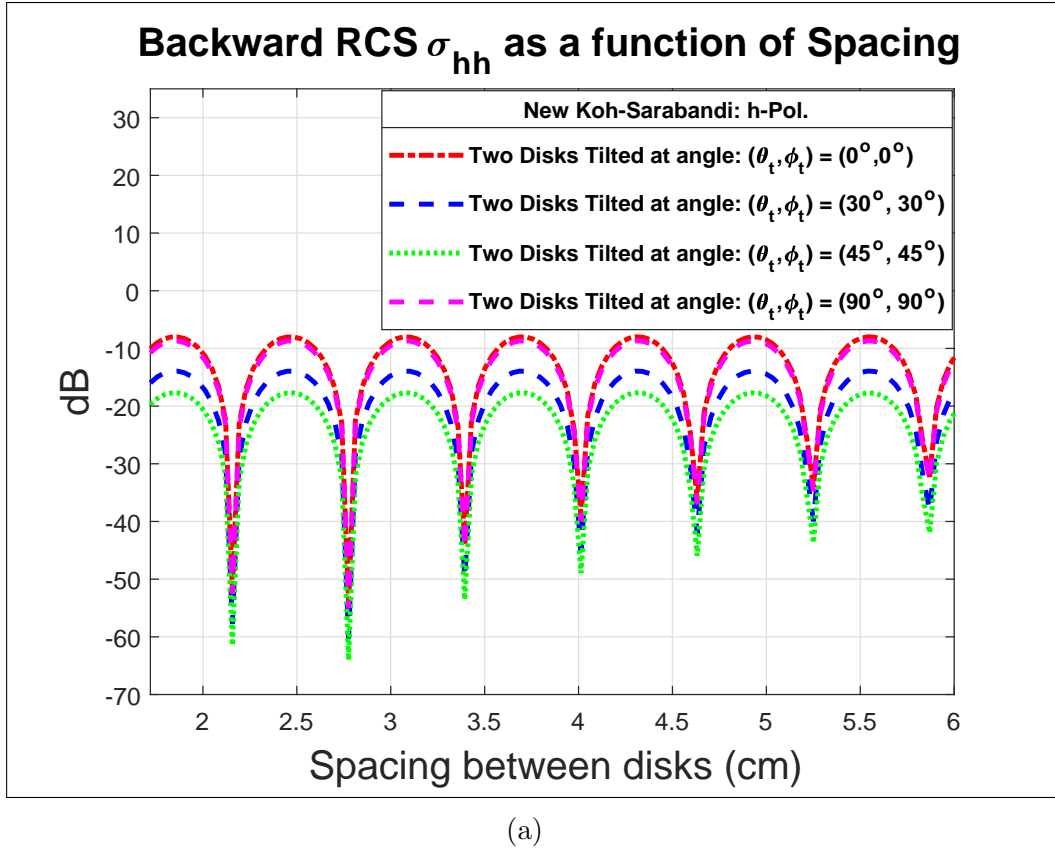
Figure 5.17: The back-scattering cross sections (a) σ_{hh} and (b) σ_{vv} as a function of the spacing between the pair of tilted thin GaAs circular disks with the orientations (θ_t, ϕ_t) of $(30^o, 30^o)$, $(45^o, 45^o)$ and $(90^o, 90^o)$. The results presented here are based on the New KS method.
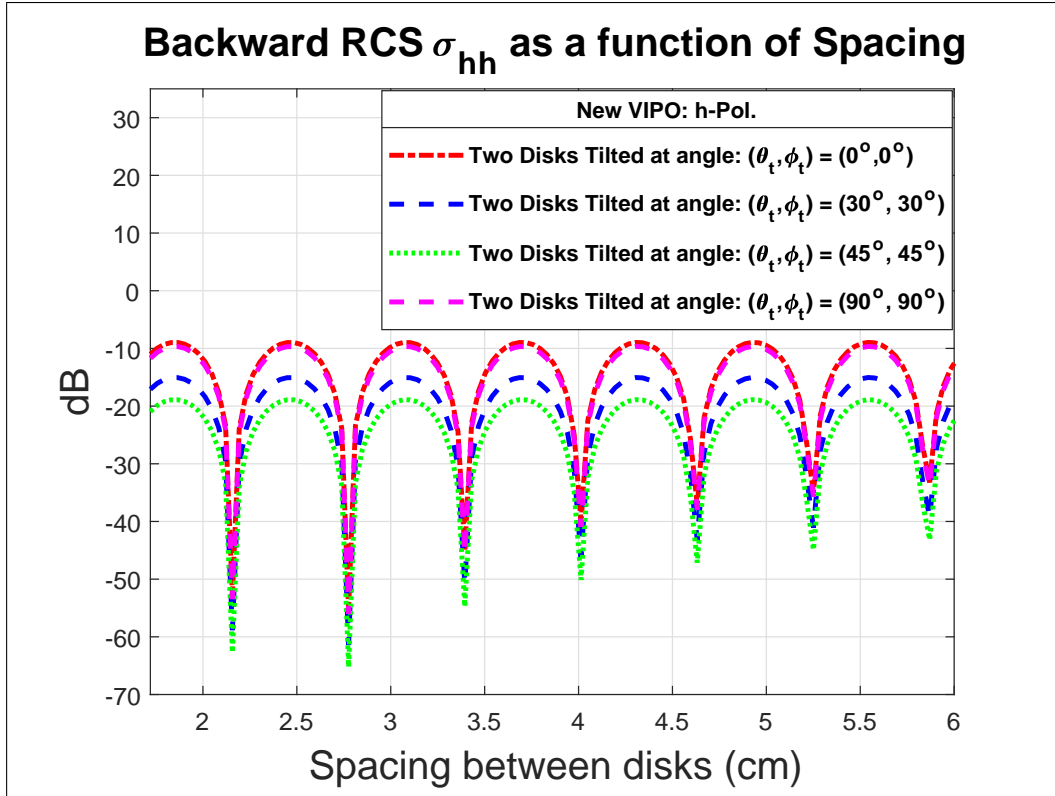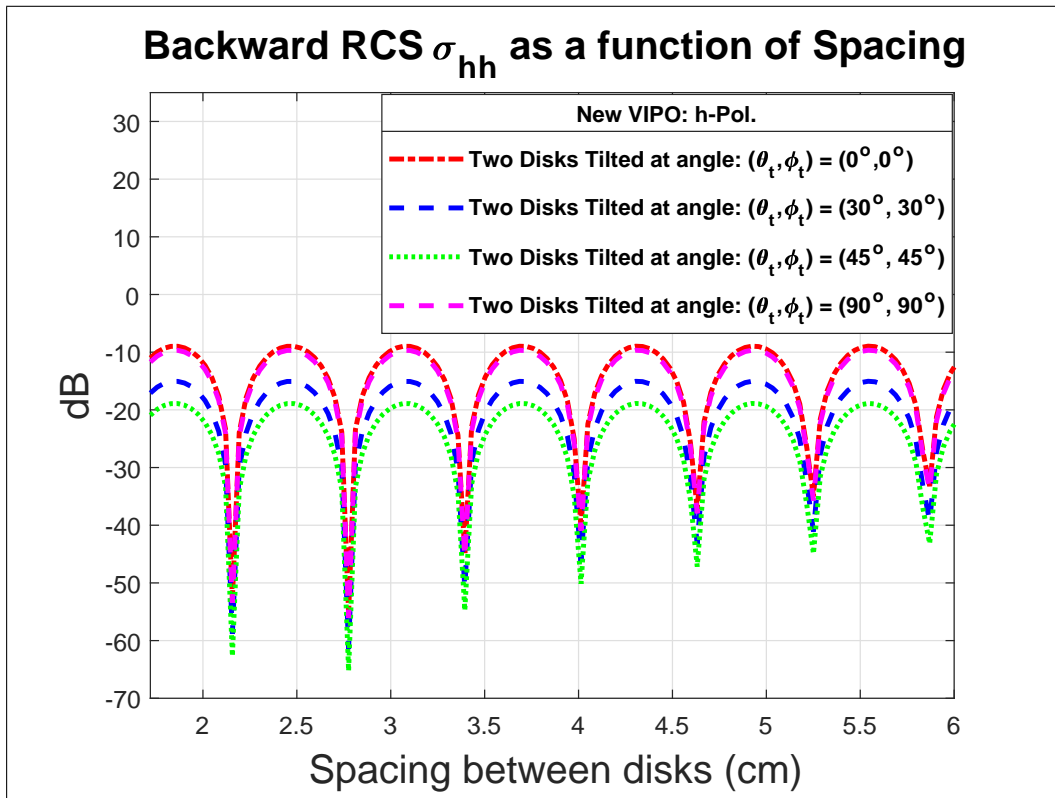
Figure 5.18: The back-scattering cross sections (a) σ_{hh} and (b) σ_{vv} as a function of the spacing between the pair of tilted thin GaAs circular disks with the orientations (θ_t, ϕ_t) of $(30^o, 30^o)$, $(45^o, 45^o)$ and $(90^o, 90^o)$. The results presented here are based on the New VIPO method.

distribution of tilted thin circular dielectric disks have been studied. Here we have considered three different sets of tilt angles which are given by $(\theta_t, \phi_t) = (30^o, 30^o)$, $(45^o, 45^o)$ and $(90^o, 90^o)$. The thickness of each disk is taken to be $t = 0.01\lambda_o$ for Figs. 4–18 which represents a thin disk.

In order to verify and validate the proposed formulation, we first reproduced the numerical results as shown in Fig.7(a) and Fig 8(a) Chapter6 [57] for the magnitudes of forward scattering elements S_{hh} and S_{vv} from three thin dielectric circular disks placed at (1.5cm,1,0), (-1.5,0,0) and (-4.5,0,0) respectively. They are shown in Fig. (5.2). The presented results of the back-scattered cross sections shown in Fig. (5.2) are based on three different well known approaches, i.e., the Rayleigh-Gans (RG), the Koh-Sarabandi (KS) and the volumetric integral physical optics (VIPO). In this work, it is assumed that $\Phi_i = 0^o$ and the relative permittivity, radius and thickness of the each disk are $\epsilon_r = 26.6 + 11.56i$, 1.5 cm, 0.02 mm, respectively at an operating frequency of 10 GHz (i.e., all the parameters are identical to those used in [57]). It is evident that the simulated results of S_{hh} and S_{vv} are in excellent agreement with the previous results in the literature [57].

In Fig. (5.3), the back-scattered cross sections σ_{hh} and σ_{vv} for a pair of tilted thin dielectric circular disks placed at (1,0,0)cm and (-1,0,0)cm and their comparison with a single tilted disk as a function of incident angle θ_i have been shown. All the other electrical and geometrical parameters are considered same as used in chapter 3 for the single tilted thin circular dielectric disk scattering. The presented results are based on the New Koh-Sarabandi approach for the specific tilt angles of $(\theta_t, \phi_t) = (30^o, 30^o)$ and $(\theta_t, \phi_t) = (45^o, 45^o)$. It is evident that the results of σ_{hh} and σ_{vv} for a single tilted low loss Gallium Arsenide (GaAs) disk are in excellent agreement with the previous

results reported in Chapter 3. It should be noted that the relative permittivity of a low loss Gallium Arsenide (GaAs) material is $\epsilon_r = 12.88 + 0.0004i$ [87]. It is clear from Fig. (5.3) that the back-scattered cross sections σ_{hh}, σ_{vv} for a pair of tilted thin GaAs circular disks are very different from the respective σ_{hh}, σ_{vv} for a single tilted thin GaAs circular disk for the considered disk orientations. It is found that for a pair of tilted disks, a significant reduction in the back-scattered cross sections for both types of incident polarizations is observed as compared to a single tilted disk at $\theta_i = 20^o$ for disk orientations of $\theta_t = \phi_t = 30^o$. This reduction is equal to -80.01 dB and can be considered as almost zero back scattering. Thus, it is concluded that a pair of tilted GaAs disks significantly reduced the back-scattered cross sections for horizontal and vertical polarizations at a specific incident polar angle as a compared to single GaAs tiled disk having same orientations as that of a pair of tilted disks. This almost zero back scattering is a desirable feature in the stealth technology.

The Figs. 4-6 deal with the influences of various orientations of the two tilted thin circular disks upon the back-scattered cross sections σ_{hh}, σ_{vv} as a function of incident angle θ_i. It is assumed that two GaAs disks are placed at (1,0,0)cm and (-1,0,0)cm. The radius a of each disk is equal to one free space wavelength at an operating frequency of 35 GHz. Here one of the incident angle ϕ_i is fixed at 20°. It is studied that the σ_{hh} pattern is almost same as that of σ_{vv} for the incident angle θ_i lying in the range $0 \leq \theta_i \leq 45^o$ for disk orientations of $(\theta_t, \phi_t) = (0^o, 0^o)$, $(\theta_t, \phi_t) = (30^o, 30^o)$ and $(\theta_t, \phi_t) = (45^o, 45^o)$ based on all the considered three approaches such as New RG, New KS and New VIPO. However, there exists an obvious change in (σ_{hh}) as compared to σ_{vv} for the incident angles lying in the range, i.e., $45^o \leq \theta_i \leq 90^o$. It is studied that for the orientations of the disk having $(\theta_t, \phi_t) = (90^o, 90^o)$, both patterns

of σ_{hh}, σ_{vv} are same for the considered three approaches. It is found that new VIPO approach deteriorates rapidly at the near-grazing incidence, i.e., edge-on incidence is not allowed by this approach. It is also noticed that the back-scattered cross sections σ_{hh}, σ_{vv} have the lowest values for the orientations of $(\theta_t, \phi_t) = (30^o, 30^o)$ having $\theta_i = 20^o$, i.e., less than -80 dB for all the three approaches.

In Figs. 7–9, the effects of different orientations of two tilted thin circular GaAs disks upon the back-scattered cross sections σ_{hh}, σ_{vv} as a function of the size parameter k_oa have been shown. Here $\theta_i = 45^o$ and $\phi_i = 22.5^o$. It is assumed that these two tilted disks are placed at (1.5,0,0)cm and (-1.5,0,0)cm. These two locations are selected in such a way so that sparse condition is not violated for the considered range of k_oa. It is observed that the minimum values of back-scattered cross sections for both types of incident polarizations are found for disk orientations of $\theta_t = \phi_t = 30^o$ having size parameter of $k_oa = 2$ for all the New RG, New KS and New VIPO methods. These minimum values are almost less than -87 dB and can be considered as zero back scattering. If we take $\phi_i = 10^o$ instead of $\phi_i = 22.5^o$ as considered above then all the other parameters become same as considered in the case of single tilted GaAs disk as given in Chapter 3. In this case for $\theta_t = \phi_t = 30^o$ and $k_oa = 2$, it is studied that there exists a reduction of almost -10 dB in the back-scattered cross sections for two sparse disks as compared to a single tilted disk for both types of incident polarization. But this is not shown in the figure and for the case (i.e., $\phi_i = 22.5^o$) under study for Figs. 7–9, it is found that a reduction up to -21 dB is observed for the two tilted thin GaAs disks as compared to a single tilted GaAs disk having $\theta_t = \phi_t = 30^o$ and $k_oa = 2$. Thus, it is concluded that two specific sparsely located tilted disks significantly reduced the back-scattered cross sections as compared to a single

tilted disk having same geometrical and electrical parameters. Such types of almost zero back scattering plays an important role in many radar engineering problems like stealth technology.

For completeness, it is desired to study the effects of various values of the complex relative permittivity of the disk upon the back-scattered cross sections instead of only GaAs disks. The Figs. 10–12 deal with the effects of the real part of the relative permittivity of the two tilted thin circular dielectric disks on the back-scattered cross sections σ_{hh} and σ_{vv}. These two disks are placed at (1.5,0,0)cm and (-1.5,0,0)cm at an operating frequency of 35 GHz. It is assumed that the real part of the relative permittivity of the two tilted thin circular disks is varying from 1 to 15 whereas the imaginary part is fixed at 0.5. Here $a = \lambda_o$, $\theta_i = 45^o$ and $\phi_i = 22.5^o$. It is observed from Figs. 10–12 that σ_{hh} and σ_{vv} give the same rising trend with $\text{Re}(\epsilon_r)$ in all three cases. By comparing σ_{hh} with σ_{vv} for all these three methods, it is found that σ_{vv} is quite different from σ_{hh} for tilt angle $(\theta_t, \phi_t) = (0^o, 0^o)$ case, i.e., $\sigma_{hh} > \sigma_{vv}$ over the considered range of the real part of the relative permittivity. However, there exists a rapid decrease in this difference as the tilt angle changes to $(\theta_t, \phi_t) = (30^o, 30^o)$ and $(\theta_t, \phi_t) = (45^o, 45^o)$, respectively. For the tilt angle $(\theta_t, \phi_t) = (90^o, 90^o)$ case, σ_{hh} and σ_{vv} gives the similar response over the considered range of $\text{Re}(\epsilon_r)$.

In Figs. 13–15, the influences of the imaginary part of the relative permittivity of the two tilted thin dielectric disks upon the back-scattered cross sections σ_{hh}, σ_{vv} have been shown whereas the real part of the the relative permittivity is fixed at 5. All the other electrical and geometrical parameters are considered same as in Figs. 13–15. It is studied that the σ_{hh} and σ_{vv} patterns are horizontal constant straight lines for the considered range of the imaginary part of the relative permittivity. It is

found that σ_{vv} is quite different from σ_{hh} when the two disks having no tilt, i.e., $\theta_t = \phi_t = 0^o$. In this case, $\sigma_{hh} > \sigma_{vv}$ for the considered range of $\text{Im}(\epsilon_r)$. Again there exists a rapid decrease in this difference as the tilt angles change from $\theta_t = \phi_t = 30^o$ to 45°. On the other hand, σ_{hh} and σ_{vv} have the same constant levels for the tilt angle $\theta_t = \phi_t = 90^o$.

For the sparse distribution of two tilted dielectric disks, one of the most important parameter is the spacing among them. The back-scattered cross sections σ_{hh}, σ_{vv} as a function of spacing d between these two tilted GaAs disks have been shown in Figs. 16–18. Here it is assumed that $a = \lambda_o$ at an operating frequency of 35 GHz whereas $\theta_i = 45^o$ and $\phi_i = 10.6^o$. It is obvious that the overall patterns of σ_{hh}, σ_{vv} are fluctuating with increasing d for all the considered three techniques. This is expected because of the constructive and destructive phenomenon associated with the scattering from these two disks at different spacings. It is observed that σ_{vv} is apparently different from σ_{hh} for the no tilt case for all the considered three approaches. However, this difference decreases for the disk orientations of $\theta_t = \phi_t = 30^o$ and $\theta_t = \phi_t = 45^o$. For the case where $\theta_t = \phi_t = 90^o$, σ_{hh} and σ_{vv} become same. It is further studied that the minimum value of σ_{hh} and σ_{vv} occurs at the disk spacing of 2.77 cm for the disk orientations of $\theta_t = \phi_t = 45^o$ for all the three techniques. This minimum value is less than -63 dB which gives almost zero back scattering for both types of incident polarization.

5.3   Concluding Remarks

An analysis about the back-scattered cross section from the sparse distribution of N-tilted thin dielectric circular disks have been presented. This analysis is based

upon the three widely-known scattering approximations such as Rayleigh-Gans, Koh-Sarabandi and the Volumetric Integral Physical Optics. The influences of the various parameters including incident angle, size parameter of the disk, relative permittivity of the disk and spacing among disks upon the back-scattered cross sections have been shown and discussed for incident horizontal and vertical polarizations. Some optimal conditions are discussed where the back-scattered cross sections from a pair of tilted low loss Gallium Arsenide disks are almost zero for both types of incident polarization. These optimal conditions for a pair of tilted GaAs disks are also compared with a single tilted GaAs disk published previously. It is investigated that a pair of tilted GaAs disks significantly reduced the back-scattered cross sections as a compared to single GaAs tiled disk having same orientations as that of a pair of tilted disks. Such types of reduced back-scattered cross sections for both types of incident polarization find applications in the design of the modern remote sensing systems and stealth technologies.

Chapter 6

Effective Parameters of a metamaterial composed of dielectric coated conducting cylindrical rods

In this Chapter 6, the scattering characteristics of an isolated dielectric coated conducting rod have been investigated. The types of considered coatings for the scattering analysis are realistic materials including Barium Strontium Titanate (BST) $Ba_{0.5}Sr_{0.5}TiO_3$, magnetodielectric, Gallium Arsenide (GaAs) and Silicon Carbide (SiC). It is found that the Gallium Arsenide (GaAs) coating significantly reduced the scattering from a thin perfectly electric conducting cylindrical rod at specific observation angles.

The effective permittivity and permeability of metamaterials composed of two dimensional periodic arrangements of these dielectric coated conducting cylindrical rods have also been studied. An increase in the double negative bandwidth of a metamaterial composed of barium strontium titanate coated conducting rods has been observed in contrast to the corresponding bandwidth of a metamaterial composed of only Barium Strontium Titanate (BST) material rods. Also an additional plasmonic

epsilon negative bandwidth has been found in case of a metamaterial composed of Barium Strontium Titanate (BST) coated conducting rods.It is further studied that the widest epsilon negative, mu negative and double negative bandwidths exist for a metamaterial composed of gallium arsenide rods.

6.1 Scattering characteristics of an isolated dielectric coated conducting rod

An infinite length circular cylindrical rod made of a perfectly electric conducting (PEC) material having radius a is considered. This cylindrical rod is coated with a dielectric or magneto-dielectric material. The electromagnetic parameters of the coating are $\epsilon_c = \epsilon_o \epsilon_{rc}$ and $\mu_c = \mu_o \mu_{rc}$ where ϵ_o and μ_o are the permittivity and permeability of the free space respectively. Likewise, the parameters ϵ_{rc} and μ_{rc} represent the relative permittivity and relative permeability of the coating material respectively. A word magneto-dielectric is used for those materials whose relative permeability is different from unity. An outer radius of the coating is taken to be b with coating thickness of $\delta = b - a$. The coating region has a propagation constant of $k_c = k_o(\epsilon_{rc}\mu_{rc})^{1/2}$ and an intrinsic impedance of $\eta_c = \eta_o(\mu_{rc}/\epsilon_{rc})^{1/2}$. The factors k_o and η_o represent the free space propagation constant and the free space intrinsic impedance respectively. This dielectric coated cylindrical rod is placed in a certain background medium whose propagation constant is $k_1 = k_o(\epsilon_{r1}\mu_{r1})^{1/2}$ and its intrinsic impedance is $\eta_1 = \eta_o(\mu_{r1}/\epsilon_{r1})^{1/2}$. It should be noted that a time convention of $e^{j\omega t}$ has been assumed for the current study and suppressed throughout. The geometrical configuration of an isolated dielectric coated conducting rod has been given in the upper panel of Fig. 6.1.
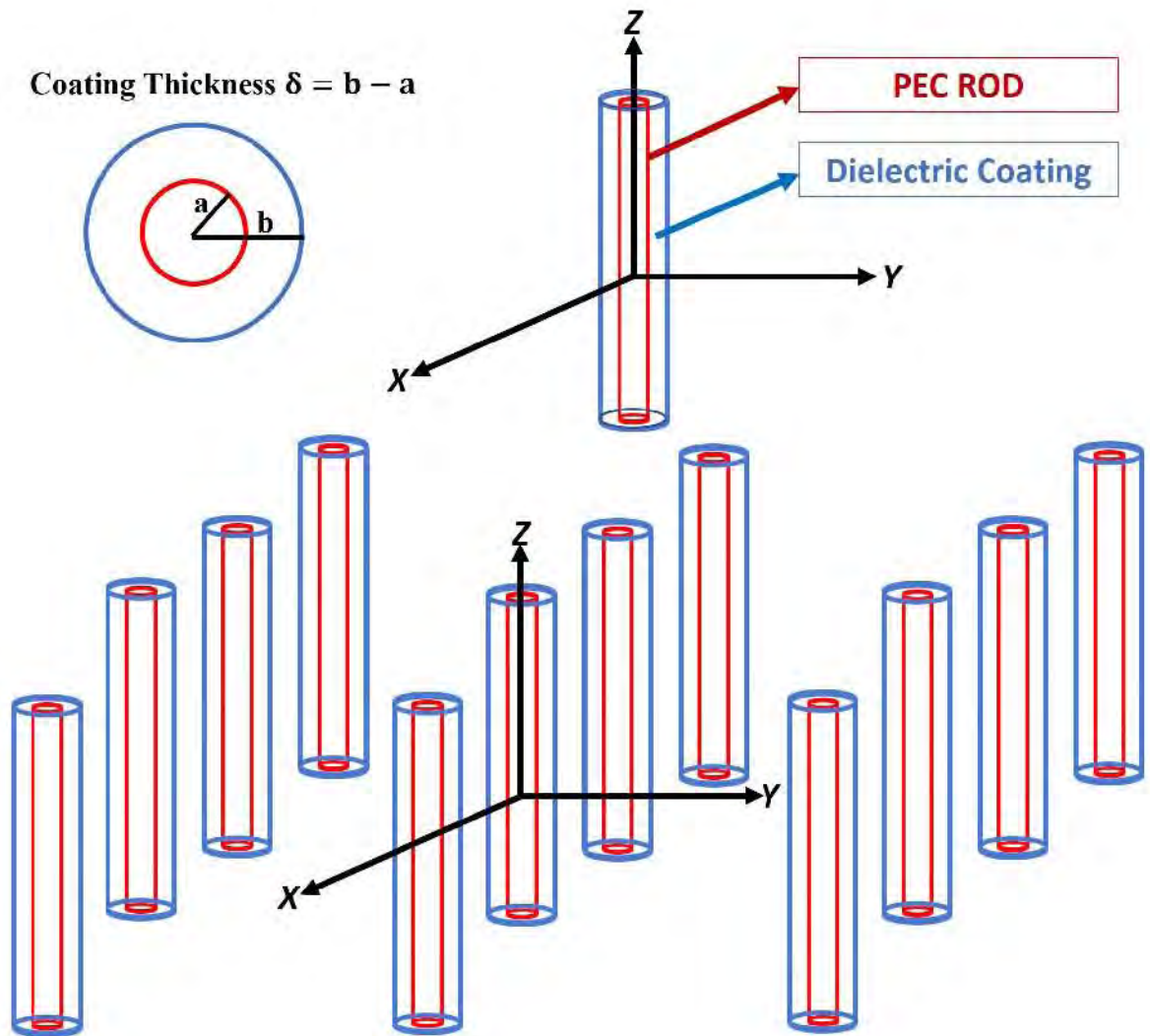
Figure 6.1: The upper panel of the figure shows an isolated dielectric coated conducting cylindrical rod whereas the lower panel shows a medium composed of dielectric coated conducting rods.

This dielectric coated cylindrical rod is illuminated by a normal incident plane wave which travels in the direction that makes an angle ϕ_o with the $+ x$–axis. The incident wave polarization is taken to be Transverse Magnetic (TM) type whereas one can also extend this formulation for the Transverse Electric (TE) case. For the incident TM polarization, the z–component of the incident electric field E_z^i can be expressed as a sum of infinite cylindrical waves as follows [26, 27],

$$E_z^i = E_o e^{-jk_o\rho\cos(\phi-\phi_o)} = E_o \sum_{n=-\infty}^{n=+\infty} j^{-n} J_n(k_o\rho) e^{jn(\phi-\phi_o)} \qquad (6.1.1)$$

where E_o is a constant magnitude of the electric field. The function $J_n(\cdot)$ represents an nth order Bessel function of first kind. The z-component of the scattered electric field E_z^s in the region defined by $0 \leq \phi \leq 2\pi$ and $\rho > b$ can be written as,

$$E_z^s = E_o \sum_{n=-\infty}^{n=+\infty} j^{-n} C_n^{TM} H_n^{(2)}(k_o\rho) e^{jn(\phi-\phi_o)} \qquad (6.1.2)$$

Likewise, the z-component of the electric field E_z^c inside the coating region which occupies the space defined by $0 \leq \phi \leq 2\pi$ and $a < \rho < b$ can be written as,

$$E_z^c = E_o \sum_{n=-\infty}^{n=+\infty} j^{-n} \Big[A_n^{TM} J_n(k_c\rho) + B_n^{TM} Y_n(k_c\rho) \Big] e^{jn(\phi-\phi_o)} \qquad (6.1.3)$$

The factors A_n^{TM}, B_n^{TM} and C_n^{TM} are the unknown expansion coefficients and needed to be determined. Here $Y_n(\cdot)$ is the nth order Bessel function of second kind and $H_n^{(2)}(\cdot)$ is the nth order Hankel function of second kind which represents an outward traveling cylindrical wave. The ϕ–components of the incident magnetic, scattered magnetic and magnetic field inside the coating can be found from the Maxwell's equations. The unknown coefficients A_n^{TM}, B_n^{TM} and C_n^{TM} can be found by applying the tangential boundary conditions at interfaces $\rho = a$ and $\rho = b$ and solving the resulting system of linear equations. Once these unknowns become known then the

z- components of electric field in each region can be found from Eqs.(6.1.1– 6.1.3). The unknown coefficient C_n^{TM} which is of an interest for the scattered electric field can be found as below,

$$C_n^{TM} = -\frac{(1/\eta_c)J_n(k_1b)P_n + (1/\eta_1)J_n'(k_1b)Q_n}{(1/\eta_c)H_n^{(2)}(k_1b)P_n + (1/\eta_1)H_n^{(2)'}(k_1b)Q_n} \tag{6.1.4}$$

$$P_n = J_n'(k_cb)Y_n(k_ca) - J_n(k_ca)Y_n'(k_cb) \tag{6.1.5}$$

$$Q_n = J_n(k_ca)Y_n(k_cb) - J_n(k_cb)Y_n(k_cb) \tag{6.1.6}$$

where the prime $'$ shows the derivative with respect to the argument. If there exists no inner core of perfectly conducting material then the scattering coefficient C_n^{TM} for a dielectric cylindrical rod of radius b using the above procedure can be written as,

$$C_n^{TM} = -\frac{(1/\eta_c)J_n(k_1b)J_n'(k_cb) - (1/\eta_1)J_n(k_cb)J_n'(k_1b)}{(1/\eta_c)J_n'(k_cb)H_n^{(2)}(k_1b) - (1/\eta_1)J_n(k_cb)H_n^{(2)'}(k_1b)} \tag{6.1.7}$$

In case if the cylindrical rod is made of perfectly conducting material having radius b and placed in the free space background, i.e., $k_1 = k_o$ then the scattering coefficient C_n^{TM} can be written as follows,

$$C_n^{TM} = -\frac{J_n(k_ob)}{H_n^{(2)}(k_ob)} \tag{6.1.8}$$

In this case, it is assumed that cylindrical rod have finite conductivity σ_c which shows that the permittivity ϵ_c is a complex quantity with an imaginary part of $\sigma_c/j\omega$. Now by taking $\sigma_c \to \infty$ in Eq.(6.1.7), we obtain Eq.(6.1.8). The unknown coefficients C_n^{TM} given by Eqs.(6.1.4- 6.1.8) are consistent with [83-85]. In the far zone, the z-component of the scattered electric field can be found from Eq.(6.1.2) using the asymptotic expansion of Hankel function for large argument as given in [83]. Using this far zone scattered electric field in the standard definition of scattering width σ^{TM}

Figure 6.2: The magnitude of first three Mie scattering coefficients $|C_n^{TM}|$ as a function of normalized frequency b/λ_o for a BST cylindrical rod and for $n = 0,1,2$. The proposed scattering coefficients for BST rod are in good agreement with those reported by Vynck et al. [77].

[83], one can write the normalized scattering width σ_N as below,

$$\sigma_N = \frac{\sigma^{TM}}{\lambda_1} = \frac{2}{\pi} \left| \sum_{n=-\infty}^{n=+\infty} C_n^{TM} e^{jn(\phi-\phi_o)} \right|^2 \tag{6.1.9}$$

where λ_1 is the wavelength in the background medium. For sake of convenience, the azimuth angle ϕ_o is assumed to be zero for the current study.
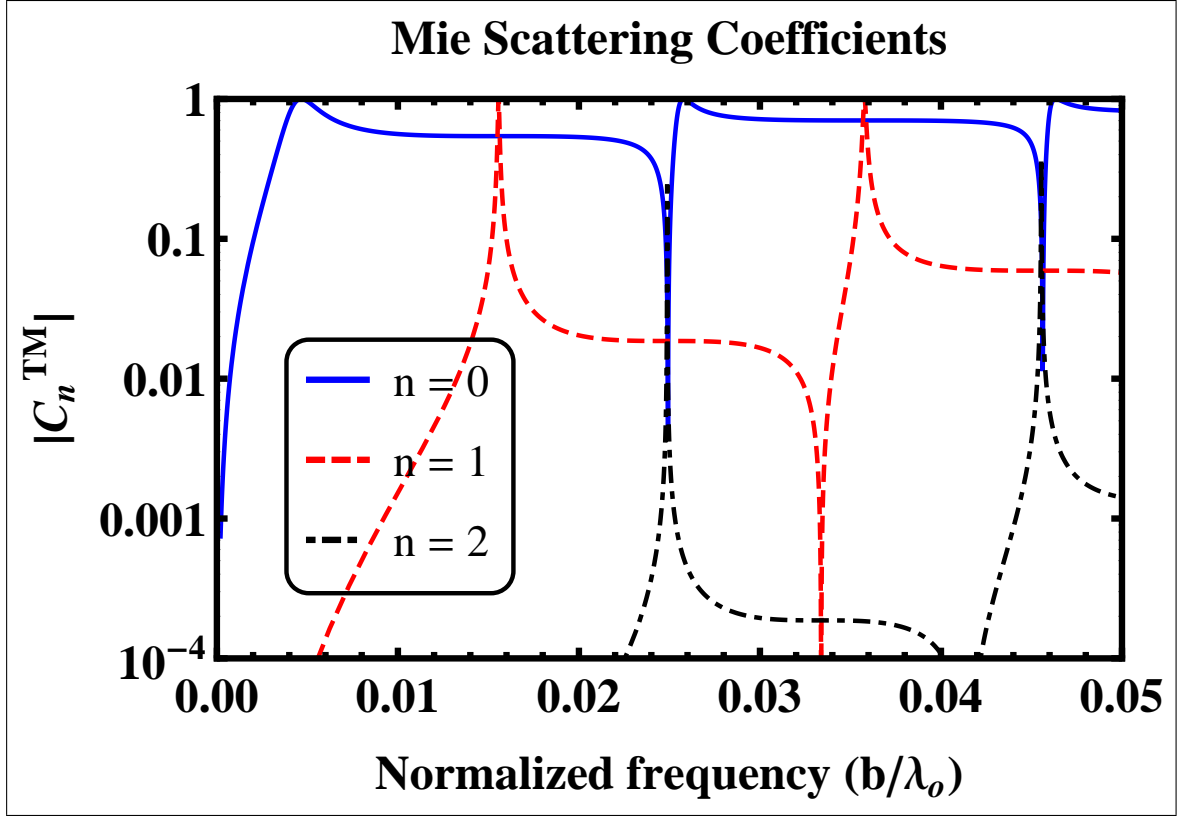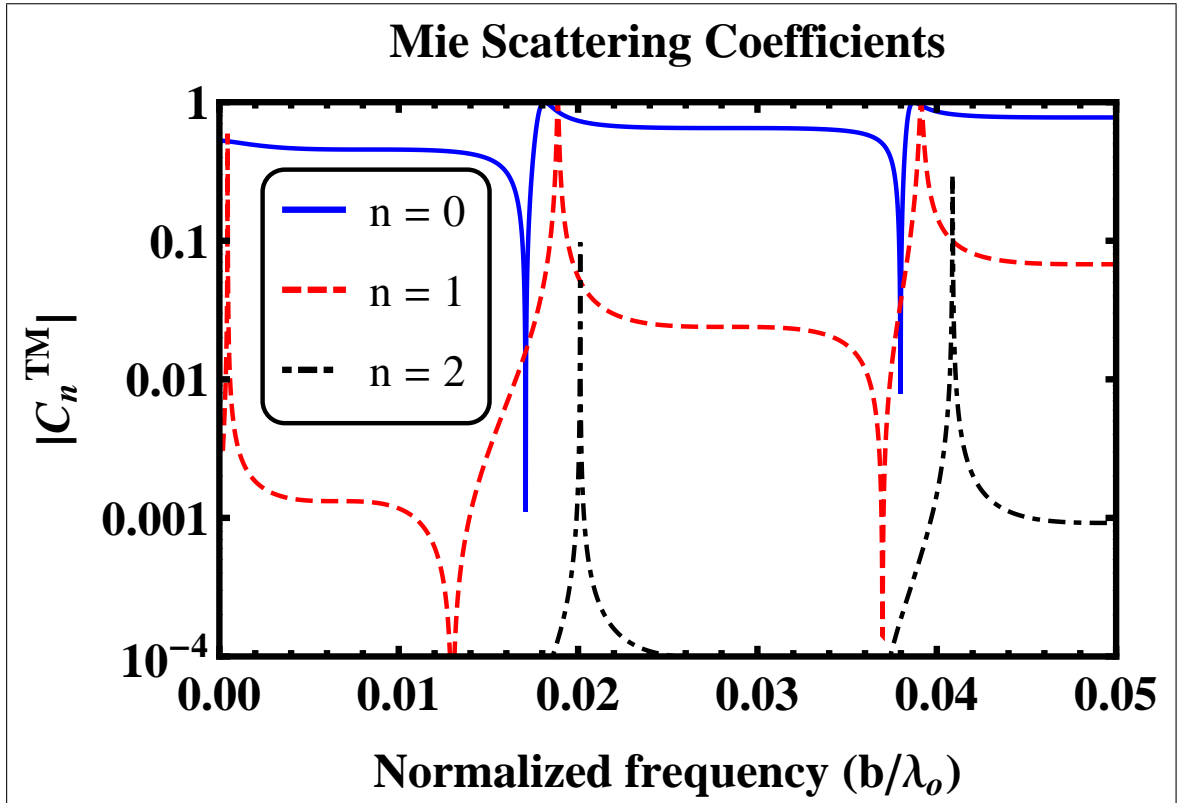
Figure 6.3: The magnitude of first three Mie scattering coefficients $|C_n^{TM}|$ as a function of normalized frequency b/λ_o for a BST coated PEC cylindrical rod and for $n = 0,1,2$. The proposed scattering coefficients for BST rod are in good agreement with those reported by Vynck et al. [77].

6.2 Effective parameters of a metamaterial composed of dielectric coated conducting rods

In this section, we consider a composite material which consists of an infinite two dimensional periodic arrangements of these dielectric coated perfectly electric conducting cylindrical rods. The background medium is taken to be the free space. All the rods are assumed to be parallel to the z–axis. The spacing s among rods along x and y–axes are taken to be d. Its geometrical configuration has been given in lower panel of Fig. 6.1. For the homogenized description of an artificial material containing dielectric coated conducting rods, it is required to satisfy two conditions, i.e., $k_o b <<$ 1 and $k_o d < 2\pi$. If these two conditions are satisfied then an artificial material composed of these cylindrical rods can be homogenized. In this way, we can assign the effective permittivity and effective permeability (i.e., effective parameters to such an artificial material). It should be noted that the condition $k_o d < 2\pi$ can be used only if the incident wave is normal as the case under study. In the present study, we have taken normal TM incidence. On the other hand, for the oblique angles of incidence, the second necessary condition become $k_o d < \pi$ instead of $k_o d < 2\pi$.

It can be seen that if the dielectric coated conducting rod is thin, i.e., $k_o b <<$ 1 then the dominant Mie scattering coefficients C_n^{TM} as given by Eqs.(6.1.4– 6.1.8) exists only for $n = 0$ and $n = 1$. On the other hand, the higher order Mie scattering coefficients for $n > 1$ become negligible for thin rods. Therefore, for the homogenized description of an artificial medium containing dielectric coated conducting rods, it is desired to take only leading Mie scattering coefficients, i.e., C_0^{TM} and C_1^{TM}. To justify this statement, it is assumed that the dielectric coating is assumed to be made of a nonmagnetic and ferroelectric ceramic material, i.e., $Ba_{0.5}Sr_{0.5}TiO_3$ (BST) [76]. It

has a relative permittivity of 600 at microwave frequencies and at room temperature. The magnitude of first three Mie scattering coefficients C_n^{TM} for BST cylindrical rod and BST coated conducting cylindrical rod have been shown in Figs.(6.2-6.3). In this case, both types of rods have the same radius of $b = (0.68/3)(\lambda_o/4)$ at an operating free space wavelength of 25 mm. For the BST coated conducting rod, the inner radius a of the conducting rod is assumed to be $b/2$. It is found from Figs.(6.2-6.3) that for both types of rods, the higher order Mie scattering coefficients which also represent the higher order multipole moments for $n > 1$ induce spectrally narrow features near their resonance frequencies and can be ignored. It is argued that the lowest order Mie scattering coefficient C_0^{TM} is responsible for an induced electric dipole moment whereas the Mie scattering coefficient C_1^{TM} is responsible for an induced magnetic dipole moment.

Using the procedure as outlined in [75,77] and taking the incident electric field aligned along $z-$axis and the incident magnetic field along $y-$axis, the electric polarizability per unit length Υ_e^{zz} and the magnetic polarizability per unit length Υ_m^{yy} can be computed using the following relations,

$$\Upsilon_e^{zz} = 4j\frac{C_0^{TM}}{k_o^2} \qquad \Upsilon_m^{yy} = 4j\frac{C_1^{TM}}{k_o^2} \tag{6.2.1}$$

Once the electric and magnetic polarizabilities per unit length of an isolated dielectric coated conducting rod are known then the effective parameters, i.e., effective permittivity ϵ_{zz} and effective permeability μ_{yy} can be found using the non-local homogenization approach given in [69,75]. Thus, the effective permittivity and effective permeability of an artificial material or a metamaterial composed of dielectric coated

conducting rods can be written as,

$$\epsilon_{zz} = 1 + \frac{n}{(\Upsilon_e^{zz})^{-1} - C_{zz}^{int}} \tag{6.2.2}$$

$$\mu_{yy} = 1 + \frac{n}{(\Upsilon_m^{yy})^{-1} - C_{yy}^{int}} \tag{6.2.3}$$

where $n = 1/d^2$. The factors C_{zz}^{int} and C_{yy}^{int} represent the zz- and yy-components of the dynamic interaction dyadic given by Silveirinha [75].

6.3 Numerical results

The numerical results, the normalized scattering widths of dielectric coated conducting rods with various realistic dielectric materials have been studied. The scattering widths of these dielectric coated conducting rods have also been compared with the scattering widths of dielectric and perfectly electric conducting (PEC) rods having the same radii. The types of assumed realistic dielectric materials are $Ba_{0.5}Sr_{0.5}TiO_3$ (BST) [76] magnetodielectric [86], low loss Gallium Arsenide (GaAs) [87] and Silicon Carbide (SiC) [88]. A BST material has relative permittivity of nearly 600 and is nonmagnetic. A magneto-dielectric material has ϵ_{rc} = 13.8 - j0.1 and μ_{rc} = 11. Its relative permittivity is different from unity that is why it is called magnetodielectric. These values are chosen because a low loss garnet material with these parameters can be obtained relatively inexpensively. This material is commercially available in the form of aluminum doped ferrite. The relative permittivity and permeability of a low loss GaAs are taken to be ϵ_{rc} = 12.88 - j0.0004 and μ_{rc} = 1 respectively. A SiC is a well-known wave-absorbing material with excellent dielectric property, good corrosion resistance, hardness and high strength, and high thermal conductivity and stability. Moreover, SiC material in the microwave regime behaves an absorbing agent. Therefore, SiC material is a good candidate for the absorbing materials in the microwave
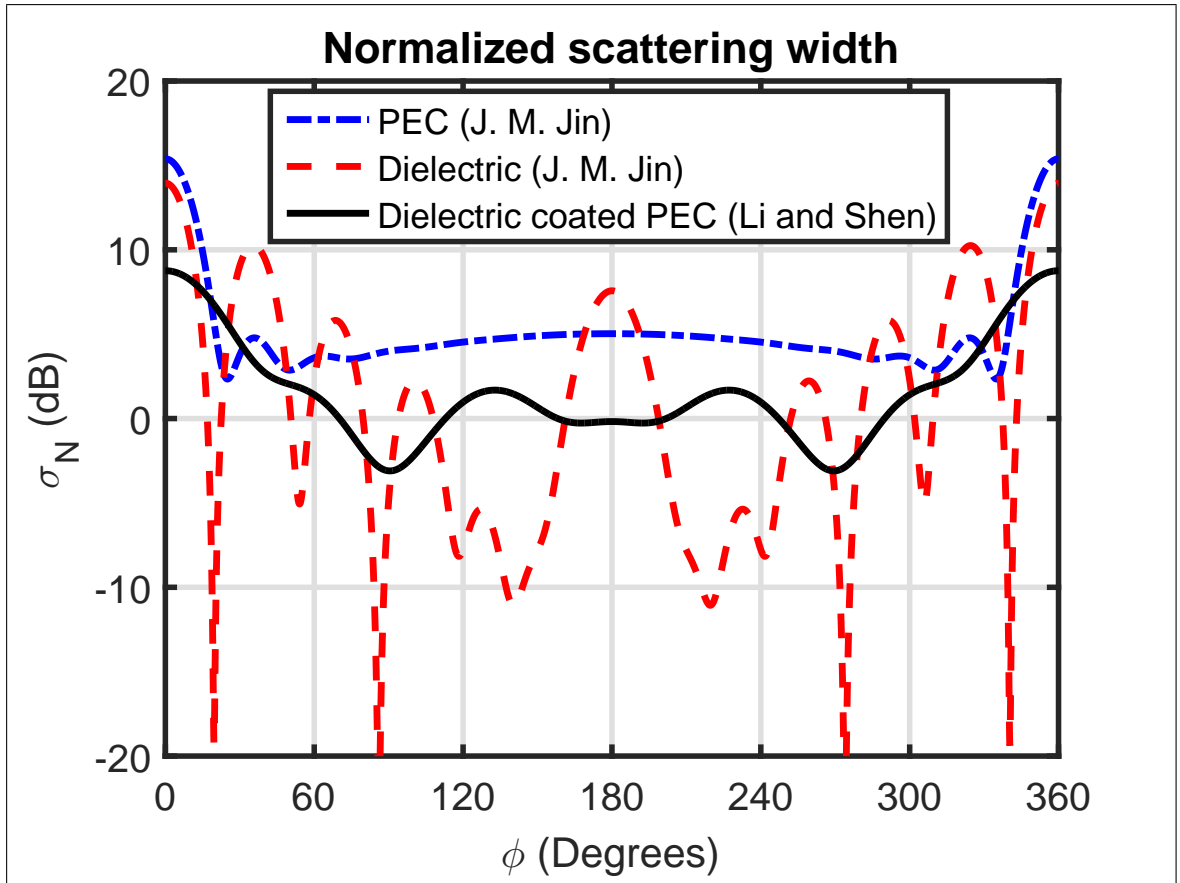
Figure 6.4: The normalized scattering widths of PEC, dielectric and dielectric coated PEC cylindrical rods. The electrical and geometrical parameters of PEC and dielectric cylinders or cylindrical rods have been taken from [85] and from [83] in case of dielectric coated cylindrical rod. These normalized scattering widths are in good agreement with [83, 85].
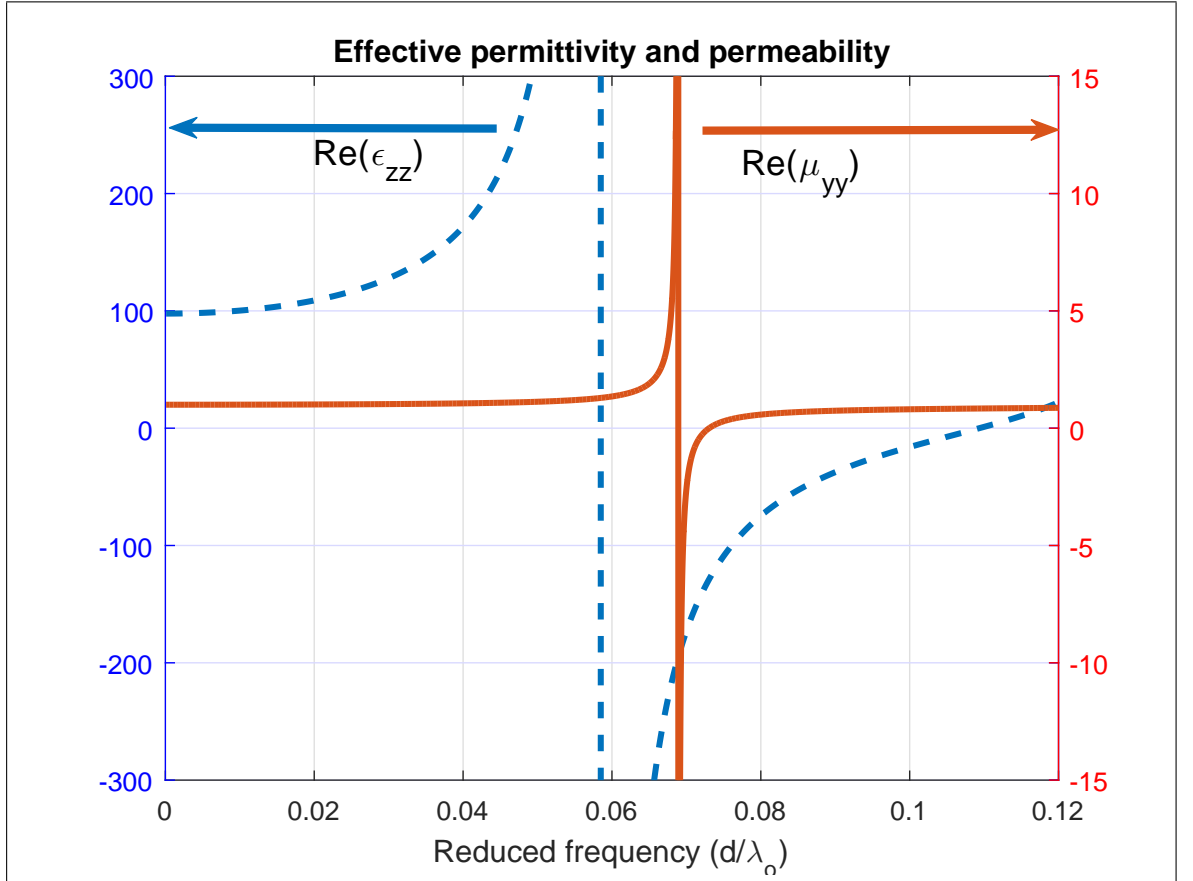
Figure 6.5: The real parts of the effective permittivity and permeability of a metamaterial composed of BST cylindrical rods based upon the proposed formulation and are found to be in good agreement with those reported by Vynck et al. [77]. All these agreements with reported works validate the proposed theory.
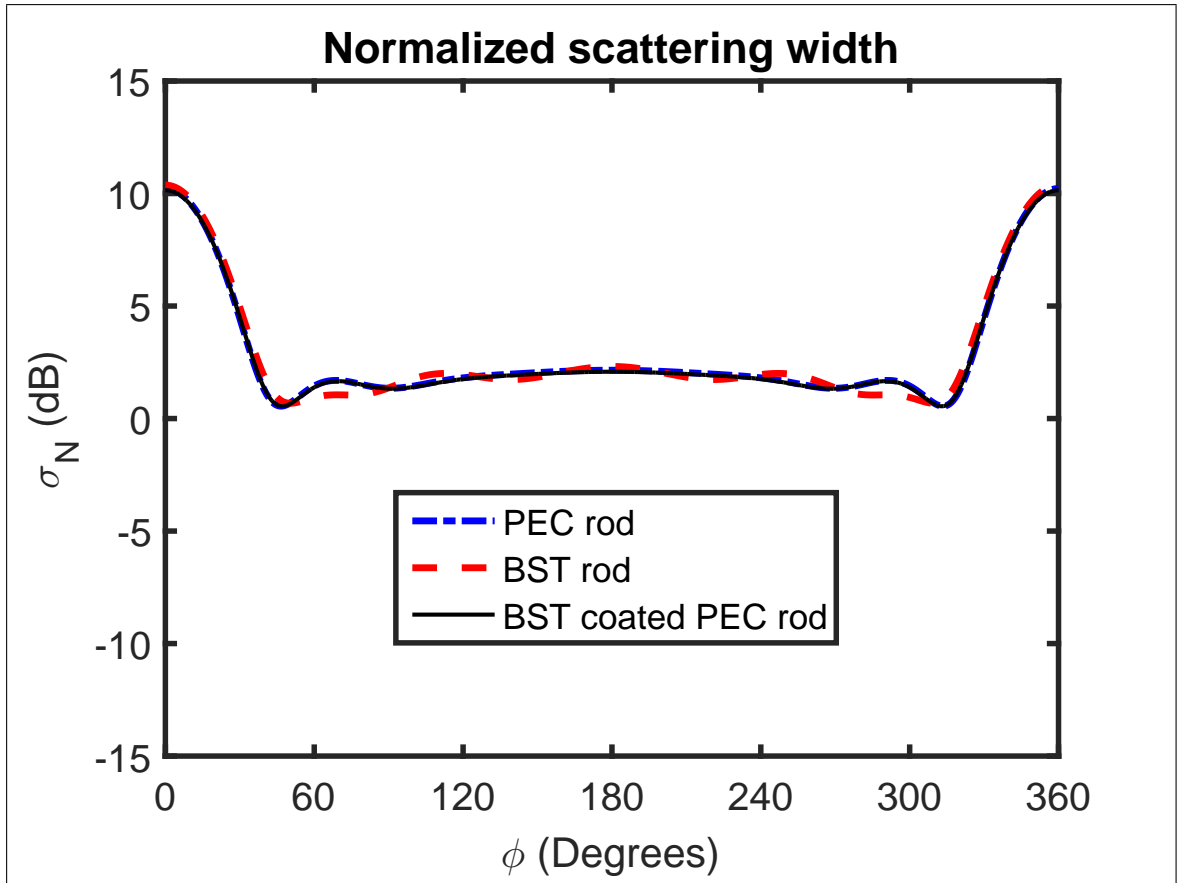
Figure 6.6: The normalized scattering widths of (a) BST and BST coated PEC cylindrical rods. Here for all the considered cylindrical rods including various material rods, material coated PEC rods and PEC rod, an outer radius of $b = 50$ mm has been assumed. In case of material coated PEC rods, an inner core radius of PEC material is taken to be $a = 0.5b$.
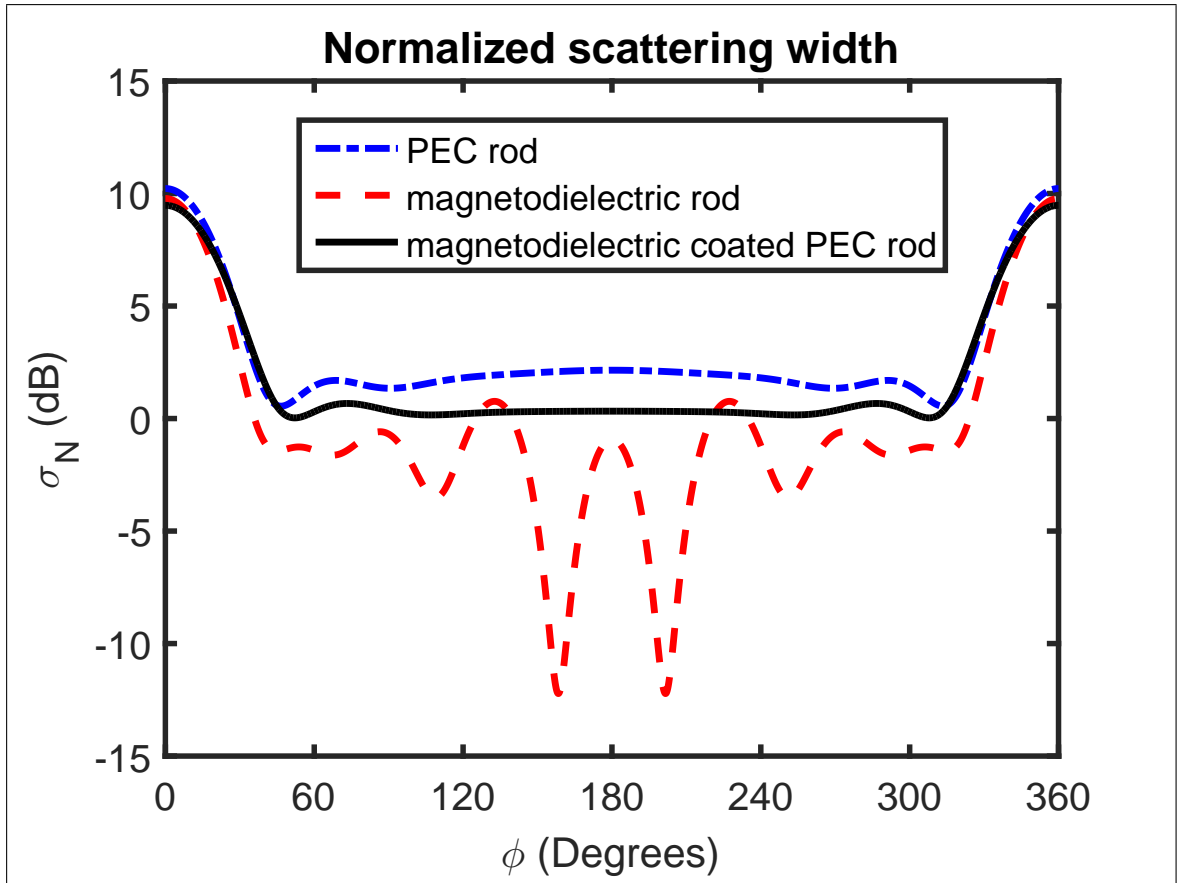
Figure 6.7: The normalized scattering widths of magnetodielectric and magnetodielectric coated PEC rods. Here for all the considered cylindrical rods including various material rods, material coated PEC rods and PEC rod, an outer radius of $b = 50$ mm has been assumed. In case of material coated PEC rods, an inner core radius of PEC material is taken to be $a = 0.5b$.
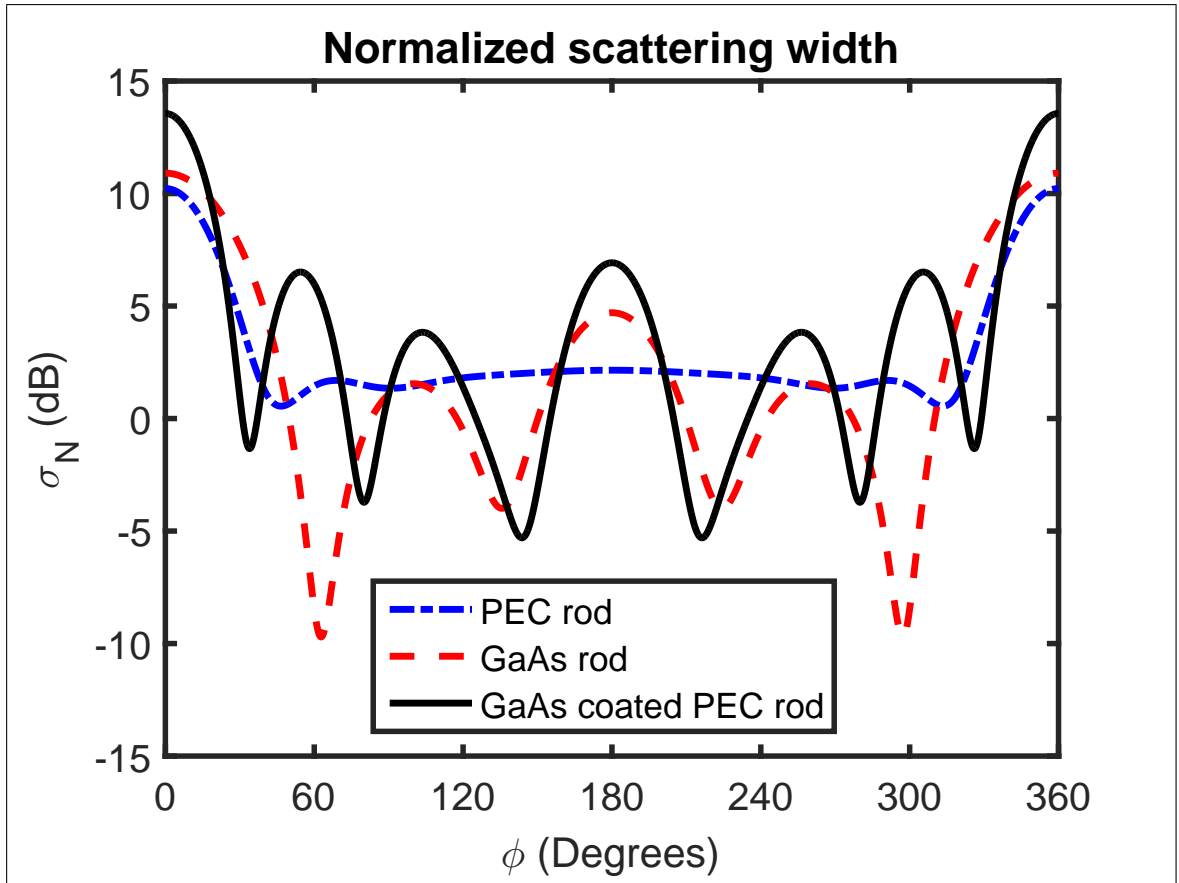
Figure 6.8: The normalized scattering widths of GaAs and GaAs coated PEC rods. Here for all the considered cylindrical rods including various material rods, material coated PEC rods and PEC rod, an outer radius of $b = 50$ mm has been assumed. In case of material coated PEC rods, an inner core radius of PEC material is taken to be $a = 0.5b$.
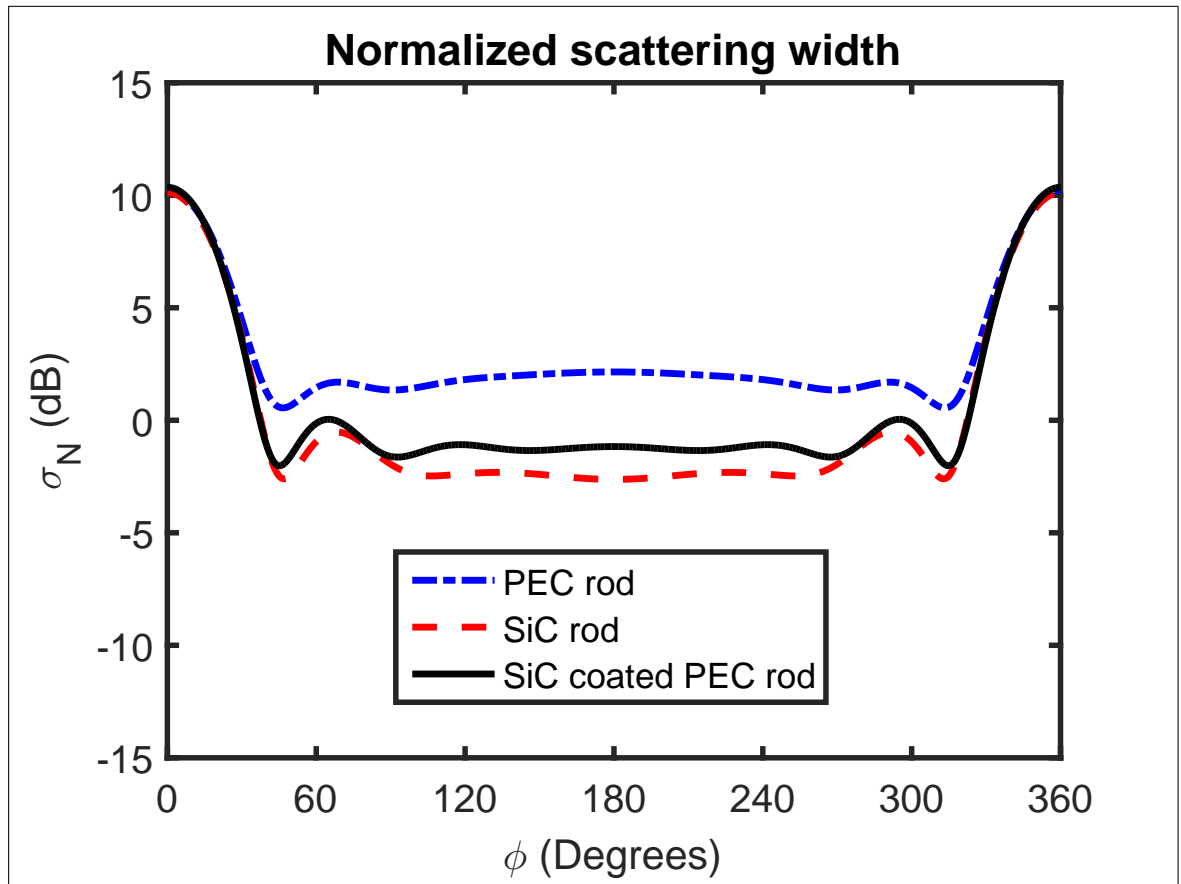
Figure 6.9: The normalized scattering widths of SiC and SiC coated PEC rods and their comparisons with the normalized scattering width of a PEC rod. Here for all the considered cylindrical rods including various material rods, material coated PEC rods and PEC rod, an outer radius of $b = 50$ mm has been assumed. In case of material coated PEC rods, an inner core radius of PEC material is taken to be $a = 0.5b$.
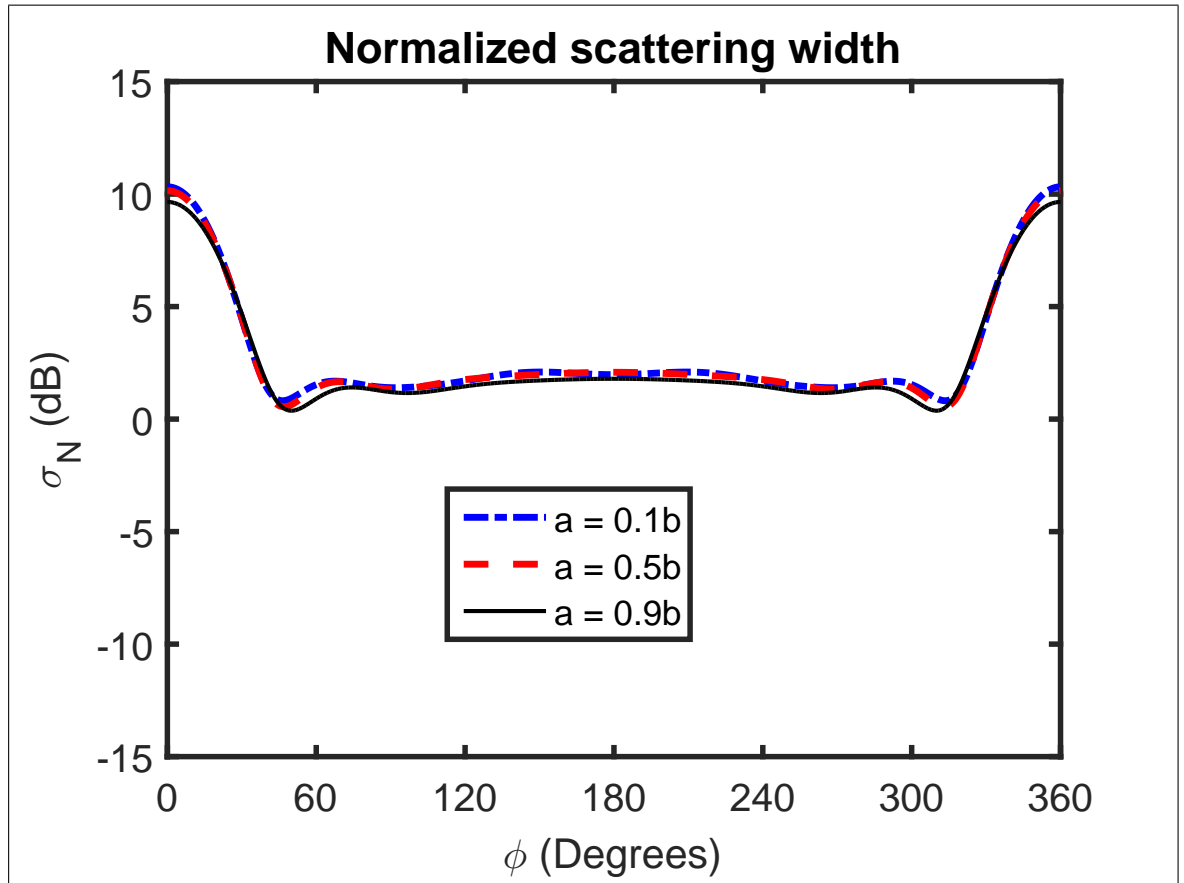
Figure 6.10: The normalized scattering widths of BST coated PEC rod. For this case, the coated rod has an outer radius of $b = 50$ mm whereas an inner radius a of a PEC cylindrical rod is variable.
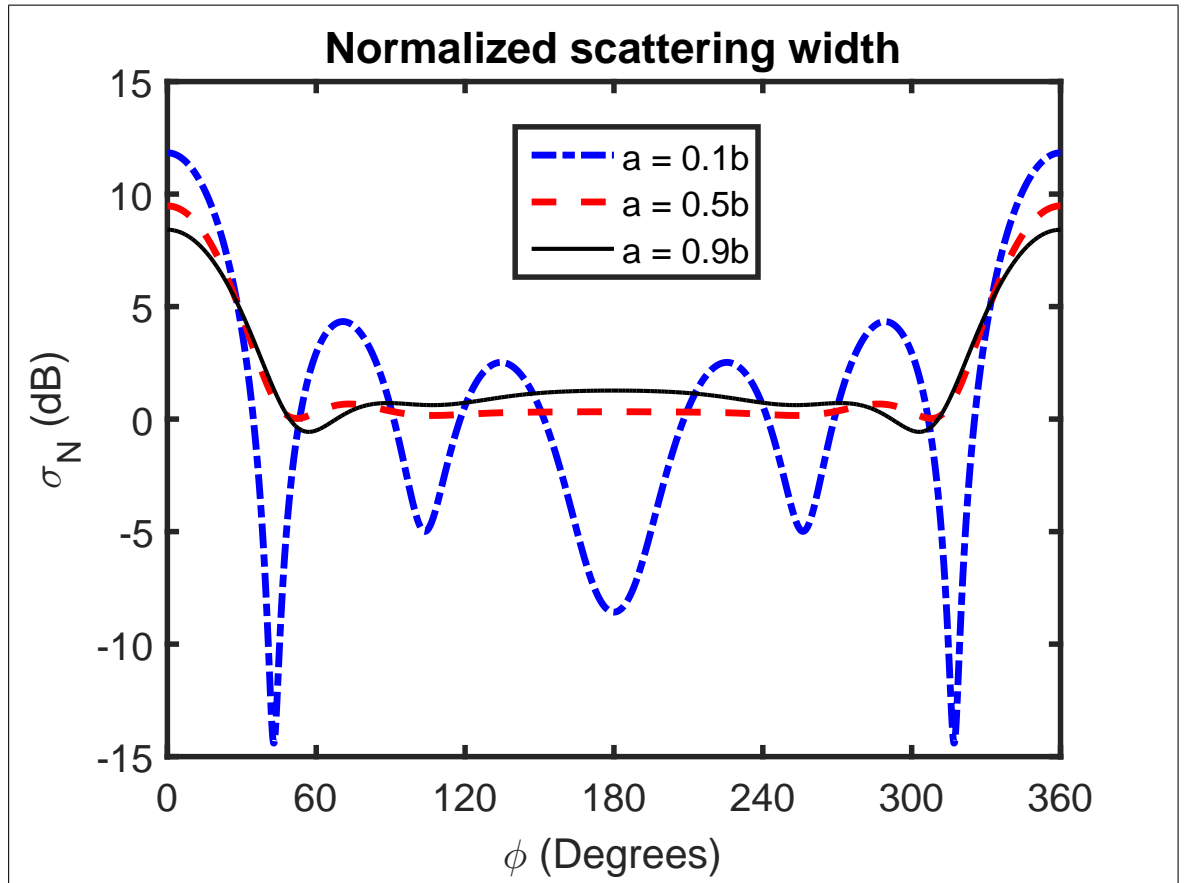
Figure 6.11: The normalized scattering widths of magnetodielectric coated PEC rod. For this case, the coated rod has an outer radius of $b = 50$ mm whereas an inner radius a of a PEC cylindrical rod is variable.
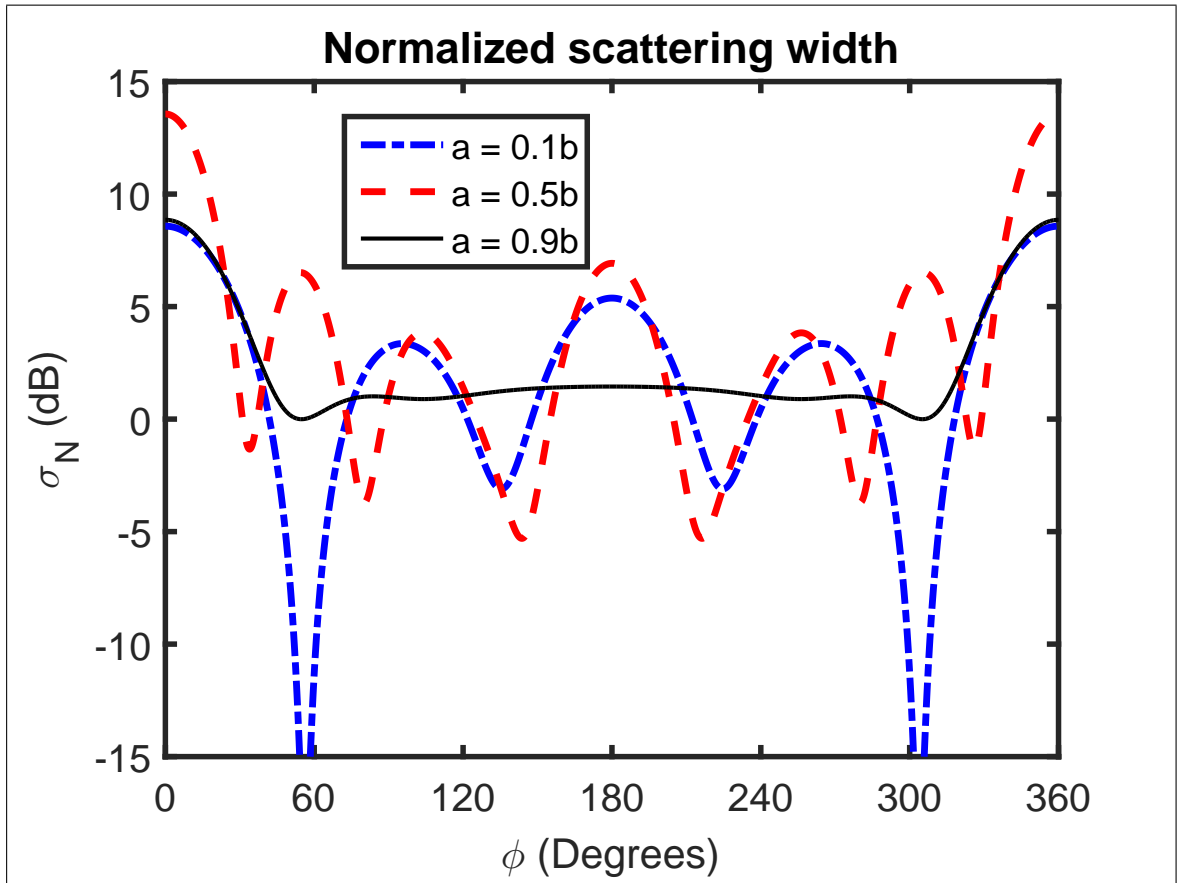
Figure 6.12: The normalized scattering widths of GaAs coated PEC rod. For this case, the coated rod has an outer radius of $b = 50$ mm whereas an inner radius a of a PEC cylindrical rod is variable.
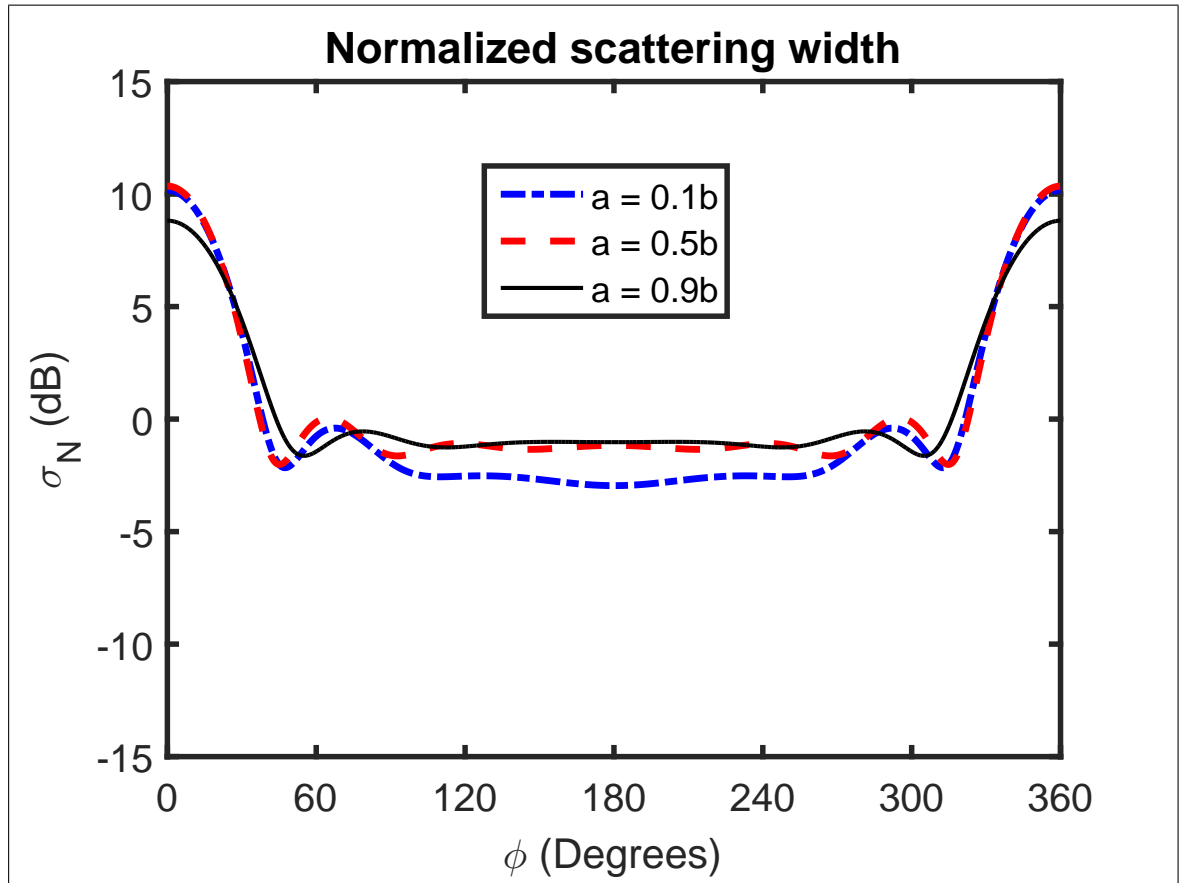
Figure 6.13: The normalized scattering widths of SiC coated PEC rod. For this case, the coated rod has an outer radius of $b = 50$ mm whereas an inner radius a of a PEC cylindrical rod is variable.
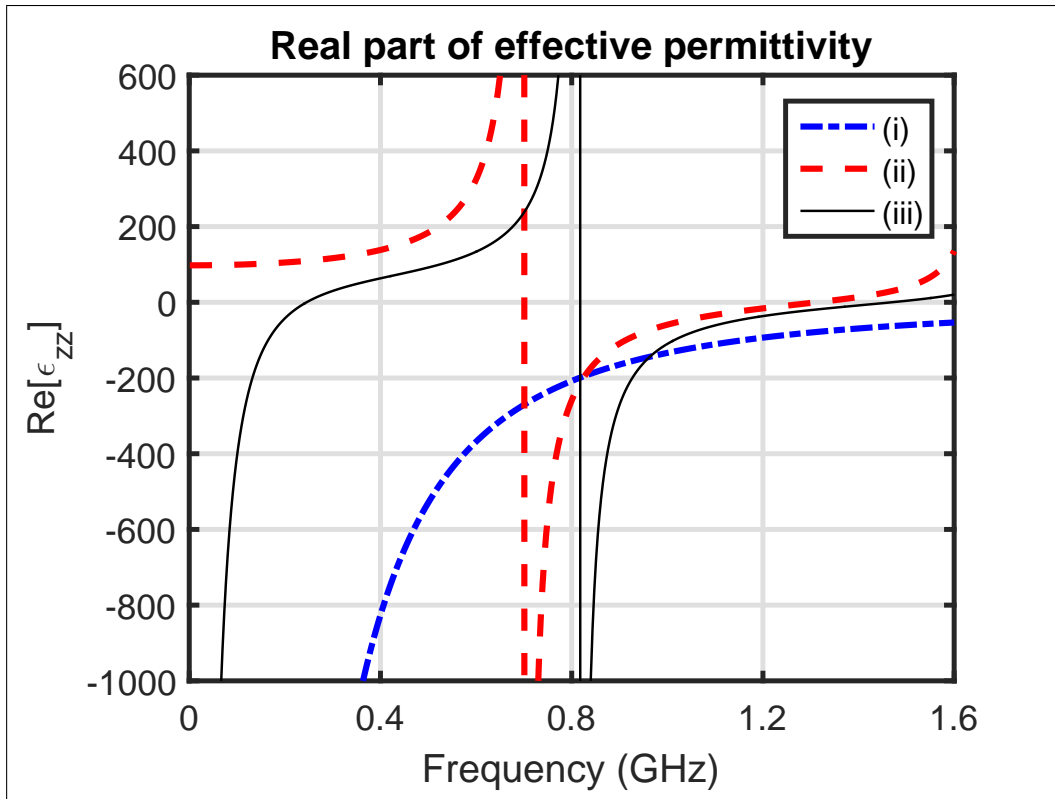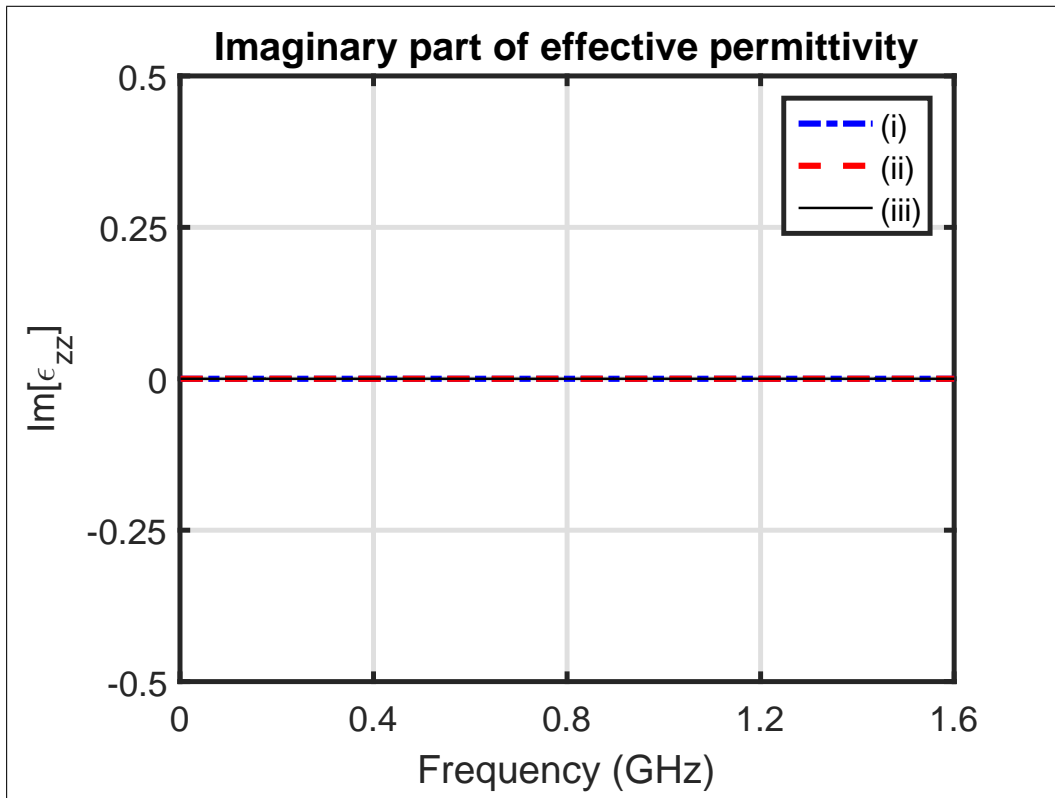
Figure 6.14: The (a) real and (b) imaginary parts of the effective permittivity ϵ_{zz} of artificial materials or metamaterials composed of (i) PEC rods (ii) BST rods and (iii) BST coated PEC rods.
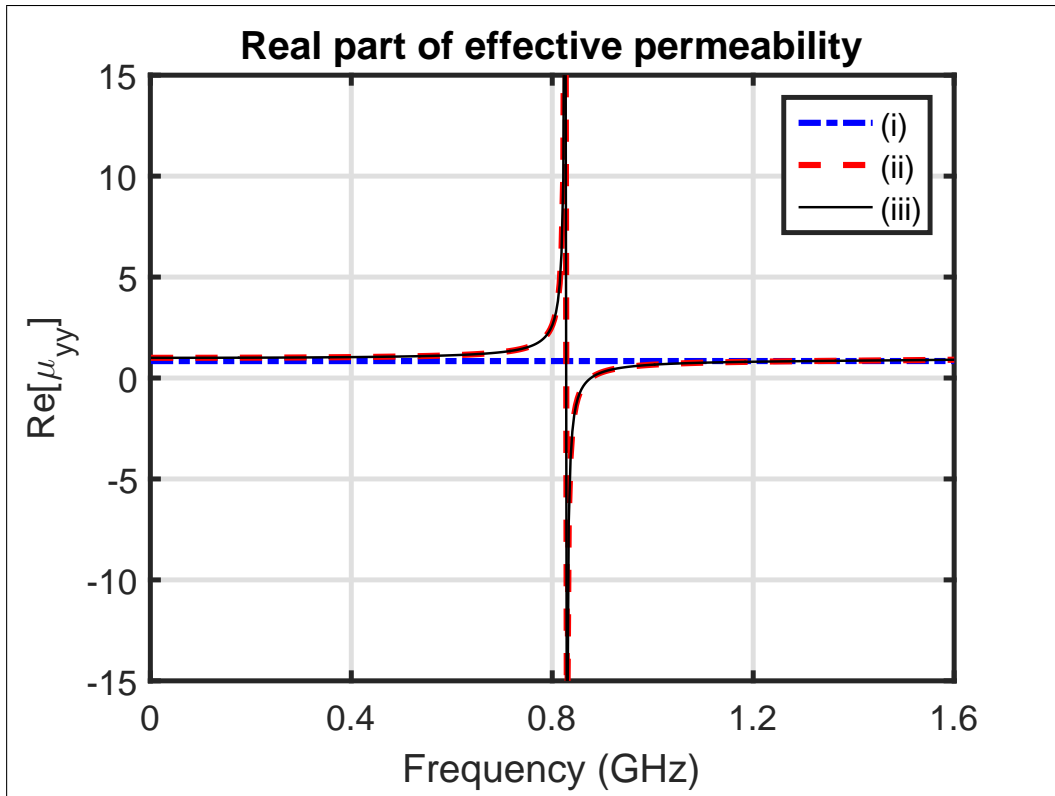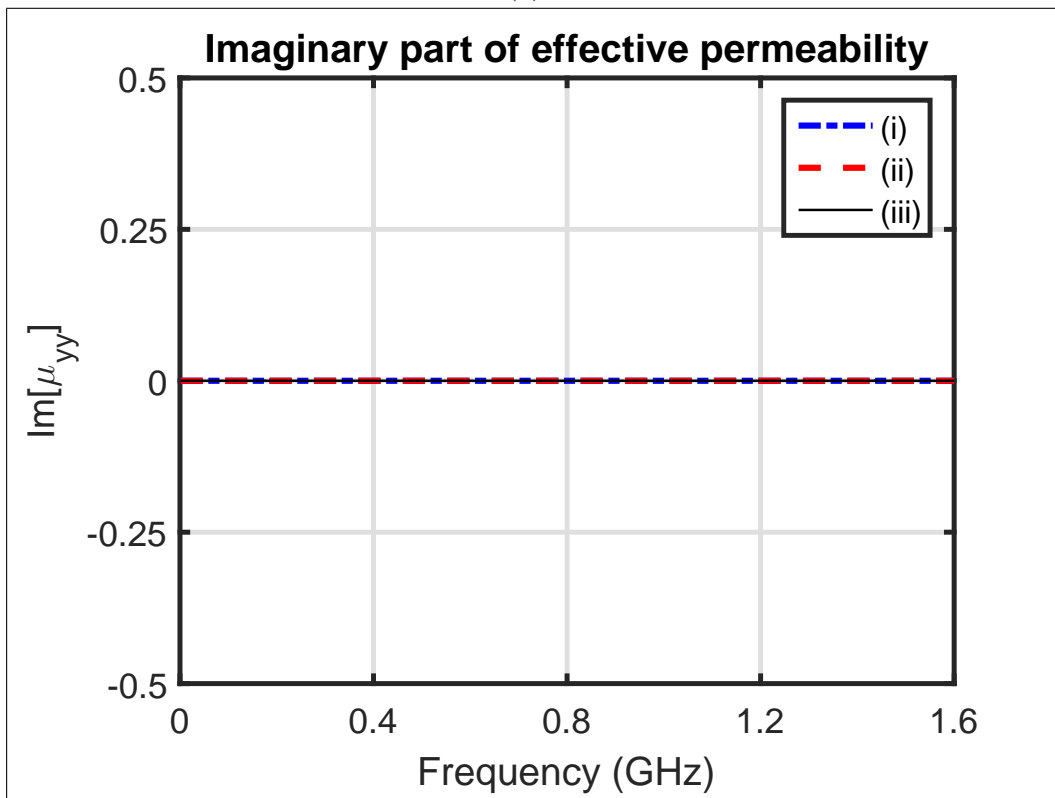
Figure 6.15: The (a) real and (b) imaginary parts of the effective permeability μ_{yy} of artificial materials or metamaterials composed of (i) PEC rods (ii) BST rods and (iii) BST coated PEC rods.

Real part of effective permittivity

(a)

Imaginary part of effective permittivity
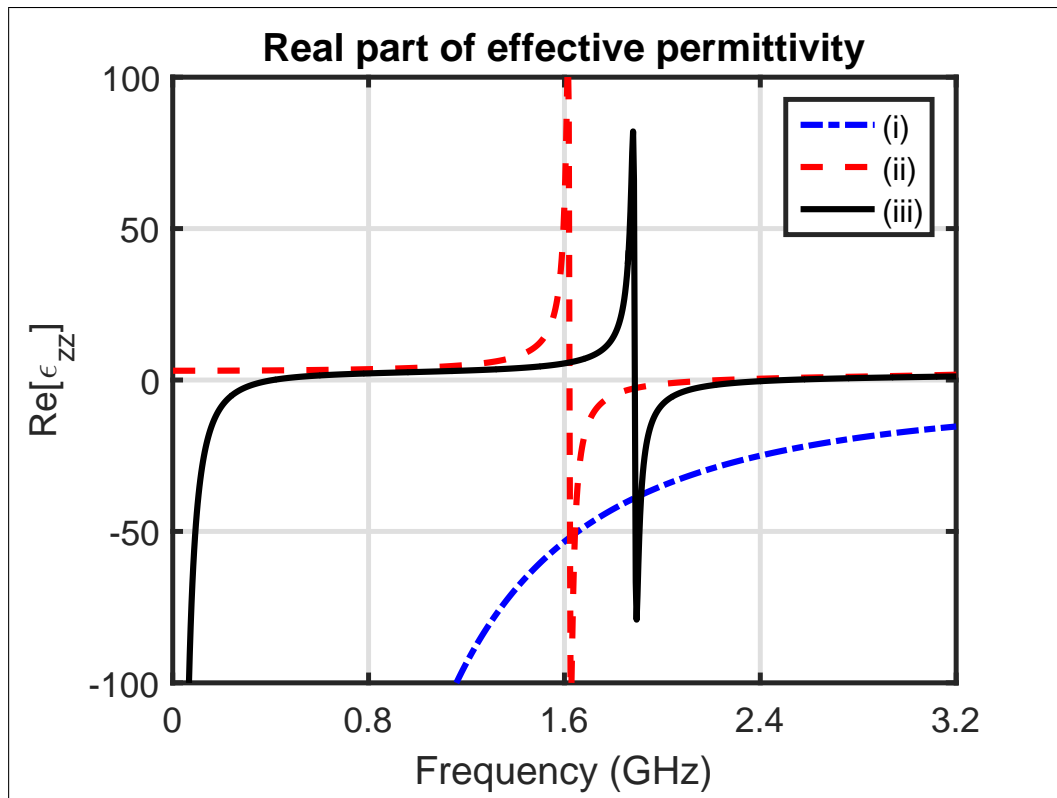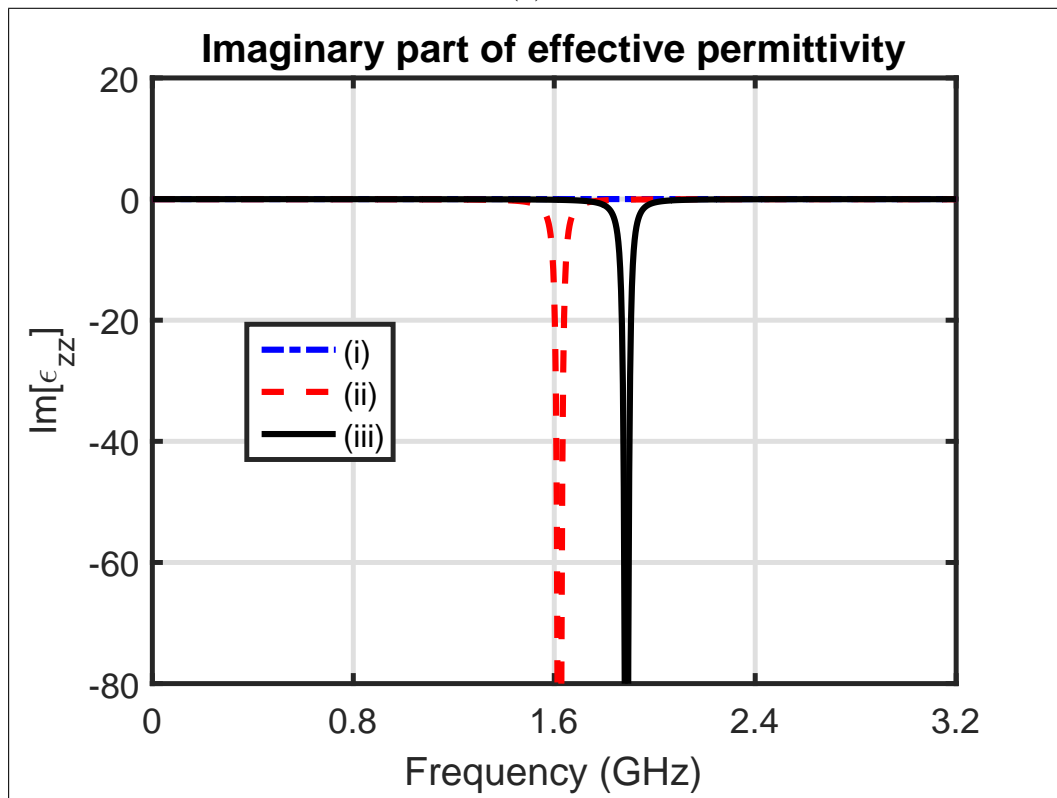
(b)

Figure 6.16: The (a) real and (b) imaginary parts of the effective permittivity of metamaterials composed of (i) PEC rods (ii) magnetodielectric rods and (iii) magnetodielectric coated PEC rods.
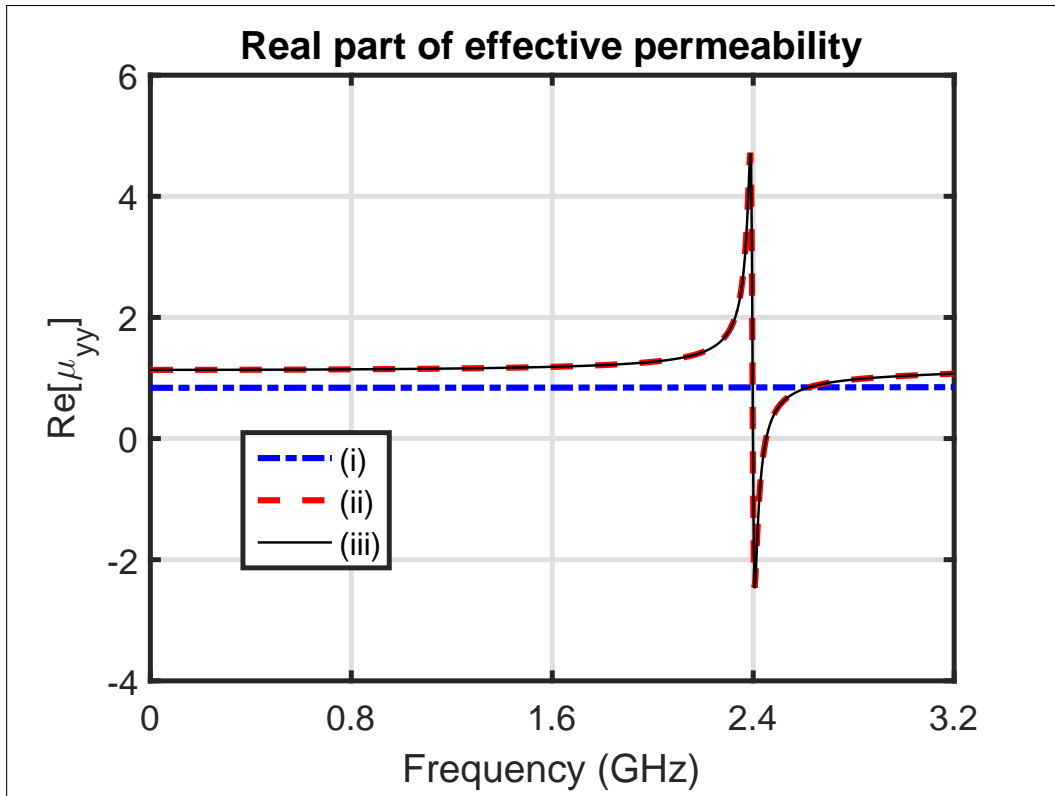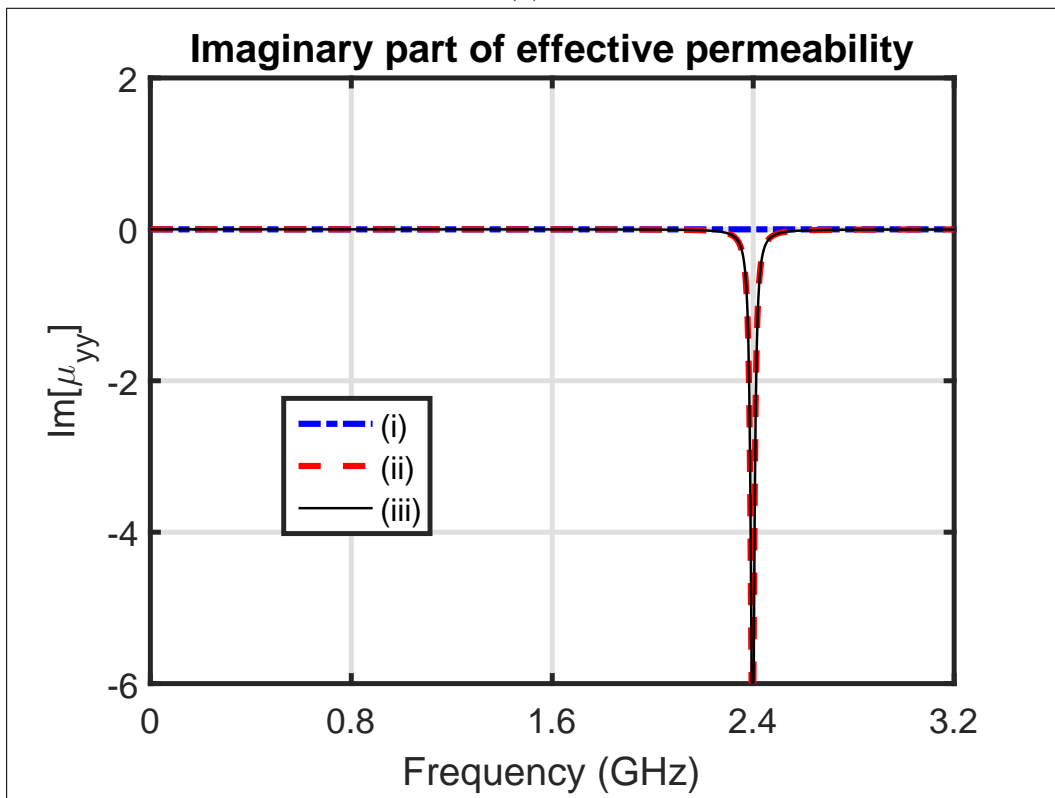
Figure 6.17: The (a) real and (b) imaginary parts of the effective permeability of metamaterials composed of (i) PEC rods (ii) magnetodielectric rods and (iii) magnetodielectric coated PEC rods.
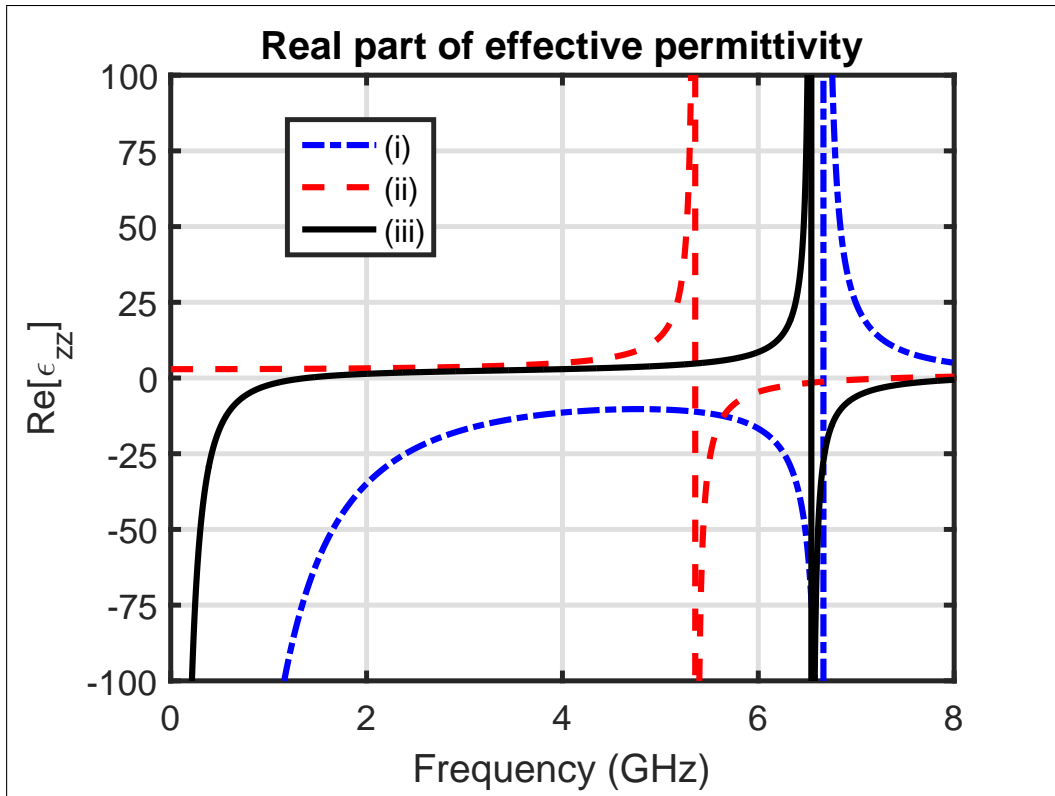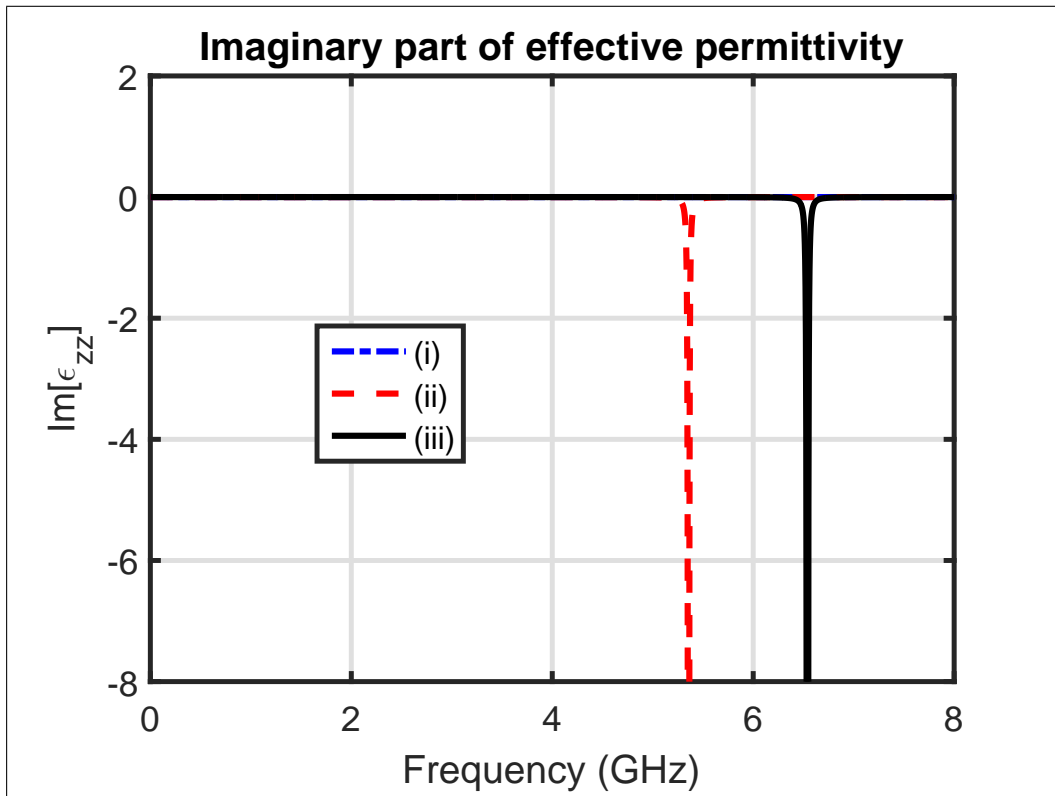
Figure 6.18: The (a) real and (b) imaginary parts of the effective permittivity of metamaterials composed of (i) PEC rods (ii) GaAs rods and (iii) GaAs coated PEC rods.

Real part of effective permeability

(a)

Imaginary part of effective permeability
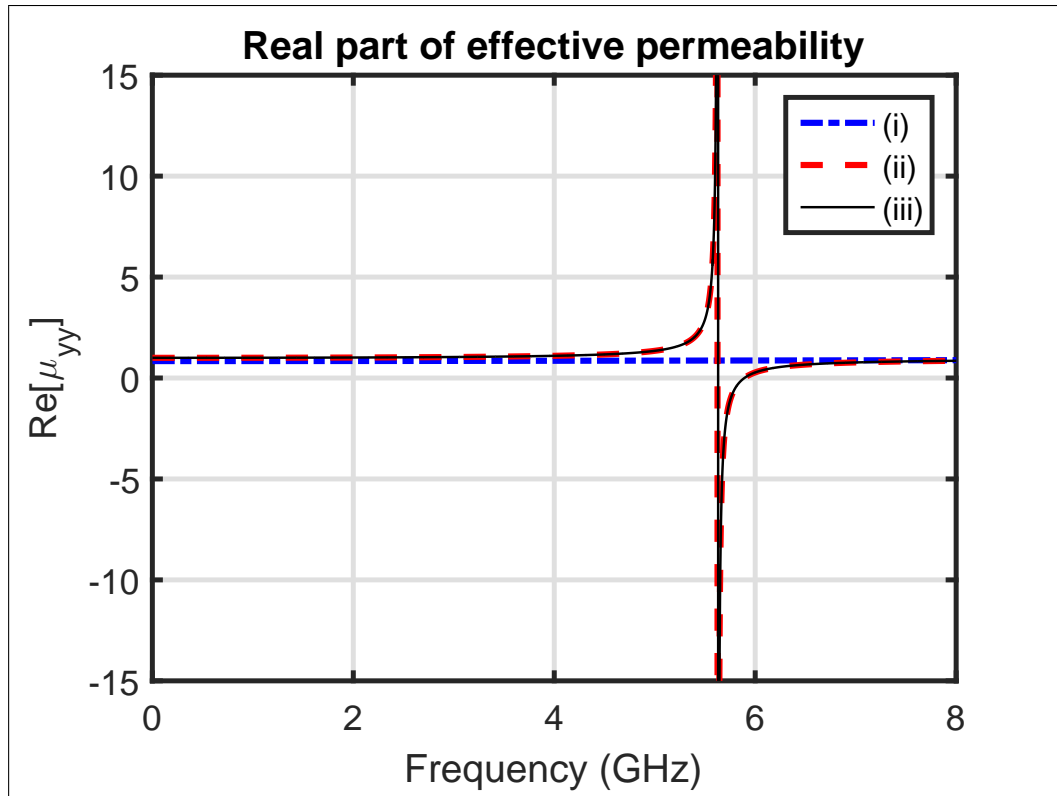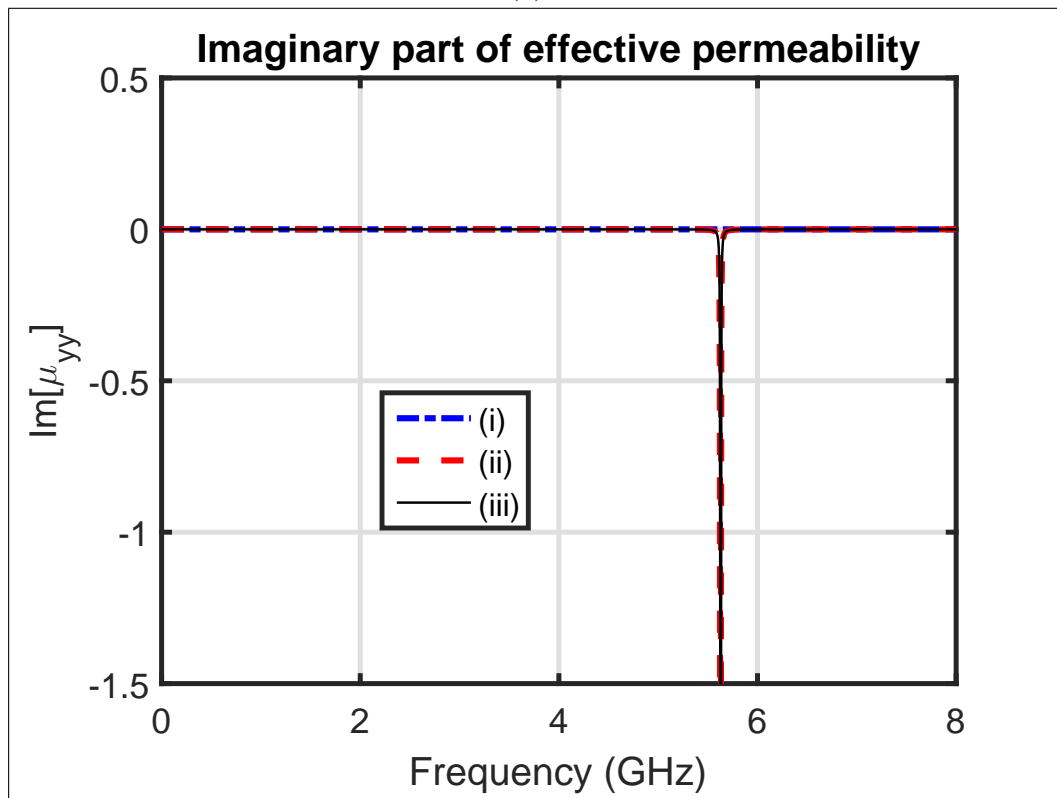
(b)

Figure 6.19: The (a) real and (b) imaginary parts of the effective permeability of metamaterials composed of (i) PEC rods (ii) GaAs rods and (iii) GaAs coated PEC rods.
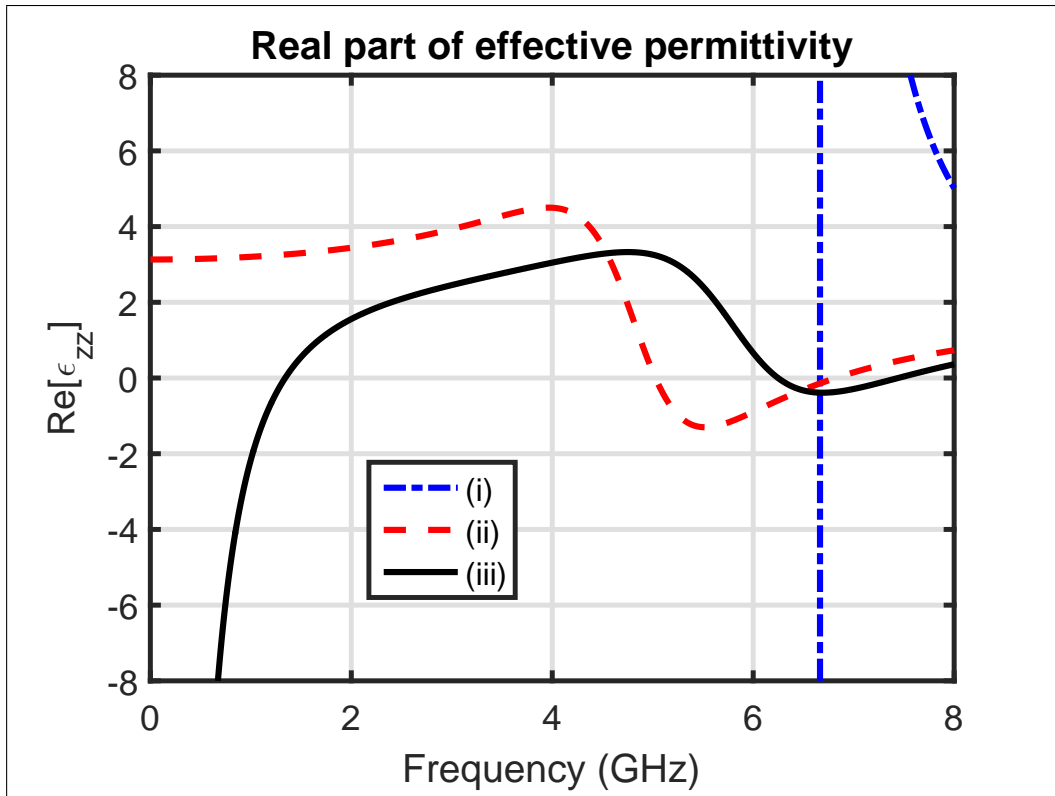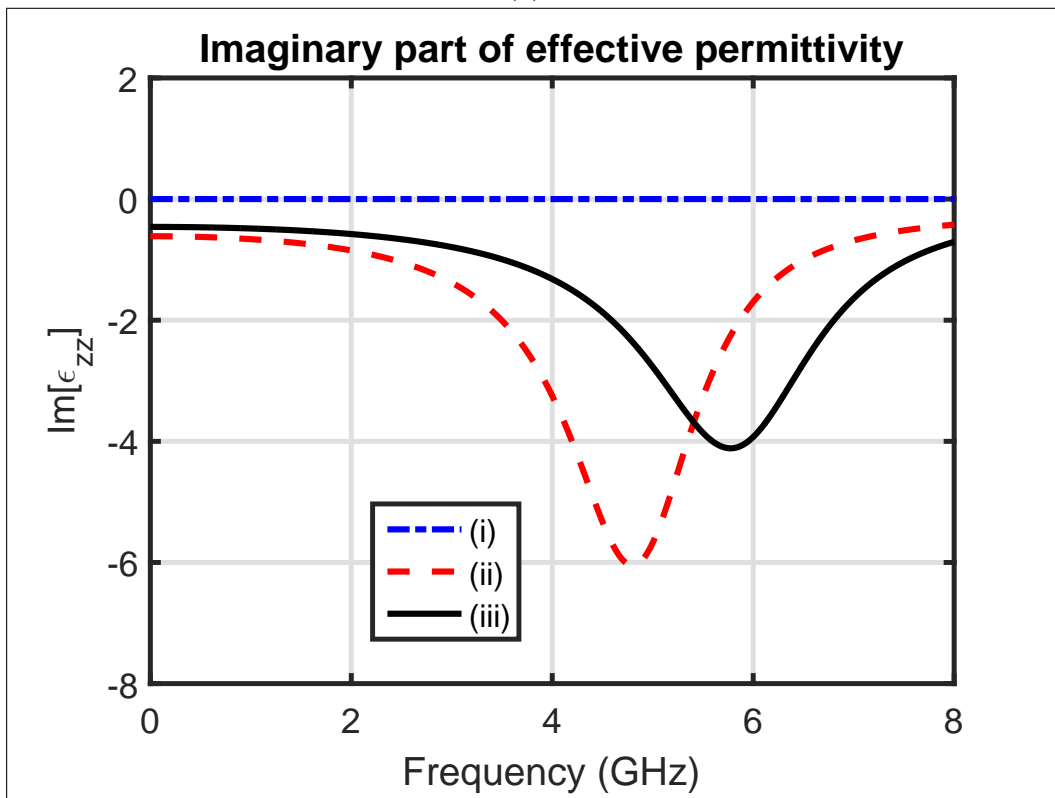
Figure 6.20: The (a) real and (b) imaginary parts of the effective permittivity of metamaterials composed of (i) PEC rods (ii) SiC rods and (iii) SiC coated PEC rods.
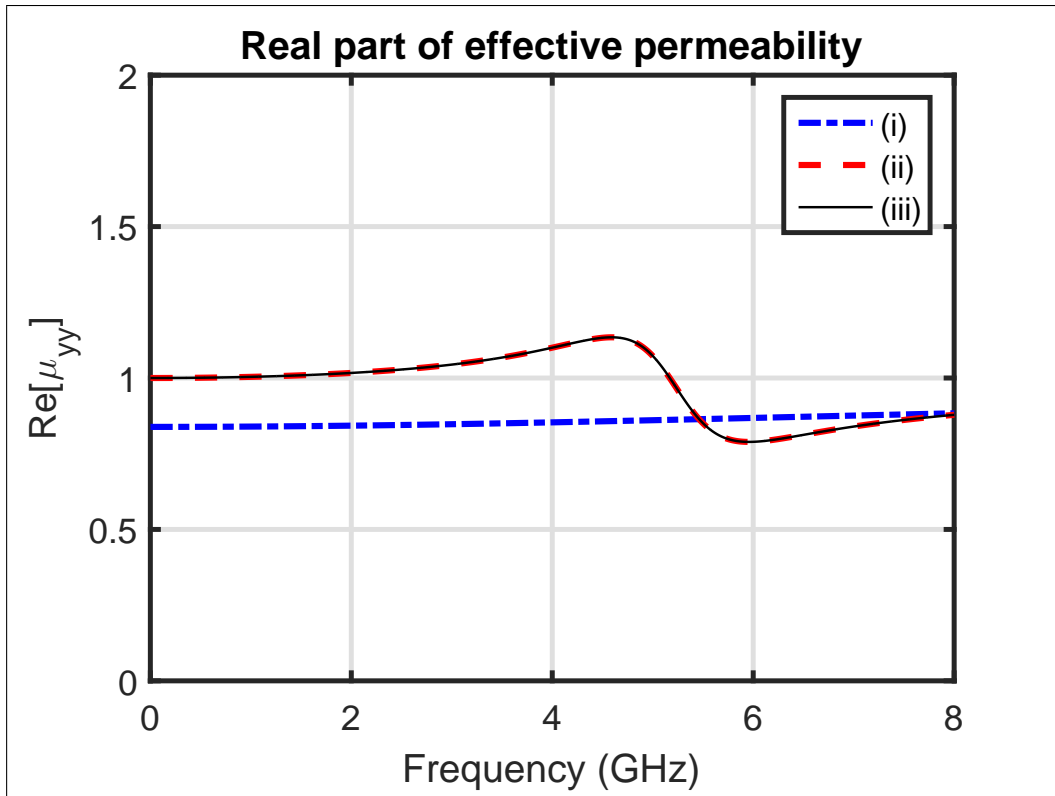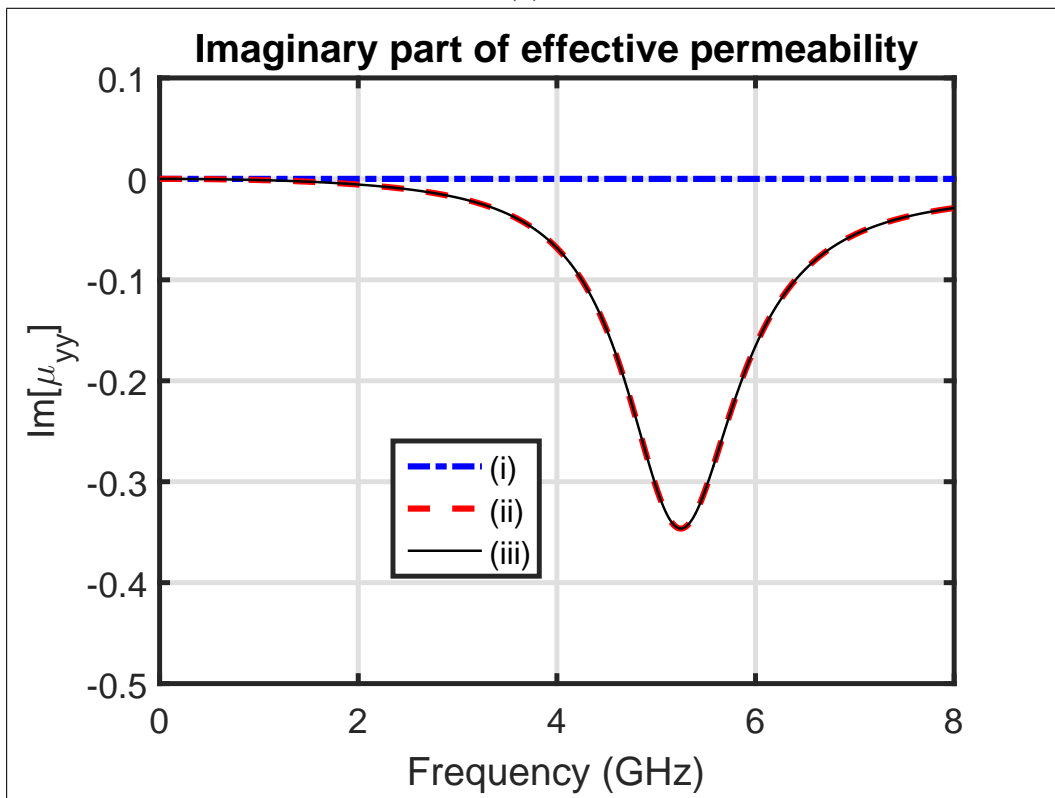
Figure 6.21: The (a) real and (b) imaginary parts of the effective permeability of metamaterials composed of (i) PEC rods (ii) SiC rods and (iii) SiC coated PEC rods.
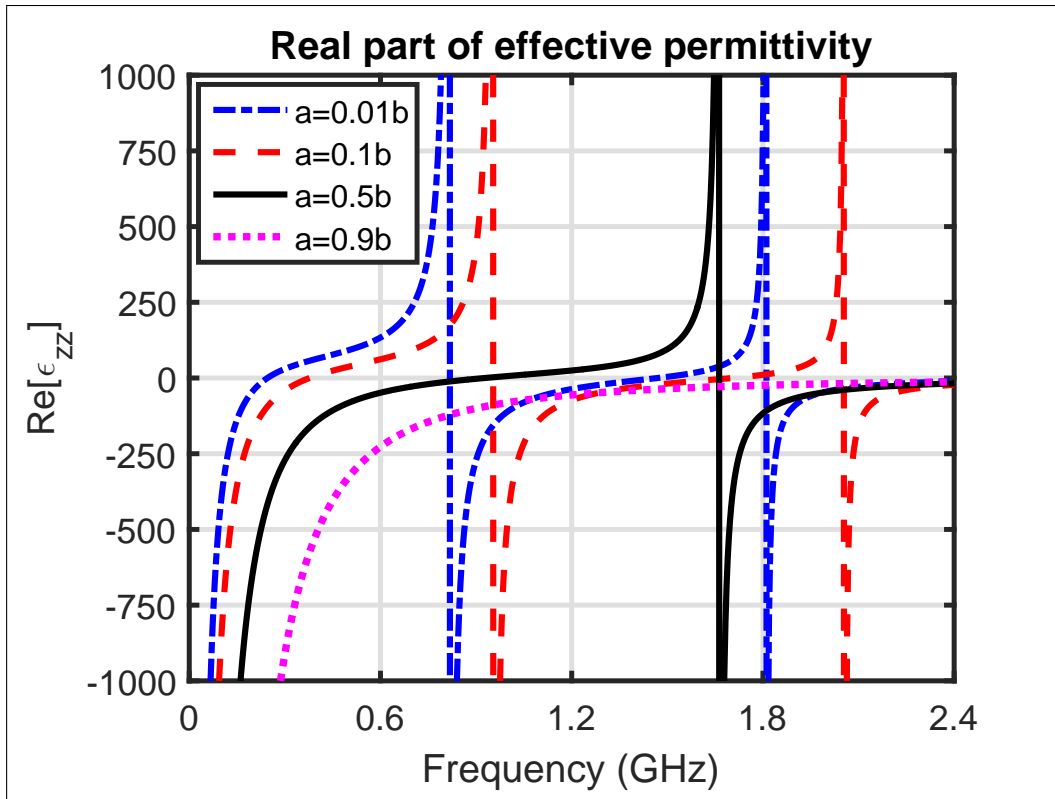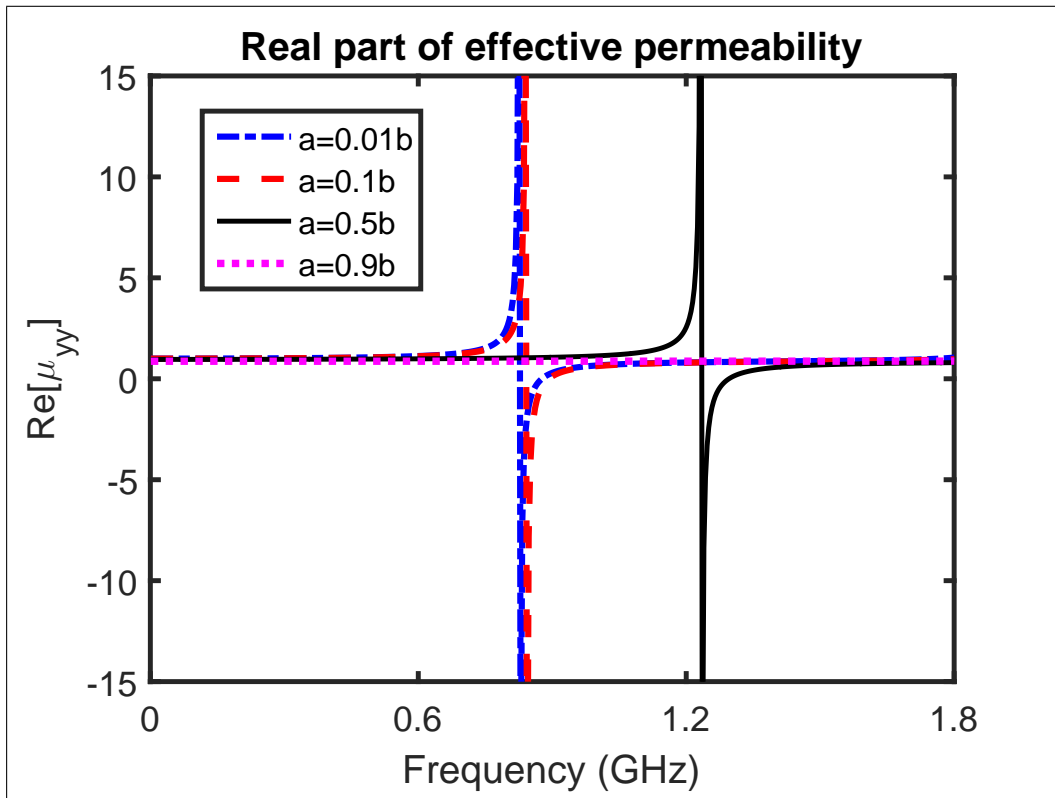
Figure 6.22: The influences of inner core radius a of PEC cylinder upon the (a) real part of the effective permittivity ϵ_{zz} and (b) real part of the effective permeability μ_{yy} of a metamaterial composed of BST coated perfectly conducting rods.

band. For the present analysis, the assumed values of SiC are taken to be $\epsilon_{rc} \approx 14.2$ - $j3.8$ and $\mu_{rc} = 1$.

In order to validate the proposed formulation presented in Sections 2 and 3, the normalized scattering widths of PEC, dielectric and dielectric coated conducting rods have been shown in Fig.(6.4). For PEC and dielectric rods, the radii are taken to be λ_o and the relative permittivity for a non-magnetic dielectric cylinder is taken to be 4. These parameters have been taken from Jin [85]. For a dielectric coated conducting rod, it is assumed that the radius of inner PEC cylinder is 50 mm whereas the radius of outer dielectric cylinder is 100 mm at an operating frequency of 1 GHz. In this case, the relative permittivity of non-magnetic dielectric coating is 9.8 [83]. From Fig.(6.4), it is found that the normalized scattering width (NSW) results are in good agreement with those reported in [83, 85]. Likewise, Fig.(6.5) deals with the real parts of the effective permittivity and permeability of a medium composed of BST rods [77]. In this case, the real parts of the effective permittivity and permeability as a function of reduced frequency d/λ_o have been shown and are consistent with those reported by Vynck et al. [77]. It should be noted that the truncation index criteria for summation appearing in Eq.(6.1.9) has been adopted from Li and Shen [83]. For the numerical results of the normalized scattering width given in Figs.(6.6-6.9) and Figs.(6.10-6.13), an operating frequency of 3 GHz has been assumed. In these figures, the radii of all types of cylindrical rods are taken to be $b = 50$ mm. Here NSW for a PEC rod has been used only for comparison. It should be noted that here $\sigma_N(\phi = 0°)$ corresponds to the normalized forward scattering width (NFSW) whereas $\sigma_N(\phi = 180°)$ represents the normalized backward scattering width (NBSW). The forward scattering width has applications in point to point communications whereas the backward scattering

width is important for radar related communication problems. In case of dielectric coated conducting rods considered in Figs.(6.6-6.9), the inner radius of PEC core is $a = 0.5b$. It is clear from Fig.(6.6) that the normalized scattering patterns for PEC, BST and BST coated PEC cylindrical rods are nearly the same. This is because the relative permittivity of BST material is very high and it seems to behave like a PEC material. It is seen that the scattering width pattern of a magnetodielectric material rod is fluctuating having NFSW = 9.78 dB and NBSW = -0.92 dB. It is clear from Fig.(6.7). In this case, the minimum value of NSW is -12.22 dB which occurs at angles $\phi = 158.4°$ and $201.6°$. In case of magnetodielectric coated conducting rod, the NFSW slightly decreases and becomes 9.47 whereas its NBSW increases to a value of 0.33 dB as compared to their respective values of magneto dielectric rod. In case of GaAs and GaAs coated conducting rods, it is found that the scattering patterns are fluctuating. In case of GaAs rod, the NFSW is 10.90 dB and NBSW is 4.70 dB. The minimum value of NSW for a GaAs rod comes out to be -9.70 dB which occurs at $\phi = 62.8°$ and $297.2°$. For a GaAs coated conducting rod, the values of NFSW and NBSW increases as compared to a GaAs rod without having inner PEC core. Thus, it is found from Fig.(6.8) that NFSW = 13.55 dB and NBSW = 6.92 dB for a GaAs coated conducting rod. As we know that the loss tangent of the SiC material is relatively large, therefore, it is seen from Fig.(6.9) that the scattering patterns of SiC and SiC coated conducting rods are not very much fluctuating. In case of SiC rod, we found that NFSW is 10.11 dB and NBSW is equal to -2.62 dB. In case of a SiC coated PEC rod, there exists slight enhancements in NFSW and NBSW as compared to SiC rod which are 10.35 dB and -1.16 dB respectively.

From Table 1, it is concluded that the highest value of NFSW is found for a

Table 6.1: Comparative study of normalized forward and backward scattering widths for various types of cylindrical rods considered in Figs.(6.6-6.9).

Types of rods	$NFSW(dB)$	$NBSW(dB)$
PEC rod	10.22	2.15
BST rod	10.37	2.31
BST coated conducting rod	10.14	2.08
Magnetodielectric rod	9.78	-0.92
Magnetodielectric coated conducting rod	9.47	0.33
GaAs rod	10.90	4.70
GaAs coated conducting rod	13.55	6.92
SiC rod	10.11	-2.62
SiC coated conducting rod	10.35	-1.16

GaAs coated conducting rod and the lowest value of NFSW is observed in case of magnetodielectric coated conducting rod. Likewise, the highest value of NBSW is observed for a GaAs coated conducting rod and the lowest value of NBSW is found for SiC rod. The influences of inner core radius a of a PEC rod upon the scattering pattern for various types of dielectric coated conducting rods have been shown in Figs. (6.10-6.13). It is found from Fig.(6.10) that for a BST coated conducting rod, the scattering pattern is almost independent of the variation of the inner core radius a, i.e., $a = 0.1b$, $0.5b$ and $0.9b$. This is because of the high value of the relative permittivity of the BST material. It is seen from Fig. (6.11) that the scattering pattern for a magnetodielectric coated PEC rod having $a = 0.1b$ is very much fluctuating. In this case, it is found that the minimum value of the NSW is -14.40 dB for specific angles ϕ = 42.9° and 317.1°. It is argued that for these specific angles, the scattered field form the inner PEC rod destructively interferes with the scattered field of magnetodielectric

coating. In this case, NFSW is 11.83 dB whereas NBSW is -8.57 dB. It is further studied that as the value of a increases to $0.5b$ and $0.9b$ then the value of NFSW decreases to 9.47 dB and 8.41 dB respectively. Likewise, the values NBSW increases to 0.32 and 1.26 with the increase of a from $0.5b$ to $0.9b$. Thus, it is concluded that by expanding the inner core of PEC cylinder inside the magnetodielectric coated conducting rod, the NFSW can be reduced whereas its NBSW can be enhanced. It is also observed that for $a = 0.5b$ and $0.9b$, the overall scattering pattern is not very much fluctuating in contrast to the scattering pattern for $a = 0.1b$. In Fig. (6.12), the influences of inner core radius a upon the scattering width of a GaAs coated conducting rod have been shown. It is studied that for $a = 0.1b$, the overall scattering pattern is fluctuating with the NFSW = 8.57 dB and NBSW = 5.37 dB. The minimum value of the scattering width is found to be -20 dB which occurs at angles $\phi = 56.25°$ and $303.75°$. Therefore, it is concluded that the GaAs coating significantly reduced the scattering width of a small radius PEC cylindrical rod at specific scattering or observation angles. As the value of inner core radius increases to $a = 0.5b$, it enhances the NFSW as well as the NBSW as compared to the respective NSW values in the case of $a = 0.1b$. In this case, we have NFSW = 13.56 dB and NBSW = 6.92 dB. For $a = 0.9b$, i.e., the GaAs coating layer is very thin then the values of NFSW and NBSW become closer to the corresponding values of the PEC cylindrical rod having radius b, i.e., NFSW = 8.90 dB and NBSW = 1.44 dB. In case of SiC coated conducting rod, it is observed that the maximum value of NFSW is 10.35 dB which exists for $a = 0.5b$ whereas the minimum value of NFSW which is equal to -2.95 dB occurs for $a = 0.1b$. This is clear from Fig. (6.13).

In the second part of numerical results, we investigate the effective parameters of

a metamaterial composed of dielectric coated conducting rods and their comparisons with the respective effective parameters of metamaterials composed of dielectric and PEC rods. These effective parameters have been shown in Figs.(6.14-6.21). The types of considered dielectric coatings are BST, magnetodielectric, GaAs and SiC. For all these Figs.(6.14-6.21), it is assumed that $b = (0.68d)/3$ for lattice spacing of $d = 25$ mm. This value of b has been adopted from [20] with $a = 0.01b$. The significance of the chosen value of $a = 0.01b$ has been discussed in the last paragraph of this section. In case of a metamaterial composed of PEC rods, the low frequency plasmonic epsilon negative BW which extends from zero frequency to plasma frequency f_p comes out to be 6.665 GHz. In this case, we have the plasma frequency of 6.665 GHz. Thus such type of a metamaterial composed of PEC rods can only be used for an ENG metamaterial and is very well known in the literature. Thus, the effective parameters of a metamaterial composed of PEC rods have been shown in the next coming figures only for comparison purposes. The effective parameters of metamaterials composed of BST rods and BST coated conducting rods have been shown in Figs.(6.14-6.15). In case of a BST rodded medium, it is studied that resonance frequency $f_r^\epsilon = 0.701$ GHz whereas its plasma frequency $f_p^\epsilon = 1.3122$ GHz. In this case, the resonant ENG BW can be found from f_p^ϵ - f_r^ϵ which is equal to 0.6112 GHz. For a BST coated conducting rodded medium, we have $f_r^\epsilon = 0.8178$ GHz and $f_p^\epsilon = 1.4689$ GHz. Based upon these frequencies, an ENG bandwidth of 0.6511 GHz has been found. This shows an enhancement of 0.0399 GHz in an ENG bandwidth as compared to an ENG bandwidth of a metamaterial composed of BST rods. This is clear from Fig.(6.14a). Also an additional plasmonic ENG bandwidth of 0.2453 GHz has been found in case of a metamaterial composed of BST coated conducting rods. On the other hand,

for the real part of the effective permeability of a metamaterial composed of BST rods, it is analyzed that resonance frequency $f_r^\mu = 0.8278$ GHz and plasma frequency $f_p^\mu = 0.8767$ GHz. Therefore, an MNG bandwidth of 0.0489 GHz is observed. For a metamaterial composed of BST coated conducting rods, a blueshift in resonance and plasma frequencies has been observed in contrast to a metamaterial composed of BST rods, i.e., $f_r^\mu = 0.8277$ GHz and $f_p^\mu = 0.8769$ GHz. Thus, a % increase in the MNG bandwidth of 0.6135 % in case of a metamaterial composed of BST coated conducting rods is observed as compared to a metamaterial composed of BST rods. From the above analysis, it is concluded that a metamaterial composed of BST rods has a DNG bandwidth of 0.0489 GHz whereas a metamaterial comprised of BST coated conducting rods has a DNG bandwidth of 0.0492 GHz. This shows that a % increase of 0.6135 % in a DNG bandwidth for a metamaterial composed of BST coated conducting rods has been observed as compared to a metamaterial composed of only BST rods as given by Vynck and co-workers [77]. From Figs.(6.14b) and (6.15b), it is seen that the imaginary parts of effective permittivity and effective permeability are zeros as expected because of lossless and non-magnetic natures of the BST and PEC materials.

In Figs.(6.16-6.17), the effective parameters of metamaterials composed of magnetodielectric and magnetodielectric coated conducting rods have been shown. It is studied that for a metamaterial composed of magnetodielectric rods, we have resonance frequency $f_r^\epsilon = 1.6206$ GHz and plasma frequency $f_p^\epsilon = 2.2443$ GHz. Therefore, an ENG bandwidth of 0.6237 GHz has been found for a metamaterial composed of magnetodielectric rods. In case of a metamaterial composed of magnetodielectric coated conducting rods, a blueshift in resonance and plasma frequencies has been

observed as compared to a metamaterial composed of magnetodielectric rods, i.e., f_r^ϵ = 1.8874 GHz and f_p^ϵ = 2.5052 GHz. In this case, we have an ENG bandwidth of 0.6178 GHz. Thus, by an insertion of a very thin PEC rod inside a magnetodielectric rod causes a reduction in an ENG bandwidth. In addition to this, there also exists a plasmonic ENG bandwidth of 0.4096 GHz for a metamaterial composed of magnetodielectric coated conducting rods. The absorption peaks associated with the imaginary parts of the effective permittivity which occur at resonance frequencies of these metamaterials are apparent from Fig.(6.16b). It is studied from Figs.(6.17a-6.17b) that the effective permeability characteristics of metamaterials composed of magnetodielectric and magnetodielectric coated conducting rods are almost identical. In both cases, we have $f_r^\mu \approx 2.3984$ GHz and $f_p^\mu \approx 2.4512$ GHz with an MNG bandwidth of 0.0528 GHz. As there exists no overlap among the ENG and MNG bandwidths for a magnetodielectric rodded metamaterial, therefore, no DNG bandwidth exists for a metamaterial composed of magnetodielectric rods. On the other hand, there exists an overlap among the ENG and MNG bandwidths for a metamaterial composed of magnetodielectric coated conducting rods and we have a DNG bandwidth of 0.0528 GHz. The effective parameters of metamaterials composed of GaAs and GaAs coated conducting rods have been shown in Figs.(6.18-6.19). For a metamaterial composed of GaAs rods, we have $f_r^\epsilon = 5.356$ GHz, $f_p^\epsilon = 7.425$ GHz, $f_r^\mu = 5.6249$ GHz and $f_p^\mu =$ 5.8913 GHz. Using these information, it is argued that ENG bandwidth is 2.069 GHz and MNG bandwidth is 0.2664 GHz. In case of a metamaterial composed of GaAs coated conducting rods, a blueshift in resonance as well as plasma frequencies associated with the effective permittivity and effective permeability is observed in contrast

to the respective frequencies for a metamaterial composed of GaAs rods. These frequencies become $f_r^\epsilon = 6.5416$ GHz, $f_p^\epsilon = 8.4197$ GHz, $f_r^\mu = 5.631$ GHz and $f_p^\mu = 5.8924$ GHz. Thus, we have ENG bandwidth of 1.8781 GHz and MNG bandwidth of 0.2614 GHz. In this case, an additional plasmonic ENG bandwidth of 1.3844 GHz has also been observed. From the above analysis, it is concluded that there exists a DNG bandwidth of 0.2664 GHz for a metamaterial composed of GaAs rods. It is observed that a metamaterial composed of GaAs rods has wider ENG, MNG and DNG bandwidths. This is because of the relatively large There is no DNG bandwidth for a metamaterial composed of GaAs coated conducting rods. In Figs.(6.20-6.21), the effective parameters of metamaterials composed of SiC rods and SiC coated conducting rods have been shown. A metamaterial composed of SiC rods has $f_r^\epsilon = 5.0272$ GHz and $f_p^\epsilon = 6.8204$ GHz which represents an ENG bandwidth of 1.7932 GHz. By inserting a very thin PEC rod having $a = 0.01b$ as the case under consideration inside this SiC rod at its center, a blueshift in resonance and plasma frequencies has been seen from Fig. (6.20a. Thus, for a metamaterial composed of SiC coated conducting rods, we have $f_r^\epsilon = 6.2472$ GHz and $f_p^\epsilon = 7.4419$ GHz which shows an ENG bandwidth of 1.1947 GHz. It is further investigated that for metamaterials composed of SiC and SiC coated conducting rods, no MNG bandwidths exist because of the very large value of the loss tangent associated with the dielectric constant of SiC material. This is obvious from Fig. (6.21a). From Figs.(6.20b) and (6.21b), it is studied that there exists absorption peaks of wider bandwidths associated with the imaginary parts of the effective permittivity and effective permeability. This is because of the inherently increased lossy nature of SiC material which in turn broadens the absorption peaks.

In order to highlight the important findings given in Figs.(6.14-6.21), a Table 2 is

Table 6.2: Comparative study of plasmonic ENG, resonant ENG, MNG and DNG bandwidths (BWs) for metamaterials composed of various types of rods considered in (6.14-6.21). All the table entries represent the bandwidths in GHz. Here MD is used for magnetodielectric.

Types of rods	Plasmonic ENG	Resonant ENG	MNG	DNG
PEC	6.6650	-	-	-
BST	-	0.6112	0.0489	0.0489
BST coated PEC	0.2453	0.6511	0.0492	0.0492
MD	-	0.6237	0.0528	-
MD coated PEC	0.4096	0.6178	0.0528	0.0528
GaAs	-	2.0690	0.2664	0.2664
GaAs coated PEC	1.3844	1.8781	0.2614	-
SiC	-	1.7932	-	-
SiC coated PEC	1.3414	1.1947	-	-

constructed which gives the comparative analysis of plasmonic ENG, resonant ENG, MNG and DNG bandwidths associated with the considered rodded metamaterials. From Table 2, some of the important conclusions about optimal designs of meta-materials can be drawn. The widest plasmonic ENG bandwidth is observed in case of a metamaterial composed of PEC rods which is expected whereas the narrowest plasmonic ENG bandwidth is found for a metamaterial composed of BST coated conducting rods. It is further investigated that a wider DNG bandwidth has been observed for a metamaterial composed of BST coated conducting rods in contrast to the corresponding DNG bandwidth of a metamaterial composed of BST rods. A metamaterial composed of magnetodielectric coated conducting rods has overlapping ENG and MNG bandwidths which gives rise to wider DNG bandwidth as compared to DNG bandwidth of a metamaterial composed of BST coated PEC rods. Among

all the considered metamaterials, the widest ENG, MNG and DNG bandwidths have been observed in case of a metamaterial composed of GaAs rods. In case of a metamaterial composed of SiC rods, we have only resonant ENG bandwidth whereas for a metamaterial composed of SiC coated conducting rods, we have resonant as well as plasmonic ENG bandwidths. The widest DNG bandwidth in case of a metamaterial composed of coated conducting rods has been observed for a metamaterial composed of magnetodielectric coated conducting rods.

For the present study, one of the crucial parameters is the radius a of an inner PEC core which significantly modify the effective parameters of a metamaterial composed of dielectric coated conducting rods. The influences of inner core radius upon the real parts of the effective permittivity and effective permeability of a metamaterial composed of only BST coated conducting rods have been shown in Fig.(6.22). It is already mentioned in Figs.(6.14-6.15) that if $a = 0.01b$ then there exists a DNG bandwidth for a metamaterial composed of BST coated rods. In this case, the coating layer is relatively thicker whereas the inner core is very thin. As the value of a increases to $0.1b$, $0.5b$ and $0.9b$ then there exists no DNG bandwidth for a metamaterial composed of BST coated conducting rods. That is why, we have used $a = 0.01$b for all the Figs.(6.14-6.21). This is discussed in detail as below. It is seen that as the value of a becomes $0.1b$, $0.5b$ and $0.9b$ then the corresponding plasmonic ENG bandwidth increases to 0.3772 GHz, 0.9272 GHz and 4.9894 GHz respectively. Likewise, for a = $0.1b$, we have f_r^ϵ = 0.95376 GHz, f_p^ϵ = 1.7038 GHz, f_r^μ = 0.8418 GHz and f_p^μ = 0.8925 GHz. Thus, there exists no DNG bandwidth because we have non-overlapping ENG and MNG bandwidths. In this case, we have ENG bandwidth of 0.7501 GHz and MNG bandwidth of 0.0507 GHz. By increasing the inner core radius a to $0.5b$,

blueshift in resonance as well as plasma frequencies has been observed as compared to the respective frequencies for $a = 0.1b$ case. They become $f_r^\epsilon = 1.6626$ GHz, $f_p^\epsilon = 3.164$ GHz, $f_r^\mu = 1.2348$ GHz and $f_p^\mu = 1.2957$ GHz. Thus, we have non-overlapping ENG and MNG bandwidths of 1.5014 GHz and 0.0609 GHz respectively which signifies that there exists no DNG bandwidth. In the last case of $a = 0.9b$ there exists no resonant ENG bandwidth and hence no DNG bandwidth. But we have $f_r^\mu = 5.5142$ GHz and $f_p^\mu = 5.5758$ GHz which represents an MNG bandwidth of 0.0616 GHz.

6.4   Concluding Remarks

An analysis about the scattering characteristics of an isolated dielectric coated perfectly electric conducting rods have been given by assuming realistic material coatings. These realistic materials are BST, GaAs, magnetodielectric and SiC. It is found that the GaAs coating significantly reduced the scattering width of a thin PEC cylindrical rod at specific observation angles. It is also observed that by increasing the inner core radius of PEC rod inside the magnetodielectric coated conducting rod, the NFSW can be diminished whereas its NBSW can be enhanced. Based upon the scattering characteristics of an individual coated conducting rod, the problem is further extended to calculate the effective parameters of a metamaterial composed of coated conducting rods using nonlocal homogenization theory. During the study, it is found that the widest plasmonic ENG bandwidth is observed in case of a metamaterial composed of PEC rods whereas the narrowest plasmonic ENG bandwidth is found for a metamaterial composed of magnetodielectric coated conducting rods. A % increase of 0.6135 % in a DNG bandwidth for a metamaterial composed of BST coated conducting rods has been observed as compared to a metamaterial composed of only BST rods which

were reported previously by Vynck and co-workers. Also an additional plasmonic ENG bandwidth has been found in case of a metamaterial composed of BST coated conducting rods. It is shown that a metamaterial composed of MD coated conducting rods has the wider DNG bandwidth as compared to metamaterials composed of BST rods and BST coated conducting rods. It is further studied that the widest ENG, MNG and DNG bandwidths have been observed in case of a metamaterial composed of GaAs rods. The narrowest ENG, MNG and DNG bandwidths have been observed for metamaterials composed of BST rods as reported by Vynck and co-workers. It is further observed that by increasing the inner core radius of BST coated conducting rods we can increase the plasmonic ENG bandwidth. The presented parametric analysis is helpful in designing of epsilon negative, mu negative and double negative metamaterials composed of coated conducting cylindrical rods.

Chapter 7

Conclusions and Recommendations for Future Research Work

A brief summary of the research work performed in this dissertation followed by the recommendations for the future research work is given as,

In Chapter 2, three most widely used scattering approximations such as Rayleigh-Gans (low frequency approximation), Volume integral physical optics (high frequency approximation) and Koh-Sarabandi (intermediate frequency approximation) are briefly reviewed for their applications and limitations based on the simulation results for the vertical and the horizontal polarizations. The influences of the various electrical and physical parameters such as the incident angle, size parameter, the relative permittivity of the disk on the backscattering cross sections $(\sigma_{hh}, \sigma_{vv})$ have been analyzed in these simulation results.

In Chapter 3, an analytic solution for the scattering of electromagnetic waves from a tilted thin circular dielectric disk is presented. The proposed theory is based on the above mentioned three different scattering approximations. It is investigated that by varying the orientation of the disk, the back-scattering cross section can be enhanced or diminished as compared to the disk having no tilt. It is found that by

varying the tilt angles of a tilted dielectric disk, one can enhance and diminish the back-scattering cross section as compared to the back-scattering cross section of the dielectric disk having no tilt for both types of considered incident polarizations. It is also investigated that for a low loss GaAs dielectric disk having tilt angles of 30° with the size parameter of 2, the back-scattering cross sections for both types of incident polarizations are almost equal to zero. In this way, we can hide a GaAs disk in the back-scattered direction to the incoming horizontally and vertically polarized waves. This result is interesting which finds applications in the stealth technology and can not be obtained for the GaAs disk having no tilt. $(\sigma_{hh}, \sigma_{vv})$

In Chapter 4, disk-shape effects on the radar backscattering cross sections both for the horizontal (σ_{hh}) and the vertical (σ_{vv}) incident polarizations are presented. Furthermore, an analytic theory for the scattering of electromagnetic waves from a thin dielectric triangular disk is presented. The proposed theory is based on the Koh-Sarabandi approximation for the electromagnetic wave scattering from a thin dielectric disk along with the spectral representation of the dyadic Green's function. The validity of the proposed formulation is justified by comparing it with the numerical method such as method of moments. For completeness, the scattering cross sections of a triangular disk for horizontal and vertical incident polarizations are compared with their respective scattering cross sections of elliptical, circular, semi-circular and square disks having same electromagnetic and geometrical parameters. It is studied that the back scattering cross sections for a low loss Gallium Arsenide triangular disk at a specific incidence angle can be made almost zero for both types of incident polarizations. This type of almost zero back scattering has applications in the stealth technology and remote sensing.

In chapter 5, an analysis about the back-scattered cross section from the sparse distribution of N-tilted thin dielectric circular disks have been presented. This analysis is based upon the three widely-known scattering approximations such as Rayleigh-Gans, Koh-Sarabandi and the Volumetric Integral Physical Optics. The influences of the various parameters including incident angle, size parameter of the disk, relative permittivity of the disk and spacing among disks upon the back-scattered cross sections have been shown and discussed for incident horizontal and vertical polarizations. Some optimal conditions are discussed where the back-scattered cross sections from a pair of tilted low loss Gallium Arsenide disks are almost zero for both types of incident polarization. These optimal conditions for a pair of tilted GaAs disks are also compared with a single tilted GaAs disk published previously. It is investigated that a pair of tilted GaAs disks significantly reduced the back-scattered cross sections as a compared to single GaAs tiled disk having same orientations as that of a pair of tilted disks. Such types of reduced back-scattered cross sections for both types of incident polarization find applications in the design of the modern remote sensing systems and stealth technologies.

In chapter 6, the effective parameters of a metamaterial composed of dielectric and dielectric coated conducting cylindrical rods are presented. For this research work, the scattering characteristics of an isolated dielectric and dielectric coated conducting rod with realistic dielectric materials such as $Ba_{0.5}Sr_{0.5}TiO_3$ (BST), Magnetodielectric, low loss Gallium Arsenide (GaAs) and Silicon Carbide (SiC) are analytically developed and studied. It is found that the gallium arsenide coating significantly reduced the scattering width from a thin perfectly electric conducting cylindrical rod

at specific observation angles. Moreover, the effective permittivity and permeability of metamaterials composed of two dimensional periodic arrangements of these dielectric coated cylindrical rods have also been studied. An increase in the double negative bandwidth of a metamaterial composed of barium strontium titanate coated conducting rods has been observed in contrast to the corresponding bandwidth of a metamaterial composed of only barium strontium titanate $Ba_{0.5}Sr_{0.5}TiO_3$ (BST) material rods. Also an additional plasmonic epsilon negative bandwidth has been found in case of a metamaterial composed of barium strontium titanate coated conducting rods. It is further observed that the widest epsilon negative, mu negative and double negative bandwidths exist for a metamaterial composed of gallium arsenide rods.

7.1 Future Research Direction

In Future Work, it is desired to make a metamaterial composed of dielectric disks as is made for cylindrical rods. For this, it is required to have dense distribution of dielectric disks instead of sparse distribution. In this case, nonlocal homogenization theory is used to find the effective parameters of a metamaterial composed of dielectric disks.

References

[1] G. T. Ruck, Barrick, Stuart and C. K. Krichbaum, Radar Cross Section Handbook, Plenum Press, New York, 1970.

[2] J. J. Bowman, T. B. A. Senior and P. L. E. Uslenghi, Electromagnetic and acoustic Scattering by Simple Shapes, North-Holland Publishing Company, The University of California, 1970.

[3] Ishimaru. A, Wave propagation and scattering in random media, Pearson Education, 1978.

[4] Tsang L., J. A. Kong and R. T. Shin, Theory of Microwave Remote Sensing, Wiley-Interscience, New York, 1985.

[5] Ulaby F. T. and Moore, Richard K. and Fung, Adrian K., Microwave remote sensing: Active and passive, *Pearson Education.*, 1986.

[6] Sarabandi K., Electromagnetic scattering from vegetation canopies, *PhD dissertation, the University of Michigan, Ann Arbor*, 1989.

[7] Cheng. D. K and others, Field and Wave electromagnetics, *Pearson Education.* , 1989.

[8] Ulaby F. T. and Elachi C., Radar polarimetry for geoscience applications, *Artech House*, 1990.

[9] Collin, E. R., Field theory of guided waves, *John Wiley & Sons.* , Vol. 5, 1990.

[10] Lindell, Ismo. V, Methods for electromagnetic field analysis, *John Wiley & Sons.* , 1992.

[11] Harrington. R. F, Field computation by moment methods, *Wiley-IEEE Press.* , 1993.

[12] Jin, Ya-Qiu, Electromagnetic scattering modelling for quantitative remote sensing, *World Scientific* , 1993.

[13] Siqueira P. R, Wave propagation and scattering in dense random media, *PhD dissertation, the University of Michigan, Ann Arbor*, 1996.

[14] Lin, Y. C., A fractal based coherent scattering and propagation model for forest canopies, *PhD dissertation, the University of Michigan, Ann Arbor*, 1997.

[15] Chiu, T. C., Electromagnetic scattering from rough surfaces covered with short branching vegetation, *PhD dissertation, the University of Michigan, Ann Arbor*, 1998.

[16] Tsang L. and Kong, Jin. Au, Scattering of Electromagnetic Waves: Advanced topics, *John Wiley & Sons* , Vol.26, 2004.

[17] Bladel V., and Jean. G, Electromagnetic fields, *John Wiley & Sons.* , 2007.

[18] Felsen L. B. and Marcuvitz N., Radiation and scattering of waves, *John Wiley & Sons*, Vol. 31, 1994.

[19] Ramo, Simon and Whinnery, John R. and Duzer V., Theodore, Fields and waves in communication electronics, *Wiley.*, 1994.

[20] Tai, Chen-To, Dyadic Green functions in electromagnetic theory, *Institute of Electrical & Electronics Engineers (IEEE).* , 1994.

[21] J. Volakis, J. Leonidas, T. B. Senior, Approximate boundary conditions in electromagnetics, *IET.* , No. 41, 1995.

[22] Volakis, J. Leonidas, Chatterjee, Arindam and Kempel, LeoJ. C, Finite element method for electromagnetics, *Universities Press.* ,1998.

[23] Il-Suek K., Advanced diffraction and wave propagation models for characterization of wireless communication channels, *PhD dissertation, the University of Michigan, Ann Arbor*, 2002.

[24] Tretyakov, Sergei, Analytical modeling in applied electromagnetics, *Artech House* , 2003.

[25] Tsang L. and Kong, J. Au, Ding, Kung-Hau, Scattering of Electromagnetic Waves: Theories and Applications, *John Wiley & Sons* , Vol. 27, 2004.

[26] Tsang, Leung and Kong, Jin Au and Ding, Kung-Hau and Ao,Chi On, Scattering of Electromagnetic Waves: Numerical Simulations, *John Wiley & Sons*, vol. 25, 2004.

[27] J. David, Radar and laser cross section engineering, *American Institute of Aeronautics and Astronautics, Inc.* , New York, 2005.

[28] Jin, Ya-Qiu, Theory and approach of information retrievals from electromagnetic scattering and remote sensing, *Springer Science & Business Media* , 2006.

[29] Stratton. J. A, Electromagnetic theory, *John Wiley & Sons.* , Vol. 33, 2007.

[30] A. Z. Elsherbeni, and V. Demir, and others, The finite-difference time-domain method for electromagnetics with MATLAB simulations, *SciTech Pub.* , 2009.

[31] Reitz. JR. R, Foundations of electromagnetic theory, *Pearson Education.* , 2009.

[32] Marqués, Ricardo and Martin, Ferran and Sorolla, Mario, Metamaterials with negative parameters: theory, design, and microwave applications, *John Wiley & Sons.* , Vol. 183, 2011.

[33] Pozar. D. M, Microwave engineering, *John wiley & sons.* , 2011.

[34] Bouche, Daniel and Molinet, Frédéric and Mittra, Raj, Asymptotic methods in electromagnetics, *Springer Science & Business Media* , 2012.

[35] J. Volakis, Integral Equation Methods for Electromagnetics, *The Institution of Engineering and Technology* , vol. 25, 2012.

[36] Born, Max and Wolf, Emil, Principles of optics: electromagnetic theory of propagation, interference and diffraction of light, *Elsevier.*, Vol. 2, 2013.

[37] C. W. Gibson, The Method of Moments in Electromagnetics, *CRC Press*, 2014.

[38] Balanis. C. A, Antenna theory: analysis and design, *John wiley & sons.* , 2016.

[39] Sadiku. M. NO, Numerical techniques in electromagnetics with MATLAB, *CRC press.* , 2018.

[40] Feinian W., Physics-based modeling of wave propagation for terrestrial and space communications, *PhD dissertation, the University of Michigan, Ann Arbor*, 2006.

[41] Eugene F. K., Radar cross section measurements, *Springer Science & Business Media*, 2012.

[42] Mahafza, Bassem. R, Radar Systems Analysis and Design Using MATLAB Third Edition, *CRC press* , 2013.

[43] Ulaby F. T. and Long D., Microwave Radar and Radiometric Remote Sensing: Active and passive, *Artech House*, 2015.

[44] Osipov, Andrey. V and Tretyakov, Sergei, Modern electromagnetic scattering theory with applications, *John Wiley & Sons* , 2017.

[45] Ishimaru A., Electromagnetic wave propagation, radiation, and scattering: from fundamentals to applications, *John Wiley & Sons* , 2017.

[46] H-P. Weil and C-H. Chu, "Scattering and absorption of electromagnetic radiation by thin dielectric disks," *Applied optics*, vol. 15, no. 7, pp.1832-36, 1976.

[47] R. A. Schiffer and K. O.Thielheim, "Light scattering by dielectric needles and disks," *Applied optics*, vol. 50, no. 4, pp.2476-2483, 1979.

[48] D. LeVine, "The radar cross section of dielectric disks," *IEEE Trans. on Antennas and Propagation*, vol. 32, no. 1, pp. 6-12, 1984.

[49] D. Le Vine, Schneider, Lang, and Carter, "Scattering from thin dielectric disks," *IEEE Trans. on Antennas and Propagation*, vol. 33, no. 12, pp. 1410–1413, 1985.

[50] Sarabandi K., F. T. Ulaby, and T. A. Senior, "Millimeter wave scattering model for a leaf," *Radio science*, Vol. 25, no. 1, pp. 9-18, 1990.

[51] M. A. Karam, A. K. Fung, and Y. M. M. Antar, "Electromagnetic wave scattering from some vegetation samples," *IEEE Trans. on Antennas and Propagation*, Vol. 26, no. 6, pp. 799–808, 1988.

[52] M. A. Karam, Adrian K. Fung, "Leaf-shape effects in electromagnetic wave scattering from vegetation," *IEEE Trans. on Geoscience and Remote Sensing*, Vol. 27, no. 6, pp. 687-697, 1989.

[53] M. A. Karam, Adrian K. Fung, "Electromagnetic wave scattering from a forest or vegetation canopy: ongoing research at the University of Texas at Arlington," *IEEE Trans. on Antennas and Propagation*, Vol. 35, no. 2, pp. 18-26, 1993.

[54] M. A. Karam, "Bridging the quasi-static and the physical optics approximations: An elliptic disk case," *Applied optics*, Vol. 37, no. 9, pp. 1666-1673, 1998.

[55] Y. Oh and J-Y. Hong. "Re-examination of analytical models for microwave scattering from deciduous leaves," *IET Microwaves, Antennas and Propagation*, Vol. 1, no. 3, pp. 617-623, 2007.

[56] II-Suek Koh and K. Sarabandi, "A new approximate solution for scattering by thin dielectric disks of arbitrary size and shape," *IEEE Trans. on antennas and propagation*, Vol. 53, no. 6, pp. 1920-1926, 2005.

[57] Du Yang, *Electromagnetic Scattering: A Remote Sensing Perspective.* World Scientific Publishing Co., Inc., 2017.

[58] V. G. Veselago, "The electrodynamics of substances with simultaneously negative values of ϵ and μ," Soviet Physics Uspekhi **10**, 509–514 (1968).

[59] J. P. Pendry, A. J. Holden, W. J. Stewart and I. Youngs, "Extremely low frequency plasmons in metallic mesostructures," Physical Review Letters **76**, 4773–4776 (1996).

[60] J. P. Pendry, A. J. Holden, D. J. Robbins and W. J. Stewart, "Magnetism from conductors and enhanced nonlinear phenomena," IEEE Trans. on Microwave Theory and Techniques **47**, 2075–2084 (1999).

[61] D. R. Smith, W. J. Padilla, D. C. Vier, S. C. Nemat-Nasser and S. Schultz, "Composite medium with simultaneously negative permeability and permittivity," Physical Review Letters **84**, 4184–4187 (2000).

[62] R. A. Shelby, D. R. Smith and S. Schultz, "Experimental verification of a negative index of refraction," Science **292**, 77–79 (2001).

[63] A. Alu and N. Engheta, "Guided modes in a waveguide filled with a pair of single-negative (SNG), double-negative (DNG), and/or double-positive (DPS) layers ," IEEE Trans. on Microwave Theory and Techniques **52**, 199–210 (2004).

[64] A. Alu and N. Engheta, "Pairing an epsilon-negative slab with a mu-negative slab: resonance, tunneling and transparency," IEEE Trans. on Antennas and Propagation **51**, 2558–2571 (2003).

[65] A. Alu and N. Engheta, "Polarizabilities and effective parameters of collections of spherical nanoparticles formed by pairs of concentric double-negative (DNG),

single-negative (SNG) shells, and/or double-positive (DPS) metamaterial layers ," Journal of Applied Physics **97**, 094310-1–12 (2005).

[66] N. Engheta, A. Alu, M. G. Silveirinha, A. Salandrino and J. Li, "DNG, SNG, ENZ and MNZ metamaterials and their potential applications," IEEE MELECON, 16–19, Benalmadena, Spain, May 2006.

[67] R. S. Kshetrimayum, "A brief intro to metamaterials," IEEE Potentials **23**, 44–46 (2004).

[68] Z. A. Awan, "Reflection and transmission properties of a wire grid embedded in a SNG or SZ medium," Journal of Modern Optics **61**, 1147–1151 (2014).

[69] Z. A. Awan, "Nonlocal effective parameters of a coated sphere medium," Journal of Modern Optics **62**, 528–535 (2015).

[70] P. A. Belov, S. A. Tretyakov and A. J. Viitanen, "Dispersion and reflection properties of artificial media formed by regular lattices of ideally conducting wires," Journal of Electromagnetic Waves and Applications **16**, 1153-1170 (2002).

[71] Z. A. Awan, "Imperfections for an equivalent surface impedance of a uniaxial wire medium," Journal of Electromagnetic Waves and Applications **28**, 1834-1855 (2014).

[72] J. Machac, P. Protiva and J. Zehentner, "Isotropic epsilon-negative p articles," IEEE/MTT-S International Microwave Symposium, 1-4, Honolulu, HI, USA, 3–8 June 2007.

[73] Z. A. Awan and A. A. Rizvi, "Random errors for a nonlocal Epsilon Negative medium," Optics Communications **295**, 239–248 (2013).

[74] Z. A. Awan and A. A. Rizvi, "Positional disorder for a medium composed of loaded wire dipoles," Optics Communications **309**, 338–343 (2013).

[75] M. G. Silveirinha, "Nonlocal homogenization model for a periodic array of ϵ negative rods," Physical Review E **73**, 046612-1–10 (2006).

[76] L. Peng, L. Ran, H. Chen, H. Zhang, J. A. Kong and T. M. Grzegorczyk,"Experimental observation of left-handed behavior in an array of standard dielectric resonators," Physical Review Letters **98**, 157043-1–4 (2007).

[77] K. Vynck, D. Felbacq, E. Centeno, A. I. Căbuz, D. Cassagne and B. Guizal,"All-dielectric rod-type metamaterials at optical frequencies," Physical Review Letters **102**, 133901-1–4 (2009).

[78] L. Peng, L. Ran and N. A. Mortensen,"Achieving anisotropy in metamaterials made of dielectric cylindrical rods," Applied Physics Letters **96**, 241108-1–3 (2010).

[79] Y. Li and H. Ling, "Investigation of wave propagation in a dielectric rod array: toward the understanding of HF/VHF propagation in a forest," IEEE Trans. on Antennas and Propagation **58**, 4025–4032 (2010).

[80] F. J. V. Valero and M. N. Vesperinas,"Composite of resonant dielectric rods: A test of their behavior as metamaterial refractive elements," Photonics and Nanostructures: Fundamentals and Applications **10**, 423–434 (2012).

[81] C. A. Valagiannopoulos and S. A. Tretyakov, "Symmetric absorbers realized as gratings of PEC cylinders covered by ordinary dielectrics," IEEE Trans. on Antennas and Propagation **62**, 5089–5098 (2014).

[82] C. D. Giovampaola and N. Engheta, "Digital metamaterials," Nature Materials **13**, 1115–1121 (2014).

[83] C. Li and Z. Shen, "Electromagnetic scattering by a conducting cylinder coated with metamaterials," Progress In Electromagnetics Research **42**, 91–105 (2003).

[84] C. A. Balanis, Advanced Engineering Electromagnetics, Wiley, New York, 1989.

[85] J. M. Jin, Theory and computation of electromagnetic fields, Wiley, New Jersey, 2015.

[86] R. A. Shore and A. D. Yaghjian, "Traveling waves on two and three-dimensional periodic arrays of lossless acoustic monopoles, electric dipoles, and magnetodielectric spheres," Rep. AFRL-SN-HS-TR-2006-0039, Air Force Res. Lab: Hanscom Air Force Base, MA, 1–203 (2006).

[87] K. Seeger, "Microwave dielectric constants of silicon, gallium arsenide, and quartz," Journal of Applied Physics **63**, 5439–5443 (1988).

[88] J. Kuang and W. Cao, "Silicon carbide whiskers: preparation and high dielectric permittivity," Journal of American Ceramic Society **96**, 2877–2880 (2013).

[89] M. G. Silveirinha, "Metamaterial homogenization approach with application to the characterization of microstructured composites with negative parameters," Physical Review B **75**, 115104 (2007).

[90] M. G. Silveirinha, "Generalized Lorentz-Lorenz formulas for microstructured materials," Physical Review B **75**, 245117 (2007).

[91] C. R. Simovski, "Material parameters of metamaterials (a review)," Optics and Spectroscopy **107**, 726–753 (2009).

[92] C. R. Simovski and S. A. Tretyakov, "Local constitutive parameters of metamaterials from an effective-medium perspective," Physical Review B **75**, 195111 (2007).

[93] Georg B. Arfken and Hans Weber and Donald Arthur Spector, *Mathematical methods for physicists*, 1996.

Turnitin Originality Report

Interaction of Electromagnetic Waves with Dielectric Disks and Rods by Hassan Ullah .

turnitin

From DRSM (DRSM L)

- Processed on 03-Sep-2021 14:34 PKT
- ID: 1640670024
- Word Count: 29033

Similarity Index
12%
Similarity by Source

Internet Sources:
4%
Publications:
11%
Student Papers:
1%

sources:

1 1% match (publications)
Farah R. Abbasi, Z. A. Awan, Arshad Hussain. "Backscattering cross-section from a metamaterial coated sphere covered with a metasurface", International Journal of Microwave and Wireless Technologies, 2021

2 1% match (publications)
Z. A. Awan, Divitha Seetharamdoo. "Scattering characteristics of a metasurface covered chiral sphere", Applied Optics, 2020

3 1% match (Internet from 28-Feb-2021)
https://www.x-mol.com/paper/journal/1401

4 < 1% match (publications)
"Handbook of Antenna Technologies", Springer Science and Business Media LLC, 2016

5 < 1% match (publications)
I.-S. Koh. "A New Approximate Solution for Scattering by Thin Dielectric Disks of Arbitrary Size and Shape", IEEE Transactions on Antennas and Propagation, 6/2005

6 < 1% match (publications)
Z.A. Awan. "Nonlocal effective parameters of a coated sphere medium", Journal of Modern Optics, 2014

7 < 1% match (publications)
Z.A. Awan. "Scattering characteristics of a chiral-coated cylindrical reflector embedded in a double-negative metamaterial", Journal of Modern Optics, 2015

8 < 1% match (publications)
Z.A. Awan. "Reflection and transmission properties of a wire grid embedded in a SNG or SZ medium", Journal of Modern Optics, 2014

9 < 1% match (Internet from 18-Oct-2012)
http://deepblue.lib.umich.edu/bitstream/2027.42/21059/1/rl0904.0001.001.txt

10 < 1% match (Internet from 02-Oct-2009)
http://deepblue.lib.umich.edu/bitstream/2027.42/21430/1/rl2407.0001.001.txt

11 < 1% match (Internet from 24-Mar-2014)